

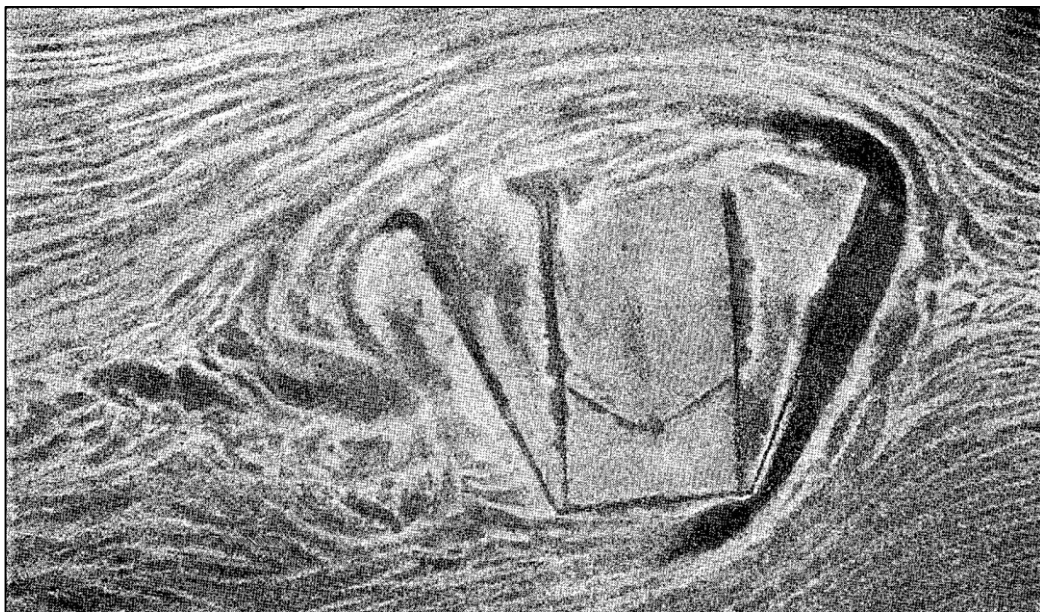
Ph.D. Program in Civil, Chemical and Environmental Engineering



Curriculum in Fluid Dynamics and Environmental Engineering

Department of Civil, Chemical and Environmental Engineering

Polytechnic School, University of Genoa, Italy.



(from Bastanoff and Witkiewitch, 1926)

**The role of turbulence in particle-fluid interaction
as induced by the outer geometry
of catching-type precipitation gauges**

Arianna Cauteruccio

THE ROLE OF TURBULENCE IN PARTICLE-FLUID INTERACTION
AS INDUCED BY THE OUTER GEOMETRY OF CATCHING-TYPE
PRECIPITATION GAUGES

BY

ARIANNA CAUTERUCCIO

*Dissertation discussed in partial fulfilment of
the requirements for the Degree of*

DOCTOR OF PHILOSOPHY

*Civil, Chemical and Environmental Engineering
curriculum in Fluid Dynamics and Environmental Engineering,
Department of Civil, Chemical and Environmental Engineering, University of Genoa, Italy*



April, 2020

Adviser:

Prof. Luca G. Lanza – Dep. of Civil, Chemical and Environmental Engineering, University of Genova

External Reviewers:

Prof. Patrick Enda O’Connell – School of Engineering, Newcastle University, UK

Prof. Julie Mireille Thériault – Dep. of Earth and Atmospheric Sciences, University of Québec at Montréal, Canada

Examination Committee:

Prof. Alessandro Bottaro – Dep. of Civil, Chemical and Environmental Engineering, University of Genova

Prof. Giorgio Bellotti – Dep. of Engineering, University of Roma

Prof. Daniele Rocchi – Dep. of Mechanical Engineering, Politecnico di Milano

Ph.D. program in Civil, Chemical and Environmental Engineering

Curriculum in Fluid Dynamics and Environmental Engineering

Cycle XXXII

*To those who know that dedication is
the best way towards a masterpiece*

Acknowledgments

I'm grateful to my family for their support throughout my whole PhD experience and their continuous interest in my post degree curriculum.

I would like to thank my thesis adviser, Prof. Luca G. Lanza, for encouraging me to participate as a candidate for the admission to the XXXII cycle of PhD program and for the high quality of the research topics addressed in this thesis work. He has accompanied me with patience and expertise in my growth as a researcher. He allowed me to experience various aspects of research, from numerical fluid dynamic computation to laboratory testing in the wind tunnel and field measurements.

I appreciated very much the stimulating atmosphere where I was able to conduct my research activity, including my colleagues and the staff of the DICCA laboratory. In the last three years I had the opportunity to join the research performed within the WMO/CIMO Lead Center "B. Castelli" on Precipitation Intensity and the national research project PRIN20154WX5NA: "Reconciling precipitation with runoff: the role of understated measurement biases in the modelling of hydrological processes". One interesting and formative aspect of my thesis work has been the extensive test session I conducted in the wind tunnel facilities of DICCA and Politecnico di Milano.

Finally, I would like to thank the PhD board of Professors for the insightful along-way discussions and the external reviewers of the thesis manuscript, Prof. Patrick Enda O'Connell and Prof. Julie Mireille Thériault, for the very useful and constructive comments, which actually improved my work.

Abstract

This thesis work investigates the particle-fluid interaction of hydrometeors along the terminal part of their fall trajectories, while approaching the collector of catching-type precipitation gauges in windy conditions. Both the turbulence generated by the bluff body aerodynamics of precipitation gauges when impacted by the wind and the free-stream turbulence inherent to the natural wind are addressed to assess their role in precipitation measurements.

The bluff body aerodynamics of precipitation gauges induces deviations in the trajectories of the approaching hydrometeors due to the acceleration, updraft and turbulence development upstream and above the collector of the gauge. The resulting wind-induced errors were studied in the literature using different approaches – field measurement campaigns, numerical simulations and wind tunnel experiments. In this work, the numerical approach based on Computational Fluid Dynamic (CFD) simulation, which reduces, when compared with field observations, the time and resources needed to investigate different configurations by varying the wind speed, type of precipitation and gauge geometry, is employed. A Lagrangian Particle Tracking (LPT) model provides the catch ratios as a function of the particle size and wind speed. The LPT model, already available from the literature, was adapted to simulate the trajectories of water droplets when falling through the atmosphere and approaching the gauge collector by parameterizing liquid particles with spherical shape and using suitable drag coefficient equations.

The first part of the work aims to validate the numerical approach against a dedicated, innovative and robust experimental campaign obtained by means of Wind Tunnel (WT) experiments (flow velocity measurements, Particle Image Velocimetry and video tracking of water drops) conducted in the wind tunnel facilities available at DICCA and at Politecnico di Milano (within the PRIN 20154WX5NA project). The video tracking experimental setup allowed to compare observed and simulated trajectories under various wind velocity and drop size conditions, and to validate the Lagrangian Particle Tracking model, here adapted to simulate particles falling at a different vertical velocity than the terminal one.

Comparison and validation of numerical simulation results against field-measured data introduce the problem of confronting this simplified approach with the natural atmospheric conditions actually affecting operational instruments in the field. Natural wind fields are indeed characterized by turbulent fluctuations, especially near to the ground where precipitation gauges are located. Dedicated CFD simulations with various turbulence generating solutions, based on imposing specific boundary conditions or inserting suitable obstacles designed to achieve the desired level of free-stream turbulence upstream of the gauge, were performed.

Wind tunnel measurements were performed in the DICCA facility using, as a turbulence-generating device, a fixed solid fence with a regular square mesh inserted upstream of a calyx shaped gauge. CFD simulations were performed reproducing the same conditions and results were validated by comparison with WT measurements. The comparison between the uniform and turbulent free-stream conditions showed that the normalized updraft in the upwind part, upstream of the centre of the collector, and the downdraft in the downwind part are less accentuated in the turbulent free-stream configuration than in uniform free-stream conditions. This is ascribable to the energy dissipation induced by turbulent fluctuations. The

dissipative effect of the free-stream turbulence also has a damping role on the acceleration of the flow above the collector as demonstrated by CFD results.

The overall free-stream turbulence effect on the collection performance of the gauges was quantified by computing and comparing the Collection Efficiency (CE) values in uniform and turbulent free-stream conditions. Results demonstrated that the CE values are higher in turbulent free-stream conditions. The effect of the free-stream turbulence on the collection efficiency of the *Hotplate*[®] snow gauge was investigated, and the literature turbulence intensity level (from Øistad, 2015) impacting on the gauge by was obtained in the simulation by imposing a constant turbulent kinetic energy value as a boundary condition upstream of the gauge. The calculated catch ratios are larger for the free-stream turbulence condition with respect to the uniform one for all characteristic sizes of snowflakes. Consequently, the same effect was observed in the calculated CE values.

In addition, in order to introduce a realistic level of turbulence at the gauge collector elevation in the simulation, wind speed measurements obtained from a 3D ultrasonic anemometer in the Nafferton Farm site (UK), recorded at high frequency (20 Hz) and at the gauge elevation, were analysed to calculate the free-stream turbulence intensity values for various wind speeds. This was used to perform a CFD simulation on a chimney shaped gauge and to calculate its effect on the collection performance. To better reproduce the decay of the turbulence intensity in space and its effect on the gauge, Large Eddy Simulations (LES) were also performed in both uniform and turbulent free-stream conditions while simulating the trajectories of solid precipitation particles, which are more sensitive than raindrops to the turbulent fluctuations. Results, in terms of the catch ratio for each characteristic size of snowflakes, show a different behaviour when compared to the uniform conditions. A larger free-stream turbulence intensity induces a more pronounced undercatch for small size particles (less than 2 mm) with respect to the uniform case, while the undercatch is reduced for larger particles. This is due to the greater aptitude of the small size particles to follow the turbulent velocity fluctuations, while larger particles are more inertial, and to the reduced velocity components that particles cross in turbulent free-stream conditions near the gauge body. The obtained CE values are higher in turbulent free-stream conditions, confirming the observations already obtained for the airflow features, where a potential overestimation of the undercatch obtained in uniform free-stream conditions was hypothesized.

Based on the CFD results and on the validation provided by wind tunnel observations it is possible to conclude that accounting for the free-stream airflow turbulence in the simulation is required to avoid underestimation of the collection efficiency of precipitation gauges. A turbulent free-stream is indeed the natural atmospheric condition of the wind impacting on operational precipitation gauges in the field. This work demonstrates that numerical derivation of correction curves for use in precipitation measurements as proposed hitherto in the literature is affected by a systematic overestimation of the wind-induced error due to the simplifying assumption of uniform free-stream conditions.

Finally, in order to achieve results that can be used in an operational context, suitable Collection Efficiency (CE) curves and the associated adjustment curves, which directly provide the expected undercatch as a function of the wind speed and the measured precipitation intensity, were derived for two sample measurement instruments. The first one is best suited for rainfall measurements and is characterised by the common cylindrical shape of traditional catching type gauges, therefore a numerical formulation of

the CE curves as a function of rainfall intensity is proposed. The second one, the *Hotplate*[®] gauge, is best suited for snowfall measurements and is characterised by an innovative measuring principle implying a dedicated geometry of the sensor. In this case, the numerically derived CE curves are expressed as a function of snowfall intensity.

For the typical cylindrical gauge, the residual dependency of the CE curves on the rainfall intensity was investigated in order to obtain a single CE expression as a function of both the rainfall intensity and wind speed. The parameters of the Particle Size Distribution (PSD) for various classes of the *RI* were derived by literature data from the Italian territory. Then the variation of the PSD parameters as a function of the *RI* was obtained, and subsequently also the parameters of the sigmoidal curves, used to fit the numerical CE values, were parametrized with the *RI*. As a result, easy to use adjustment curves as a function of both the measured rainfall intensity and wind speed were derived.

In the case of the *Hotplate*[®] snow gauge, the shape of the CE curves differs from the typical sigmoidal one due to its complex geometry. At low wind speed, the aerodynamic response of the gauge is predominant and CE values decrease with increasing the wind speed up to a wind threshold value beyond which the geometrical effect on the collection performance starts to be relevant and the CE increases. At very high wind speeds the geometrical contribution prevails and the CE becomes even larger than one.

INDEX

1. INTRODUCTION	1
1.1. BACKGROUND	1
1.2. AERODYNAMIC EFFECTS ON PRECIPITATION MEASUREMENTS	2
2. ATMOSPHERIC PRECIPITATION MEASUREMENTS	5
2.1. CATCHING TYPE GAUGES	6
2.2. NON-CATCHING TYPE GAUGES	10
3. PRECIPITATION MEASUREMENT BIASES AND UNCERTAINTIES	13
3.1. INSTRUMENTAL BIASES	13
3.1.1. Calibration of catching-type gauges and correction of systematic mechanical error	14
3.2. ENVIRONMENTAL FACTORS	18
3.2.1. Correction of wind-induced error	19
4. COMPUTATIONAL FLUID DYNAMICS SIMULATIONS	27
4.1. NAVIER-STOKES EQUATIONS	27
4.2. COMPUTATIONAL FLUID DYNAMICS MODELS	33
4.2.1. Numerical schemes and stability of the solution	39
4.3. CFD SIMULATION OF THE AERODYNAMIC RESPONSE OF VARIOUS GAUGE GEOMETRIES AND WIND TUNNEL VALIDATION	41
4.3.1. CFD simulations	43
4.3.2. Wind tunnel facility	44
4.3.3. Results and validation	48
4.4. NUMERICAL THERMO-FLUID DYNAMIC SIMULATIONS OF THE <i>HOTPLATE</i>[®] PRECIPITATION GAUGE AND WIND TUNNEL VALIDATION	56
4.4.1. Thermo-fluid and fluid dynamics simulations	58
4.4.2. Wind tunnel validation	67
5. PARTICLE TRACKING MODEL AND WIND TUNNEL VALIDATION	75
5.1. DYNAMIC CHARACTERISTICS OF PRECIPITATION	76
5.1.1. Parametrization of solid precipitation	79
5.1.2. Parametrization of liquid precipitation	80
5.2. LAGRANGIAN PARTICLE TRACKING MODEL	82
5.3. WIND TUNNEL VALIDATION OF THE PARTICLE TRACKING MODEL	83
5.3.1. Review of existing experiments	83
5.3.2. Dedicated setup for wind tunnel validation of the LPT model	86
5.3.3. Observation of the deflected trajectories	90

5.3.4. Particle Image Velocimetry velocity fields and observed drop trajectories	95
5.3.5. Comparison of measured and simulated particle trajectories	102
6. NUMERICAL COLLECTION EFFICIENCY	107
6.1. PARTICLE SIZE DISTRIBUTION	108
6.2. PARAMETERIZATION OF THE CE CURVES AS A FUNCTION OF RAINFALL INTENSITY	113
6.3. COLLECTION EFFICIENCY CURVE FOR THE <i>HOTPLATE</i>® PRECIPITATION GAUGE	123
7. THE ROLE OF FREE-STREAM TURBULENCE	131
7.1. THE FREE-STREAM TURBULENCE IN NATURAL WIND	131
7.2. THE ROLE OF FREE-STREAM TURBULENCE IN ATTENUATING THE WIND UPDRAFT AT THE COLLECTOR OF A CALYX SHAPED GAUGE	135
7.2.1. The numerical model and wind tunnel setup	135
7.2.2. Results and validation	138
7.3. THE EFFECT OF FREE-STREAM TURBULENCE ON SOLID PARTICLES DYNAMICS	145
7.3.1. Free-stream turbulence as a boundary condition for the <i>Hotplate</i> ® gauge	145
7.3.2. Numerical generation of free-stream turbulence for the chimney shaped gauge	148
8. CONCLUSIONS	155
REFERENCES	157

INTRODUCTION

1.1. BACKGROUND

Atmospheric precipitation is commonly experienced in our everyday lives and activities, in both business and leisure time, and its impact is manifest on major socio-economic sectors including transportation, agriculture, safety, tourism, recreation, etc. The extraordinary role of atmospheric precipitation in the human society (and natural ecosystems as well), justifies the need to obtain accurate quantitative measurements of the amount of water reaching the surface of the ground, and the duration and intensity of precipitation events.

According to the Guide to Meteorological Instruments and Methods of Observation (WMO, 2017) published by the World Meteorological Organization (WMO), precipitation is defined as the liquid or solid products of the condensation of water vapour falling from clouds or deposited from air onto the ground. Precipitation intensity is defined as the amount of precipitation collected per unit time interval. The total amount of precipitation which reaches the ground in a stated period is expressed in terms of the vertical depth of water (or water equivalent in the case of solid forms) to which it would cover a horizontal projection of the Earth surface.

Precipitation varies considerably in both space and time, it is erratic in nature and intermittent, and is composed of a large number of hydrometeors, each of them reaching the ground with its own size, shape, density and fall velocity, according to specific frequency distributions. Due to the complex processes of nucleation, accretion, melting and interactions between the hydrometeors (see e.g. Strangeways, 2006), the resulting characteristics of precipitation depend on the generating weather phenomenon and climate at any specific location (temperature, humidity, etc.). In addition, the fall trajectories of single particles are affected by the local conditions at a site, including wind, shading by obstacles, etc. and by the aerodynamic bluff body effect of the measurement instruments themselves.

Precipitation is among the most challenging environmental measurements, and accurate measurement of the amount of water that would ultimately land on a well-defined portion of the ground surface in undisturbed conditions is a difficult task. This is the aim of the so-called in-situ measurements at the ground, with the instrument located precisely where the information is sought, at a single location immersed in the precipitation process.

Precipitation measured at one single location is, however, representative of a limited area in space, the size of which is a function of the length of the accumulation period, the physiographic homogeneity of the region, local topography and the precipitation-producing process (WMO, 2017).

Weather radar and, more recently, satellites are used to quantify the spatial distribution of precipitation from a remote sensing perspective, with the sensor generally located far from the precipitation process. The information is inferred from the observed modifications of other physical quantities due to the interference with the precipitation process (e.g. active/passive microwave, infrared temperature, etc.).

In-situ precipitation gauges, however, provide the only direct measurements of precipitation at the ground and are usually referred to as the ground truth. Remote sensing techniques for extensive observations (essentially weather radar, aircraft and satellite borne radiometers) still require the use of in-situ measurements for calibration and validation purposes. Following Michaelides et al. (2009), *“measurements at the ground have been proved indispensable, despite advances in several areas of remotely sensing of precipitation. Ground truth seems to be inseparable from any study on precipitation. A better understanding of the behaviour of precipitation on the ground with direct measurements can lead to more effective estimations by using other methodologies”*.

1.2. AERODYNAMIC EFFECTS ON PRECIPITATION MEASUREMENTS

The role of turbulence in the assessment of the aerodynamic response of catching-type precipitation gauges when impacted by the wind is the main topic of this thesis work. This involves both the local generation of turbulence due to the obstruction to the airflow caused by the bluff body nature of the precipitation gauge and the natural free-stream turbulence inherent to the wind. The bluff body aerodynamics of precipitation gauges induces deviations in the trajectories of the approaching hydrometeors due to the acceleration, updraft and turbulence development upstream and above the collector of the gauge. Therefore, in general, a certain amount of undercatch is to be expected in precipitation measurements obtained from catching-type gauges.

The *“unsatisfactory nature of the best rain measurements”* was originally highlighted by Jevons (1861), in relation with the wind exposure problem, and such a complaint is still rather valid today, notwithstanding the progresses of precipitation measurement science experienced hitherto. Indeed, to obtain accurate measurements of liquid and solid precipitation using catching-type gauges it is desirable to ensure that the funnel collects the same amount of precipitation as that which would have fallen on the ground surface had the gauge not been present. Robinson and Rodda (1969) later commented that *“in view of the importance of wind in the measurement of rainfall, it is surprising that so few studies of the aerodynamic characteristics of rain-gauges have been carried out”*.

The first clear assessment of the aerodynamic issues in precipitation measurements, recognizing the bluff-body nature of the gauge body when immersed in a wind field, is generally attributed to Jevons (1861) who stated that *“the rain-gauge is itself an obstacle, causing the wind to swerve aside, and to change the direction in which the rain-drops fall”*. Jevons was addressing the difference in precipitation measurements observed when gauges are located at different elevations above the ground level, especially when sited on a rooftop or a tower, and suggested that a gauge with the collector levelled with the surrounding ground would be the only solution to avoid any wind-induced undercatch. After Koshmieder (1934), the wind exposure problem is also termed the *“Jevons effect”* in the literature.

However, Jevons himself referred to some previous observations of the physical processes at work, especially those by Meikle (1819) who already stated: *“I can hardly pretend to give a complete solution of this well-known paradox,”* (i.e. the increased precipitation measured by gauges sited at low elevation with

respect to those sited at high elevation) “*but am disposed to think it is in some way owing to the obstruction which the gauge itself offers to the wind. Perhaps the winds being made to rush with greater rapidity, and a little upward in beginning to pass over the mouth of the gauge, prevents the rain from falling into that part of it which is next the wind.*” Jevons attributed a lower relevance to the obstruction given by the instruments than to the presence of other types of obstacles to the wind such as buildings, vegetation, or the local topography. Therefore, it seems that the first author to clarify the aerodynamic influence of the gauge bluff-body on the catch performance was actually Meikle, in 1819, although maybe other authors in the same period could have reached similar conclusions.

Initial attempts to operationally mitigate the aerodynamic effect of precipitation gauges were based on the design and deployment of wind screens or shelters, aiming at reducing the wind velocity above the gauge collector to a magnitude that would minimise the updraft and therefore the deflection of particle trajectories. As a criterion for the usefulness of a shelter arrangement the rain gauge which under the same conditions gave the greatest quantity, and that quantity, were considered the most accurate. However, Bastamoff and Witkiewitch (1926) showed that the amount of rain is not a useful criterion since under certain conditions the influence of the shelter can even give too great amounts of rain, that is, larger amounts than a part of the earth's surface sufficiently removed from all disturbances would receive. Thériault et al. (2015a) reached similar conclusions more recently, with reference to the widely used and WMO-recommended large size windshield installation named the Double Fence Intercomparison Reference (DFIR).

Brooks (1938) already concluded that “*unshielded gauges can be deficient in catch by 5 to 50 % or more, the higher deficiencies occurring in cases of snow measurements made in windy locations*”. Alter's (1937) studies with shielded and unshielded gages likewise indicated that wind currents tend to decrease the amount of precipitation a gauge will catch. Earliest use of a shield to correct for the influence of the wind might be credited to Joseph Henry of the Smithsonian Institution in 1853. About 1879, Nipher made a notable contribution with his trumpet-shaped metal shield which was fastened directly to the gauge. This widely accepted shield gives good results when measuring rainfall, but it is unsatisfactory in the measurement of snowfall at unattended gages because of the tendency for snow to collect on the flat top of the shield and either fall into the gage or bridge over the gage orifice. By 1937, Alter had developed the Alter-type shield which is especially adapted to the measurement of snowfall and is at the present time being widely used. The individual baffles of the Alter shield are designed to prevent the collection of snow on the shield and gauge. In this respect the shield is fairly successful, although some difficulty is still experienced with sleet and ice freezing to the assembly.

Wind-induced errors were studied in the literature using different approaches – field measurement campaigns, numerical simulations and wind tunnel experiments – with the aim of formulating adjustment curves to calculate the actual precipitation falling to the ground. In field measurement campaigns, precipitation collected by a gauge installed in operational conditions is compared to a suitable reference. The numerical approach, based on Computational Fluid Dynamic (CFD) simulations of the flow field and the modelling of hydrometeors trajectories, reduces the time and resources needed to investigate different configurations by varying the wind speed, type of precipitation and gauge geometry. The validation of numerical models can be obtained by comparison with wind tunnel measurements, obtained in controlled

laboratory conditions. After validation, numerical simulation of precipitation particles trajectories leads to estimating the collection efficiency and to quantifying the wind-induced errors.

Due to the difficulties in reproducing hydrometeors trajectories under controlled wind tunnel conditions, or to observe their deflection when approaching the gauge in any real world configuration, the validation of trajectory models is not documented yet in the literature. In addition, the numerical and wind tunnel studies reported in the literature always neglect the free-stream turbulence and assume that turbulence is only generated by the interaction of the airflow with the gauge. Indeed, simulations generally impose steady and uniform incoming flow, whereas wind tunnel experiments are conducted in low free-stream turbulence conditions. The present work aims at overcoming these existing gaps in order to shed additional light on the wind exposure problem and to achieve results that can be used operationally to adjust precipitation measurements when these are obtained in windy conditions.

ATMOSPHERIC PRECIPITATION MEASUREMENTS

Traditionally, the equivalent volume of water received by a collector through an orifice of known surface area in a given period is assumed as the reference variable, namely the precipitation depth. The measurement unit of precipitation amount is therefore linear depth [L], usually expressed in millimetres, obtained as the ratio of the precipitated cumulative water volume to the surface area of the collector. Under the restrictive hypothesis that precipitation is constant over the accumulation period, a derived variable - the precipitation rate or intensity - can be calculated. Using short time intervals ensures that the estimated intensity is close to the real flow of water ultimately reaching the ground. The measurement unit of precipitation intensity is linear depth per unit time [$L T^{-1}$], usually expressed in millimetres per hour.

In-situ atmospheric precipitation measurements can be obtained by employing catching and non-catching type precipitation gauges. Instruments belonging to the first family are generally based on gravity related measuring principles (weighing, tipping buckets, floating devices – see e.g. WMO, 2017, Chapter 6), while the second group includes instruments based on optical, acoustic, and microwave principles (e.g. disdrometers). Catching type instruments are the traditional and by far the most common type of instruments employed worldwide to measure atmospheric precipitation. These gauges are equipped with a collector (funnel) to convey precipitation into a container, where the collected amount of water is measured. Both instrumental and environmental factors act as sources of systematic error (bias) in precipitation measurements, and measurements can be adjusted by means of correction curves. Instrumental factors such as the systematic mechanical error of Tipping-Bucket Rain gauges (TBRs) and the dynamic response of Weighing Gauges (WGs) can be corrected after dynamic calibration in the laboratory (Lanza and Stagi, 2008; Colli et al., 2013). Among the environmental factors, wind is the main influencing variable for precipitation measurements. Any precipitation gauge, indeed, presents an obstruction to the prevailing wind and the incoming airflow is deformed when wind overtakes the precipitation gauge. This aerodynamic effect deflects the hydrometeors (liquid/solid particles) away from the collector (Folland, 1988; Nešpor and Sevruck, 1999) and consequently influences the collection performance of the gauge.

2.1. CATCHING TYPE GAUGES

Based on the measuring principles catching-type gauges can be divided into storage, tipping bucket, weighing and drop-counter gauges.

The **storage gauge** (Figure 2.1) consists of a container with a known geometry, and the measuring principle is based on periodically measuring the level reached by the water surface in the container to obtain the volume of water accumulated in a given period, based on the known cross section area of the container. The most common gauges have a cylindrical shape, but different shapes, especially with reduced section area at the bottom, are used to enhance the measurement of light precipitation events. The gauges are made of metal, glass or plastic materials and graduation marks are drawn on the container to allow the reading of the water level. The measurement can be performed by an operator usually once or twice a day; automatic instruments reach the one-minute time resolution, as recommended by the World Meteorological Organisation (WMO), employing floating devices to record the water level on a strip chart, or sensors based on conductivity, acoustic distance or hydrostatic pressure measurements.



Figure 2.1 Plastic storage gauges developed for agricultural purposes and tested within the WMO-METAGRI project (from Cauteruccio et al., 2019).

Tipping-bucket precipitation gauges are widely employed in National Meteorological Services worldwide to measure rain and snow depth and the associated precipitation intensity. The reasons for extensive use of this kind of instrument are their relative ease of maintenance and limited production costs. This instrument uses a metallic or plastic twin bucket balance to measure the incoming water. It is equipped with a funnel that collects and conveys the water by means of a nozzle alternately in the two compartments of the tipping-bucket (Figure 2.2 left). The tipping of the bucket moves a magnet that triggers a reed relay contact and is recorded by a data logger. Usually, tipping bucket gauges have cylindrical shape (Figure 2.2 left), but with the increasing awareness of the wind effect on collection performance, new precipitation gauges characterized by aerodynamic shapes, based on observations in the field, have been recently developed (Figure 2.2 right). The main advantage of tipping bucket gauges is the automatic emptying principle: when the bucket tips the water is released outside the instrument body through dedicated apertures. However, the presence of moving parts in the sensor requires periodic maintenance of the instrument.



Figure 2.2 Tipping bucket rain gauge with cylindrical shape and scheme of the measuring principle (left-hand picture, from Cauteruccio et al. 2019) and the *EML*® aerodynamic gauges (right-hand photograph).

A **weighing gauge** consists of a bucket, usually built in metal or plastic, used to collect and measure liquid and solid precipitation by means of a weighing principle. The weight of the container, together with the collected water, is measured employing different type of sensors (balance, load cell, or vibrating wire load sensors, see Figure 2.3 left) . This type of gauge is widely used to measure solid precipitation because it does not require the snow to be melted before taking the measurement. In the absence of an automatic emptying system the dimensions of the container are usually larger than for other instruments, and this leads to a typical “chimney” shape (Figure 2.3) with an increased section area at the bottom. The large capacity of the bucket has the objective of minimizing the emptying operation, which is manually performed in many cases. Some instruments use an automatic emptying principle based on a syphon. Recently, a small size automatically emptying weighing gauge has been developed, consisting on a balance that measures the weight of the water collected alternately in the two compartments of a tipping-bucket (conveyed through a funnel and a nozzle). When the bucket tips the water is released outwards and then the empty compartment is placed under the nozzle to be filled and weighted. This automatic emptying principle leads to a reduction in the size of the instrument and ensures that the amount of weighted water is small and constant, therefore increasing the resolution of the gauge. Moreover, the presence of moving parts, typical of tipping bucket rain gauges, requires additional maintenance operation.



Figure 2.3 Scheme of the internal elements of a weighing precipitation gauges (left-hand picture, from Cauteruccio et al., 2019), and *Geonor*® T200B gauge with chimney shape (right-hand photograph).

The catching-type **drop counting gauge** (Figure 2.4) consists of a funnel that collects the precipitation and conveys water towards a calibrated nozzle, which starts dispensing droplets within an internal chamber before releasing them outside the instrument. An optical sensor is located below the nozzle and detects the passage of each falling drop. By assuming a constant volume for the calibrated droplets, the rainfall intensity can be derived from the drop release frequency. The resolution of the drop counting gauges depends on the size of the droplets generated by the nozzle, in the order of 0.005 mm of precipitation, and is suitable for the measurement of light precipitation rates. Indeed, an operational limit of this type of instruments is given by the rainfall intensity at which the water flux from the nozzle starts to be continuous or irregular, then the measured frequency abruptly decreases and large inaccuracies occur. A stand-alone installation is therefore discouraged and a co-located rain gauge is required to avoid large underestimation of severe rainfall intensity.



Figure 2.4 Drop counter precipitation gauge.

The **thermodynamic sensor** (Figure 2.5) is a new type of instrument recently developed to measure light to medium liquid or solid precipitation rate (Rasmussen et al., 2011). The system consists of two heated identical aluminium plates, one facing upward that collects the precipitation, and the other facing downwards to serve as a reference. This type of gauge can be classified between catching and non-catching type gauges because it has neither a funnel nor a container but nevertheless collects the precipitation on the surface of the top plate by means of rings a few millimetres high. The lower plate is insulated from the top plate and is only affected by wind and ambient temperature and not by precipitation. The two plates are heated to nearly identical constant temperatures (above 75 °C) which is hot enough to melt, in a few seconds, large snowflakes. The plates are maintained at a constant temperature during wind and precipitation conditions by either increasing or decreasing the supplied power. During precipitation the top plate cools because of melting and evaporation of the hydrometeors, and the difference between the power required to heat the top plate compared to the bottom one is proportional to the precipitation rate. The two plates are usually located at a height of 2 m above the ground. The diameter of the plate is large enough to permit collection of falling rain or snow particles and small enough that the power demand during heavy precipitation events and high wind speeds is not too high. To convert the power difference to liquid equivalent rate, a theoretical conversion factor is calculated, assuming that 100% of the heat of

vaporization/sublimation from the precipitation is transferred to the instrument. The conversion factor is based on the area of the plate, the heat capacity of water, the density of water, and the latent heat of sublimation and evaporation. The shape of the instrument body is designed with the objective of minimizing the wind-induced undercatch (Rasmussen et al., 2011) that is, however, not negligible and was quantified in a recent study (Cauteruccio et al., 2018). This instrument provides precipitation measurements every minute and can accurately measure rainfall rates up to 50 mm h^{-1} (WMO, 2018).



Figure 2.5 Thermodynamic sensor (from Rasmussen et al., 2011).

2.2. NON-CATCHING TYPE GAUGES

These instruments differ from traditional ones in that the precipitation flux is not collected in any container, but just sensed when crossing or impacting a given section, or a volume, of the atmosphere in the vicinity of the ground surface. They have a number of advantages over the more common catching type gauges and are especially suitable for Automatic Weather Stations. Due to the lower maintenance required and the unattended operation, the interest of National Water Services in such instruments is increasing. Furthermore, non-catching type gauges provide additional information to the precipitation intensity alone, among which the Particle Size Distribution (PSD), terminal velocity, visibility etc. Having neither a funnel nor a collector, calibration and uncertainty evaluation are more difficult than for catching type gauges since direct comparison with an equivalent, reference flow rate is not possible.

Optical disdrometers (Figure 2.6) consist of a laser or infra-red emitter, a receiver and a digital signal processing unit. The distance between the emitter and the receiver is usually of the order of some tens of centimetres, and the measuring beam is a few centimetres wide. This sensor measures the diameter and velocity of hydrometeors and from these measurements it identifies the type of precipitation and calculates the precipitation rate and amount, reflectivity, visibility, and particle size distribution. The measurement of the particle diameters typically ranges between 0.2 and 8 mm and allows the volume of each droplet to be derived. Consequently, the intensity can be directly calculated by integrating over the number of particles detected in a given time period, usually ranging from 15 seconds to one minute. Depending on the diameter and fall velocity, measurements are grouped into different precipitation classes. When hydrometeors cross the sensing volume of the disdrometer, the measuring beam is partially obscured. The shadow on the receiver leads to a decrease in the voltage generated by the receiver's photodiode. The digital signal processing unit monitors the photodiode's voltage and calculates the diameter of the drop from the minimum-observed voltage during the passage of the drop. The velocity is calculated from the duration of the voltage reduction by dividing the sum of the diameter and beam breadth by the drop's residence time. The resolution is typically between 0.001 and 0.005 mm h⁻¹ so it is possible to measure even very light rain (drizzle events). The maximum detectable precipitation rate varies with the instrument, and ranges between 200 mm h⁻¹ and more than 1000 mm h⁻¹. The collision of droplets is a possible error source; in that case, droplets are detected as one single macro-drop leading to a systematic overestimation of the measurement of the water volume. In order to reduce this error, a statistical correction is applied. Moreover, measurement errors can occur when droplets cross the rim of the light sheet; in this case the droplets are interpreted as smaller particles than they are in reality, causing an underestimation of the volume.



Figure 2.6 Optical (laser) non-catching type gauge.

Impact disdrometers (Figure 2.7) can be divided in two categories: acoustic disdrometers and displacement disdrometers.

Acoustic disdrometers record an electric signal via a piezoelectric sensor whenever a drop falls on a diaphragm. Based on the relationship between kinetic energy and drop size this electrical signal is converted into kinetic energy via the measured acoustic energy. A limitation to accuracy in drop size estimation is due to the differences in the acoustic response in the different parts of the diaphragm. This instrument is limited in measuring small drops because the diaphragm is not sensitive enough and because of the splashing. In addition, higher intensities are hardly measured due to the background noise, which reduces the measurement accuracy.

Displacement disdrometers translate via magnetic induction the energy generated by drops falling on the top surface and estimate the sizes of rain drops by analysing the associated electrical pulses. The instrument consists of a surface exposed to precipitation and connected to a magnet that, after displacement induced by the raindrop impact, slides within a coil, activating magnetic induction.

Both acoustic and displacement disdrometers are devoted to measuring liquid precipitation, since the droplets energy is directly related to the mass and density of the water droplets; snowflakes and hailstones, for example, have completely different impacts on the sensors, and lead to underestimation or overestimation of the precipitation measures. A suitable calibration method for impact disdrometers has been recently proposed with the aim of adapting this type of instruments to measure hail precipitation events (Löffler-Mang et al., 2011).



Figure 2.7 Impact disdrometer, photograph from the WMO Field Intercomparison of Rainfall Intensity Gauges.

Precipitation measurements employing **microwave sensors** (Figure 2.8) appeared in the last decades, and are based on the signal power reduction through the atmosphere during a precipitation event. The attenuation and scattering of the sensor emissions are related to the precipitation rate, but also depend on the physics of the precipitation particles, such as the liquid or solid phase and the different particles size, but also the frequency of the emitting signal has a fundamental role. Radar disdrometers have rainfall intensity resolutions up to 0.1 mm h^{-1} .



Figure 2.8 Microwave non-catching type gauge

PRECIPITATION MEASUREMENT BIASES AND UNCERTAINTIES

Measurement errors of precipitation gauges can be divided in two major categories. The first kind are catching errors, due to environmental conditions at the collector, as well as those related to wetting, splashing and evaporation. They affect the ability of the instrument to collect the exact amount of water falling over the projection of the collector's area on the ground. The second kind are the counting errors, due to systematic, mechanical, or sampling errors, and are related to the ability of the instrument to correctly quantify the amount of water that is collected or detected by the instrument. The process used to evaluate the counting errors of an instrument is called calibration and is usually performed by comparing the results of measurements with very precisely known quantities: this must be undertaken in a controlled environment to remove all other sources of error. Instruments calibration is a fundamental step for high quality measurements but cannot take into account the effects of catching errors that depends on environmental factors. In most cases, to obtain and correct this kind of error, field experiments are needed, but properly validated numerical models can be used to simulate the behaviour of the instrument under different environmental conditions.

3.1. INSTRUMENTAL BIASES

Instrumental biases affect all types of precipitation gauges, with different characteristics depending on the specific measurement principle adopted. Tipping-bucket gauges are known to suffer from systematic mechanical biases; they underestimate rainfall, especially at high precipitation intensities, because of the water amount that is lost during the tipping movement of the bucket. Although this can be remedied by dynamic calibration (Calder and Kidd, 1978) performed over the full operational range of precipitation intensity values, usual operational practice in hydro-meteorological services and instrument manufacturing companies relies on single-point calibration (obtained at one single reference intensity). Dynamic calibration is essential to reflect the actual pattern of precipitation intensity over time. The related biases, known as systematic mechanical errors, result in an overestimation at lower intensities, depending on the single-point calibration operated, and underestimation at the higher precipitation intensities.

Tipping bucket gauges are also subject to the unbalancing of the buckets that can be corrected by reproducing a constant flow rate for a sufficient duration in laboratory conditions and by recording the time between consecutive tips (inter-tip time). If the inter-tip time is not regular, the two buckets are not balanced and the volume collected in the two buckets is not the same. By acting on the stop screws, the bucket position is adjusted until accurate balancing is obtained.

Tipping-bucket gauges are finally affected by sampling errors due to the discrete nature of the measurement principle. The hypothesis at the basis of the measurement principle is that precipitation is constant between consecutive tips. The sampling errors are strongly influential in the assessment of light precipitation events, which commonly results in recording lots of isolated tips associated with remarkable overestimation of the actual precipitation rate at the corresponding time step and underestimation in the

contiguous steps. To avoid this error, the precipitation intensity should be obtained by measuring the inter-tip time instead of using a constant sampling time (one minute).

Finally, the presence of a certain amount of water previously stored in the bucket before the start of a new event and the amount that remains inside the bucket at the end of the event may affect the measurement of the precipitation rate.

A fundamental characteristic of weighing gauges when measuring precipitation intensity is the response time, which leads to measurement errors (systematic delay due to the filtering algorithm adopted to reduce the signal noise). The response time is of the order of six seconds to a few minutes depending on the gauge's design and model. The actual sensitivity of weighing gauges can be very different from gauge to gauge and depends on the transducer resolution.

Drop counting gauges are subject to biases due to the changing size of drops with precipitation intensity. The measurement principle is based on the hypothesis that the droplet generated by the nozzle has a fixed volume. The volume actually varies in a nonlinear fashion with the precipitation intensity and a corresponding bias arises in measurements that may reach 10 - 20% depending on the instrument design (Stagnaro et al., 2018).

Catching type rain gauges are also affected by the so called catching errors related to wetting and splashing. As reported by (Sevruk, 1982) the losses for wetting and splashing are about 2 - 10% and 1 - 2%, respectively. Wetting losses depend on the geometry and material of the gauge collector and container, the amount and type of precipitation and the number of events during the time needed to dry the container. For solid precipitation the loss is smaller than for liquid precipitation because the collector is wetted usually only once during snowmelt. The WMO/CIMO Guide n.8 (WMO, 2017) recommends that the collector is designed to prevent precipitation from splashing in and out. This can be achieved if the vertical wall is sufficiently deep and the slope of the funnel is sufficiently steep (at least 45%).

3.1.1. Calibration of catching-type gauges and correction of systematic mechanical error

Counting errors can be experienced both in catching and non-catching types of instruments, although in the latter case the assessment of such errors is very difficult, and hard to be performed in controlled laboratory conditions. Laboratory calibration is always needed to obtain high quality measurements and may provide a classification of catching-type measurement instruments based on their laboratory performance. The laboratory calibration is performed under constant equivalent rainfall intensity, obtained by means of steady water flow generation (using e.g. volumetric pumps or gravimetric methods). The operational status of precipitation gauges can be verified in the field by means of portable calibration devices, so as to detect malfunctions, output anomalies and calibration drifts. Field calibration tests are based on the same principles of laboratory calibration, using the generation of a few constant equivalent precipitation rates within the range of operational use of the instrument.

The Italian standard UNI 11452:2012 and the newly released European standard EN 17277:2019: "Hydrometry. Measurement requirements and classification of rainfall intensity measuring instruments" report the procedure required to perform the calibration of catching type gauges as follows. The calibration is performed in a certificated laboratory, where a constant water flow, equivalent to a reference precipitation intensity, is conveyed to the funnel of the instrument. The constant flow regime is obtained from a suitable

hydraulic device for different precipitation intensity values (dynamic calibration) within the range of operational use declared by the instrument's manufacturer. The flow is measured by weighing the water over a given period after passing through the rain gauge. The output of the instrument under test is recorded when a pulse occurs or at regular intervals. The two measurements are compared in order to assess the difference between the actual flow of water conveyed through the instrument and the precipitation intensity measured by the instrument itself. The relative percentage error can be expressed as follows:

$$e_{rel}[\%] = \frac{I_{meas} - I_{ref}}{I_{ref}} \cdot 100 \quad (3.1)$$

where I_{meas} is the measured liquid precipitation intensity and I_{ref} is the reference equivalent precipitation intensity.

In the case of weighing gauges, the performance is also based on the time response, i.e. the amount of time that is required by the instrument to measure 63.2% of the reference intensity value (assuming a first order type of response). Figure 3.1 shows the response time of a weighing gauge for different equivalent precipitation intensity values.

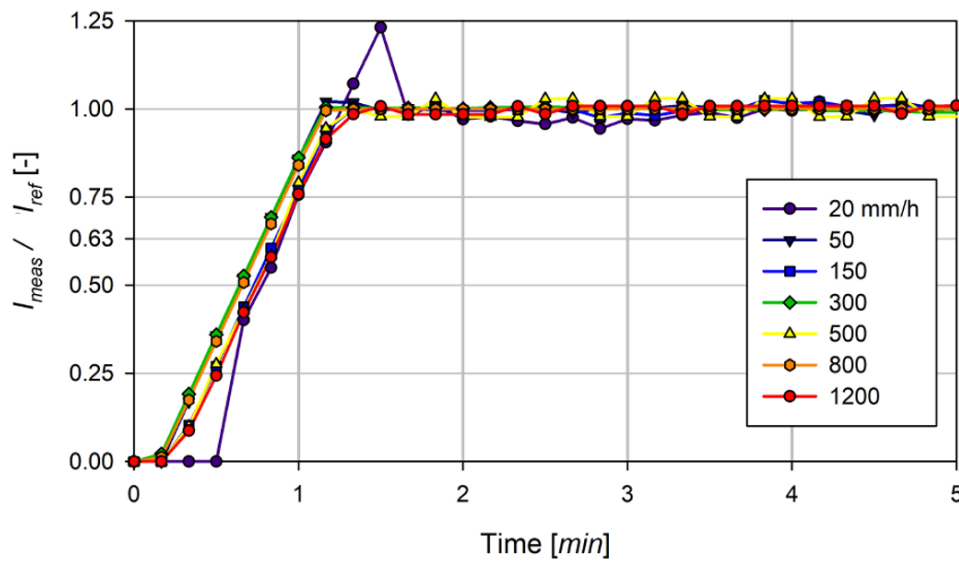


Figure 3.1 The response time of a weighing gauge: 63.2% of the reference equivalent intensity is measured in less than one minute (from Cauteruccio et al., 2019).

The European standard EN 17277:2019 classifies precipitation gauges in three classes of performance, according to the calibration results, as follows:

- Class A: the maximum deviations are less than or equal to $\pm 3\%$ against the reference precipitation intensity at the temporal resolution of 1 minute. Weighing rain gauges, shall also have a step response time within the same time interval.
- Class B: the maximum deviations are less than or equal to $\pm 5\%$ against the reference precipitation intensity at the temporal resolution of 1 minute. Weighing rain gauges, shall also have a step response time within the same time interval.
- Class C: the maximum deviations are less than or equal to $\pm 10\%$ against the reference precipitation intensity at the temporal resolution of 1 minute. This also applies to weighing rain gauges where the step response time is less than or equal to 1 minute. Where the weighing rain gauge step response is greater than one minute the maximum deviations shall be within $\pm 5\%$.

If the precipitation gauge tested has a maximum deviation greater than $\pm 10\%$ in measuring the reference precipitation intensity at the temporal resolution of one-minute it cannot be classified according to this standard. The same instrument can be attributed different classes of performance over different measuring ranges. The calibration certificate must contain the average value and the 10° and 90° percentiles of the percentage relative error distribution $e_{rel}[\%]$, for each value of the tested reference precipitation. This is presented in the form of a table. The dynamic calibration curve, obtained by fitting the relative errors of tested precipitation intensities, must be reported in the certificate to allow correcting the readings. Figure 3.2 shows the performance of a tipping bucket and a weighing gauge in terms of relative errors.

The standard also requires consistency of the information. Any inconsistency between the precipitation intensity output at one-minute resolution and other quantities provided by the instrument (e.g. the precipitation amount) must be declared.

Although less efficient, hydro-meteorological services and instrument manufacturers often rely on the single-point calibration. In this case, only one reference precipitation intensity is checked and the associated adjustment is applied mechanically by operating on the stop screws of the bucket, so that the error becomes zero at that particular intensity. For any other precipitation intensity some underestimation or overestimation persists. This is equivalent to assuming a conventional measure for the water amount associated with each tipping of the bucket, which is different from the actual bucket volume.

Systematic mechanical biases are corrected using a suitable calibration curve obtained from dynamic calibration tests, as the best-fit regression function. Figure 3.3 shows the performance of the same tipping bucket and weighing gauges of Figure 3.2 after correction is applied, therefore reporting the residual errors $e_{res}[\%]$. Dedicated post-processing algorithms must be employed to achieve sufficient accuracy and to minimize the impact of sampling errors and the discrete nature of the measurement. Various algorithms have been proposed to this aim and discussed in the literature (Castello and Williams, 1991; Habib et al., 2001; Colli et al., 2013). However, the operational practice of most users, including national weather services, still relies on the trivial counting of the number of tips occurring in the desired period. The number of tips counted in each one-minute interval (the WMO recommended time resolution for rain intensity measurements) multiplied by the nominal volume of the bucket provides the one-minute precipitation

intensity record. This method (as already observed by Castello and Williams, 1991) results in a general underestimation of precipitation intensity and in a high level of uncertainty, due to the random nature of the number of tips per minute within any real world, highly variable event. Moreover, the correction of systematic mechanical biases is not optimized with this method since it would be applied to the averaged values only, and most tipping-bucket gauges show a non-linear correction curve after laboratory calibration (Lanza and Stagi, 2009). A better method employs the inter-tip time algorithm (see e.g. Castello and Williams, 1991 and Colli et al., 2013), which is based on the assumption that the nominal volume of each bucket is equally distributed over the inter-tip period. The calculation of precipitation intensity for each minute accounts for the portion of the inter-tip period actually falling into that minute. In this way, the calibration is also the most effective since the correction applied to the volume of the bucket at the variable inter-tip scale is precisely the one corresponding to the measured precipitation intensity. The performance of different post-processing algorithms employed in the calculation of the rainfall intensity from tipping-bucket gauges is compared and discussed by Stagnaro et al. (2016) using data recorded at a field test site. Two tipping-bucket gauges using different mechanical designs were compared with a catching-type drop-counting gauge used as the working reference due to its high resolution both in time and volume for the investigated rainfall intensities. The comparison highlights the benefits of employing smart algorithms in post-processing of the raw data and their ability to improve the accuracy of precipitation intensity measurements. In particular, the results allow one to compare the performance of the inter-tip time algorithm with the more common tip-counting method. The main benefit of adopting the inter-tip time method to calculate rainfall intensity resides in a better representation of the inner variability of rainfall events. The measured rainfall intensity series shows an improved correlation coefficient and a lower root mean square error (RMSE) with respect to the reference, closely approaching the performance of an ideal gauge, which is not affected by mechanical biases.

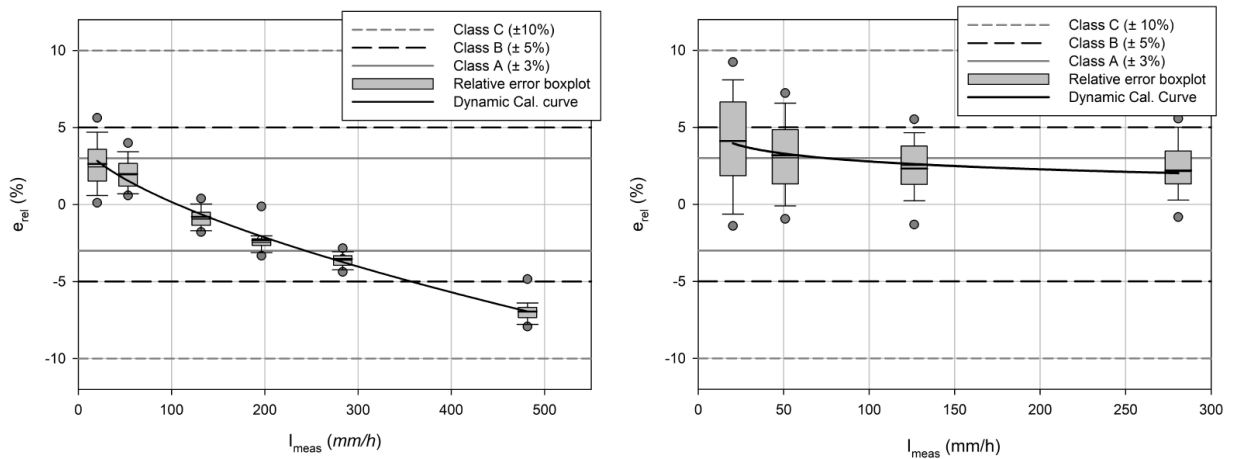


Figure 3.2 Relative percentage error (e_{rel} [%]) at various measured intensities (I_{meas}) and correction curves for a tipping bucket gauge (left) and a weighing gauge (right) (from Cauteruccio et al., 2019). The limits of the three classes of performance defined by the European Standard EN 17277:2019 are depicted with continuous grey line, long-dashed line and short-dashed line for class A, B and C, respectively.

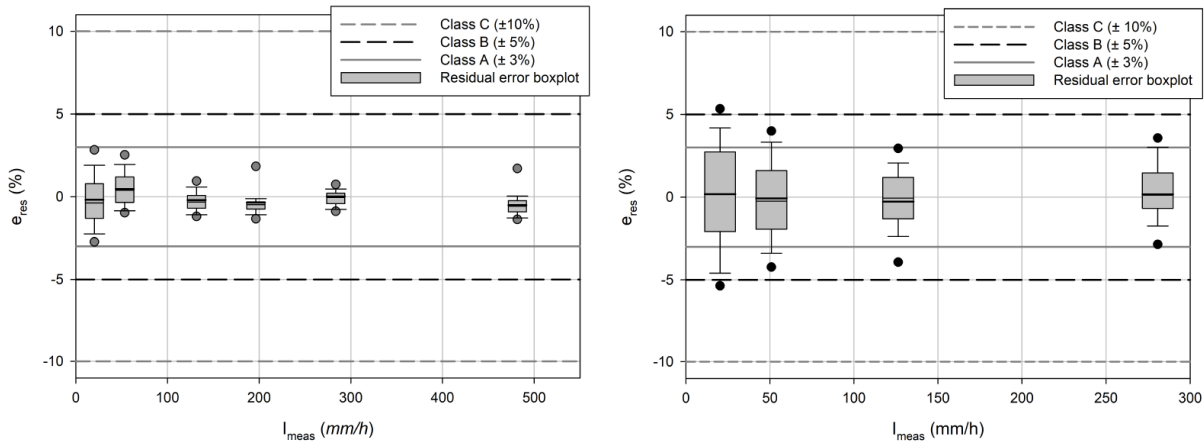


Figure 3.3 Residual error (e_{res} [%]) for a corrected tipping bucket gauge (left) and a weighing gauge (right). After the correction the tipping bucket gauge falls inside the limits of Class A (grey continuous lines), while the weighing gauge is in Class B (long-dashed line) for $I_{meas} \leq 50 \text{ mm h}^{-1}$ and in Class A for $I_{meas} \geq 130 \text{ mm h}^{-1}$.

3.2. ENVIRONMENTAL FACTORS

Catching errors also include the effects of evaporation and wind on precipitation measurements. The first measurements of evaporation losses started in the XIX century as reported by Sevruck (1982). They were based on the difference between the amounts of precipitation simultaneously measured in two storage gauges: one observed daily and the other observed monthly. The annual accumulation was corrected using the difference between the two measures but the wetting losses from daily emptying of the container were also included, therefore the method cannot be used to estimate evaporation losses only. Also, differences in readings from a pit gauge (with the orifice located at the level of the surrounding ground) and an elevated gauge are due to differences in temperature of the collected water, therefore the pit gauge is not a good reference to estimate evaporation losses. Since the end of the XIX century the method employed to assess evaporation losses is that of measuring the evaporation rate of simulated precipitation during precipitation-free periods. As an alternative, comparing the total accumulation from a storage gauge with the time integral of precipitation intensity measurements from a weighing gauge provides a good estimate of the evaporation losses. Weighing gauges may provide measurements of evaporation as negative precipitation values in case the weight of the water collected in the container should decrease. Evaporation losses are season-dependent and usually quite low, especially for rain intensity measurements: according to the WMO/CIMO Guide n.8 they may account for less than 5% of the total precipitation amount. The WMO/CIMO Guide n.8 also suggests that, in storage and weighing gauges, errors associated with evaporation are minimized using an oil surface layer in the container.

Wind is the main environmental factor to affect precipitation measurements. The effects of the immediate surroundings of the site on the wind field can give rise to local variations in precipitation. To reduce the wind effect on precipitation the choice of the measurement site, including the location of precipitation gauges within the area of interest, is important. The WMO/CIMO Guide n.8 reports that objects should not be closer to the gauge than a distance of twice their height above the gauge collector and sites on a slope or

the roof of a building should be avoided. Usually, the best sites are in clearings among trees or where other objects act as an effective wind-break for winds from all directions.

The effects of the wind, and of the site on the wind, can be reduced by using a pit gauge for liquid precipitation or by making the airflow horizontal above the gauge collector using homogeneous dense vegetation kept at the same level as the gauge collector, or appropriate fence structures, or by using windshields around the gauge. Furthermore, the wind effect on precipitation measurements is due to the interaction between the gauge body and the airflow. Any precipitation gauge, indeed, presents an obstruction to the prevailing wind and the incoming airflow is deformed when wind overtakes the precipitation gauge. Wind generally accelerates above the collector of the instrument, while vertical upward velocity components arise upwind of the collector (Warnick, 1953). This aerodynamic effect induced by the gauge body deflects the hydrometeors (liquid/solid particles) away from the collector (Folland, 1988; Nešpor and Sevruck, 1999), thus is responsible for a significant reduction of the collection performance. The main factors of influence are the gauge geometry, the wind speed and the characteristics of precipitation, including the particle size distribution (PSD) and precipitation intensity (Thériault et al., 2012; Colli et al., 2015).

3.2.1. Correction of wind-induced error

Wind-induced errors were studied in the literature using different approaches (field measurement campaigns, numerical simulation and wind tunnel experiments) with the aim of formulating correction curves to calculate the actual precipitation falling to the ground. Nevertheless, the implementation of correction curves in operational conditions is still rare. Sevruck (1982) reported that the typical magnitude of the wind related losses (undercatch) for the precipitation amount is 2-10 % in case of liquid precipitation and 10-50 % in case of solid precipitation. Pollock et al. (2018) reported an observed undercatch of about 10 to 23 % for liquid precipitation at a lowland and upland sites, respectively. Further studies focusing on solid precipitation (Rasmussen et al., 2012; Colli et al., 2015) showed collection losses up to 70-80 %.

Correction curves can be derived using data from experimental sites equipped with different precipitation gauges in operational conditions and a reference one. In the field the ratio between the precipitation measured by a gauge in operational condition (h_{meas} , usually in [mm]) for a given wind speed (U_{ref}) and the reference one (h_{ref} [mm]) is called the Collection Efficiency (CE, Eq. 3.2).

$$CE = \frac{h_{meas}(U_{ref})}{h_{ref}} \quad (3.2)$$

The WMO/CIMO recommends as a reference for liquid precipitation a gauge placed in a pit (Figure 3.4 left), with the gauge orifice at ground level, sufficiently distant from the nearest edge of the pit to avoid in-splashing. A strong plastic or metal anti-splash grid with a central opening for the gauge should span the pit. Because of the absence of wind-induced error, pit gauges generally report more precipitation than any elevated gauge. The reference installation for solid precipitation (Figure 3.4 right) is known as the Double Fence Intercomparison Reference (DFIR). It has octagonal vertical double fences surrounding a storage or

automatic gauge, which itself has a particular form of wind-deflecting shield known as the Single Alter shield. Note that this field reference gauge is not free from measurement biases itself, and its construction could be improved (Thériault et al., 2015).

At an experimental site in Haukeliseter (Norway) two *Geonor*® T200B weighing gauges, one unshielded and one equipped with a single Alter shield, were installed together with the DFIR. Temperature measurements were also available and anemometers were located at the height of ten meters and at the gauge collector height. Figure 3.5 (from Wolff et al., 2015) Figure 3.5 shows the catch ratios between the Single Alter shielded gauge and the reference measurements as a function of wind speed and colour coded according to the air temperature. The authors classified the precipitation in solid, mixed or liquid, according to the air temperature thresholds reported by Sims and Liu (2015). For temperatures below -2°C the precipitation is mainly falling as snow, and the catch ratio has a characteristic fast decreasing shape with wind speed. For temperatures above 2°C , where the precipitation is mainly falling as rain, the catch ratio is less influenced by the wind. For temperatures between -2°C and 2°C where rain, snow and mixed precipitation occur, increased scatter appears depending on the precipitation type. The four temperature classes, highlighted in the figure as colour bands, suggest a continuous change from higher to lower temperature consistent with a gradual change of the distribution of liquid and solid precipitation particles during a mixed phase event. Based on a three years data set from the Haukeliseter test site, that contains a number of concurrent observations of the catch ratio (R_i), the following correction curve was formulated by Wolff et al. (2015):

$$R_i = \left[1 - \tau_1 - (\tau_2 - \tau_1) \frac{e^{\left(\frac{T_i - T_\tau}{s_\tau}\right)}}{1 + e^{\left(\frac{T_i - T_\tau}{s_\tau}\right)}} \right] e^{-\left(\frac{V_i}{\theta}\right)^\beta} + \tau_1 + (\tau_2 - \tau_1) \frac{e^{\left(\frac{T_i - T_\tau}{s_\tau}\right)}}{1 + e^{\left(\frac{T_i - T_\tau}{s_\tau}\right)}} + \sigma(T_i)\varepsilon_i \quad (3.3)$$

where T_τ is the threshold of temperature and defines the transition between the two limits above, while s_τ dictates the type of change, and $\sigma(T_i)$ is a parameter governing the variance of the measurement error.

The equation was obtained starting from the assumption that the catch ratio is a function of wind speed (V) and air temperature (T) in the form:

$$R = f(V, T) = [1 - \tau(T)] e^{-\left[\frac{V}{\theta(T)}\right]^\beta} + \tau(T) \quad (3.4)$$

The parameter $\tau(T)$ goes from one limit, dry snow, to another, mixed precipitation, when the temperature increases/decreases. A sigmoid function reasonably fits experimental data yielding the parametric function as follows:

$$\tau(T) = \tau_1 + (\tau_2 - \tau_1) \frac{e^{\left(\frac{T-T_r}{s_\tau}\right)}}{1 + e^{\left(\frac{T-T_r}{s_\tau}\right)}} \quad (3.5)$$

An application of the correction curve is shown in Figure 3.6 (from Wolff et al., 2015). Some difference between the adjusted accumulation (blue line) and the reference one (black line) remains, which is probably ascribable to the actual (unknown) particle size distribution.



Figure 3.4 The realization of the Reference Rain Gauge Pit at Vigna di Valle, Italy (2007) (WMO field InterComparison of rainfall intensity gauges, 2009) and a DFIR equipped with a Geonor® T-200B weighing gauge located at the Marshall (Colorado) experimental site.

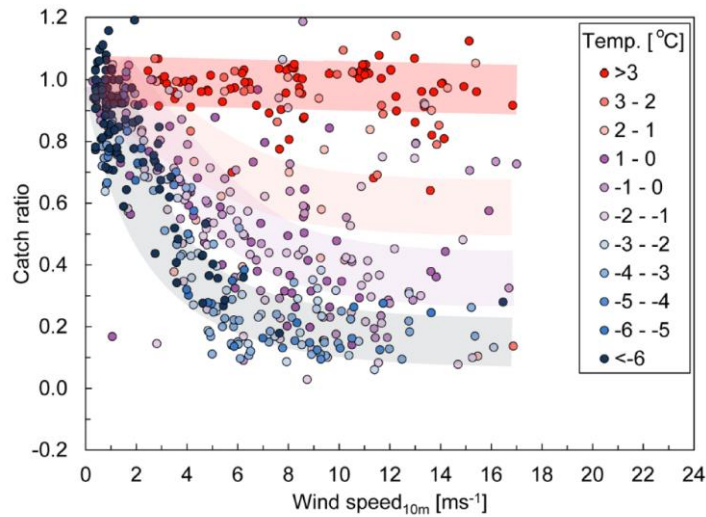


Figure 3.5 Catch ratio of the Geonor® T200B gauge equipped with a single Alter shield when compared to the DFIR as a function of wind speed (at 10 m height), for various temperature classes (from Wolff et al., 2015).

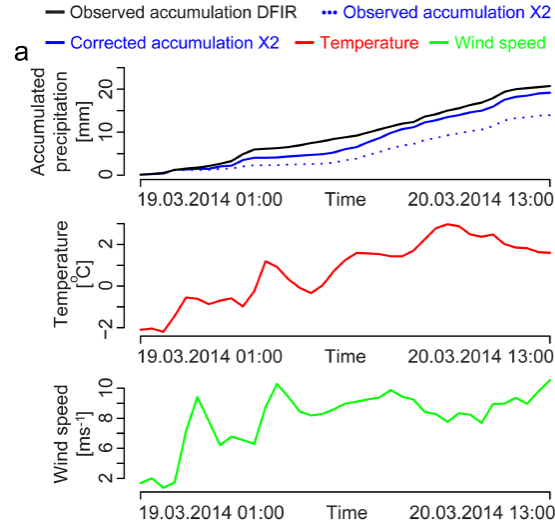


Figure 3.6 Observed and adjusted accumulation from one sample precipitation event compared to the accumulation observed by the DFIR. Temperature and wind speed during the event are shown in the middle and lower panel, respectively. (From Wolff et al., 2015)

Data from the 2010 winter in the two experimental sites of Marshall (USA) and Haukeliseter (Norway) were analysed by Kochendorfer et al. (2017a). The authors proposed the following correction function with exponential shape:

$$R = e^{-a(U)}(1 - [\tan^{-1}(b(T_{air})) + c]) \quad (3.6)$$

where the experimental parameters a , b and c vary with the height of the anemometer and the type of precipitation gauge (unshielded, Single Alter shielded, etc.). The effect of the correction is shown in Figure 3.7 where the uncorrected and corrected precipitation is compared with the DFIR measurements in panels (a) and (b), respectively. After the correction a significant scatter of data persists, which is probably due to the effect of noise, the spatial variability of precipitation and also the spatial variability in crystal type that are not fully taken into account in this study.

With the aim of deriving correction curves that could be extended to other sites, data from eight experimental sites were analyzed by Kochendorfer et al. (2017b). The study provided the parameters of Eq. 3.6 for Single Alter shielded and unshielded chimney shaped weighing gauges, by separating mixed and solid precipitation and for wind speed measured at ten meters or at the collector elevation.

The data set obtained by Buisán et al. (2017) at the Formigal (Spain) experimental site was divided into two samples and the correction curves derived for Tipping-Bucket rain gauges at one and three hours accumulation scales are shown in Figure 3.8. For one-hour accumulation, the authors propose Eq. 3.7, where a contribution of the melting of snow during the previous hour of accumulation is also included.

$$TrueAcc(1h) = \frac{Acc}{CR} - 0.095 \frac{Acc}{CR} + 0.095 Acc(prevh) \quad (3.7)$$

where the authors define CR as the ratio between the precipitation measured by Tipping-Bucket gauge and that measured by the Double Fence Automatic Reference and function of wind speed and air temperature.

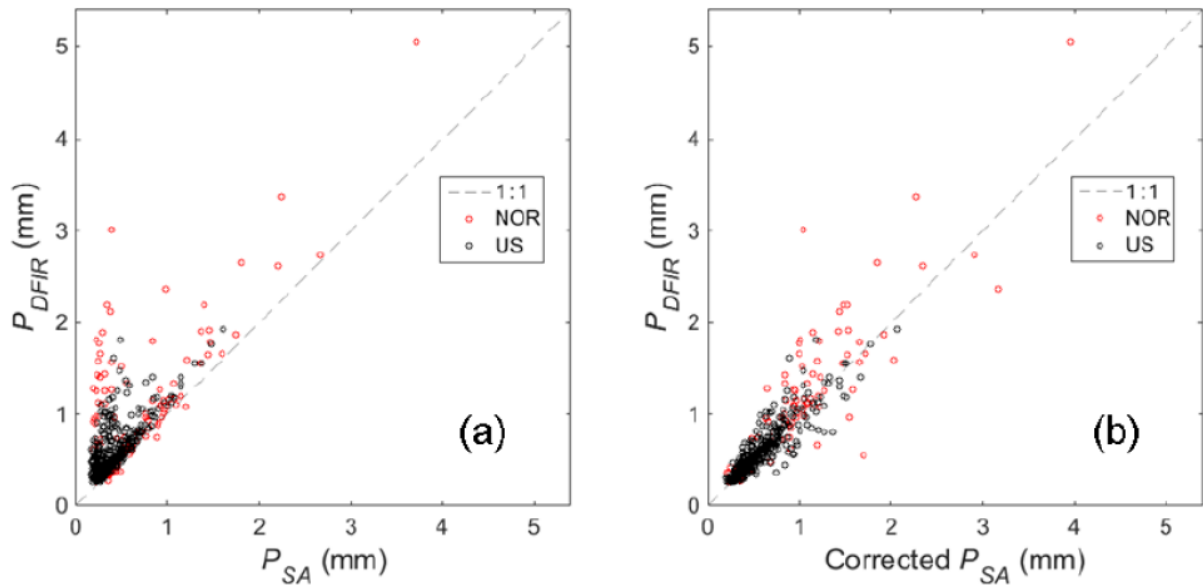


Figure 3.7 Uncorrected (a) and corrected (b) precipitation from a Geonor® T200 weighing gauge equipped with a Single Alter shield (P_{SA}) vs. the DFIR (P_{DFIR}) for snow events (from Kochendorfer et al., 2017a).

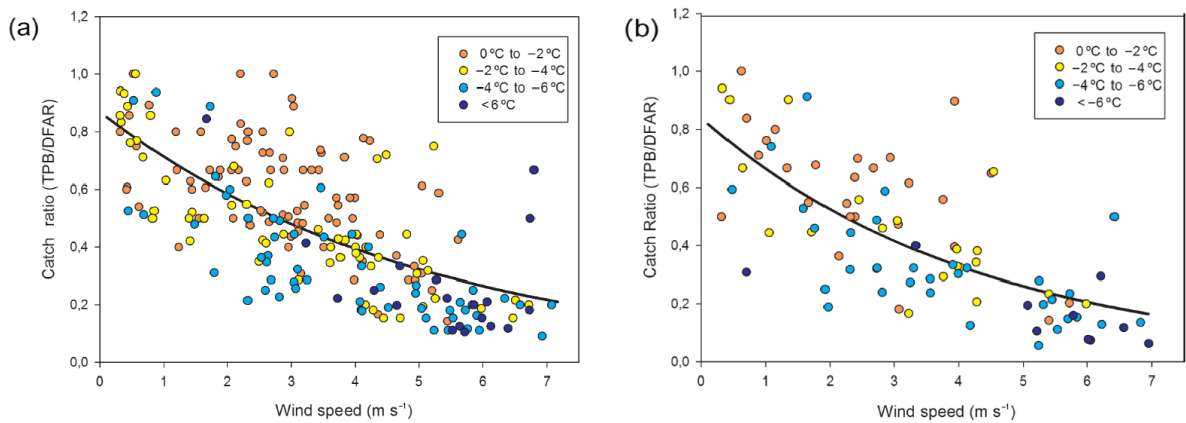


Figure 3.8 Correction curves and ratio between the precipitation measured by a Tipping-Bucket gauge and the Double Fence Automatic Reference as functions of wind speed for accumulation periods of (a) 1 and (b) 3 hours.

Data are colored with the mean temperature during each accumulation period (from Buisán et al., 2017).

Drawbacks of the transfer functions, or collection efficiency curves, that are derived from field experiments alone are related to their strict dependence on the site where the test field is located, its

precipitation and wind climatology, and to the reliability and accuracy of the assumed reference gauge (see e.g. Thériault et al., 2015). The observed collection efficiency values derive from the actual drop size distribution of precipitation events and the microphysical characteristics of the hydrometeors, and the complete parameterization of these curves is rarely achieved, so that a large dispersion of the field measured data around the best-fit curves usually persists.

It is evident that a more theoretically based approach is needed, though always based on real world observations to ensure proper validation of the algorithms and results, to achieve a complete coverage of various local climatological characteristics, precipitation microphysics, gauge shapes and wind conditions. This can be done by exploiting the potential of numerically solving the basic equations of fluid motion and of particle-fluid interactions as is the method used in the present work. Although a few examples of this approach were already available in the literature, the experimental studies presented in this chapter and the wide experimental campaign carried out by the WMO on this topic (called SPICE – the Solid Precipitation Inter-Comparison Experiment) did not include any numerical method.

As an example of this approach, with the aim of reducing the dispersion of field measurements around the collection efficiency curves of solid precipitation measurements, and shedding light on the dependence of such curves on the drop size distribution and its link with the precipitation intensity, Colli et al. (2020) recently showed that such dispersion can be reduced by including the results of the numerical simulation into the best-fit methodology applied on field measurements.

The authors analysed WMO-SPICE quality controlled 30-min accumulation data from the Marshall field-test site (CO, USA) and revealed that the wind-induced undercatch of solid precipitation gauges is best correlated with the measured snowfall intensity, rather than temperature, in addition to wind speed. The measured snowfall intensity has indeed the advantage of including information about the particle size distribution (Pruppacher and Klett, 1997). Optimal curve fitting used to derive the transfer function for the Geonor® T200B gauge in a Single Alter shield and in a DFIR configuration indicated that accounting for snowfall intensity indeed reduces the scatter of the residuals. This result is confirmed by the analysis of data from other field sites, such as CARE (Canada) and Haukeliseter (Norway), and shows a consistent behaviour under different climatological conditions.

The physical basis for the improved parameterisation of the transfer function by using the measured snowfall intensity was shown, through numerical modelling of the gauge snow collection process, to be due to the correlation of large particles with high intensities. Large particles are preferentially collected by a snow gauge, even in strong wind, due to their higher fall velocity, allowing them to break through streamlines of flow above the gauge and be collected. The numerical modelling was able to reproduce the collection efficiency pattern observed in the field.

The added value of using the snowfall intensity in the transfer function is best visualised in Figure 3.9 (here replicated from the paper of Colli et al., 2020), where SI_{REF} is the reference snowfall intensity (assumed coincident with the DFIR measurements for the field data). In this graph, where the wind speed is colour-coded according to the side bar, the iso-CE lines would be linear (grey dotted lines) in the absence of a clear influence of the measured snowfall intensity on the collection efficiency. A clear deviation from linearity is observed, showing that the collection efficiency increases far beyond linearity with the measured snowfall intensity at any wind speed class. This deviation vanishes together with the wind and increases

with the wind speed, therefore justifying the larger spread of field measured values observed towards the stronger winds in typical collection efficiency best-fit representations.

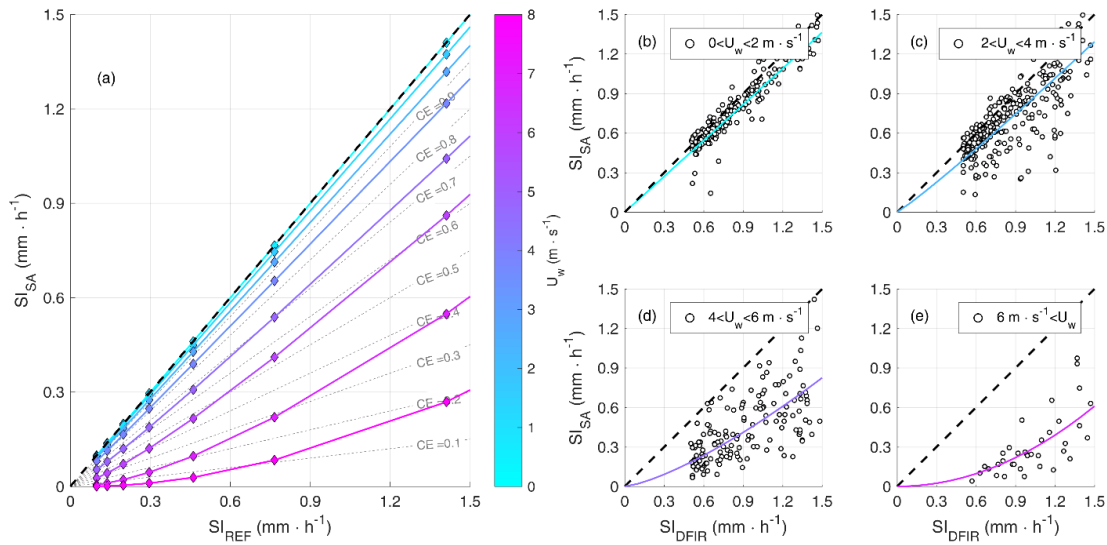


Figure 3.9 Deviation from linearity of the collection efficiency (grey dotted lines in (a)) when increasing the wind speed (colour coded according to the side bar) in the measured vs. reference snowfall intensity plane (from Colli et al., 2020). The deviation is evident in both the results of numerical simulation (solid coloured lines and diamonds in panel a) and field data (white circles in panels b, c, d, e) although with some residual scatter. The field data is presented together with power law regressions performed for various wind speed classes.

The authors' findings provide an attractive method to improve operational measurements since no additional instrument, except for a wind sensor, is required to derive the adjusted estimates of snow accumulation.

COMPUTATIONAL FLUID DYNAMICS SIMULATIONS

In this work the airflow fields around precipitation gauges for various wind speeds were calculated by means of Computational Fluid Dynamics simulations based on both Unsteady Reynolds Average Navier Stokes (URANS) and Large Eddy Simulations (LES) models. The Navier-Stokes equations were solved numerically by employing the solvers of the open-source OpenFOAM software.

4.1 NAVIER-STOKES EQUATIONS

The general differential equation for conservation of linear momentum is known as the *Cauchy's equation* (eq. 4.1):

$$\frac{\partial}{\partial t}(\rho \mathbf{v}) + \nabla \cdot (\rho \mathbf{v} \mathbf{v}) = \rho \mathbf{g} + \nabla \cdot \sigma_{ij} \quad (4.1)$$

where σ_{ij} is the stress tensor, \mathbf{g} is the gravity vector, \mathbf{v} the velocity vector and $\nabla \cdot$ the divergence operator. The stress tensor includes the viscous stress tensor (τ_{ij}) and the local hydrostatic pressure P , which always acts inward and normal to the surface as $-P\mathbf{I}$ where \mathbf{I} is the Identity matrix.

$$\sigma_{ij} = \begin{pmatrix} \sigma_{xx} & \sigma_{xy} & \sigma_{xz} \\ \sigma_{yx} & \sigma_{yy} & \sigma_{yz} \\ \sigma_{zx} & \sigma_{zy} & \sigma_{zz} \end{pmatrix} = -P \begin{pmatrix} 1 & 0 & 0 \\ 0 & 1 & 0 \\ 0 & 0 & 1 \end{pmatrix} + \begin{pmatrix} \tau_{xx} & \tau_{xy} & \tau_{xz} \\ \tau_{yx} & \tau_{yy} & \tau_{yz} \\ \tau_{zx} & \tau_{zy} & \tau_{zz} \end{pmatrix} = -P\mathbf{I} + \tau_{ij} \quad (4.2)$$

Air is a Newtonian fluid. For Newtonian fluids the shear stress is linearly proportional to the shear strain rate. By assuming incompressible (constant density ρ) and isothermal (small or null local changes in temperature) flow the dynamic viscosity μ and the kinematic viscosity ν , can be assumed as constant. With these assumptions, the viscous stress tensor reduces to:

$$\tau_{ij} = 2\mu \varepsilon_{ij} \quad (4.3)$$

where ε_{ij} is the strain rate tensor.

Equation 4.3 shows that stress is linearly proportional to strain. In Cartesian coordinates, only six out of the nine components of the viscous stress tensor (τ_{ij}) are independent for symmetry considerations. The viscous stress tensor consists of both normal and shear stresses as follows:

$$\tau_{ij} = \begin{pmatrix} \tau_{xx} & \tau_{xy} & \tau_{xz} \\ \tau_{yx} & \tau_{yy} & \tau_{yz} \\ \tau_{zx} & \tau_{zy} & \tau_{zz} \end{pmatrix} = \begin{pmatrix} 2\mu \frac{\partial u}{\partial x} & \mu \left(\frac{\partial u}{\partial y} + \frac{\partial v}{\partial x} \right) & \mu \left(\frac{\partial u}{\partial z} + \frac{\partial w}{\partial x} \right) \\ \mu \left(\frac{\partial v}{\partial x} + \frac{\partial u}{\partial y} \right) & 2\mu \frac{\partial v}{\partial y} & \mu \left(\frac{\partial v}{\partial z} + \frac{\partial w}{\partial y} \right) \\ \mu \left(\frac{\partial w}{\partial x} + \frac{\partial u}{\partial z} \right) & \mu \left(\frac{\partial w}{\partial y} + \frac{\partial v}{\partial z} \right) & 2\mu \frac{\partial w}{\partial z} \end{pmatrix} \quad (4.4)$$

The stress tensor σ_{ij} is used in the three Cartesian components of the Cauchy equation, with τ_{ij} expressed by Eq. 4.4, then the three expressions are rearranged in order to adopt the Laplacian operator and the *continuity equation* for incompressible flows, as reported in Eq. 4.5.

$$\frac{\partial u}{\partial x} + \frac{\partial v}{\partial y} + \frac{\partial w}{\partial z} = 0 \quad (4.5)$$

Finally, after combining the three components in a vector notation, the *Navier-Stokes (NS) momentum equation* for incompressible flow with constant viscosity is derived (Eq. 4.6).

$$\rho \frac{D\mathbf{v}}{Dt} = -\nabla P + \rho \mathbf{g} + \mu \nabla^2 \mathbf{v} \quad (4.6)$$

where ∇ is the gradient operator, ∇^2 the Laplacian operator and $\frac{D}{Dt}$ the material derivative.

The i^{th} -component of the NS equation is:

$$\rho \left(\frac{\partial u_i}{\partial t} + \frac{\partial u_j u_i}{\partial x_j} \right) = -\frac{\partial P}{\partial x_i} + \rho g_i + \mu \frac{\partial^2 u_i}{\partial x_l \partial x_l} \quad (4.7)$$

The Navier-Stokes (NS) system of equations, which includes the continuity equation and the momentum equations, is three-dimensional and time-dependent and fully governs the motion of fluid.

The fluid mechanical regime of a flow that impacts on a bluff body could be evaluated from the balance between the inertial and the viscous forces, usually expressed by means of the non-dimensional ratio $Re = UL/v$, called the Reynolds number and function of the kinematic viscosity v , the velocity scale U and the length scale L of the object impacted by the flow. The Reynolds number is used to describe the condition of the flow, whether it be laminar, transitional or turbulent. The laminar flow is defined as flow under conditions where forces due to viscosity are more significant than forces due to inertia, which results in fluid particles moving along essentially parallel lines. On the other hand, the turbulent flow exists where forces due to inertia are more significant than forces due to viscosity with the consequence that adjacent fluid particles do not move along parallel paths. The transitional flow is representative of an intermediate condition where the turbulence behavior of the flow is not yet fully developed.

The turbulent flow is a three dimensional and time dependent motion of fluid particles. Sometimes the definition of turbulence is simplified in irregular motion. Turbulent motion is irregular in the sense that it can be described by the laws of probability where the various quantities show a random variation with time and space but statistical averages of the instantaneous properties can be discerned. The first work on turbulence was carried out by Osborne Reynolds in 1883. His experiments in pipe flows showed that the flow becomes turbulent or irregular when the Reynolds number exceeds a certain critical value. Turbulent flows are characterized by the formation of structures, usually called eddies, induced by the physical interaction with some object of spatial scale L . A wide range of eddy sizes exists and the largest eddies have a size of the order of the width of the region intersected by the turbulent flow or of the object impacted by the flow. The large eddies contain most of the energy that is handed down to small eddies until the smallest ones (*Kolmogorov scale* η , defined in Eq. 4.8) which dissipate the energy into heat through the molecular viscosity (*energy cascade*). Kolmogorov, following Richardson's idea of the spectral energy cascade, hypothesized that the statistics of small scales are isotropic and depend on two parameters, the viscosity ν and the rate of dissipation ϵ . An inertial subrange between the largest scale (L) and the smallest one (η) exists, and in this range the statistics only depend on a single parameter, ϵ , while ν plays no role. The spectrum in the inertial subrange is proportional to $\epsilon^{2/3} K^{-5/3}$ (*the five-third law*), where K is the wave number.

$$\eta = \left(\frac{\nu^3}{\epsilon} \right)^{1/4} \quad (4.8)$$

The fluid motion regime can be classified based on the Reynolds number as proposed by Belvins 1990:

- $Re < 5$, laminar flow regime

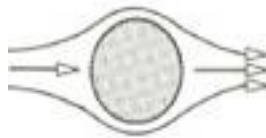


Figure 4.1 $Re < 5$, laminar flow regime.

- $5 < Re < 40$, formation of recirculation zones contained in the laminar substrate



Figure 4.2 Formations of two vortex downstream a cylinder

- $40 < Re < 150$, alternating vortex shedding - Von Karman vortex street



Figure 4.3 Alternating vortex shedding

- $150 < Re < 300$, transitional flow regime, the vortex street becomes turbulent

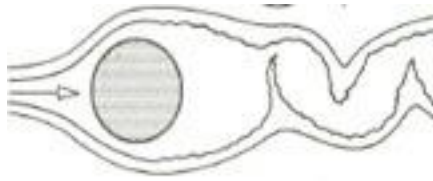


Figure 4.4 Transition from laminar to turbulent regime

- $300 < Re < 3 \cdot 10^5$, turbulent flow regime, the vortex street is fully turbulent

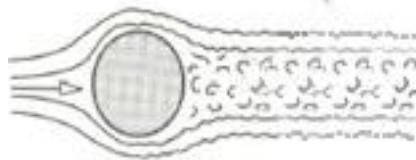


Figure 4.5 Turbulent flow regime

- $3 \cdot 10^5 < Re$, the turbulent flow regime becomes chaotic, the boundary layer is getting thinner and the separation point moves to the wake of the cylinder



Figure 4.6 Turbulent flow regime with vortex shedding downstream a cylinder

The unsteady solution of all scales of a turbulent flow can be obtained by means of the Direct Numerical Simulation (DNS), without any analytical approximation of the different turbulent scale of the motion. The size difference and the time scale difference between the largest and smallest eddies can be several orders of magnitude ($L \gg \eta$) and furthermore, these differences increase with the Reynolds number making DNS calculations of turbulent flows even more difficult as the Reynolds number increases. DNS solutions require extremely fine, fully three-dimensional grids and a very high computational cost. With today's computers, DNS results are not yet feasible for various practical high Reynolds number turbulent flows of engineering interest and this technique is adopted to describe the motion of fluids at low Re numbers (Laminar Regime). To solve the equation of motion for fluids characterized by high Reynolds numbers, *Large Eddy Simulations* (LES) are more commonly adopted. This technique is suited to solve unsteady features of the

large turbulent scale, while the small dissipative scales are modeled using a *subgrid-scale* model (SBS), which operates on the eddies lengths which are smaller than the modeled volume elements size (i.e. the dimensions of the computational mesh). The LES model takes advantage of the Kolmogorov theory, which assumes that the large eddies are dependent on the length scale of the object impacted by the flow while the smaller scales are more universal. In general, the most widely adopted numerical approach, thanks to the reduced computational burden, is the Reynolds Average Navier-Stokes model (RANS). The RANS model assumes that the instantaneous velocity of the flow can be decomposed into a mean value and a turbulent fluctuation, and all scales of turbulence are modelled by means of some turbulent closure model. The possible time dependence of the average terms of the velocity can be considered by solving the Unsteady Reynolds Average Navier-Stokes equations (URANS).

Reynolds in 1895 proposed the average approach to describe turbulent flows. Stationary turbulence characterizes a turbulent flow which does not vary, on the average, with time, while the homogeneous turbulence is a turbulent flow that, on the average, is uniform in all directions.

Considering a stationary turbulent flow the instantaneous velocity $u_i(\mathbf{x}, t)$, along the i direction, can be expressed as the sum of the mean, $U_i(\mathbf{x})$, and a fluctuating part, $u'_i(\mathbf{x}, t)$:

$$u_i(\mathbf{x}, t) = U_i(\mathbf{x}) + u'_i(\mathbf{x}, t) \quad (4.9)$$

where \mathbf{x} is the position vector and t is the time.

The quantity $U_i(\mathbf{x})$ is the time-averaged, or mean, velocity defined by:

$$U_i(\mathbf{x}) = \lim_{T \rightarrow \infty} \frac{1}{T} \int_t^{t+T} u_i(\mathbf{x}, t) dt \quad (4.10)$$

and the time average of the mean part is again the same time-average value:

$$\overline{U_i(\mathbf{x})} = \lim_{T \rightarrow \infty} \frac{1}{T} \int_t^{t+T} U_i(\mathbf{x}) dt = U_i(\mathbf{x}) \quad (4.11)$$

where the bar indicates the mean operator.

The time average of the fluctuating part of the velocity is zero:

$$\overline{u'_i(\mathbf{x}, t)} = \lim_{T \rightarrow \infty} \frac{1}{T} \int_t^{t+T} [u_i(\mathbf{x}, t) - U_i(\mathbf{x})] dt = U_i(\mathbf{x}) - \overline{U_i(\mathbf{x})} = 0 \quad (4.12)$$

The integration time T must be very long compared to the maximum period of the velocity fluctuation T_1 . Therefore, the expression $T \rightarrow \infty$ in the limits above actually indicates $T \gg T_1$.

When the mean flow contains slow variations with time, Eq. 4.9 becomes:

$$u_i(\mathbf{x}, t) = U_i(\mathbf{x}, t) + u'_i(\mathbf{x}, t) \quad (4.13)$$

and

$$U_i(\mathbf{x}) = \frac{1}{T} \int_t^{t+T} u_i(\mathbf{x}, t) dt, \quad T_1 \ll T \ll T_2 \quad (4.14)$$

where T_2 is the time scale of the slow variation of the flow.

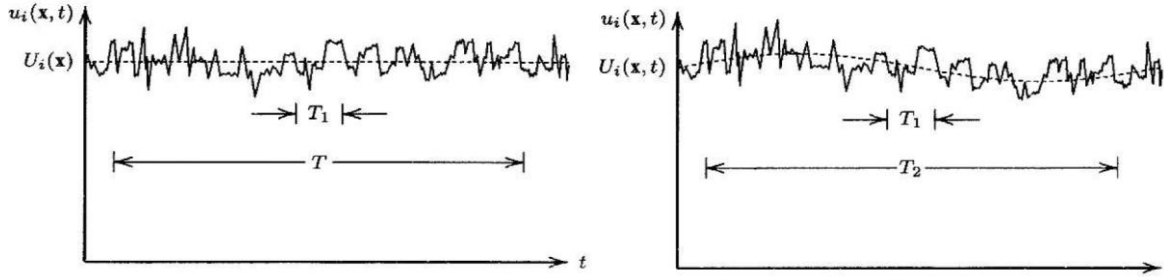


Figure 4.7 Time averaging for stationary turbulence (left) and nonstationary turbulence (right) from Wilcox (2006).

Starting from the fluctuating part, $u'_i(\mathbf{x}, t)$ which along the three coordinates direction (i) can be written also as u' , v' , w' , the specific normal Reynolds stress components are defined as $\overline{u'^2}$, $\overline{v'^2}$ and $\overline{w'^2}$ and normalized with the free-stream mean flow velocity U_{ref} to provide the **relative turbulence intensities**, I_u , I_v and I_w :

$$I_u = \frac{\sqrt{\overline{u'^2}}}{U_{ref}}, \quad I_v = \frac{\sqrt{\overline{v'^2}}}{U_{ref}} \quad \text{and} \quad I_w = \frac{\sqrt{\overline{w'^2}}}{U_{ref}} \quad (4.15)$$

The three components are not identical because turbulence is anisotropic in nature. Half the sum of the normal Reynolds stresses is the **turbulence kinetic energy** (k) per unit mass:

$$k = \frac{1}{2} (\overline{u'^2} + \overline{v'^2} + \overline{w'^2}) \quad (4.16)$$

Many turbulence model cannot distinguish the individual normal Reynolds stresses and provide only k as a quantitative turbulence indicator. This assumption implies that the turbulent fluctuations are more-or-less isotropic, therefore $\overline{u'^2} \approx \overline{v'^2} \approx \overline{w'^2}$ and the **Turbulence Intensity** can be written as:

$$I_{turb} = \frac{\sqrt{\frac{2k}{3}}}{U_{ref}} \quad (4.17)$$

4.2 COMPUTATIONAL FLUID DYNAMICS MODELS

The Unsteady Reynolds Navier-Stokes equations (URANS) were derived by assuming the decomposition of the flow into the average and the fluctuating part. Using this hypothesis both the velocity (u) and pressure (p) can be decomposed as Eq. 4.9 and 4.18.

$$p(\mathbf{x}, t) = P(\mathbf{x}) + p'(\mathbf{x}, t) \quad (4.18)$$

By averaging the pressure as in 4.11 and 4.12 it is possible to demonstrate that:

$$\overline{P(\mathbf{x})} = P(\mathbf{x}) \quad (4.19)$$

$$\overline{p'(\mathbf{x}, t)} = 0 \quad (4.20)$$

The continuity equation (4.5) can be written as:

$$\nabla \cdot \mathbf{v} = 0 \quad (4.21)$$

and by using the decomposition reported in Eq. 4.9 it is possible to obtain:

$$\nabla \cdot \mathbf{v} = \nabla \cdot \bar{\mathbf{v}} + \nabla \cdot \mathbf{v}' = 0 \quad (4.22)$$

Averaging the decomposed continuity equation yields:

$$\overline{\nabla \cdot \bar{\mathbf{v}}} = 0 \text{ and } \overline{\nabla \cdot \mathbf{v}'} = 0 \quad (4.23)$$

By using the decompositions (4.9 and 4.18) in Eq. 4.7, the i^{th} -component of the NS equation becomes:

$$\rho \left(\frac{\partial (U_i + u'_i)}{\partial t} + \frac{\partial ((U_j + u'_j)(U_i + u'_i))}{\partial x_j} \right) = - \frac{\partial (P + p')}{\partial x_i} + \rho g_i + \mu \frac{\partial^2 (U_i + u'_i)}{\partial x_l \partial x_l} \quad (4.24)$$

Using the mean operator and following the Reynolds hypothesis (see 4.11 and 4.12) the so-called Reynolds Average Navier-Stokes equation can be obtained as follows:

$$\rho \left(\frac{\partial U_i}{\partial t} + U_j \frac{\partial U_j}{\partial x_j} \right) = -\frac{\partial P}{\partial x_i} + \rho g_i + \mu \frac{\partial^2 U_i}{\partial x_l \partial x_l} + \frac{\partial(-\rho \overline{u'_i u'_l})}{\partial x_l} \quad (4.25)$$

The RANS model differs from the URANS one in that the time dependence of the mean flow velocity is neglected. In Eq. 4.25 the contribution of the turbulent fluctuations is concentrated in the last term and it is possible to define the Reynolds stress tensor T^R as follows:

$$T^R = \begin{pmatrix} -\rho \overline{u'_1 u'_1} & -\rho \overline{u'_1 u'_2} & -\rho \overline{u'_1 u'_3} \\ -\rho \overline{u'_2 u'_1} & -\rho \overline{u'_2 u'_2} & -\rho \overline{u'_2 u'_3} \\ -\rho \overline{u'_3 u'_1} & -\rho \overline{u'_3 u'_2} & -\rho \overline{u'_3 u'_3} \end{pmatrix} \quad (4.26)$$

Replacing T^R and using the material derivative the i^{th} -component of the Reynolds Average Navier-Stokes equations becomes:

$$\rho \frac{DU_i}{Dt} = -\frac{\partial P}{\partial x_i} + \rho g_i + \mu \frac{\partial^2 U_i}{\partial x_l \partial x_l} + \frac{\partial(T_{li}^R)}{\partial x_l} \quad (4.27)$$

The Boussinesq hypothesis allows one to write the components of the Reynolds stress tensor assuming:

$$\overline{u'_i u'_j} = -2\mu_T D \quad (4.28)$$

where

$$D = \frac{1}{2} \left(\frac{\partial \bar{u}_i}{\partial x_j} + \frac{\partial \bar{u}_j}{\partial x_i} \right) \quad (4.29)$$

and μ_T is called the *Eddy Viscosity*, and becomes the new unknown element of the Reynolds Average Navier-Stokes equations. The ratio between μ_T and ρ provides the *kinematic eddy viscosity* (ν_T).

For numerically solving this system of equations it is necessary to obtain the value of ν_T that, unlike the kinematic viscosity is not a constant, and varies both in space and time. Over the years, various methods were proposed to obtain ν_T , which mainly differ in the number and type of equations used to calculate the eddy viscosity. There are zero equation models that use a simple algebraic expression, one equation models that use a single partial differential equation (PDE) and two equation models that are the most sophisticated ones and use two PDEs to calculate ν_T . For the purposes of this thesis the $k-\omega$ Shear Stress Transport (SST) turbulence model was used. This is a two equations model that is commonly used for solving engineering problems. This closure model is based on the (*specific*) *turbulence kinetic energy* k defined in Eq. 4.16, the *energy dissipation per unit mass* ϵ and the *turbulent specific dissipation rate* ω reported below and defined as in Wilcox (2006).

The energy dissipation per unit mass ε is the rate at which k is converted into thermal internal energy per unit mass and is given, for incompressible flow, by Eq. 4.30:

$$\varepsilon = \nu \overline{\frac{\partial u'_i}{\partial x_k} \frac{\partial u'_j}{\partial x_k}} \quad (4.30)$$

where ν is the kinematic viscosity of the air.

Finally, ω is related to k by means of the kinematic eddy viscosity ν_T as in Eq. 4.31:

$$\omega \sim \frac{k}{\nu_T} \quad (4.31)$$

The SST k - ω closure model concentrates the advantages of the k - ε and k - ω models because it is able to switch to a k - ε behaviour in the free stream far from the object and to the k - ω model near the walls. The k - ε model formulated by Jones and Launder, (1972), is robust and reliable in the free flow region but it proved to be unreliable near the boundary layer, while the k - ω model formulated by Wilcox (1988), is capable of correctly modelling turbulence near the boundary layer but presents a strong dependency on arbitrary values in the free flow. The idea behind the SST k - ω closure model was developed by Menter (1992).

Concerning the topic of this thesis, Constantinescu et al. (2007), while investigating the shielding problem between two contiguous precipitation gauges, tested different numerical methods and concluded that the SST k - ω model is more consistent with the LES results for the upstream gauge, in conditions that are similar to the present work.

The two additional equations of the SST k - ω model for k and ω are:

$$\frac{\partial}{\partial t}(\rho k) + \frac{\partial \rho U_j k}{\partial x_j} = \widetilde{P}_k - \rho \beta^* \omega k + \frac{\partial}{\partial x_j} \left[\left(\mu + \frac{\mu_T}{\sigma_k} \right) \frac{\partial k}{\partial x_j} \right] \quad (4.32)$$

$$\frac{\partial}{\partial t}(\rho \omega) + \frac{\partial \rho U_j \omega}{\partial x_j} = \frac{\gamma}{\nu_T} P_k - \rho \beta \omega^2 + \frac{\partial}{\partial x_j} \left[\left(\mu + \frac{\mu_T}{\sigma_\omega} \right) \frac{\partial \omega}{\partial x_j} \right] + (1 - F_1) 2 \rho \sigma_{\omega 2} \frac{1}{\omega} \frac{\partial k}{\partial x_j} \frac{\partial \omega}{\partial x_j} \quad (4.33)$$

where

$$P_k = \tau_{ij} \frac{\partial U_i}{\partial x_j} \quad (4.34)$$

$$\widetilde{P}_k = \min(P_k; c_l \varepsilon) \quad (4.35)$$

and the turbulent viscosity is obtained as:

$$\mu_T = \rho a_1 \frac{k}{\max(a_1 \omega, SF_2)} \quad (4.36)$$

The combination between the two closure models is obtained thanks to the blending function F_1 that assumes the value one near the surface and is zero in the outer part and for free shear flows. Therefore, the generic coefficient φ is calculated as:

$$\varphi = F_1 \varphi_1 + (1 - F_1) \varphi_2 \quad (4.37)$$

where φ_1 and φ_2 indicate the coefficients of the k- ε and k- ω models, respectively.

For the numerical simulations performed in this thesis the default values of these coefficients, here listed in Table 4.1, were adopted with no further calibration.

Table 4.1 coefficients the k- ε and k- ω models

σ_{k1}	1.176
σ_{k2}	1.000
$\sigma_{\omega1}$	2.000
$\sigma_{\omega2}$	1.168
K	0.41
γ_1	0.5532
γ_2	0.4403
β_1	0.0750
β_2	0.0828
β^*	0.09
c_1	10

Finally, the other terms of the additional equations are expressed as follows:

$$F_1 = \tanh(\arg_1^4); \arg_1 = \min\left(\max\left(\frac{\sqrt{k}}{\beta^* \omega y}; \frac{500\nu}{y^2 \omega}\right); \frac{4\rho\sigma_{\omega 2}k}{CD_{k\omega}y^2}\right);$$

$$CD_{k\omega} = \max\left(2\rho\sigma_{\omega 2} \frac{1}{\omega} \frac{\partial k}{\partial x_j} \frac{\partial \omega}{\partial x_j}; 1.0e^{-10}\right) \quad (4.38)$$

$$F_2 = \tanh(\arg_2^2); \arg_2 = \max\left(2 \frac{\sqrt{k}}{\beta^* \omega y}; \frac{500\nu}{y^2 \omega}\right) \quad (4.39)$$

$$\tau_{ij} = \mu_T \left(\frac{\partial U_i}{\partial x_j} + \frac{\partial U_j}{\partial x_i} - \frac{2}{3} \frac{\partial U_k}{\partial x_k} \right) - \frac{2}{3} \rho k \delta_{ij} \quad (4.40)$$

In this thesis the role of the natural free-stream turbulence was also investigated by imposing that the precipitation gauge is impacted by a flow characterized by a certain level of turbulence. The airflow fields obtained in uniform and turbulent free-stream conditions were compared. Three different approaches were tested:

1. The free-stream turbulence was generated by introducing a solid fence with regular square grid upstream of the gauge and by employing the URANS model.
2. The free-stream turbulence was obtained, with the URANS model, by setting a constant turbulent kinetic energy value as a boundary condition upstream of the gauge.
3. The turbulence generated by obstacles located upstream of the gauge was obtained by performing Large Eddy Simulations (LES).

The LES make use of a filtering operation to define the threshold (Δ) between the directly solved turbulent scales and those that are modelled.

$$u'_i = u_i - \bar{u}_i \quad (4.41)$$

$$\Delta = (\Delta x \Delta y \Delta z)^{1/3} \quad (4.42)$$

where \bar{u}_i denotes the *filtered-scale velocity* that is directly solved by the model meanwhile u'_i is the *subgrid-scale (SGS) velocity*.

Using this notation, it is possible to generalize the filter with a convolution integral between u_i and the *filter function* G :

$$\bar{u}_i(\mathbf{x}, t) = \iiint G(\mathbf{x} - \boldsymbol{\zeta}; \Delta) u_i(\boldsymbol{\zeta}, t) d^3 \boldsymbol{\zeta} \quad (4.43)$$

The Navier-Stokes continuity and momentum equations obtained by using Eq. 4.41 become:

$$\frac{\partial \bar{u}_i}{\partial x_i} = 0 \quad (4.44)$$

$$\frac{\partial \bar{u}_i}{\partial t} + \bar{u}_j \frac{\partial \bar{u}_i}{\partial x_j} = -\frac{1}{\rho} \frac{\partial \bar{p}}{\partial x_i} + \nu \frac{\partial^2 \bar{u}_i}{\partial x_j^2} - \frac{\partial \tau_{ij}}{\partial x_j} \quad (4.45)$$

Here, the over-bar indicates the spatial filtering and not the time-averaging as is the case of RANS, moreover it is possible to highlight that the filtered equations are similar to the RANS ones. The Smagorinsky SGS approach was adopted to model the sub-grid stresses (τ_{ij}) with a gradient-diffusion process in a similar way to a molecular motion, in the form:

$$\tau_{ij} = 2\nu_T S_{ij} \quad (4.46)$$

$$S_{ij} = \frac{1}{2} \left(\frac{\partial \bar{u}_i}{\partial x_j} + \frac{\partial \bar{u}_j}{\partial x_i} \right) \quad (4.47)$$

$$\nu_T = (C_S \Delta)^2 \sqrt{S_{ij} S_{ij}} \quad (4.48)$$

where $C_S = 0.2$ is the Smagorinsky dimensionless empirical parameter.

The numerical CFD models allow wall functions to be introduced in order to model the solution very close to the surface by reducing the computational burden. To check that the grid size near the precipitation gauge surface was consistent with the use of a wall function (see e.g. Menter and Esch, 2001), the wall y^+ was calculated. The wall y^+ is a non-dimensional distance defined as Eq. 4.49:

$$y^+ = \frac{u_\tau y_n}{\nu_a} \quad (4.49)$$

where y_n is the distance from the wall to the mid-point of the wall-adjacent cells, ν_a is the kinematic viscosity of the air and u_τ is the friction velocity.

4.2.1 Numerical schemes and stability of the solution

Numerically solving a Partial Differential Equation (PDE) involves a small error for each discretization step, this is due to the fact that the function is substituted with an approximation of itself. The OpenFOAM software, here adopted to perform CFD simulations provides numerous schemes that can be chosen by the user, their choice can greatly affect both the results and the required computational resources. Numerical schemes can be either implicit, which are unconditionally stable, meaning that the solution remain always bounded regardless of the chosen time step, or explicit, which remains bounded only if the time step is small enough.

An increase in stability of the numerical scheme usually produces an increase of the computational burden at the same order of approximation. For these reasons, an approach that is commonly adopted for solving CFD studies is to start the simulation with an implicit scheme at the first order of approximation to initialize the model and then switch to an explicit scheme of higher order to improve the precision. The condition used to evaluate the stability of the solution is given by the Courant-Friedrichs-Lewy inequality:

$$C = \Delta t \sum_{i=1}^n \frac{u_{xi}}{\Delta x_i} < C_{max} \quad (4.50)$$

where u_{xi} is the speed in the i^{th} cell, Δx_i is the length of the i^{th} cell in the direction of u_{xi} , Δt is the chosen time step and C_{max} is the maximum Courant number. For most explicit schemes a Courant number strictly below one is needed, requiring an extremely small time step, whose consequence is a high computational cost. In practical applications, a relaxation factor ϕ is usually applied at every computational step to improve convergence, especially during the initialization phase, which allows using a larger time step.

For the results presented in this thesis two different combinations of the numerical schemes were used, the first is an initialization scheme used with a relatively large time step and first order accuracy, while the latter is a second order scheme calculated using a smaller time step. Six numerical schemes are needed to solve the Navier-Stokes equations as listed below:

- The *time scheme*, is used to calculate the first order time derivatives. For the initialization the *Euler* scheme was used, a first order, always bounded implicit scheme, then for the final calculation, the implicit *CranckNicolson* scheme was adopted, an implicit second order accurate scheme.
- *Gradient scheme*, is used to discretize the gradient terms. The *Gauss* entry specifies the standard finite volume discretization of Gaussian integration which requires the interpolation of values from the cell centres to the face centres. The interpolation scheme is then given by the *linear* entry, meaning linear interpolation or central differencing. It also possible to set limiters in order to get stability. The *cellMDlimited* option bounds the cell gradient to ensure that the face values obtained by extrapolating the cell value to the cell faces using the gradient are bounded by the neighboring cells minimum and maximum. The initialization was performed using a *standard Gauss* scheme with linear interpolation, that is a first order accuracy scheme, while for the final calculation a second order *LeastSquare* scheme was used.

- *Divergence schemes*, are used to evaluate the divergence term and then calculate the flux of the properties through the cell faces using the Gauss integration, these scheme are also usually limited to improve the stability, the limiter can be calculated in all three directions or only in the direction of the resultant vector. These are the most critical schemes because they affect the advection terms. Here the initialization was done using the *Upwind* scheme, that is first order and bounded, and then it was changed to improve the accuracy for the final calculation with a *LinearUpwind* scheme that is second order but unbounded. A blending function was applied to improve stability in regions with high values of *Courant* number.
- The *surface normal gradient schemes* are required to solve the Laplacian term using Gaussian integration. The solution can be stabilized by introducing a correction factor ϕ set between 0 (great stability/low accuracy) and 1 (low stability/great accuracy). This scheme was maintained unchanged, applying a moderate correction for non-orthogonality.
- The *Laplacian scheme* discretizes the Laplacian term. The *Gauss* scheme is the only choice of discretization and requires a selection of both an interpolation scheme for the diffusion coefficient and a surface normal gradient scheme. In this case the scheme was maintained unchanged using a linear interpolation and a bounding coefficient.
- The *interpolation scheme*, is used to transform cell-centre quantities to face centres. The operation is used in many of the finite volume calculations, e.g. for the calculation of gradient, divergence, and Laplacian terms. Usually the increase in precision of more sophisticated schemes is negligible if confronted with the increase in computational requirement.

The numerical schemes used are listed in the Table 4.2.

The transition between the two combinations was done gradually, first by reducing the Courant number and then by exchanging one scheme at a time and waiting for convergence between changes.

Table 4.2 Numerical schemes adopted in the initial phase of the simulations and in the finalization phase.

Scheme	Initial combination	Final combination
Time	<i>Euler</i>	<i>CrankNicolson 0.9</i>
Gradient	<i>CellMDLimited Gauss linear 0.5</i>	<i>CellLimited leastSquares 1.0</i>
Divergence	<i>Gauss upwind</i>	<i>GaussCoBlended 0.5 linearUpwind</i>
Surface normal gradient	<i>Limited 0.5</i>	<i>Limited 0.5</i>
Laplacian	<i>Gauss Linear Limited 0.5</i>	<i>Gauss Linear Limited 0.5</i>
Interpolation	<i>Linear</i>	<i>Linear</i>

4.3 CFD SIMULATION OF THE AERODYNAMIC RESPONSE OF VARIOUS GAUGE GEOMETRIES AND WIND TUNNEL VALIDATION

The bluff-body aerodynamics of catching-type precipitation gauges, characterized by the spatial scale (L) expressed by the diameter of the collector (D), generates turbulence when impacted by wind. Turbulent fluctuations arise downstream and above the gauge collector. In the literature, both RANS and LES simulations were conducted to obtain the flow fields for various gauge geometries and wind speeds (Nešpor and Sevruck, 1999; Thériault et al., 2012; Colli et al., 2016a; Colli et al., 2018). Following the literature approach, in this thesis, URANS simulations were conducted to obtain the airflow fields around various gauge geometries: the cylindrical shape of the *CAE-PMB25*[®] (Figure 4.8), the chimney shape of the *Geonor-T200B*[®] (Figure 4.9), the inverted conical shape of the *EML-SBS500*[®] (Figure 4.10), and the inverted conical shape of the *Nipher*[®] wind-shield (Figure 4.11) installed around the gauge collector. The numerical simulations have been robustly supported and validated by means of an extensive wind tunnel experimental campaign. In this chapter, results are visualized in terms of normalized maps and profiles of the flow velocity magnitude (U_{mag}) and updraft (U_z) on the vertical along-wind symmetry plane of the gauge collector ($y = 0$) and along the horizontal plane at the collector elevation ($z = 0$). The validation of numerical results was obtained by means of comparison with wind tunnel local flow velocity measurements obtained in selected positions close to the gauge collector.

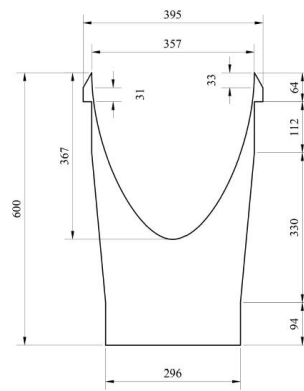


Figure 4.8 *CAE-PMB25*[®] gauge: dimensional drawing in mm (left) and operational installation (right).

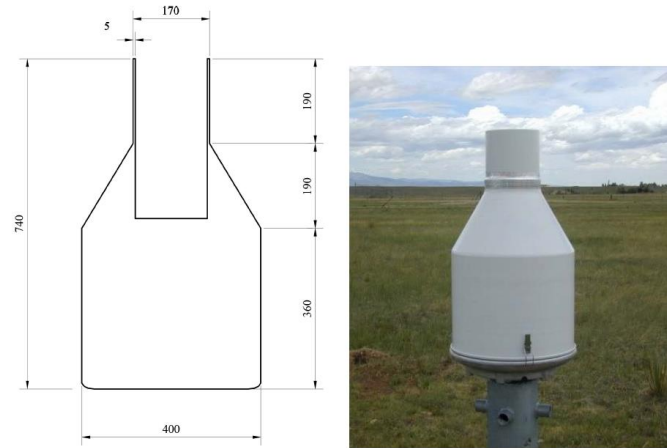


Figure 4.9 *Geonor-T200B*® gauge: dimensional drawing in mm (left) and operational installation (right).

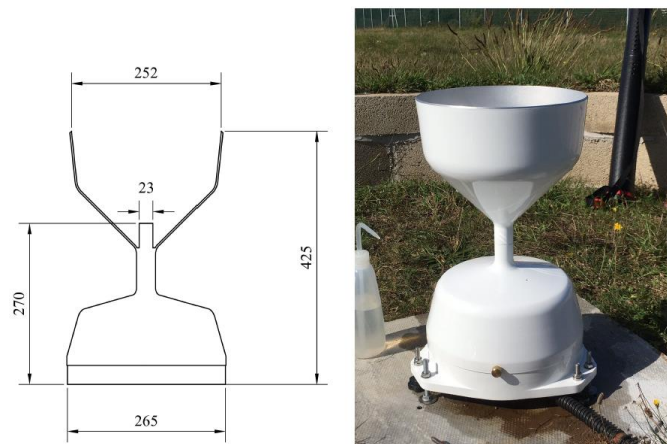


Figure 4.10 *EML-SBS500*® gauge: dimensional drawing in mm (left) and operational installation (right).

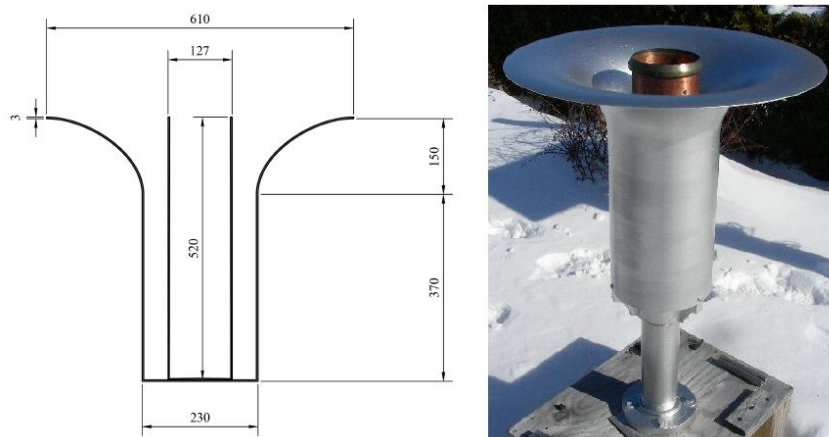


Figure 4.11 *Nipher*® shield: dimensional drawing in mm (left) and operational installation (right).

4.3.1 CFD simulations

Numerical simulations were conducted at the wind speed of 5, 10 and 20 m s⁻¹ for each gauge geometry under uniform free-stream conditions. The Reynolds number for each gauge (Table 3) was calculated by assuming as a characteristic dimension, the diameter of the gauge collector for the unshielded gauges and the diameter of the shield for the collector equipped with the *Nipher*[®] shield. Reynolds numbers reveal that the flow regime is in all cases fully turbulent.

Table 3 Reynolds number for the simulated gauge geometries and for each wind speed tested.

	D [m]	$Re (U_{ref} = 5 \text{ m s}^{-1})$	$Re (U_{ref} = 10 \text{ m s}^{-1})$	$Re (U_{ref} = 20 \text{ m s}^{-1})$
<i>CAE-PMB25</i> [®]	0.357	$1.19 \cdot 10^5$	$2.38 \cdot 10^5$	$4.76 \cdot 10^5$
<i>Geonor-T200B</i> [®]	0.160	$5.67 \cdot 10^4$	$1.13 \cdot 10^5$	$2.27 \cdot 10^5$
<i>EML-SBS500</i> [®]	0.252	$8.40 \cdot 10^4$	$1.68 \cdot 10^5$	$3.36 \cdot 10^5$
<i>Nipher</i> [®] Shield	0.610	$2.03 \cdot 10^5$	$4.07 \cdot 10^5$	$8.13 \cdot 10^5$

Numerical models of the gauge geometries were realized in the Standard Triangulation Language (STL) format using a 3D CAD software. The three-dimensional computational spatial domains, whose dimensions are listed in Table 4, were discretized using an unstructured hybrid hexahedral/prismatic finite volume mesh. For all gauges the number of cells of the computational mesh is about 1.5×10^6 elements. Refinements boxes and layers were realized close to the gauge and on the surface in order to ensure the quality of the solution in the region affected by large gradients of velocity and pressure. The quality of the mesh was checked by using the geometry parameters of orthogonality, skewness and aspect ratio. The maximum value obtained for these parameters is reported for each geometry in Table 4.

Table 4 Size of the computational domains [m]

	Size of the computation domain	Max skewness	Max non-orthogonality	Max aspect ratio
<i>CAE-PMB25</i> [®]	8 x 6 x 4	2.44	56.76	17.29
<i>Geonor-T200B</i> [®]	7 x 5 x 4	1.16	44.65	15.12
<i>EML-SBS500</i> [®]	5.8 x 5 x 2.2	2.48	64.70	23.43
<i>Nipher</i> [®] Shield	9 x 6 x 4.6	2.26	60.12	20.80

In the following panels some details of the computational mesh along the stream-wise direction in the central crosswise sections of the simulated domain are shown.

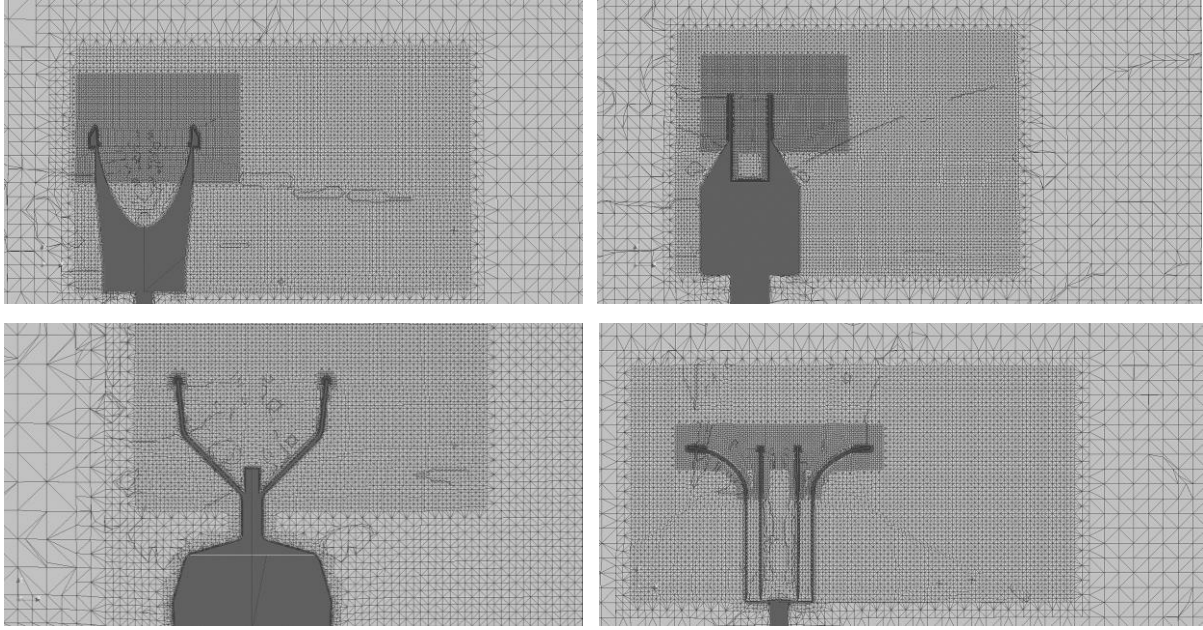


Figure 4.12 Details of the computational mesh, for each gauge geometry, in the vertical plane along the stream-wise direction in central crosswise section.

URANS simulations were conducted to obtain the disturbed airflow around the gauges. The “pimpleFoam” solver of the open-source OpenFOAM software was employed to solve the Reynolds Average Navier-Stokes equations. The SST $k-\omega$ turbulent closure model was set using the “kOmegaSST” function. The fluid air was modelled as a Newtonian incompressible fluid with kinematic viscosity $\nu_a = 1.5 \times 10^{-5} \text{ m}^2 \text{ s}^{-1}$ and density $\rho_a = 1.25 \text{ kg m}^{-3}$ at a reference environmental temperature $T_a = 20^\circ \text{C}$.

For each configuration, at the inlet of the computational domain (y - z plane) the undisturbed wind speed, U_{ref} , was imposed parallel to the x axis and was maintained uniform and constant in time, while a null gradient condition was set for pressure. At the outlet, y - z plane opposite to the inlet, the pressure was imposed equal to the atmospheric one and a null gradient condition for the velocity was set. The lateral surfaces of the domain were set as symmetry planes while the ground and the gauge surface were assumed impermeable with a no-slip condition. In all computational cells of the spatial domain, initial conditions were imposed equal to U_{ref} for the velocity and equal to zero for the relative pressure.

4.3.2 Wind tunnel facility

For this part of the work the wind tunnel facility available in the Department of Civil Chemical and Environmental engineering (DICCA) at the University of Genova was adopted. The wind tunnel is a closed circuit system made of metal carpentry, with a footprint of $8 \times 21 \text{ m}$ and a cross section of the test chamber of $1.35 \times 1.70 \text{ m}$ (Figure 4.13). The measurement portion of the tunnel has a length of 8.8 m and is divided in two parts, the first section, is located at 1.5 m downstream of the convergent and is usually used for measurements in homogeneous flow, being characterized by very low values of the index of turbulence. The second measurement section is located in the terminal part of the test chamber, it is equipped with a rotary table used for positioning the models immersed in the flow; this section is usually adopted for

aerodynamic or aeroelastic tests and to measure the flow field in turbulent conditions generated by introducing bespoke obstacles along the chamber upstream of the measuring section or by inserting various types of grid in the first section. After the measuring sections the tunnel changes from a rectangular cross-section to a circular section, where the fan is located. The fan, the motor and the flow straightener (stator), are placed on a steel base with dampening pads and the base is anchored to a rigid foundation made of reinforced concrete, isolated from the rest of the pavement. The fan, with a maximum speed of 900 rev/min, is controlled by a frequency converter that allows the speed in the test chamber to be continuously adjusted with an accuracy of $\pm 0.1 \text{ m s}^{-1}$. The reference speed of the flow inside the tunnel is detected by means of a Pitot static tube positioned near the roof of the test chamber, upstream of the section engaged by the model, in an undisturbed region of the flow. The kinetic pressure is obtained as the difference between the total pressure and the static pressure, and is measured by a differential pressure gauge. The value of the air density used to convert the kinetic pressure measurement into the corresponding velocity value is assessed on the basis of the air temperature measured in the test chamber.



Figure 4.13 Pictures of the measurement chamber of the DICCA wind tunnel

Due to the limited dimensions of the cross section of the test chamber, three precipitation gauges under test were reproduced in scaled 3-D printed models (see Figure 4.14) according to the following ratios:

- *CAE-PMB25*[®] 1:1.5
- *Geonor T200B*[®] 1:2
- *Nipher*[®] shield 1:1.5

According to the Reynold similitude the WT flow velocities have been adequately scaled.



Figure 4.14 3-D printed scaled models of the *Geonor-T200B*® gauge (on the left), the *CAE-PMB25*® gauge (on the right) and of the cylindrical collector equipped with a *Nipher*® shield (in the centre).

Local measurements of the wind speed were acquired using a fast-response multi-hole probe (a 4 holes “Cobra” probe) characterized by an acceptance cone of $\pm 45^\circ$, mounted on a 3 degrees of freedom traversing system, which allowed measurements to be obtained at any coordinates of interest. Measurements were sampled at 2 kHz. The measurement positions for each gauge geometry, summarized in the following panels, are expressed in mm and refer to the scaled models.

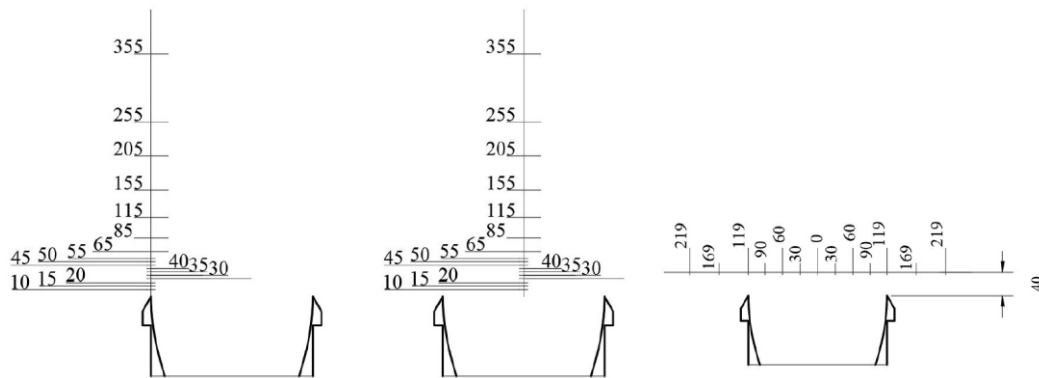


Figure 4.15 Local flow velocity positions, expressed in mm, above the collector of the *CAE-PMB25*® scaled gauge model, along the vertical (left-hand panels) in the upwind edge of the collector and in the centre of the collector and along the longitudinal and transversal directions (right-hand panel).

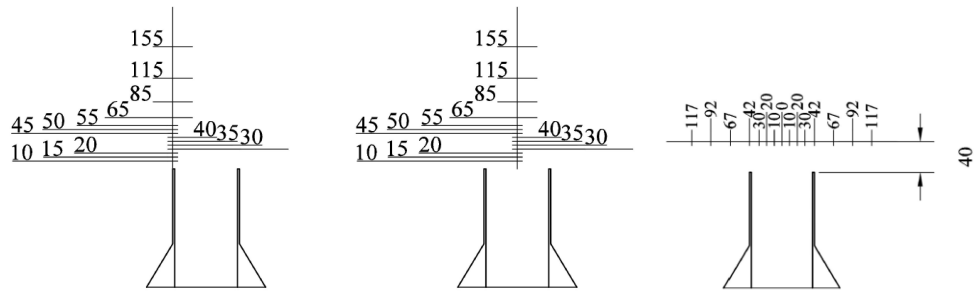


Figure 4.16 Local flow velocity positions, expressed in mm, above the collector of the *Geonor-T200B*[®] scaled gauge model, along the vertical (left-hand panels) in the upwind edge of the collector and in the centre of the collector and along the longitudinal and transversal directions (right-hand panel).

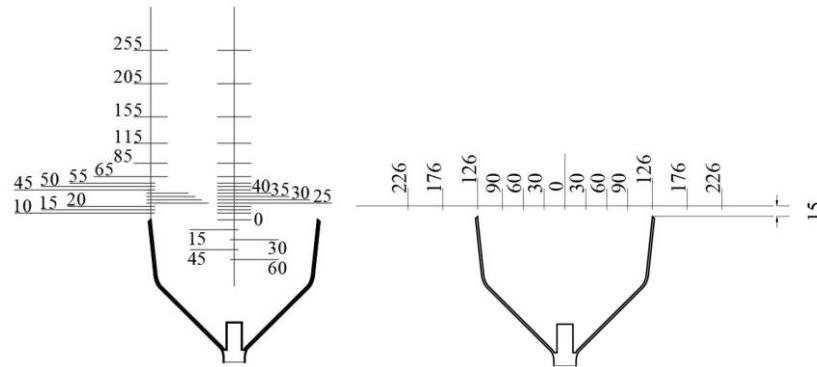


Figure 4.17 Local flow velocity positions, expressed in mm, above the collector of the *EML-SBS500*[®] scaled gauge model, along the vertical direction (left-hand panel) in the upwind edge of the collector and in the centre of the collector and along the longitudinal and transversal directions (right-hand panel).

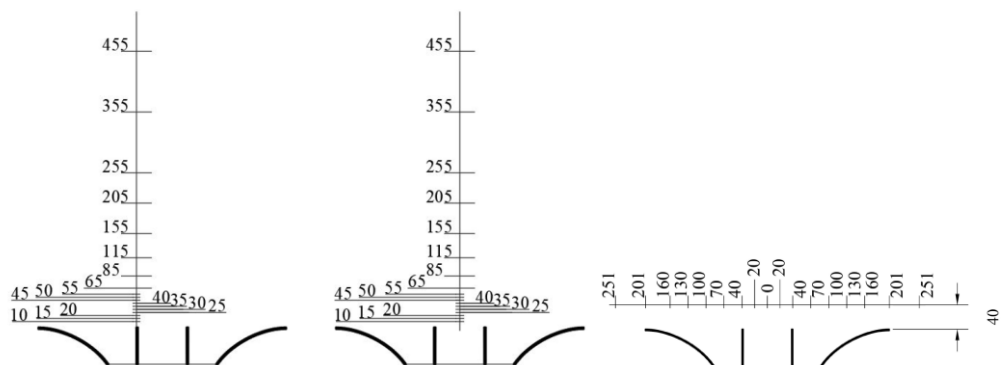


Figure 4.18 Local flow velocity positions, expressed in mm, above the cylindrical collector equipped with a scaled *Nipher*[®] shield model, along the vertical (left-hand panels) in the upwind edge of the collector and in the centre of the collector and along the longitudinal and transversal directions (right-hand panel).

4.3.3 Results and validation

In this section, numerical results are shown in the form of normalized flow velocity profiles and colour coded maps. Validation of the numerical results was obtained by comparison with WT local flow velocity measurements in terms of both the normalized magnitude and components of the flow velocity. The spatial coordinates are normalized with the gauge collector diameter (D), while the flow velocity is normalized with the reference flow velocity (U_{ref}) for the simulations and with the undisturbed wind speed, measured in the wind tunnel upstream of the obstacle, for the experimental measurements.

Figure 4.19 shows the calculated velocity profiles in terms of normalized magnitude (U_{mag}/U_{ref}) of flow velocity along the normalized vertical direction (z/D) at the upwind edge of the collector ($x/D = -0.5$, $y/D = 0$) and at the centre of the collector ($x/D = 0$, $y/D = 0$) for each gauge geometry and for the different wind speeds investigated. For all gauges these results show almost full scalability of the velocity profiles with the wind speed, since the maximum differences between the normalised velocity profiles for $U_{ref} = 5 \text{ m s}^{-1}$ and $U_{ref} = 20 \text{ m s}^{-1}$ are about 4%. Based on this observation the colour coded maps of the velocity fields, close to the gauges, are reported here as normalized magnitude or updraft for the undisturbed wind speed of 10 m s^{-1} .

In Figure 4.20 longitudinal profiles of the normalized vertical velocity (U_z/U_{ref}) along the stream-wise direction at $z = 0.015 \text{ m}$ above the collector and $y = 0$ are reported for each gauge geometry and for the three simulated wind speeds ($5\text{-}10\text{-}20 \text{ m s}^{-1}$), for the *CAE-PMB25*[®] (upper left), *Geonor-T200B*[®] (upper right), *EML-SBS500*[®] (lower left) and *Nipher*[®] shield (lower right). It is evident from the graphs that the maximum updraft (a bit larger than 0.6) is associated with the *Geonor-T200B*[®] gauge, due to the chimney shape of the gauge body, while the cylindrical (*CAE-PMB25*[®]) and inverted conical (*EML-SBS500*[®]) gauges show just a slightly lower maximum. On the contrary, the efficacy of the *Nipher*[®] gauge in reducing the wind-induced errors is highlighted in the right-hand lower panel by the reduced updraft (about 0.4) and the nearly constant and null vertical velocity observed along the whole longitudinal profile above the gauge collector. The numerical values of the normalized maximum updraft and downdraft obtained for each gauge geometry are reported in Table 4.5.

Also the longitudinal profiles are quite scalable in all panels, with the exception of the wake region where the effect of the turbulence generated by the obstruction of the gauge to the flow is most relevant. This effect is especially significant for the cylindrical (*CAE-PMB25*[®]) and inverted conical (*EML-SBS500*[®]) gauges.

Table 4.5 Maximum normalized updraft and downdraft obtained for the four gauge geometries investigated.

	Max updraft [-]	Max downdraft [-]
<i>CAE-PMB25</i>	0.684	-0.305
<i>Geonor-T200B</i>	0.693	-0.144
<i>EML-SBS</i>	0.610	-0.374
<i>Nipher Shield</i>	0.370	-0.169

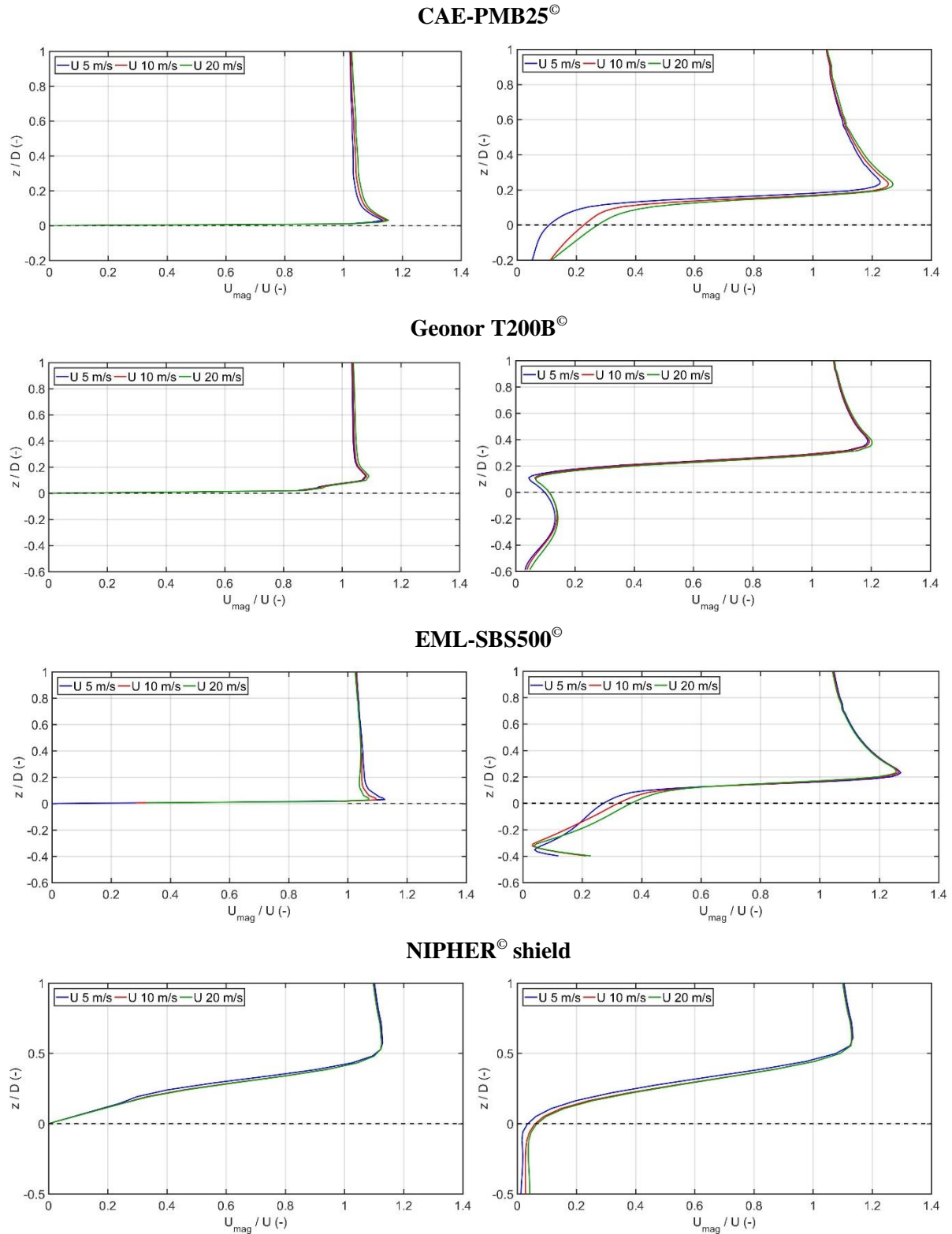


Figure 4.19 Numerical profiles of the normalized velocity magnitude (U_{mag}/U_{ref}) along the vertical direction (z/D) at the upwind edge of the collector ($x/D = -0.5$) on the left and at the centre of the collector ($x/D = 0$) on the right, for each gauge geometry and for the three simulated wind speeds (5-10-20 m s^{-1}).

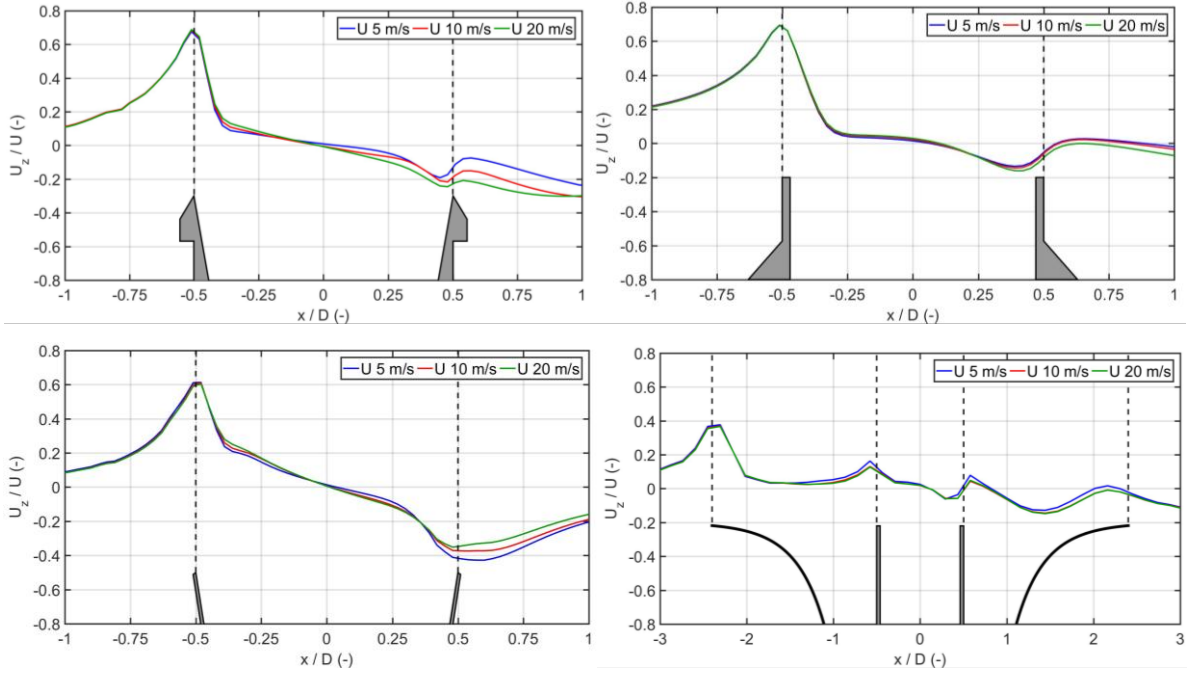


Figure 4.20 Numerical profiles of the normalized vertical velocity (U_z/U_{ref}) along the stream-wise direction above the collector at $z = 0.015$ m and $y = 0$ for each gauge geometry and for the three simulated wind speeds (5-10-20 m s^{-1}) for the *CAE-PMB25*[®] (upper left), *Geonor-T200B*[®] (upper right), *EML-SBS500*[®] (lower left) and *Nipher*[®] shield (lower right).

In Figure 4.21 the patterns of the normalized magnitude of flow velocity in the vertical section along the wind direction at $y/D = 0$ for the four gauge geometries are depicted. These maps reveal that the region where the flow velocity is higher than the undisturbed flow (red zone) remains confined within the limits of the downwind part of the collector for the gauge with inverted conical shape (*EML-SBS500*[®]) while it remains unconfined (because it tends to develop further upward) for the gauge with chimney shape (*Geonor-T200B*[®]). In addition, the velocity values in the accelerated zone are higher for the inverted conical gauge. The behaviour of the gauge with cylindrical shape is intermediate. Different is the case of the collector equipped with the *Nipher*[®] shield; in this case the gauge collector is interested by a smoothed velocity field thanks to the efficient shielding effect.

In Figure 4.22 the vertical section of the normalized magnitude of flow velocity, (U_{mag}/U_{ref}) along the stream-wise direction at the gauge collector elevation $z/D = 0$ is depicted on the left column, while the normalized updraft, (U_z/U_{ref}) is on the right-hand column, for each gauge geometry and $U_{ref} = 10 \text{ m s}^{-1}$. The images show the acceleration of the airflow with respect to the undisturbed velocity magnitude both around the gauge body and above it, highlighting the bluff-body nature of the obstacle. All gauges produce lateral accelerated flow patterns with again a limited effect in the case of the *Nipher*[®] shield, and the inverted conical (*EML-SBS500*[®]) gauge is peculiar in that the detachment of the turbulent wake from the gauge body occurs quite late in the leeward part of the gauge with respect to the cylindrical (*CAE-PMB25*[®]) and chimney shaped (*Geonor-T200B*[®]) gauge. The inverted conical (*EML-SBS500*[®]) gauge also shows the weaker wake of reduced velocity, associated with the development of turbulence, indicating that the obstruction to the wind is less strong with this particular gauge.

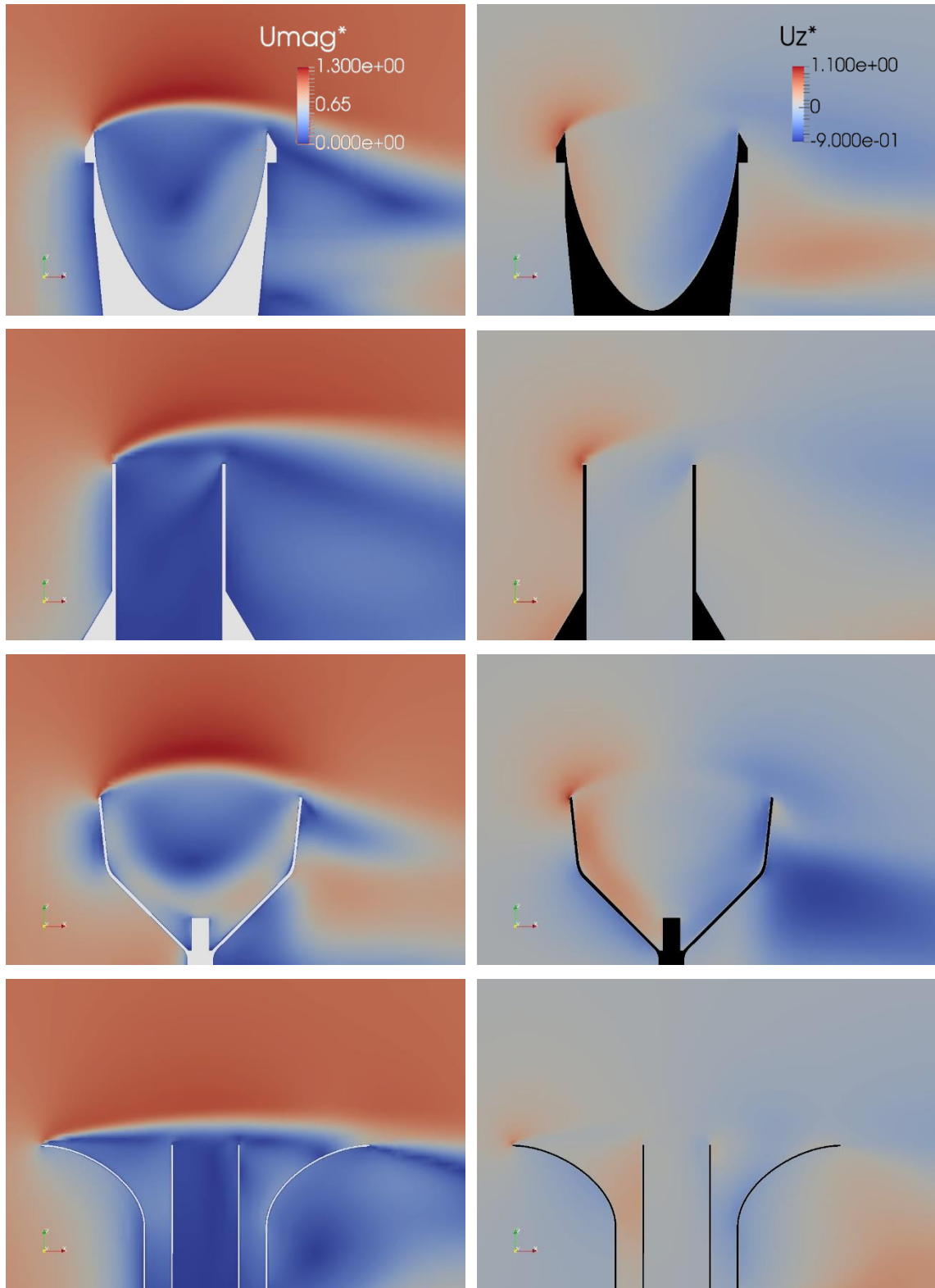


Figure 4.21 Vertical section of the normalized magnitude of flow velocity (U_{mag}/U_{ref}) on the left and the normalized updraft (U_z/U_{ref}) on the right along the stream-wise direction at $y/D = 0$, for each gauge geometry and $U_{ref} = 10 \text{ m s}^{-1}$. The color bars shown in the top panels are valid for all pictures.

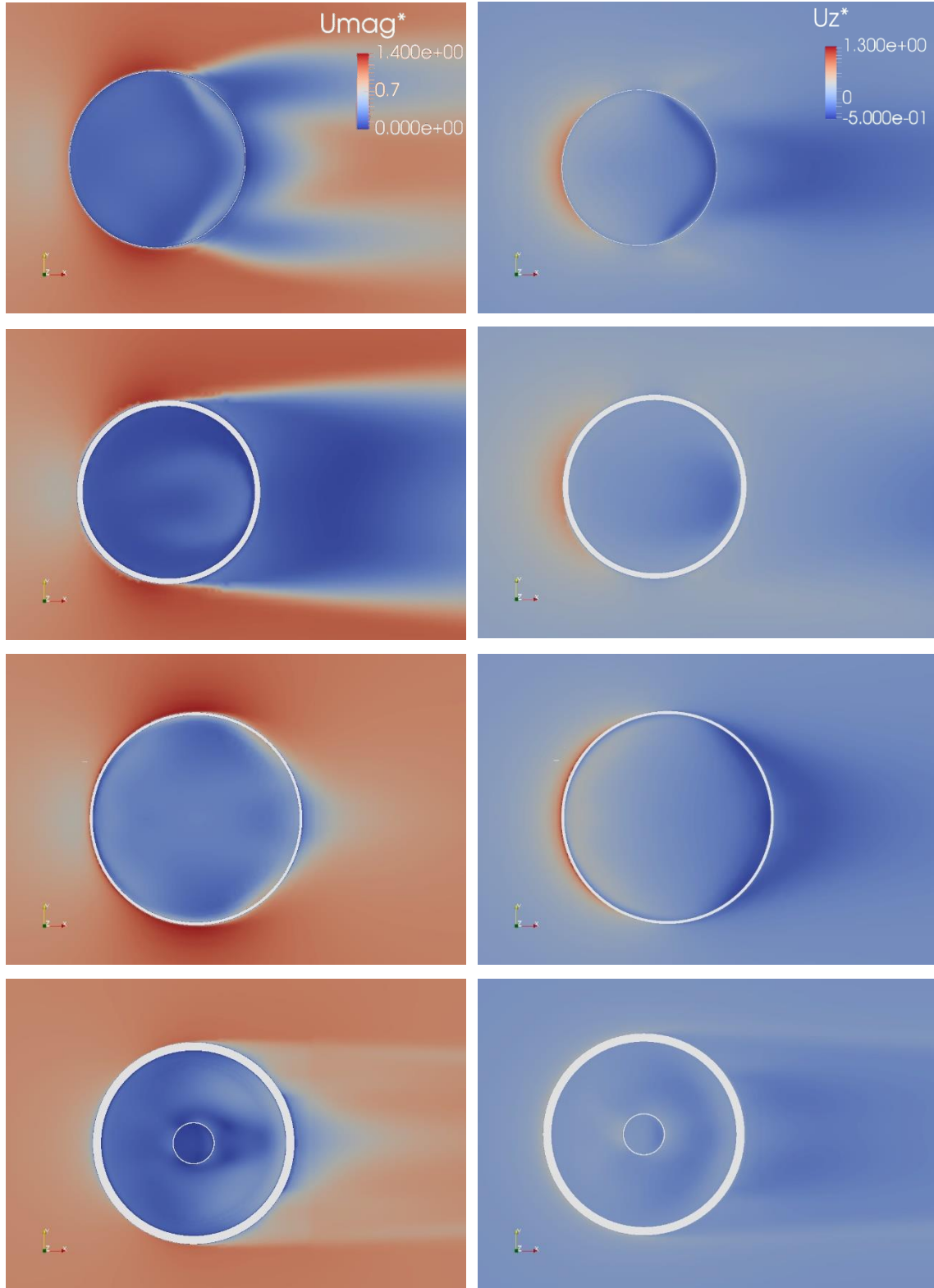


Figure 4.22 Vertical section of the normalized magnitude of flow velocity, (U_{mag}/U_{ref}) on the left, and the normalized updraft, (U_z/U_{ref}) on the right, along the stream-wise direction at the gauge collector elevation $z/D = 0$, for each gauge geometry and $U_{ref} = 10 \text{ m s}^{-1}$. The color bars shown in the top panels are valid for all pictures.

On the right-hand column of Figure 4.22, the updraft and downdraft region above the gauge collector are clearly visible for all gauges, together with their normalized magnitude. In all cases, except for the *Nipher*[®] shield that is quite efficient in reducing the impact of the gauge body on the incoming wind, significant updraft is obtained just in front of the gauge collector, and downdraft in the second half of the collector and in the turbulent wake.

The profiles of the vertical velocity component over the gauge collector are compared in Figure 4.23 for the investigated gauges. It is evident that – except for the *Nipher*[®] shield – all gauges exhibit similar maximum updraft values (between 0.6 and 0.7), while the downward values reach the strongest magnitude for the inverted conical gauge (about -0.4), nearly twice the value of the cylindrical (*CAE-PMB25*[®]) gauge and even more than that when compared to the chimney shaped (*Geonor-T200B*[®]) gauge.

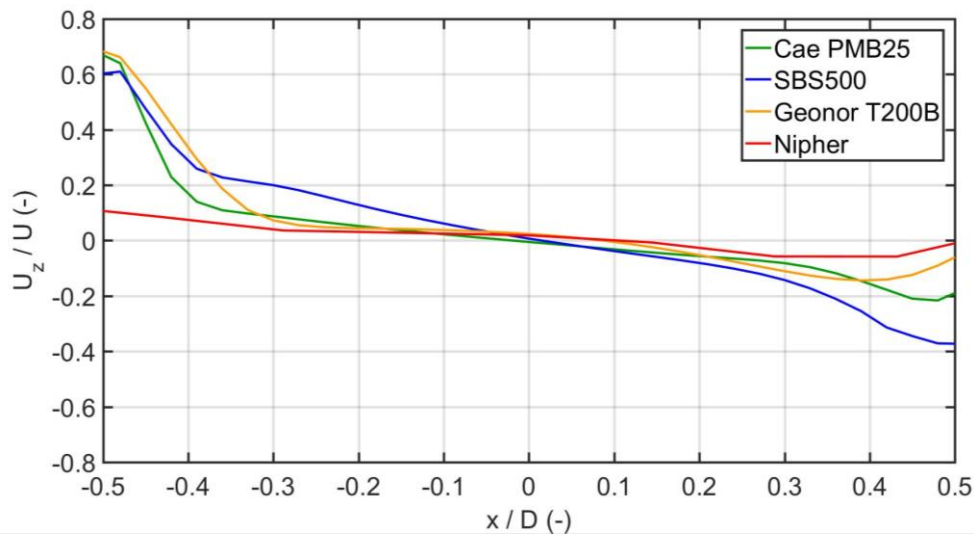


Figure 4.23 Horizontal profiles of the normalized vertical velocity above the collector of the investigated gauges.

Anticipating the influence that these vertical components would have on the trajectories of approaching hydrometeors, discussed later in this work, it must be considered that the balance between the updraft and downdraft above the gauge collector is the relevant takeover information, useful to compare different gauge shapes. Indeed, the hydrometeor trajectories will be deflected upward – depending on their shape and vertical velocity – when the vertical velocity is positive, while they will tend to recover their original undisturbed trajectory when the vertical velocity is negative.

Therefore, as a gross approximation, it can be assumed that the balance between the integral updraft experienced by a generic hydrometeor while travelling above the gauge collector and the eventual integral downdraft before overcoming the leeward edge of the collector is a measure of the overall effect of the airflow deformation induced by the gauge body. The higher the net positive updraft experienced in the region just above the gauge collector, the higher the likelihood that a generic particle is deflected away from the collector, and therefore missed by the gauge. A visual indication of these integral values is reported in Figure 4.24, where it can be noted that the chimney shaped (*Geonor-T200B*[®]) gauge is the one producing the most unbalanced vertical forces, with a predominant upward component and an inversion to the downward component located a bit downwind of the centre of the gauge collector.

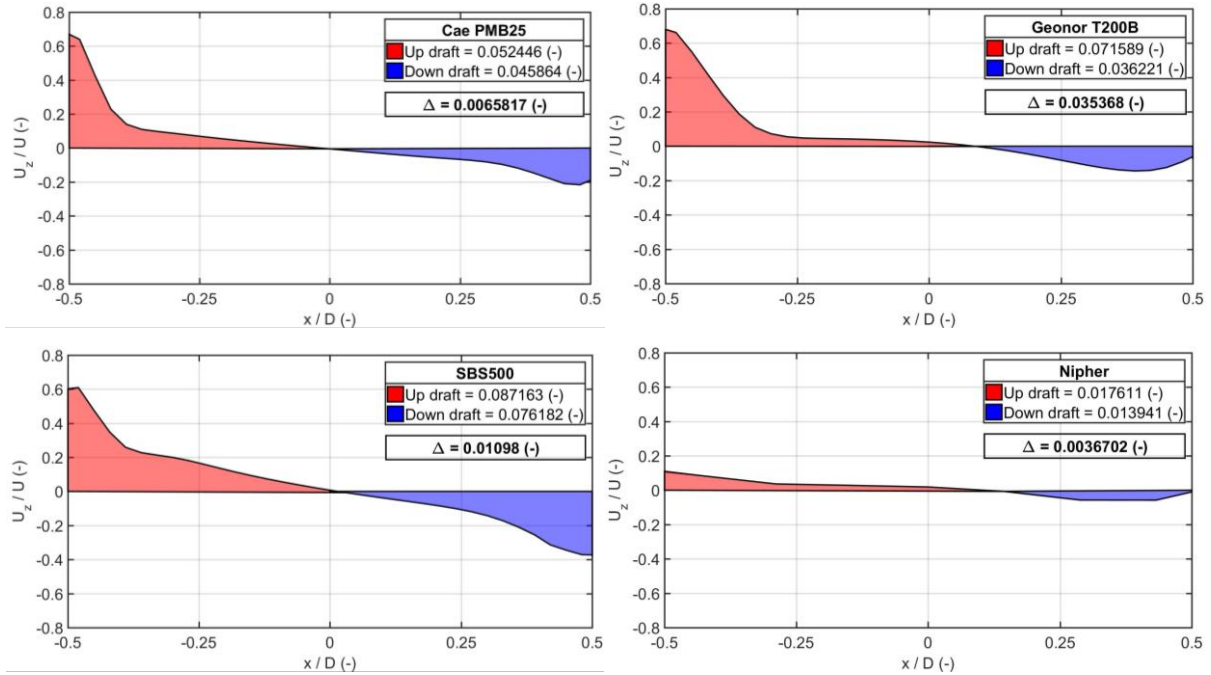


Figure 4.24 Comparison of the integral normalized updraft (red area) and downdraft (blue area) components above the collector of the investigated gauges.

The absolute values of the integral normalized upward and downward components are reported in Table 4.6, together with their algebraic difference. A positive difference indicates a predominant upward component, while a negative difference would indicate a predominant negative component. Positive values are obtained for all four investigated gauges, suggesting that some deflection of the trajectories of incoming hydrometeors is to be expected in all cases, with a likely resulting undercatch. However, the *Nipher*[®] shield has very low values and a small difference, confirming its efficiency in reducing the wind-induced undercatch. The cylindrical (*CAE-PMB25*[®]) and inverted conical (*EML-SBS500*[®]) gauges have similar intermediate values, while the chimney shapes (*Geono-T200B*[®]) gauge is the worst performing one.

Table 4.6 Integral of the normalized updraft and downdraft components (absolute values) above the collector of the investigated gauges and their algebraic difference.

	Integral of the updraft [-]	Integral of the downdraft [-]	Difference [-]
<i>CAE-PMB25</i> [®]	0.052	0.046	0.006
<i>Geonor T200B</i> [®]	0.072	0.036	0.036
<i>EML-SBS</i> [®]	0.087	0.076	0.011
<i>Nipher</i> [®] Shield	0.018	0.014	0.004

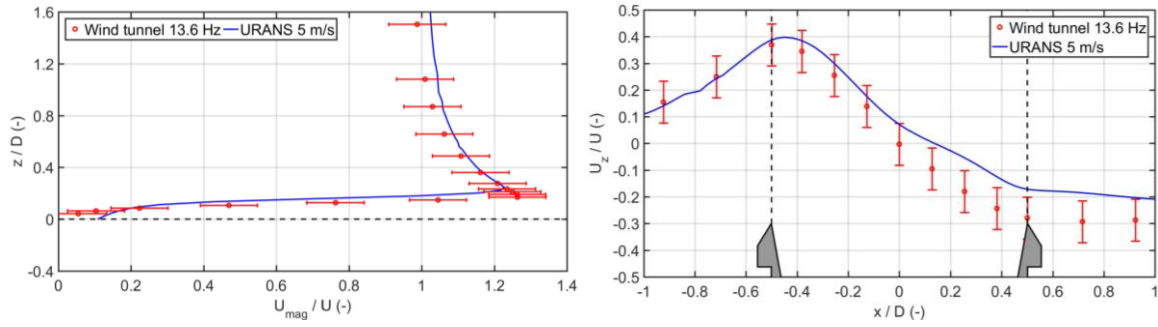
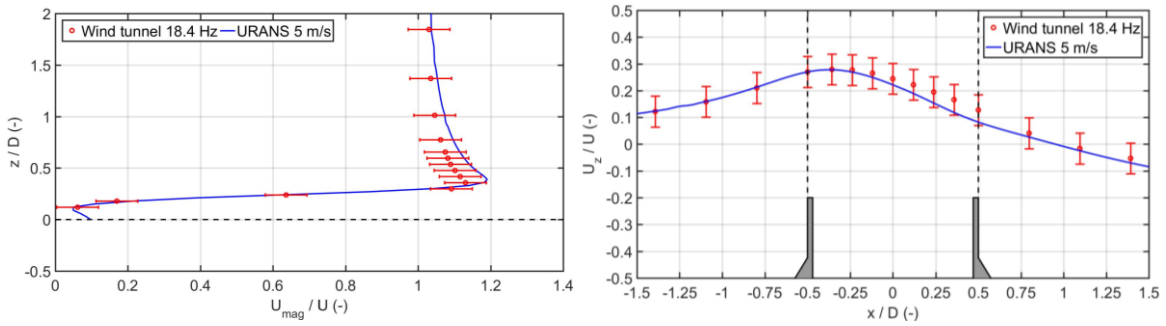
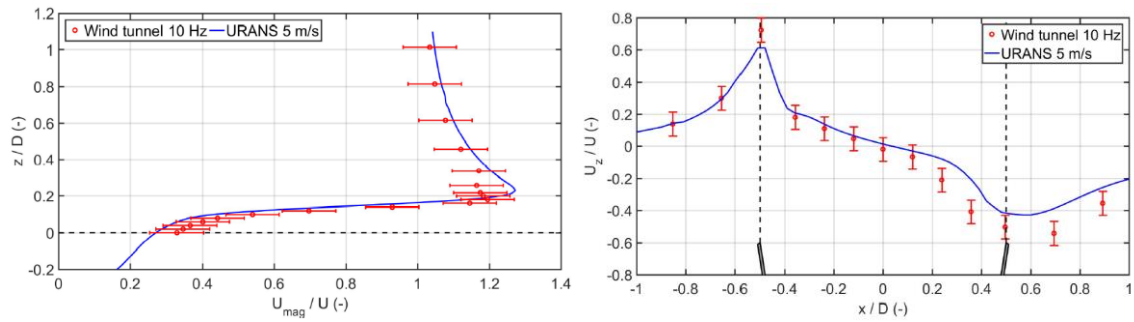
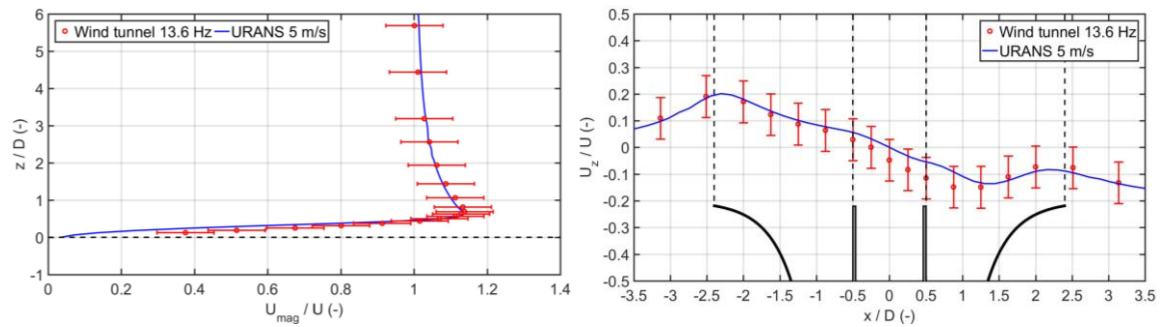
CAE-PMB25[®] cylindrical gauge**Geonor-T200B[®] chimney shaped gauge****EML-SBS500[®] inverted conical gauge****Nipher[®] shield and cylindrical gauge**

Figure 4.25 Comparison between flow velocity measurements (circles with bars) and CFD velocity profiles (continuous line) along the vertical direction in the centre of the gauge collector (left column) and along the investigated stream-wise directions (right column) at $U_{ref} = 5 \text{ m s}^{-1}$.

Validation of the performed simulations was obtained in the wind-tunnel using full scale and scaled models. The comparison between flow velocity measurements and CFD velocity profiles along the vertical direction in the centre of the gauge collector and along the investigated stream-wise directions is reported in Figure 4.25 at $U_{ref} = 5 \text{ m s}^{-1}$.

An overall good agreement of the simulated profiles with wind tunnel local measurements is obtained, with the exception of the downwind part of the *CAE-PMB25*[®] and *EML-SBS500*[®] gauges, where the simulations slightly overestimate the flow velocity. These are strong recirculation regions, where significant negative components of the horizontal velocity occur, and where the accuracy of the pressure probes used for local velocity measurements is lower. It can be concluded that the simulations are validated by the wind tunnel measurements and that the approach and approximations involved in the adopted numerical scheme are suitable to represent the airflow pattern around and above of the collector of catching-type precipitation gauges.

4.4 NUMERICAL THERMO-FLUID DYNAMIC SIMULATIONS OF THE *HOTPLATE*[®] PRECIPITATION GAUGE AND WIND TUNNEL VALIDATION

The *Hotplate*[®] precipitation gauge is a recently developed instrument design aimed to improve the quality and reliability of snowfall measurements and able to measure low intensity solid precipitation in very harsh environmental condition, while requiring little maintenance. The instrument was developed at the Research Applications Laboratory at the National Center for Atmospheric Research in Boulder, Colorado. It can be classified between the two categories described in chapter 2 (catching and non-catching type gauges) because it still need to catch the hydrometeors but it is not equipped with any funnel to collect the precipitation which is measured by means of an indirect thermodynamic principle.

The *Hotplate*[®] precipitation gauge is a small disk of 13 cm in diameter, supported laterally by an inclined arm attached to the main circuitry box, that maintains the system at 2 m over the ground. On the upper and lower faces of the disk there are two thin aluminium plates each with three uniformly spaced concentric rings, placed orthogonal to the plates in order to prevent snow/rain particles from sliding off the top plate during high wind conditions. The dimensions of the disk were chosen to be large enough to permit the collection of solid and liquid particles in a relevant area but small enough that power demands, needed to heat the plates, during a heavy precipitation event with high wind speeds is not too large.

The measuring principle of the *Hotplate*[®], already described in Chapter 2, is based on the latent heat required for completely evaporate the hydrometeors impacting on the instrument. The lower plate serves as a reference because it is exposed only to the air temperature and the wind speed, while the upper plate collects the precipitation. A specific algorithm allows to correlate the volume of the precipitation to the difference in power consumption between the two resistances which heat the plates. The temperature of each plate is monitored and is maintained at a constant value above 75°C, capable of evaporating even the larger hydrometeors in a couple of seconds. Between the two faces of the disk an insulating material is present allowing the plates to heat up or cool down independently. During non-precipitation conditions the heat exchange of the two plates, caused by the external temperature and the wind, is nearly identical and

the average difference in power absorption of the two electric resistances is zero. During precipitation events the hydrometeors only impact the upper plate, cooling it down, and the electrical power needed to maintain a constant temperature increases. Using the lower plate as a reference, the latent heat of evaporation is directly proportional to the difference in power absorption between the two electrical resistances. Data output is at either one second or one minute intervals.

The *Hotplate*® precipitation gauge has undergone 7 years of testing at the National Center for Atmospheric Research (NCAR) Marshall Field Site (near Boulder, Colorado) as well as testing under more extreme conditions at Mount Washington, New Hampshire. The *Hotplate*® was also used operationally during the WMO-Solid Precipitations Intercomparison Experiment (SPICE) in different sites with different climatology showing in all cases very promising results. As reported in WMO (2018) during the SPICE project the *Hotplate*® was compared against the Double Fence Intercomparison Reference (DFIR) showing median catch efficiency values between 0.9 and 1.3 for mean wind speeds below 7 m s^{-1} at all three sites at which it was tested (Haukelisetter, Marshall, Sodankylä). For mean wind speeds above 7 m s^{-1} , the median catch efficiency values vary more broadly, within about 0.5 and 1.3.

The *Hotplate*®'s major strong points are the ability to obtain one-minute liquid equivalent rate without the need of knowing the snow density, the reduced need of maintenance and the natural de-icing due to the high temperature, that also repels birds and insects. On the other hand, the high power consumption of the *Hotplate*® limits the instrument's range of usability, requiring a permanent connection to the power grid. The instrument is incapable of evaluating one-minute liquid-equivalent rates above 50 mm h^{-1} due to power limitation.



Figure 4.26 The *Hotplate*® precipitation gauge installed at the NCAR Marshall Field Site, picture from Rasmussen et al. (2010).

In this thesis work, due to the specific measurement principle exploited by the *Hotplate*® gauge, preliminary thermo-fluid dynamic simulations were conducted for various wind speeds, with the objective of quantifying the heat role on the aerodynamic disturbance which affects the airflow around the gauge. These are based on a simplified geometry of the gauge, precisely without the supporting arm, and employ a coarse computational mesh. This preliminary investigation demonstrated that the heat effect on the airflow

dynamics is totally negligible for wind speeds larger than 1 m s^{-1} , allowing the computational burden to be reduced by solving standard fluid dynamic simulations not coupled with the conservation of energy theorem. URANS simulations were then performed on the complete gauge geometry (including the supporting arm) and by improving the refinement of the computational mesh. Both local flow velocity measurements obtained by employing multi hole pressure probes and Particles Image Velocimetry (PIV) measurements in selected 2-D sections above the gauge collector were adopted to validate the numerical simulations.

4.4.1 Thermo-fluid and fluid dynamics simulations

The evolution of any fluid system could be completely described by coupling the thermal and fluid dynamics characteristics. Assuming the absence of other natural phenomena (electromagnetic, chemical, etc. ...) the knowledge of the system state is completed by the thermodynamic variables as the pressure (that in this case is not only a mechanical variable), the temperature, the internal energy, the enthalpy, the entropy etc. They are all linked to each other by relationships called "state equations" that define the system. The first principle of thermodynamics (Eq. 4.51) is expressed as the difference between the variation of the heat transfer and the work (dQ and dL) and provides the variation of the total energy (E_t) expressed as the sum of the internal (e) and kinetic energy (E_k) (see Eq. 4.52).

$$dE_t = dQ - dL \quad (4.51)$$

$$E_t = e + E_k = e + \frac{1}{2}u^2 \quad (4.52)$$

The conservation of energy theorem states that the rate of change of total energy for a particle of material must equal the input of mechanical and thermodynamic power from fluxes and sources or sinks acting on the particle. In the limit where the particle size is infinitesimally small, the conservation of energy can be written as:

$$\frac{d(\rho e)}{dt} + \frac{d(\rho E_k)}{dt} = \rho \mathbf{g} \cdot \mathbf{u} + \nabla \cdot (\boldsymbol{\tau} \cdot \mathbf{u}) - \nabla \cdot (\mathbf{u}p) + \rho r - \nabla \cdot \mathbf{q} \quad (4.53)$$

where:

1. $\frac{d(\rho e)}{dt}$ is the rate of change of internal energy that represents the thermal energy contribution;
2. $\frac{d(\rho E_k)}{dt}$ is the rate of change of kinetic energy that represents the mechanical energy contribution;
3. $\rho \mathbf{g} \cdot \mathbf{u}$ is the rate of change of potential energy, where \mathbf{g} is the gravity acceleration;
4. $\nabla \cdot (\boldsymbol{\tau} \cdot \mathbf{u}) - \nabla \cdot (\mathbf{u}p)$ is the rate of change of strain energy where $\boldsymbol{\tau}$ is the surface tension and p is the pressure;

5. pr is the heat source from irradiation;
6. $\nabla \cdot \mathbf{q}$ is the heat flux with \mathbf{q} defined as positive inwards.

In this section, the preliminary numerical simulations conducted to establish the role of the heat on the airflow features around the *Hotplate*® gauge are described. Both the thermo-fluid and fluid dynamics simulations were performed by using the OpenFOAM software. Thermo-fluid dynamic simulations were conducted for wind speed (U_{ref}) equal to 0.5, 5 and 10 m s⁻¹ while fluid dynamic simulations were performed at 1, 5, 10 and 16 m s⁻¹.

The numerical geometry of the *Hotplate*® was realized in the STL format suited to generate the computational mesh (Figure 4.27); its geometry was divided into three portions (upper plate, inner disk and bottom plate) in order to better assign the boundary conditions. For the thermo-fluid dynamics simulations, the refinement boxes of the computational mesh around the gauge were stretched upward (see Figure 4.28 right) in order to better calculate the flow field considering the buoyance effect due to the heat. The computational domain is composed by 7×10^5 and 9×10^5 cells for the fluid and thermo-fluid dynamic simulations, respectively. Thin layers were added on the gauge surface so as to closely follow the right angles of the gauge rings geometry (see Figure 4.29).



Figure 4.27 Numerical geometry of the *Hotplate*® gauge in STL format, without the supporting arm, and computational mesh on its surface for the preliminary thermo-fluid dynamic simulations.

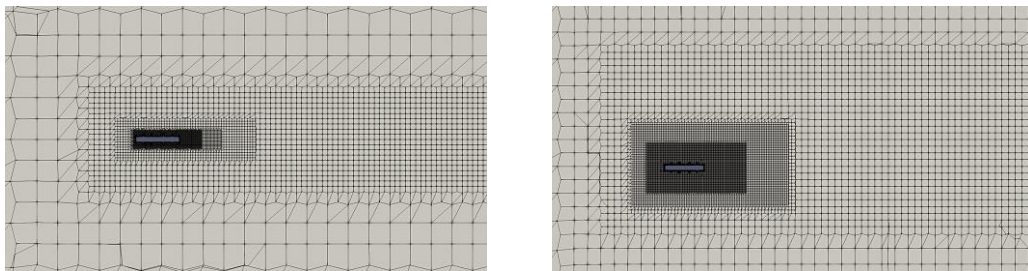


Figure 4.28 Refinements boxes of the computational mesh in the x - z plane for fluid (left) and thermo-fluid dynamic (right) simulations, respectively.

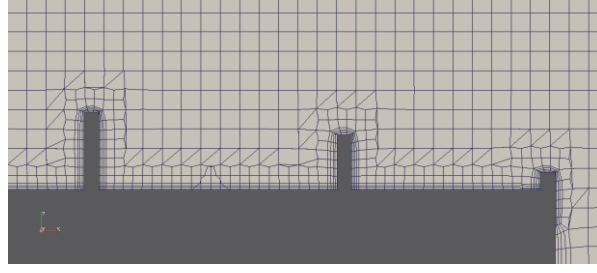


Figure 4.29 Details of the computational mesh close to the *Hotplate*® surface.

For fluid dynamic simulations, the fluid air was modelled as a Newtonian incompressible fluid with kinematic viscosity $\nu_a = 1.2 \times 10^{-5} \text{ m}^2\text{s}^{-1}$ and density $\rho_a = 1.3 \text{ kg m}^{-3}$ at a reference environmental temperature $T_a = 0^\circ\text{C}$ that acts as the threshold between solid and liquid precipitation. At the inlet of the computational domain (y-z plane) the undisturbed wind speed, U_{ref} , was imposed parallel to the x axis and is maintained uniform and constant in time, while a null gradient condition was set for pressure. Atmospheric pressure and null gradient conditions for the velocity were imposed at the outlet (y-z plane opposite to the inlet). The lateral surfaces of the domain were set as symmetry planes. The gauge surface was assumed impermeable with a no-slip condition.

For thermo-fluid dynamic simulations, the fluid air was assumed as a compressible fluid with the same kinematic viscosity $\nu_a = 1.2 \times 10^{-5} \text{ m}^2\text{s}^{-1}$ and initial density $\rho_a = 1.3 \text{ kg m}^{-3}$ at a reference environmental temperature $T_a = 0^\circ\text{C}$. A transient solver for turbulent flow of compressible fluids that introduces the energy equation to the turbulence model was adopted. The following hypotheses were implemented:

1. thermo-physical model without any reaction, therefore the mixture composition is fixed;
2. the dynamic viscosity μ and Prandtl number are assumed as constant values;
3. the specific heat c_p and the heat of fusion H_f are assumed as constant values;
4. the density ρ is calculated by using the ideal gas equation.

Initial and boundary conditions were set equal to the previous case with the some additional variables: the difference between the pressure and the hydrostatic pressure, Δp , was set in the inlet with a fixed flux linked with the velocity value. In the outlet the Δp was imposed equal to the atmospheric pressure with a fixed value. On the *Hotplate*® surface a null normal gradient condition for Δp was adopted. As initial conditions, the temperature of the plates was fixed equal to 75°C , while the air temperature was set at 0°C . Both the pressure p and Δp were initially set equal to the atmospheric pressure.

Results are shown as comparisons between normalized velocity profiles, for both the magnitude U_{mag}/U_{ref} and vertical component U_z/U_{ref} , along the vertical direction at the upwind edge ($x/D = -0.42$) and in the centre ($x/D = 0$) of the top plate and along the longitudinal direction at $z/D = \pm 0.20$ above and below the instrument by assuming that the origin of the 3-D Cartesian reference system is located in the centre of the *Hotplate*®. In Figure 4.30 and Figure 4.31, the normalized velocity profiles obtained from fluid-dynamic simulations for the four wind speeds investigated are reported. The velocity profiles for $U_{ref} = 1 \text{ m s}^{-1}$ are not totally overlapped to the ones associated with the other velocities, both in terms of normalized magnitude and updraft. For $U_{ref} = 5, 10$ and 16 m s^{-1} the velocity profiles of the vertical component start to differ from each other in the downwind part of the gauge where turbulence arises.

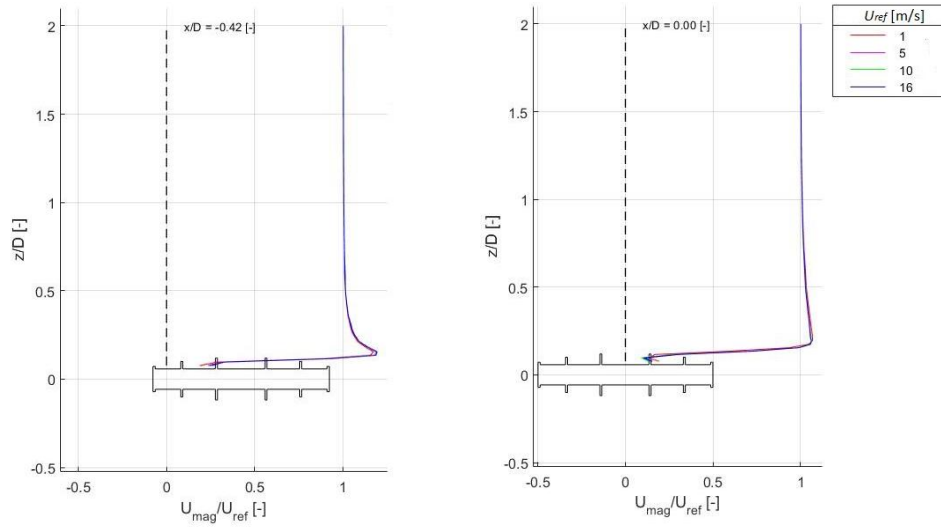


Figure 4.30 Comparison between vertical velocity profiles, along the normalized vertical direction z/D at the upwind edge ($x/D = -0.42$) (left) and at the centre of the gauge ($x/D = 0$) (right), of the normalized magnitude of flow velocity U_{mag}/U_{ref} obtained for different wind speed by performing fluid dynamic simulations.

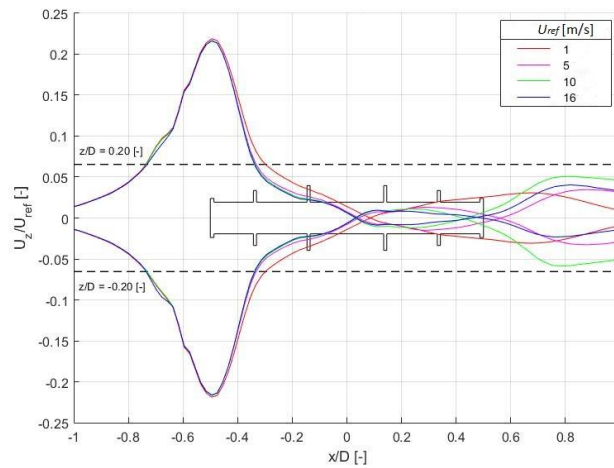


Figure 4.31 Comparison between longitudinal profiles from fluid dynamic simulations of the normalized vertical velocity component (U_z/U_{ref}) at $z/D = \pm 0.20$ above and below the instrument.

Similar comparisons are shown in Figure 4.32 and Figure 4.33 for the thermo-fluid dynamic results. Also in this case the velocity profiles for the lowest wind speed ($U_{ref} = 0.5 \text{ m s}^{-1}$) differ from the other ones and the longitudinal profiles reveal that the heat effect is only relevant at very low wind speed.

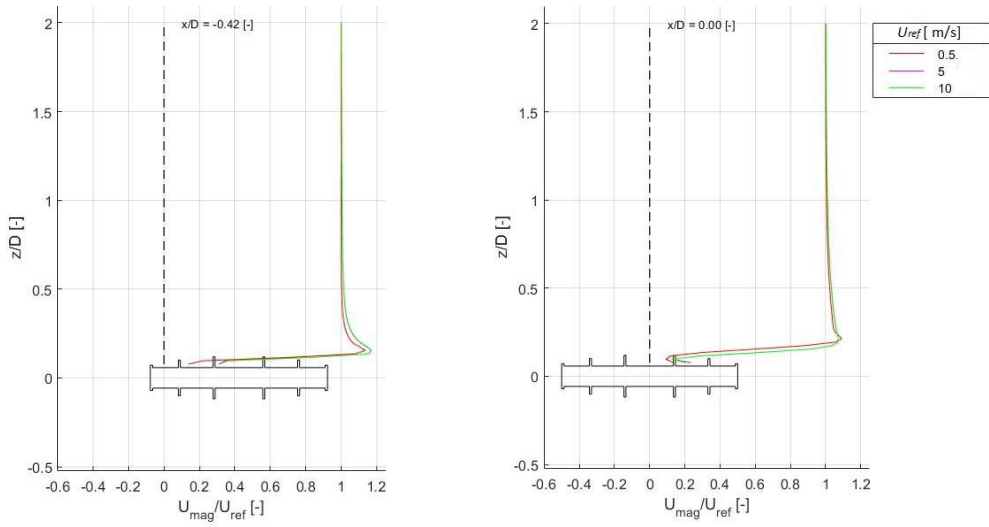


Figure 4.32 Comparison between vertical velocity profiles, along the normalized vertical direction z/D at the upwind edge ($x/D = -0.42$) (left) and at the centre of the gauge ($x/D = 0$) (right), of the normalized magnitude of flow velocity U_{mag}/U_{ref} obtained for different wind speed by performing thermo-fluid dynamic simulations.

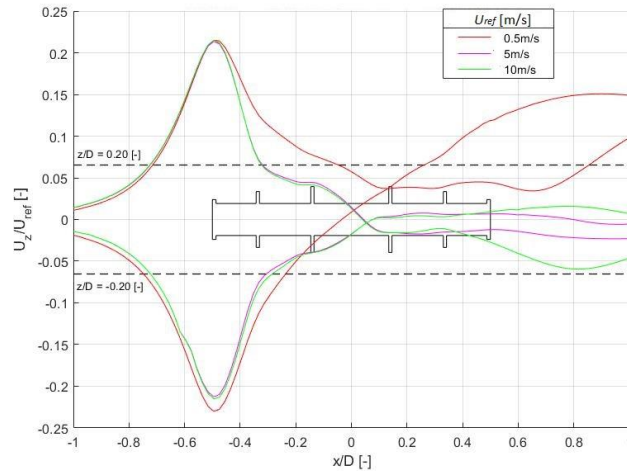


Figure 4.33 Comparison between longitudinal profiles from thermo-fluid dynamic simulations of the normalized vertical velocity component (U_z/U_{ref}) at $z/D = \pm 0.20$ above and below the instrument.

Based on the results of the preliminary thermo-fluid dynamic simulations, the analysis was then carried out by neglecting the heat effect and performing fluid dynamic simulations only. The advantage due to this simplification was offset by an increase of the computational cost associated with the geometry of the gauge, completed with its supporting arm (Figure 4.34), and the refined computational mesh (Figure 4.35). Because of the non-symmetrical shape of the *Hotplate*® and arm assembly, two different geometries were considered, the first is generated with the supporting arm oriented along the flow (0°) while the other is rotated by 180° . The number of cells and the quality parameters of the computational mesh for the two cases are listed in Table 4.7. The number of cells, compared with the computational mesh adopted for the preliminary fluid dynamic simulations, is doubled.

URANS simulations with the support arm located downwind of the plate were conducted for wind speed equal to 2, 5, 10, 15 and 20 m s^{-1} , while for the geometry rotated by 180° the wind speed was set equal to 10 m s^{-1} .

Table 4.7 Number of cells of the computational mesh and quality parameters

Orientation	n. of cells	Max skewness	Max non-orthogonality	Max aspect ratio
0°	$1.3 \cdot 10^6$	2.38	72.65	21.52
180°	$1.5 \cdot 10^6$	2.60	78.60	25.51



Figure 4.34 *Hotplate*[®] geometry in STL format with the supporting arm and computational mesh on its surface for the improved fluid dynamic simulations.

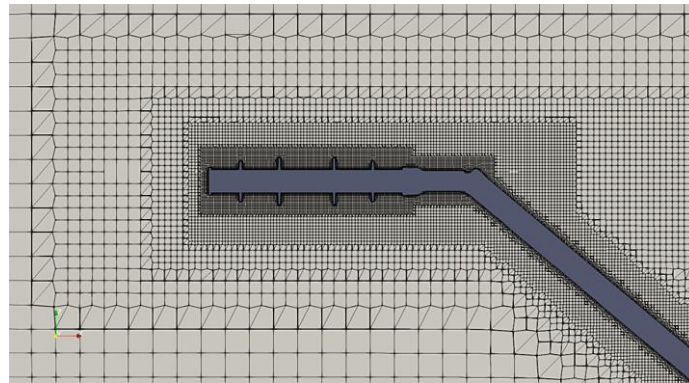


Figure 4.35 Details of the computational mesh close to the *Hotplate*[®] surface for the improved simulations.

Numerical results are shown in terms of normalized velocity fields in the vertical (x/D , z/D) and horizontal (x/D , y/D) sections and considering the origin of the 3-D Cartesian reference system located in the centre of the top plate. As an example, the following figures (Figure 4.36 and Figure 4.37) reports the velocity fields for the wind speed of 10 m s^{-1} . In all figures, the updraft and acceleration regions around the gauge geometry are evident, with a clear asymmetric pattern due to the presence of the supporting arm. A complex pattern of the vertical velocity component (Figure 4.37) appears above the upper plate as a consequence of the collecting rings, with an expected impact on the hydrometeor trajectories close to the plate. The distribution of the flow velocity components on the horizontal section is symmetrical with strong

gradients due to the obstruction caused by the rings, inducing a large variability of the flow conditions just above the collecting surface of the plate.

Further to the deformation of the airflow, the obstruction to the flow caused by the bluff-body nature of the gauge also generates the development of turbulence close to the gauge surfaces. The amount of turbulence produced by the *Hotplate*® gauge is visualized here in terms of maps of the normalized turbulent kinetic energy (k/U_{ref}^2), over the same horizontal and vertical sections used to represent the flow field, as shown in Figure 4.38. The most turbulent zones, depicted in red in the maps, arise just above and below the upper and lower plate due to the separation layer induced by the presence of the gauge, and propagate downwind beyond the gauge to generate a turbulent wake. On the horizontal section at $z/D = 0.077$ above the upper plate, the most turbulent area is confined to the central part of the gauge vertical projection. In both maps, the role of the rings is highlighted in both producing the development of turbulence above the plate and shielding the small areas leeward of the rings.

When the instrument is rotated 180° with respect to the wind direction, the supporting arm has the maximum impact on the airflow field around the gauge, and the resulting horizontal and vertical components of the velocity (Figure 4.39 and Figure 4.40) are different from those described above. This geometrical configuration was simulated only at $U_{ref} = 10 \text{ m s}^{-1}$ with the objective of showing the effect of the not fully symmetric design of the instrument. By comparing the normalized velocity fields with the ones in Figure 4.36 and Figure 4.37, it is evident that the supporting arm does have an influence on the airflow deformation, especially along the depicted stream-wise central section of the *Hotplate*®, resulting in lower horizontal velocity components and higher vertical ones.

Looking at the horizontal section of the flow field at an elevation of $z/D = 0.077$ above the upper plate, as depicted in Figure 4.39 and Figure 4.40, the impact of the supporting arm is even more evident, especially in the central part of the gauge where a shading effect on both the horizontal and vertical components of the flow velocity occurs.

The generated turbulence, expressed in terms of the normalized turbulent kinetic energy (k/U_{ref}^2), follows this behavior – as expected – and a turbulent wake develops from the arm geometry in the stream-wise central section of the gauge, with a lower magnitude than in the previous case. The turbulent kinetic energy field is depicted along the vertical stream-wise central section and the horizontal section at an elevation of $z/D = 0.077$ in the left- and right-hand panels of Figure 4.41, respectively.

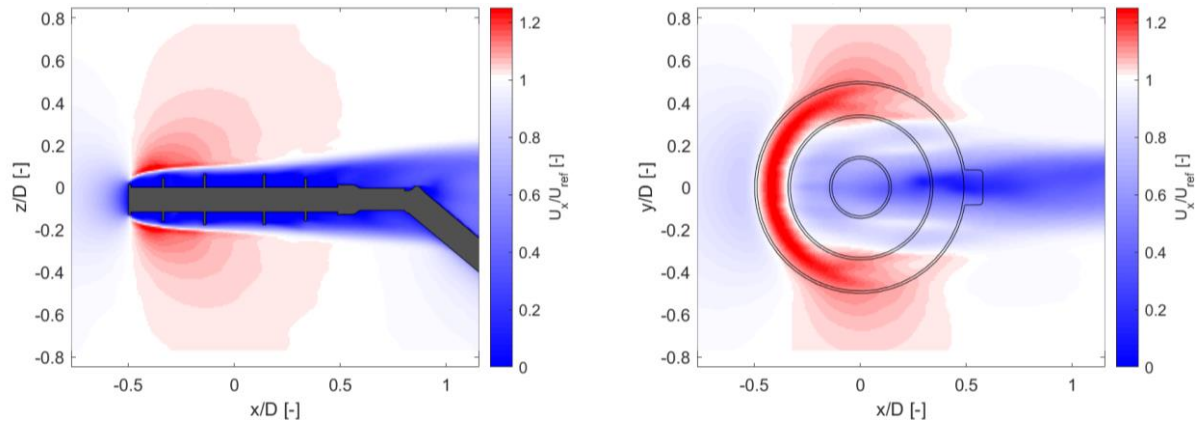


Figure 4.36 Normalized horizontal velocity fields (U_x/U_{ref}) at $U_{ref} = 10 \text{ m s}^{-1}$ in the vertical plane ($x/D, z/D$) – left-hand panel, and in the horizontal plane ($x/D, y/D$) at an elevation of $z/D = 0.077$ – right-hand panel.

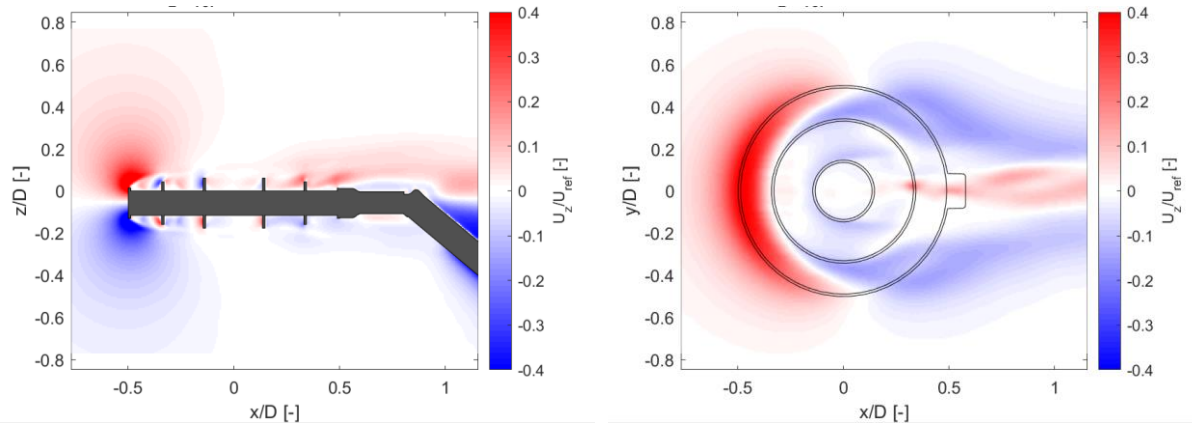


Figure 4.37 Normalized vertical velocity fields (U_z/U_{ref}) at $U_{ref} = 10 \text{ m s}^{-1}$ in the vertical plane ($x/D, z/D$) – left-hand panel, and in the horizontal plane ($x/D, y/D$) at an elevation of $z/D = 0.077$ – right-hand panel.

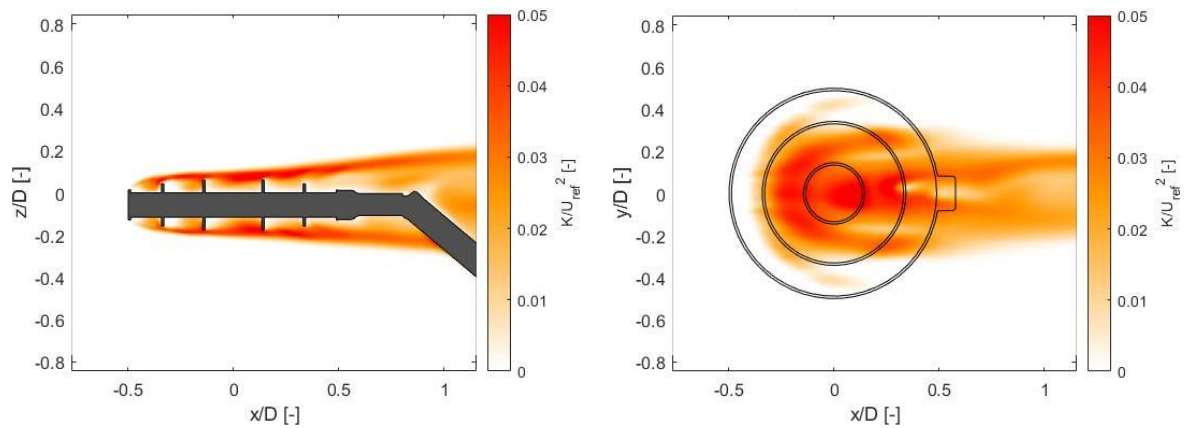


Figure 4.38 Normalized turbulent kinetic energy (k/U_{ref}^2 [-]) fields at $U_{ref} = 10 \text{ m s}^{-1}$ in the vertical ($x/D, z/D$) and horizontal plane ($x/D, y/D$) at an elevation of $z/D = 0.077$.

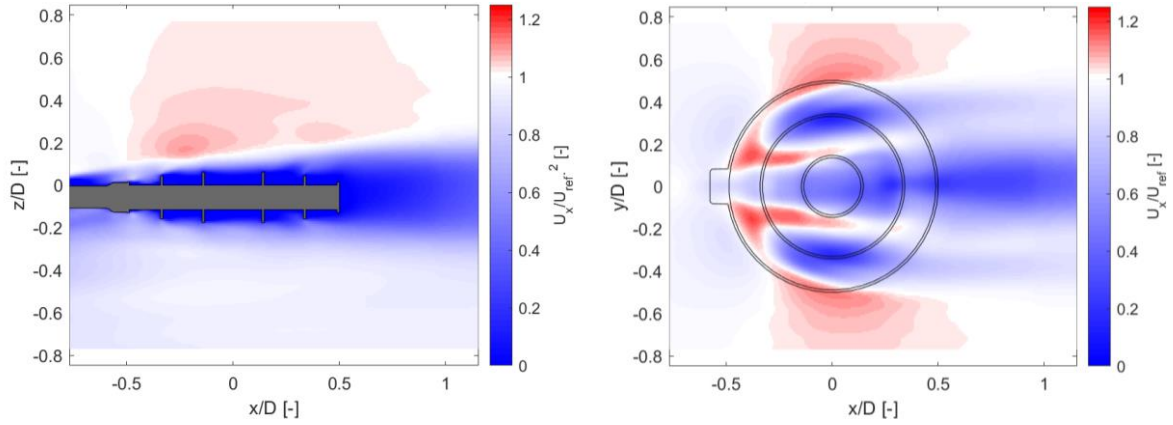


Figure 4.39 Normalized horizontal velocity fields (U_x/U_{ref}) at $U_{ref} = 10 \text{ m s}^{-1}$ for the configuration with the *Hotplate*® rotated by 180° in the vertical plane ($x/D, z/D$) – left-hand panel, and in the horizontal plane ($x/D, y/D$) at an elevation of $z/D = 0.077$ – right-hand panel.

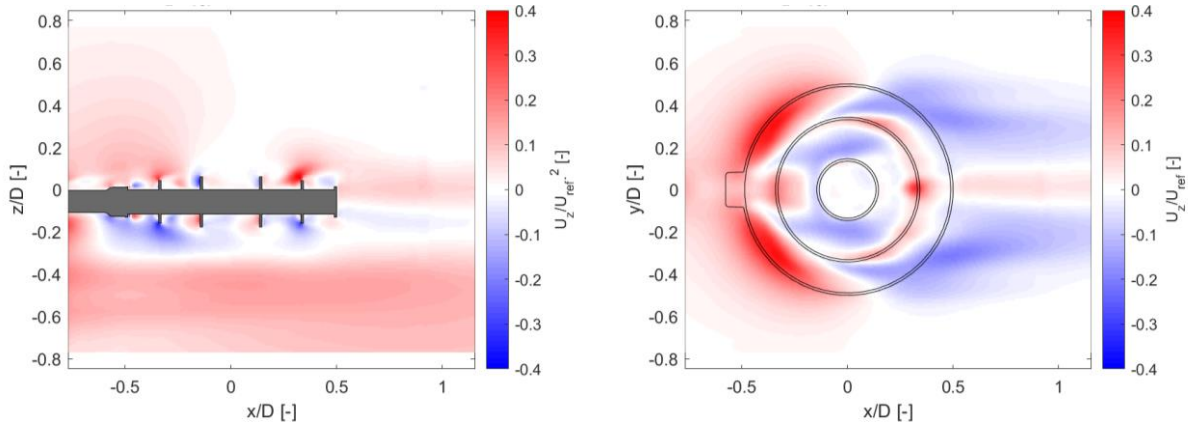


Figure 4.40 Normalized vertical velocity fields (U_z/U_{ref}) at $U_{ref} = 10 \text{ m s}^{-1}$ for the configuration with the *Hotplate*® rotated by 180° in the vertical plane ($x/D, z/D$) – left-hand panel, and in the horizontal plane ($x/D, y/D$) at an elevation of $z/D = 0.077$ – right-hand panel.

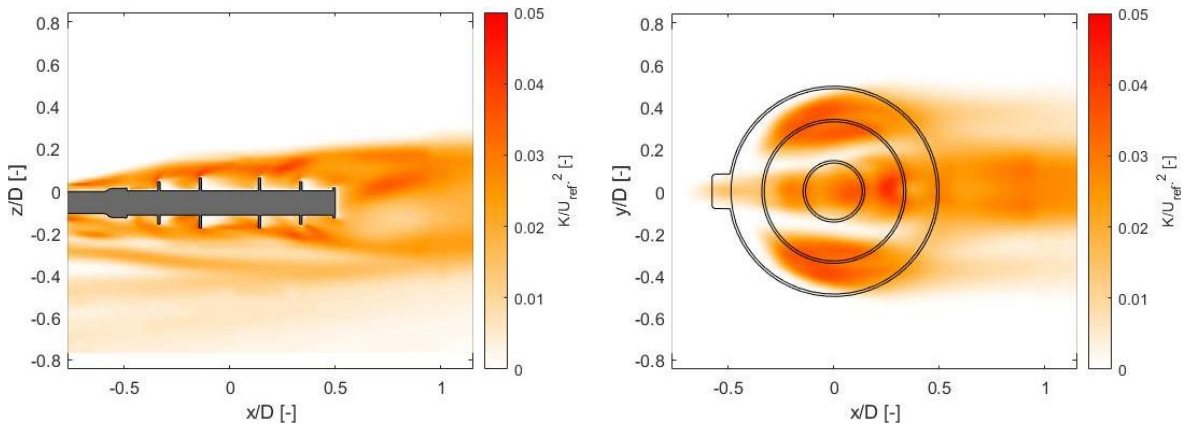


Figure 4.41 Normalized turbulent kinetic energy (k/U_{ref}^2) fields for $U_{ref} = 10 \text{ m s}^{-1}$ in the vertical ($x/D, z/D$) and horizontal plane ($x/D, y/D$) at an elevation of $z/D = 0.077$ and for the configuration with the *Hotplate*® rotated by 180° .

In Figure 4.42 the normalized profiles of the magnitude of flow velocity along the stream-wise direction, at $z/D = 0.23$ above the top plate, for different wind speeds are compared in order to evaluate the scalability of the solution. The behavior of the flow remains almost the same while changing the wind speed. This characteristic is useful to rescale the flow field and calculate the collection efficiency of the gauge as a function of wind speed without solving the airflow simulation for each specific wind speed of interest.

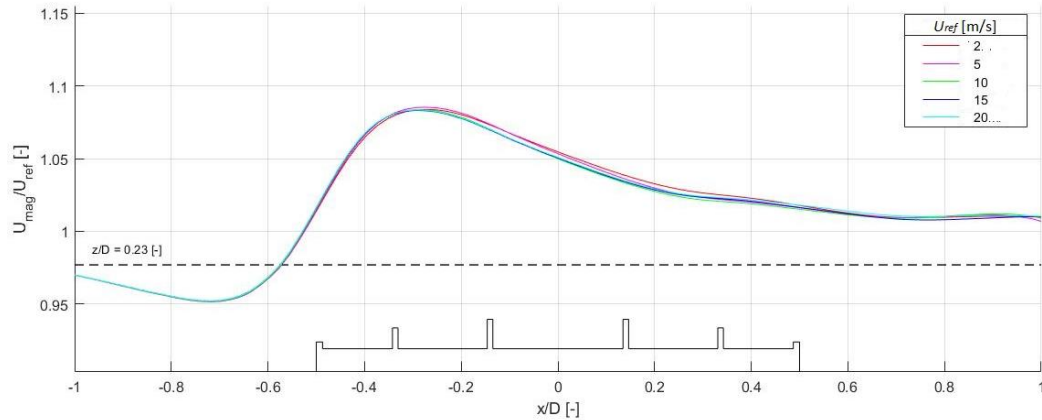


Figure 4.42 Comparison between the longitudinal numerical profiles for each wind speed investigated and for the normalized magnitude of the flow velocity, along the stream wise direction at $z/D = 0.23$ above the top plate.

4.4.2 Wind tunnel validation

Numerical simulations were validated by performing wind tunnel tests. Both pressure probes and the Particles Image Velocimetry (PIV) technique were employed to characterize the flow field around the gauge. The experimental campaign was conducted in the wind tunnel (WT) of the Department of Civil, Chemical and Environmental Engineering (DICCA) of the Polytechnic School of the University of Genoa and in the wind tunnel facility available at Politecnico di Milano (POLIMI).

The wind tunnel of Politecnico di Milano is a closed circuit facility in vertical arrangement having two test sections: a 4x4 high speed low turbulence and a 14x4 low speed boundary layer test section; the overall wind tunnel characteristics are summarized in Table 4.8. A peculiarity of the facility is the presence of two test sections of very different characteristics, offering a very wide spectrum of flow conditions from very low turbulence and high speed in the contracted 4x4m section to earth boundary layer simulation in the large wind engineering test section. The facility is powered by an array of powerful fan organized in two rows of seven 2x2 m independent cells. All motors are powered independently with inverters, allowing continuous control of the rotation speed of each fan to obtain the desired wind speed in the test section. After the fans two corners fitted with vanes conduct the flow to the upper level of the facility, then a second set of two corners fitted with vanes conducts the flow back to the lower level where, after a 2 meters long settling chamber, it passes a honeycomb screen and a set of three different porosity wire nets to reduce axial and lateral turbulence and to promote a more uniform axial flow. A two-dimensional contraction cone with area ratio 3.46:1 reduces the duct section to fit the low turbulence test section size. Finally, a short diffuser expands the duct section back to the fans array size.

Table 4.8 Characteristics of the POLIMI wind tunnel test chamber

Test section	Size [m]	Max flow velocity [m s^{-1}]	Free-turbulence Intensity [%]
Low speed	14 x 4	16	< 1.5
High speed	4 x 4	55	< 0.15

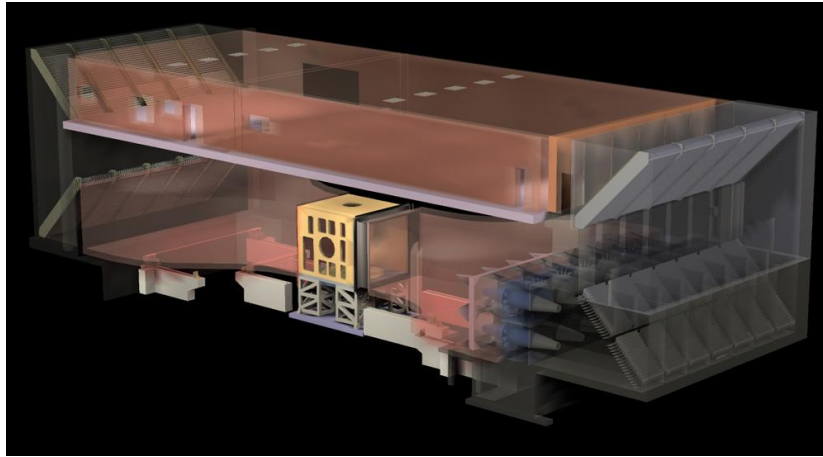
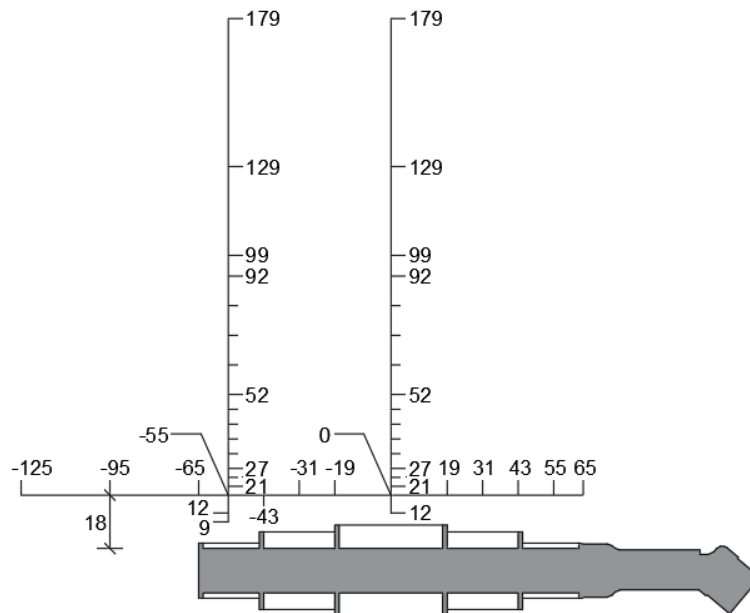


Figure 4.43 Schematic of the wind tunnel facility available at Politecnico di Milano.

Figure 4.44 Local flow velocity positions of the *Cobra* probe in the DICCA wind tunnel, expressed in mm, above the upper plate of the *Hotplate*® gauge.

The high-speed test section was adopted here to measure, in low free-stream turbulence conditions, the flow field along the axial vertical section of the *Hotplate*®, at $y = 0$, by means of PIV technique.

Furthermore, local flow velocity measurements obtained by using *Cobra* probes were carried out in the DICCA wind tunnel. The coordinates, in millimeters, of the selected measurement positions are summarized in Figure 4.44.

The Particle Image Velocimetry (PIV) is an optical method to visualize the flow and measure its velocity and direction. A passive tracer, usually smoke, able to follow the streamlines is injected in the incoming airflow until it is uniformly dispersed in the wind tunnel measurement chamber. A thin beam of light, usually a laser sheet, is then used to illuminate the flow section under investigation and to highlight the dispersed particles. The images of the particles in motion are recorded by using a high-speed digital camera that records two subsequent images (see Figure 4.45) and by using a cross-correlation algorithm the local direction and velocity of the particles in the whole domain are computed.

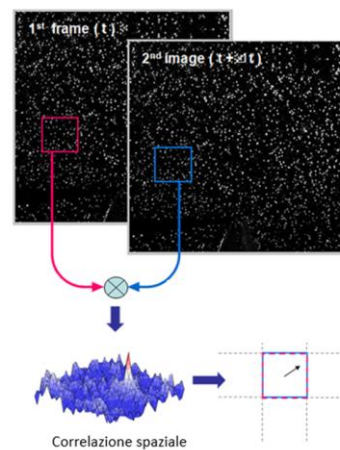


Figure 4.45 Scheme of the two subsequent images recorded by the high-speed camera and elaborated by the cross-correlation algorithm in order to provides the local velocity and direction of the airflow.

The high speed and low turbulence test chamber of the POLIMI wind tunnel was uniformly filled with Castor oil smoke here adopted as a passive tracer (see Figure 4.46). A laser emitter was mounted on the ceiling of the test chamber in order to illuminate a vertical section in the 2-D (x,z) plane, the surrounding environment was kept in the dark and the surface of the *Hotplate*® was painted in black in order to avoid the reflection of light. The video camera was fixed in the tunnel on a rigid pole with its central axis normal to the stream-wise direction and centred on the middle of the lateral surface of the *Hotplate*®. A simplified scheme of the PIV experimental setup is shown in Figure 4.47.

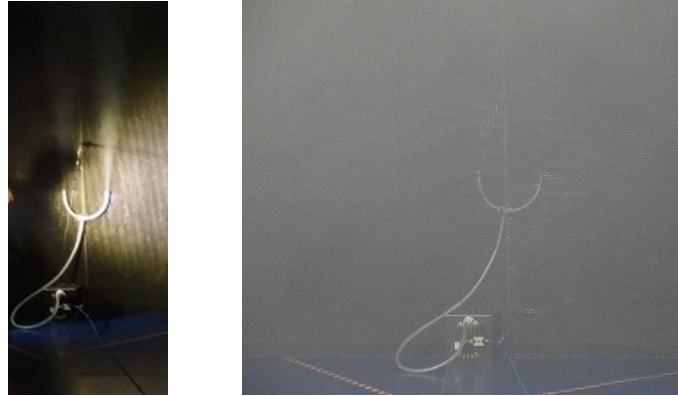


Figure 4.46 Detail of the injection system of the passive tracer which starts to work in the wind tunnel (left-hand picture) and final uniform dispersion of the castor oil smoke in the test chamber (right-hand picture).

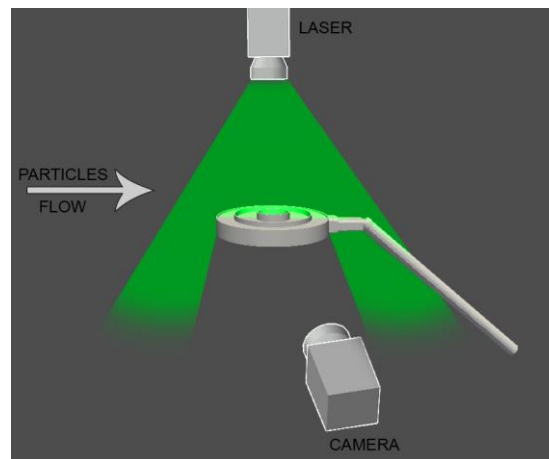


Figure 4.47 Scheme of the PIV experimental setup.

Before running the post processing, part of the data, acquired very close to the gauge surface and disturbed by the reflection of light, were masked. The post processing provided the flow velocity discretized in a regular grid with cell size of 7.5×7.5 mm. This spatial discretization is quite coarse in relation to the dimension of the *Hotplate*[®] details, e.g. the thickness of the collecting rings, and furthermore the flow field changes abruptly in a few millimeters in the region just above the plate where strong velocity gradients arise. The spatial discretization is evident in the following figures where the maps of the normalized horizontal and vertical components of the flow velocity for wind speed of 10 m s^{-1} are reported. It clearly emerges that the numerical simulation described above closely match the PIV measured field (see Figure 4.48). With the objective of obtaining a quantitative estimation of the agreement between PIV measurements and simulation results the comparisons are here proposed along selected profiles, consistently with the *Cobra* probes measurements obtained during the DICCA experimental tests.

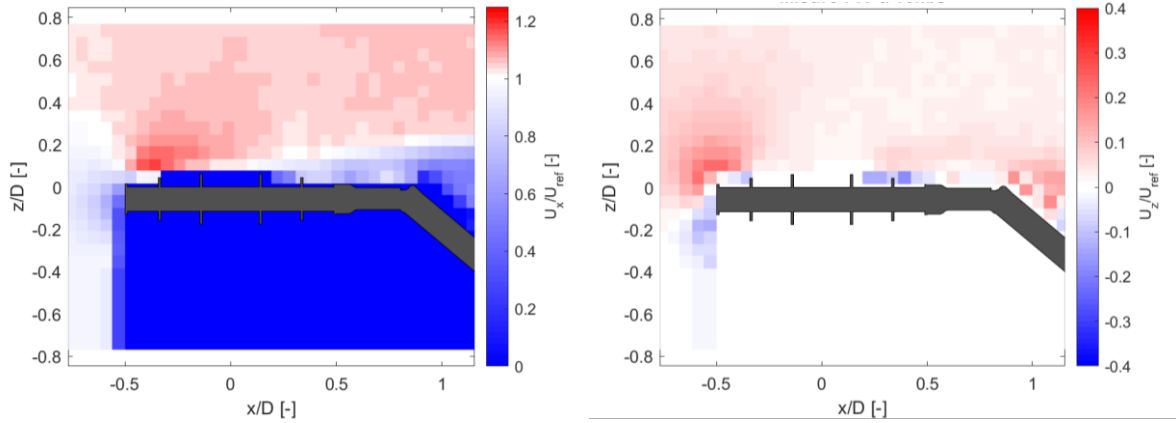


Figure 4.48 PIV velocity fields of the normalized horizontal and vertical components of the flow velocity along the stream wise direction in the central section ($y/D = 0$) of the *Hotplate*®.

Figure 4.49 shows the longitudinal profiles of the horizontal component of the flow velocity at $z/D = 0.14$ above the top plate as measured by the PIV technique and calculated by the URANS simulation. The numerical velocity profile follows quite closely the PIV measurements. The relative maximum and minimum of the numerical profile are not caught by the PIV measurements due to the coarse discretization of the spatial domain, which introduces a smoothing effect on the measured flow field. The same numerical velocity profile is compared with the *Cobra* probe measurements, from the DICCA dataset, in Figure 4.50. For a large number of data, the simulation does not even fall within the uncertainty limits of the probe measurements (bars). The high gradients generated by the presence of the instrument means that any small error in the probe position, in the order of magnitude of a few millimeters, can lead to a significant over or under estimation of the velocity value. The longitudinal section at $z/D = 0.14$ above the top plate intersects the separation layer and is almost completely included in an area of extremely high velocity gradients.

The errors on the positioning were quantified by using a least squares approach, searching for each probe velocity value the shift in 3-D spatial coordinates (dx , dy , dz) that minimizes the difference between the numerical velocity profile and each measured value. The obtained shift, as reported in Figure 4.51, suggests that the instrument was slightly tilted upward at an angle $\theta = 2.5^\circ$ from the horizontal plane when installed in the DICCA wind tunnel. As shown in Figure 4.52, by shifting the simulation according to this result the numerical velocity profile (indicated with a dashed line) is satisfactorily close to the flow measurements, and lies within the uncertainty limits of the probe measurements.

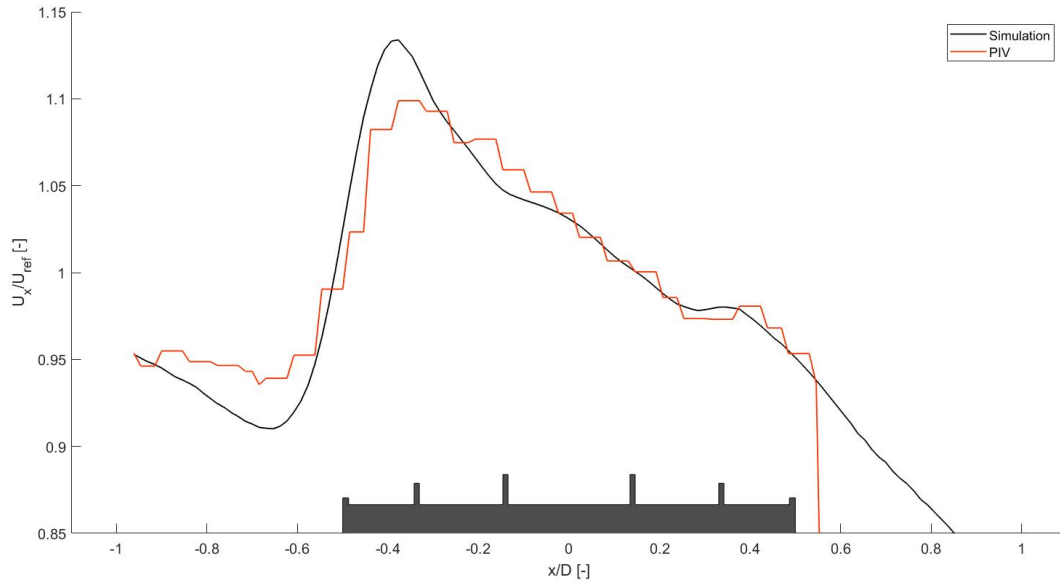


Figure 4.49 Comparison between the longitudinal profiles of PIV velocity measurements (red line) and numerical simulation (black line), for the normalized horizontal component of the flow velocity, along the stream wise direction at $z/D = 0.14$ above the top plate.

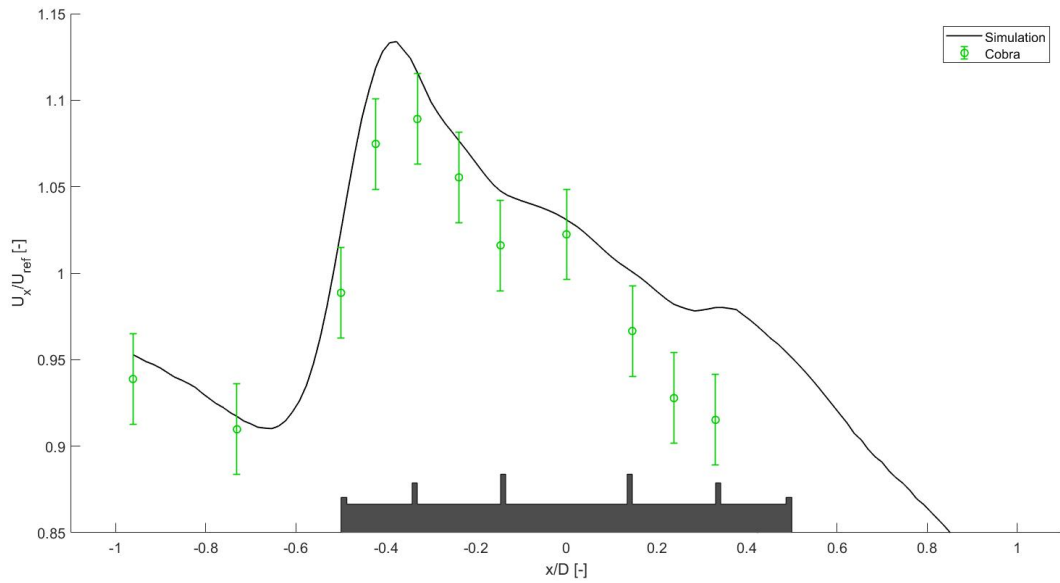


Figure 4.50 Comparison between *Cobra* probe velocity measurements (green circles with uncertainty bars) and the simulated longitudinal profile (black line), for the normalized horizontal component of the flow velocity, along the stream wise direction at $z/D = 0.14$ above the top plate.

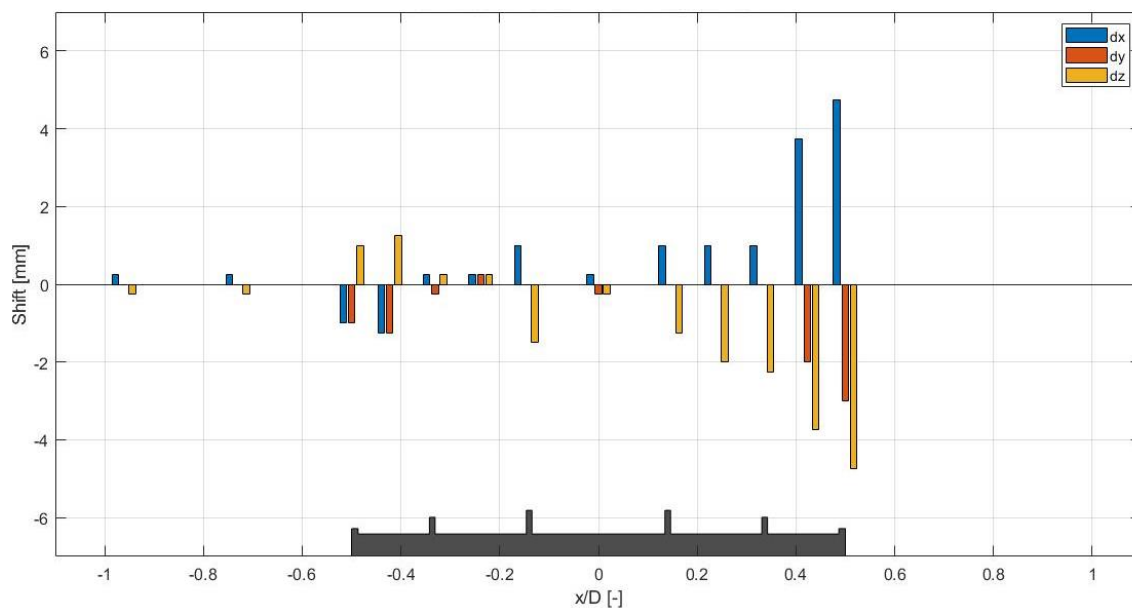


Figure 4.51 Magnitude of the shift in 3-D spatial coordinates that minimizes the difference between the numerical velocity profile and each *Cobra* measurement.

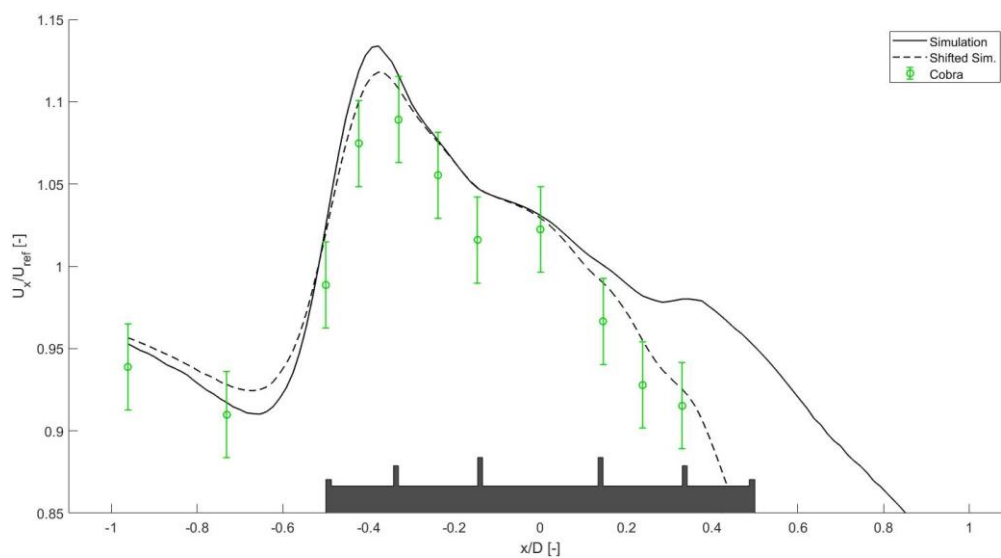


Figure 4.52 Adjusted comparison of the numerical profile and the *Cobra* probe measurements obtained after shifting the profile according to an angle $\theta = 2.5^\circ$.

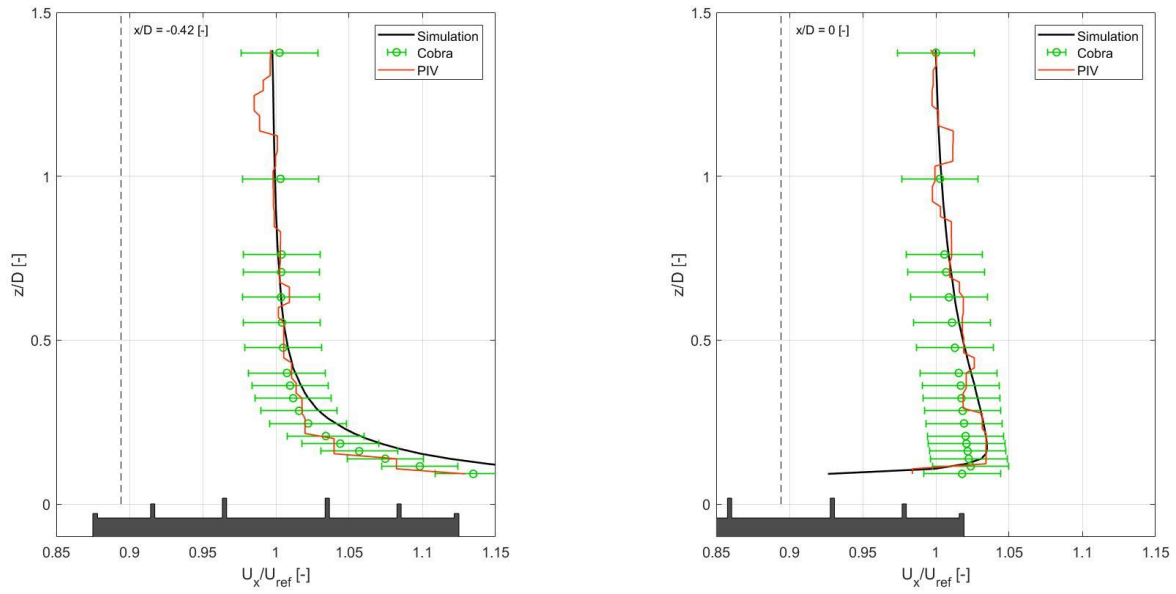


Figure 4.53 Comparison between *Cobra* probe velocity measurements (green circles with uncertainty bars), PIV (red line) and the simulated longitudinal profile (black line), for the normalized vertical component of the flow velocity, along the vertical direction at $x/D = -0.42$ and in the centre of the *Hotplate*®.

In Figure 4.53 the vertical velocity profiles at $x/D = -0.42$ and in the centre of the *Hotplate*® ($x/D = 0$), of the normalized vertical velocity component (U_z/U_{ref}) calculated by means of URANS simulations are compared with the PIV velocity profiles and the local flow velocity measurements. In both cases, the simulations are well located between the probe measurements and in agreement with the PIV field.

Based on these results it is possible to affirm that the experimental campaign allowed the CFD simulations of the aerodynamic response of the *Hotplate*® precipitation gauge to be fully validated, and that such simulations can be used to derive the collection efficiency of the gauge as a function of wind speed and particle characteristics as shown in Chapter 6.

PARTICLE TRACKING MODEL AND WIND TUNNEL VALIDATION

The earliest study where trajectories of hydrometeors were modelled was published by Mueller and Kidder (1972); in that work, particle trajectories were simulated based on the flow field measured in the wind tunnel using hot film anemometers. Folland (1988) later developed two simplified trajectory models to estimate the wind-induced catch losses, based on flow patterns (flow velocity and direction) observed along the main flow direction in the vertical plane centred on the gauge collector. These were partially published by Robinson and Rodda (1969) and the flow field close to the windward edge was described thanks to Warnik's observations. Folland's trajectory models were based on the equation of motion of the particles. In the first model a numerical solution was obtained by simulating one by one droplets of fixed diameter until the expected drop size distribution was generated. Then the two-dimensional losses model was extended to a three-dimensional model considering the variation of the orifice width in the transversal direction. The second model, which the author term "semi-analytical", uses geometrical considerations to calculate the number of particles which fall outside instead of inside of the gauge collector.

Nešpor and Sevruck (1999), conducted numerical simulations on three cylindrical gauges with different sizes and varying the shape of the collector rim. The airflow velocity (magnitude and directional components) was first calculated using a time average approach based on a turbulence closure model, and then liquid particle trajectories were computed. A simplified model, which neglects the interaction between particles and the effect of the particles on the air (one-way coupled model) was employed. Spherical particles were separately simulated for each diameter and the collection efficiency was evaluated by computing the integral, over the particle size distribution, of the number of particles collected by the gauge with respect to the total precipitation. This simulation scheme was adopted also by Thériault et al. (2012) and Colli et al. (2015, 2016a, 2016b) for solid precipitation, by increasing the details of the computational mesh to better capture the airflow features. In the work of Thériault et al. (2012) different crystal types were modelled by using a power law parametrization of the terminal velocity, volume, density and cross section of the particles. A fixed drag coefficient for each crystal type was adopted. In the work of Colli et al. (2016b) solid precipitation was modelled by defining two macro categories: wet and dry snow as suggested by Rasmussen et al. (1999). Results were compared with field measurements in terms of collection efficiency. The obtained collection efficiency curves for the two macro categories act as upper and lower thresholds of the wide spreading of experimental data. Colli et al. (2015) obtained a better fit of the collection efficiency curves with real-world data by calculating the snowflake trajectories while accounting for the dependence of the aerodynamic drag coefficient on the local Reynolds number of solid particles. The drag coefficient of a falling particle is influenced by the instantaneous particle-to-air magnitude of velocity through the particle Reynolds number and at each time step the particle trajectory is obtained by updating the Reynolds number and the associated drag coefficient.

5.1. DYNAMIC CHARACTERISTICS OF PRECIPITATION

The balance among the forces of surface tension, hydrostatic pressure, and aerodynamic pressure from airflow around the drop determines the shape and the terminal fall velocity of hydrometeors. Green (1975), using a simple hydrostatic model, represented droplets as oblate spheroids with axis ratios determined by the balance of surface tension and hydrostatic forces. Pruppacher and Beard (1970) through wind tunnel experiments found that the raindrop shape can be defined in terms of the axial ratio (b/a) between the vertical (b) and the horizontal axis (a). They obtained for raindrops with the equivolumetric drop diameter $D > 0.5$ mm the following empirical equation:

$$\frac{b}{a} = 1.03 - 0.062 D \quad (5.1)$$

while for $D < 0.5$ mm the axial ratio is $b/a = 1$.

Beard and Chuang (1987), introducing in the equilibrium condition the contribution of the aerodynamic pressure, provided a model able to explain the drop shape with its characteristic flattened base that increases with drop size and can be expressed in terms of the following polynomial:

$$\frac{b}{a} = 1.0048 + 5.7 \cdot 10^{-4} D - 2.628 \cdot 10^{-2} D^2 + 3.682 \cdot 10^{-3} D^3 - 1.677 \cdot 10^{-4} D^4 \quad (5.2)$$

Model results of Beard and Chuang (1987) were consistent with the experiments of Chandrasekar et al. (1988) and by Bringi et al. (1998), which employed aircraft to study the shape of raindrops in natural rainfall.

Rainfall drops fall in the atmosphere with their terminal velocity, w_T . The terminal velocity is defined as the maximum velocity attainable by an object as it falls through a fluid. This condition is reached when the sum of the drag force and the buoyancy force is equal to the downward force of gravity acting on the object. In this condition the motion of the object is not accelerated.

The equation of motion of a particle is expressed by the following equation:

$$\rho_p V_p \mathbf{a}_p = -\frac{1}{2} C_D A_p \rho_a (\mathbf{v}_p - \mathbf{v}_a) |\mathbf{v}_p - \mathbf{v}_a| + V_p (\rho_a - \rho_p) \mathbf{g} \quad (5.3)$$

where \mathbf{a}_p is the particle acceleration, \mathbf{v}_a and \mathbf{v}_p are the velocity vectors of the air and the particle, \mathbf{g} is the gravity acceleration, C_D is the drag coefficient, A_p is the particle cross section area and ρ_a and ρ_p are the density of the air and the particle. Eq. 5.3 is written assuming the positive orientation of the z axis upward and the velocity and acceleration components are positive in the positive direction of the related axes. In Eq. 5.3 the quantity $\mathbf{v}_p - \mathbf{v}_a$ is the relative particle-to-air velocity with magnitude:

$$|\mathbf{v}_p - \mathbf{v}_a| = \sqrt{(u_p - u_a)^2 + (v_p - v_a)^2 + (w_p - w_a)^2} \quad (5.4)$$

where u , v and w represent the stream wise, crosswise and vertical components of the velocity vector. The three components of the particle acceleration from Eq. 5.3 become:

$$a_{px} = -\frac{1}{2} C_D A_p \frac{\rho_a}{\rho_p V_p} (u_p - u_a) |\mathbf{v}_p - \mathbf{v}_a| \quad (5.5)$$

$$a_{py} = -\frac{1}{2} C_D A_p \frac{\rho_a}{\rho_p V_p} (v_p - v_a) |\mathbf{v}_p - \mathbf{v}_a| \quad (5.6)$$

$$a_{pz} = -\frac{1}{2} C_D A_p \frac{\rho_a}{\rho_p V_p} (w_p - w_a) |\mathbf{v}_p - \mathbf{v}_a| + \frac{(\rho_p - \rho_a)}{\rho_p} g \quad (5.7)$$

where the gravity acceleration (g) assumes the negative value of -9.81 m s^{-2} .

When a generic drop falls in a stagnant air, from Eq. 5.7 it is possible to obtain its terminal velocity as:

$$w_T = \left[\frac{2V_p(\rho_p - \rho_a)g}{C_D A_p \rho_a} \right]^{1/2} \quad (5.8)$$

The drag coefficient (C_D) is a dimensionless quantity used to represent the resistance of an object in motion in a fluid, such as air or water. It is associated with the cross-sectional area of the object (A_p).

The estimation of the drag coefficient is not easy. In the literature, different experiments were carried out with the objective of identifying a relationship between the drag coefficient and the particle dimension and/or its terminal velocity for hydrometeors which fall in the atmosphere.

Beard (1976) after performing experiments in stagnant air, by measuring the dimension d [mm] of the drops and their fall velocity w_T [m s^{-1}], derived the following values for C_D :

Table 5.1 Drag coefficients of drops with diameter d [mm] which fall in a stagnant air at terminal velocity w_T [m s^{-1}], from Beard (1976).

d [mm]	w_T [m s^{-1}]	C_D
2	6.401	0.510
3	7.885	0.504
4	8.601	0.565
5	8.839	0.668

6	8.867	0.797
7	8.866	0.930
8	8.941	1.045

Any object in motion within a fluid, or impacted by a fluid with a certain velocity, can be associated with a Reynolds number. When a particle falls in a stagnant air its Reynold number is expressed as:

$$Re_p = \frac{w_T d}{\nu_a} \quad (5.9)$$

where ν_a is the air viscosity in $\text{m}^2 \text{s}^{-1}$. The drag coefficient is directly related to the Reynolds number of the particle in motion. When a particle is immersed in a flow field the relation 5.9 becomes a function of the particle-to-air velocity as follows:

$$Re_p = \frac{|\mathbf{v}_p - \mathbf{v}_a| d}{\nu_a} \quad (5.10)$$

Folland (1988) proposed different relationships between Re_p and C_D , for various ranges of Re_p as listed below and assumed that the minimum value for C_D must be fixed at 0.55.

$$Re_p < 0.01 \quad C_D = 2547 \quad (5.11)$$

$$0.01 \leq Re_p < 2 \quad C_D = 1.06(24 Re_p^{-1} + 2.400 Re_p^{-0.045}) \quad (5.12)$$

$$2 \leq Re_p \leq 21 \quad C_D = 1.06(24 Re_p^{-1} + 2.640 Re_p^{-0.19}) \quad (5.13)$$

$$21 < Re_p \quad C_D = 1.06(24 Re_p^{-1} + 4.536 Re_p^{-0.368}) \quad (5.14)$$

The equation proposed by Folland (1988) gives terminal velocities of raindrops in still air at the temperature of 7.5°C and atmospheric pressure that agree to within 2% with those of Mason (1971) over the range of terminal velocities $0.1 < w_T < 8.3 \text{ m s}^{-1}$.

In the work of Khvorostyanov and Curry (2005), hereafter called KC05, different formulations of C_D , as a function of Re_p obtained from experimental studies and analytical models, were summarised as shown in Figure 5.1.

Some of the following curves are derived for spherical particles and other for crystals. The authors introduce a correction parametrization, when the particle Reynolds number exceeds the value of 10^3 , in order to account for the turbulence effect due to the flow.

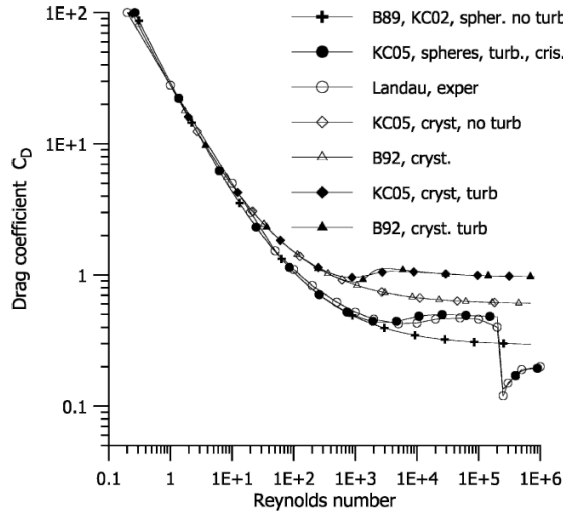


Figure 5.1 Drag coefficient C_D vs. particle Reynolds number Re_p obtained from different literature works and summarized by Khvorostyanov and Curry (2005) for both spherical particles and crystals in turbulent and non-turbulent flow.

5.1.1. Parametrization of solid precipitation

In the work of Rasmussen et al. (1999) observed data from the Marshall Snowfall Test Site, near Boulder (Colorado), of the National Center for Atmospheric Research, were classified in a large number of crystal types and aggregated in two macro categories: “dry” and “wet” snow. In that work, the volume V_p , the cross-section area A_p , density ρ_p and terminal velocity w_T of each type of snowflake are parametrized with a power law curve as a function of the particle diameter d :

$$Y(d) = a_Y d^{b_Y} \quad (5.15)$$

where Y assumes the nomenclature of the volume V_p , the cross-section area A_p , density ρ_p and terminal velocity w_T while a_Y and b_Y are the parameters associated to each type of snowflake.

The values of the parameters are provided by both Rasmussen et al. (1999) and Thériault et al. (2012) for different classes of crystal types and for *wet* and *dry* snow categories. In Table 5.2 the values of the power law parameters for dry and wet snow used in this thesis are reported. When the particle diameter is expressed in centimetres the following parameters provide V_p in $[\text{cm}^3]$, A_p in $[\text{cm}^2]$, and ρ_p in $[\text{g cm}^{-3}]$.

Table 5.2 Parameters a_V and b_V of Eq. 5.15, from Rasmussen et al (1999), for the computation of the snowflake volume V_p , cross-section area A_p and density ρ_p

Crystal type	a_{V_p}	b_{V_p}	a_{A_p}	b_{A_p}	a_{ρ_p}	b_{ρ_p}
Dry snow	$\pi/6$	3	$\pi/4$	2	0.017	-1
Wet snow	$\pi/6$	3	$\pi/4$	2	0.072	-1

In the list above the parameters associated with the terminal velocity, used in the previous literature works, are not reported because the power law formulation for the terminal velocity is not adopted in this thesis. The terminal velocity of each snowflake is obtained here by imposing the equilibrium between the acting forces associated with the drag coefficient for the crystal types proposed by Khvorostyanov and Curry (2005).

5.1.2. Parametrization of liquid precipitation

In this thesis, the numerical model used by Colli et al. (2015) to compute the trajectories of solid particles was adopted to simulate the motion of water droplets when falling through the atmosphere and approaching the gauge collector, as well as to calculate the number of particles $n(d)$, collected by the gauge in aerodynamic disturbed conditions, for each particle diameter d . Liquid particles are parametrized with spherical shape of equivalent diameter d . The particle density was set equal to 1000 kg m^{-3} at the air temperature of 20°C . According to the work of Colli et al. (2015) the particles Reynolds number (5.10) was calculated at each computational step and the associated drag coefficient was derived and adopted in the equation of motion of the particle.

The drag coefficient values as a function of the particle Reynold number proposed by Khvorostyanov and Curry (2005) for spherical particles in turbulent condition, (black circles in Figure 5.1) were fitted with a three parameters law (Eq. 5.16), with the values of such parameters listed in Table 5.3. The parameters of the best-fit curve were derived for the Re_p range between 50 and 7200; these thresholds were adopted to include the Reynolds value for a drop of 1 mm which falls in the air ($v_a = 1.5 \cdot 10^{-5} \text{ m}^2\text{s}^{-1}$) at an indicative fall velocity of 1 m s^{-1} and the Re_p value associated with a particle of $d = 8 \text{ mm}$ and fall velocity of about 9 m s^{-1} as reported by Beard (1976).

$$C_D = y_0 + \frac{(a \ b)}{b + Re_p} \quad (5.16)$$

Table 5.3 Parameters of the best-fit curve, and correlation factor, obtained by interpolating the KC05 C_D values expressed as a function of Re_p

y_0	a	b	R^2
0.442	3,402	21,383	0.996

Also the relations proposed by Folland (1988) were compared with the raw data provided by KC05 as shown in Figure 5.2. Based on this comparison the best-fit curve reported in Eq. 5.16 was implemented in the particle tracking model to calculate the drag coefficient for Re_p larger than 400, while the equations proposed by Folland were adopted for Re_p lower than 400.

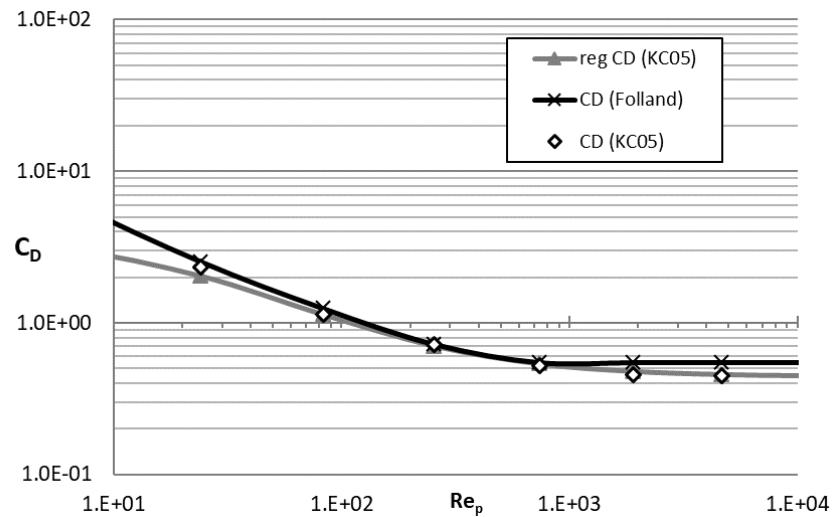


Figure 5.2 Comparison between the raw data proposed by KC05 (diamond) , the best-fit curve in Eq. 5.16 (grey line) and the formulation proposed by Folland (1988) (black line).

5.2. LAGRANGIAN PARTICLE TRACKING MODEL

The Lagrangian Particle Tracking (LPT) model, based on the equation of particle motion described above, allows the trajectory of a single particle immersed in a fluid to be followed by describing its properties at each time interval. The trajectories are computed with a forward step procedure by calculating at short time intervals the particle positions. This model is one-way coupled since the potential influence of the particles on the airflow field is neglected. This simplification is acceptable since the particles concentration in the air is very low as will be demonstrated in chapter 6.

The relative particle-to-air velocity is updated at every time step by interpolating the CFD airflow field to obtain the flow velocity \mathbf{v}_a in the exact position of the drop. Therefore, the components of the new position of the drop at step $(i+1)$ are calculated by the following equations:

$$x^{(i+1)} = x^{(i)} + \left(u_p^{(i)} + \frac{1}{2} a_{px}^{(i)} \Delta t \right) \Delta t \quad (5.17)$$

$$y^{(i+1)} = y^{(i)} + \left(v_p^{(i)} + \frac{1}{2} a_{py}^{(i)} \Delta t \right) \Delta t \quad (5.18)$$

$$z^{(i+1)} = z^{(i)} + \left(w_p^{(i)} + \frac{1}{2} a_{pz}^{(i)} \Delta t \right) \Delta t \quad (5.19)$$

where $x^{(i)}, y^{(i)}, z^{(i)}$ and $x^{(i+1)}, y^{(i+1)}, z^{(i+1)}$ are, respectively, the previous and the new spatial coordinates of the particle.

At every time step also the velocity components of the particle are calculated as follows:

$$u^{(i+1)} = u^{(i)} + a_{px}^{(i)} \Delta t \quad (5.20)$$

$$v^{(i+1)} = v^{(i)} + a_{py}^{(i)} \Delta t \quad (5.21)$$

$$w^{(i+1)} = w^{(i)} + a_{pz}^{(i)} \Delta t \quad (5.22)$$

and the components of the particle acceleration are calculated as in Eq. 5.5, 5.6, 5.7.

The acceleration of the particle depends on the drag coefficient; as proposed by the literature work of Colli et al. (2015) its value is updated at every time step consistently with the particle Reynolds number calculated from Eq. 5.10 as a function of the relative particle-to-air velocity. The velocity of each simulated particle was initialized by imposing the terminal velocity value in the vertical direction and the same velocity of the wind in the horizontal direction. The third component was set equal to zero.

5.3. WIND TUNNEL VALIDATION OF THE PARTICLE TRACKING MODEL

Particle tracking models have been used in the literature to simulate hydrometeors trajectories by assuming that, since physically based, they would accurately reproduce the path of particle motion when immersed in the airflow pattern. However, a number of empirical considerations lie behind the application of the particle tracking model to any real-world situation, and validation is required before the results can be extended to operational applications. The wind tunnel is the most suitable environment to validate the model since both the airflow and the fluid-particle interactions can be accurately measured in controlled conditions for various wind speed and particle size arrangements.

Full validation of the simulated trajectories was not yet performed in the literature due to the difficulties of injecting water droplets into the wind tunnel and measuring their trajectories. In this work, a validation setup was designed and realised in the wind tunnel, able to detect the deviation of droplet trajectories as induced by the bluff body aerodynamics of various precipitation gauges. Results allowed observed and simulated trajectories to be compared under various wind velocity and drop size conditions, so as to validate the Lagrangian Particle Tracking model, here adapted to simulate particles falling at a different vertical velocity than the terminal one, and using suitable drag coefficients equations as a function of the particle Reynolds number.

5.3.1. Review of existing experiments

Wind tunnel testing of the aerodynamics of precipitation gauges and windshields has been a suitable investigation tool in precipitation measurement studies since the early work of Bastamoff and Witkiewitch (1926), although Jevons (1861) had already used a simple wind tunnel test using smoke trails from smouldering brown paper to support his explanation of the wind exposure problem. However, the actual trajectories of precipitation particles were seldom detected, let alone quantitatively measured. Most studies concentrated mainly on identifying optimal design solutions to minimise the airflow acceleration and updraft and therefore the impact of the gauge body on the surrounding wind field.

For example, Sanuki et al. (1952) tested two types of wind shields for rain gauges (conical and hollow ring-shaped designs) both in a water tank and in the wind tunnel. The air speed at which the test was conducted ranged from 1.5 to 20 m/s, the corresponding Reynolds number being from 1 to 1.5×10^5 with respect to the rain gauge funnel diameter. The flow around the funnel and wind shield was visualized by means of short, black and white wool strings tied to the main positions of the model. Further, air speed measurement was done at a position of 0.5 diameters above the funnel mouth. The flow patterns were photographed by means of aluminium powder spread over the water surface of the tank, or wool strings tied to the model in the wind tunnel. The conclusions obtained from the tank test are valid for two-dimensional cases only, while for three-dimensional confirmation the wind tunnel test was resorted to for the models selected from the tank test. Only the airflow features were observed and visualised in these experiments, even if minimum generation of eddies at all parts of the flow was sought in the assessment of windshield design.

With little relevant precedent, the wind-induced undercatch of shielded and unshielded precipitation gauges was measured in a wind tunnel by Warnik (1953) using injected real and sawdust snow. Sawdust

was injected into the airstream of the tunnel to define the air-flow patterns and was also used as artificial snow in studying the quantitative catch of the model gauges. A very dry, low-density real snow, was also blown into the tunnel. In the wind tunnel the air flow was fairly smooth, with no large eddies, and at prototype speeds of about 5 to 10 m/s.

Warnik used photographs taken against a grid work background to measure the drift angle and velocity of undisturbed particles in the absence of the gauge so as to infer the theoretically true catch of an imaginary horizontal area equal to the area of the gauge orifice. This was necessary because the actual intensity of the simulated precipitation was not known a-priori and both sawdust and real snow entered the airstream horizontally, therefore not similar to real-world precipitating snow.

Warnik (1953) also visualised the airflow pattern above the gauge collector by using titanium dioxide vapour as a tracer, which was introduced into the moist air passing through the tunnel to produce a dense white smoke. This allowed visualisation of the tendency for the path lines of the sawdust particles, smoke, and actual snow to blow upward owing to updrafts along the elements of the gauge body. Various windshield shapes and designs were tested in the wind tunnel to get an improved air-flow pattern over the gauges.

The effect of turbulence was not explicitly addressed and the free-stream turbulence was even avoided by using a honeycomb baffle system in the throat just forward of the test section so as to cut down turbulence and provide a relatively smooth flow of air.

The extensive wind tunnel experiments performed by Warnik were a pioneering work where the trajectories of precipitating solid particles under windy conditions and their deviations when approaching the gauge were first visualised. However, no attempt to quantitatively measure and model the deviation of particles in the presence of the gauge collector was made and just the overall undercatch was quantitatively obtained. The main objective of this study is to define the air-flow behaviour around the gauges and to give definite information about the inconsistencies observed in records of snow catch in precipitation gauges. Results were used to design the geometry of two windshields with better performance than the shields in use at that time. In particular, the author recommended that the Alter shield be modified by using a larger diameter supporting ring, more and longer baffles, and substituting for the restraining chain a set of annular spacers between the baffles around the supporting ring.

About 15 years later, Robinson and Rodda (1969) performed wind tunnel experiments to examine the airflow around four types of rain gauges in a series of wind-tunnel experiments using tuft indicators and smoke trajectories. The aerodynamics of two gauges with cylindrical shapes, one drop counter gauge characterized by bluff shape and a gauge with champagne glass shape, named metal Funnel Gauge, was studied. Quantitative assessment of the wind velocity over the gauges was obtained from measurements made by a hot-wire anemometer which could be moved in a vertical plane oriented along the direction of the wind.

Results of these experiments, using indicator tufts stuck to the gauges, showed that the flow velocity increased as the air passed over the top of the gauge and turbulence occurred above each gauge. Then, smoke was injected into the airstream and photographs were taken of the smoke trajectory over each gauge for wind speeds between 0.5 and 5 m/s at 0.5 m/s intervals.

The hot-wire anemometer measurements showed that the gauges exhibited similar aerodynamic behaviours characterized by a separation zone which starts from the leading edge of each gauge and that curve backwards over the collector. Above the separation zone the wind speed reached a maximum while below it the flow velocity drops and a turbulent zone develops. The authors concluded that the two gauges with simple cylindrical and near cylindrical shapes appeared to produce the least satisfactory patterns of airflow. The more complex shapes of the drop counter gauge and the Funnel Gauge caused less distortion of the wind field. Observations identified the wind speed at which a clear lift of the smoke at the tops of the gauges is evident, and for high wind speed smoke trajectories flattened out above the orifice of the gauges. The height of the lift of the smoke trajectory above the gauge appeared to increase with increasing diameter of the gauge and with increasing sharpness of the leading edge of the gauge for equal wind speeds. For the Funnel Gauge a complete lift occurred at a much higher wind speed and for the same wind speed the amount of lift appeared to be less than for the other gauges.

Robinson and Rodda (1969) also raised the problem of determining the relationship between catch and the aerodynamic characteristics of a gauge, suggesting that “an examination of drop trajectories above the gauge by photography might provide the best solution, but there would be considerable difficulties in analysing the enormous amounts of data that would be produced. In addition, drop size would have to be measured continuously and this is not an easy task”. Due to such difficulties the authors resorted to field experiments to quantify the associated precipitation undercatch.

Apart from the work of Green and Helliwell (1972), the impact of the exposure problem of catching type precipitation gauges on the approaching hydrometeors has not been accurately observed, nor measured yet in controlled and replicable laboratory conditions. The authors measured wind profiles and raindrop trajectories above a cylindrical rain gauge in a wind tunnel. The flow field was measured using a grid of hotwire anemometers and the trajectories of injected drops tracked using photographs from a still reflex camera. Furthermore, they simulated the drop trajectories based on the streamlines obtained by visually interpreting the pattern of smoke injected in the wind tunnel. Little details are provided about the algorithms and procedures used in that work. Four wind speeds between 1 and 10 m s⁻¹ were tested and the trajectories of drops characterized by diameters of 1.2, 2.2 and 3.5 mm were visualised.

The drop diameter was estimated by means of three control procedures in stagnant air, therefore the wind effect on the detachment of drops from the generating apparatus was not taken into account. The experimental measurements were conducted only on a gauge model with cylindrical shape, and drop trajectories were recorded with low details. The gauge catch was calculated as the ratio between the apparent, assumed circular, collector's area required to catch the same amount of rainfall as a gauge without the influence of wind and the actual area of the investigated gauge collector. The apparent catchment area was defined considering the positions reached at the gauge collector level by two deflected drop trajectories which, in undisturbed conditions, would aim to the upwind and downwind edges of the collector. The distance between these two droplets was assumed as the diameter of the circle which defines the apparent catchment area. This assumption implies that the most deflected trajectory is that which, in undisturbed conditions, aims to the leeward edge of the collector. Actually this characteristic is not known a priori, nor is necessarily true. The authors cared to mention that the turbulence level in the tunnel was less than 0,4% and 0,1 % of the air speed in the low and high speed sections, respectively.

To the author's knowledge, no further investigation is described in the literature leading to improved measurements of hydrometeors trajectories and their wind-induced deviation in the wind tunnel. Flow streamlines of natural wind around and within rain gauges were visualised by Strangeways (2004) in a field experiment using video records of light nylon-thread tracers on a hand-held rod, able to indicate the path of the wind. Streamlines were investigated in turbulent, real-world conditions rather than in the controlled and simplified environment of a wind tunnel, but no quantitative measures were reported. In addition, the focus of the experiment was on the recirculating pattern inside the collector, while little attention was paid to the updraft in that work.

5.3.2. Dedicated setup for wind tunnel validation of the LPT model

In this thesis work, a dedicated setup was designed and installed in the wind tunnel to generate and release water droplets in the incoming airflow and to precisely measure their trajectories when approaching the gauge collector. The objective was to measure the deviation of the drop trajectories due to the bluff body aerodynamics of the gauge and to quantify the effect of different gauge geometries. This allowed the validation of the particle tracking model later used to calculate the collection efficiency and the resulting correction as a function of wind speed and precipitation intensity.

Tests were carried out in the wind tunnel facility available at Politecnico di Milano within the activities of the PRIN 20154WX5NA project. The chimney shape of the *GeonorT200B*[®] gauge, the cylindrical shape of the *Lambrecht Rain[e]H3*[®] gauge and the inverted conical shape of the *EML-SBS500*[®] were tested. The wind tunnel was equipped with a hydraulic system to generate droplets, a high-speed camera and a high-power lamp to photograph and illuminate droplets along their trajectories. The experimental setup is illustrated in Figure 5.3.

The hydraulic system consists of a water tank which feeds a volumetric pump (model Ismatec Reglo-Z digital) connected to a nozzle; the nozzle releases droplets with a frequency that can be adjusted by varying the pump flow rate between 0.4 and 18.0 ml/min. The tests were conducted using a fixed flow rate of 0.8 ml/min and a nozzle orifice size of 0.008'' (about 0.2 mm). The support for the nozzle was shaped (see Figure 5.4) to have a reduced impact on the airflow close to the orifice and to minimize the oscillations at the edge where droplets are released.



Figure 5.3 Experimental setup to release drops and photograph their trajectories in the wind tunnel.



Figure 5.4 Nozzle with orifice diameter 0.2 mm installed in the wind tunnel on a thin plastic support realized in order to minimize the impact on the airflow in the drops releasing position.

To visualize the drop trajectories, a high-speed camera was placed in front of the gauge. The camera lens and the distance from the gauge collector were optimised so as to increase the resolution of the captured drop images without affecting the airflow field near the target. The plane of focus was set as the vertical plane passing through the central along-wind section of the gauge collector. Two types of video acquisition were carried out: at high-frame rate (fps) and at low-frame rate. The recording speed was optimized to maintain a high image quality, in terms of resolution and luminosity, suitable for capturing the drop movement with no streaks appearing due to an excessive exposure time with respect to the drop displacement. The recording speed was set to 1000 fps, with an image resolution of 1600x900 pixels for the high frame rate. During the low frame rate acquisition, the recording speed was purportedly kept low, in order to increase the exposure time. In this way the trajectory of a bright moving object was imprinted in a single image in the form of a streak. In this configuration the recording speed was set to 10 fps, with the same image resolution of 1600x900 pixels. In order to switch, during the video post-processing phase, from

the pixel dimensions of the images to the real dimensions in mm, before each test a graduated scale is placed in the focus plane, allowing the conversion rate from pixel to mm to be determined. The WT campaign was realized in subsequent time slots, in each of them the dimension of the image was about 40 x 20 cm with the pixel sizes listed in Table 5.4, where G is the code which identifies the *GeonorT200B*[®] gauge, L indicates the *Lambrecht Rain[e]H3*[®] gauge and S indicates the *EML-SBS500*[®] gauge. The wind speed range investigated is between 9 and 13 m s⁻¹.

Table 5.4 Pixel size for each WT experiment.

G – 1 st period	1pixel : 0.2370 mm
G – 2 nd period	1pixel : 0.1988
L – 1 st period	1pixel : 0.2424
L – 2 nd period	1pixel : 0.1944
S – all tests	1pixel : 0.2435

The lighting was designed to increase the drops visibility in the videos: an incandescent lamp was used to illuminate the volume near the gauge collector. The tests were conducted in a dark environment while backlighting the gauge from above using the lamp. The lamp lights are suitably directed in order to avoid the saturation of the recorded videos.

The investigated precipitation gauges were positioned downstream of the drop generator, so that drops are released along the symmetry axis of the gauge parallel to the wind direction. The drop release position was determined a priori using the Lagrangian Particle Tracking model based on the flow field provided by CFD simulations at a wind speed equal to 10 m s⁻¹. The drop size was set equal to the minimum dimension that the video camera is able to capture (1 mm) following dedicated tests performed in stagnant air. The initial velocity of the drop was imposed equal to zero in all directions. This configuration allowed a significant deformation of the trajectories to be observed when travelling in the region where the flow field is disturbed by the aerodynamic response of the gauge. This configuration was necessary because drops could not be generated with their terminal velocity, otherwise – given the constraints on the drop size mentioned above – the high inertia of such large drops would have resulted into an imperceptible deflection of the drop trajectories above the gauge collector.

The videos recorded by the camera have been imported and analyzed in the MATLAB environment. The drops detection methodology differs depending on the type of acquisition. In high-fps, the path of each drop is identified by many frames: in every frame the drop is in a given position, which evolves in the next frame. Due to the reduced exposure time of each image, little light hits the camera sensor and the image appears dark. To increase the visibility of the drops, each image is then converted to greyscale and a combination of a Gaussian and Laplacian filter is applied. The image is binarized using a threshold level, with the zeroes indicating the background while the ones indicate the presence of the drop. Finally, using a moving window over the image, the center of the drop is identified and stored. The results of these operations are visible in

Figure 5.5. Knowing the time interval between two subsequent images and the conversion rate from pixels to mm, it is also possible to calculate the drop speed in the 2-D shooting plane.

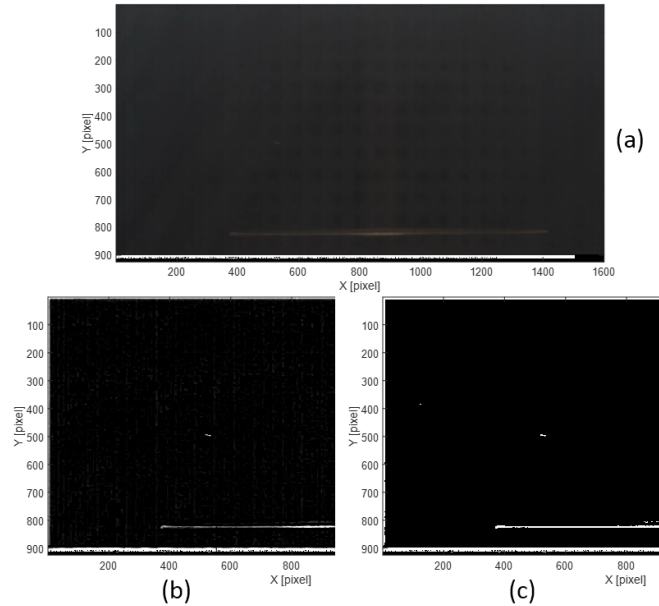


Figure 5.5 Original image, in the vertical plane (X,Y in pixel) along the main flow direction, with the gauge collector rim and the approaching water drop as captured by the high-speed camera at 1000 fps (panel a), post processed greyscale image after the application of suitable filters (panel b), and final image after binarization (panel c) where the rim of the gauge collector and the drop are depicted in white while the background is in black.

In low-fps acquisition, due to the high exposure time, every frame appears much more bright and contains a streak representing the trajectory of each single drop. The same filtering and binarization operations are used, adapting the filter and threshold parameters. Finally, morphological operations are carried out, in order to extract the image skeleton represented by the middle line streak and directly corresponding to the trajectory of the drop. The result of these operations is shown in Figure 5.6.

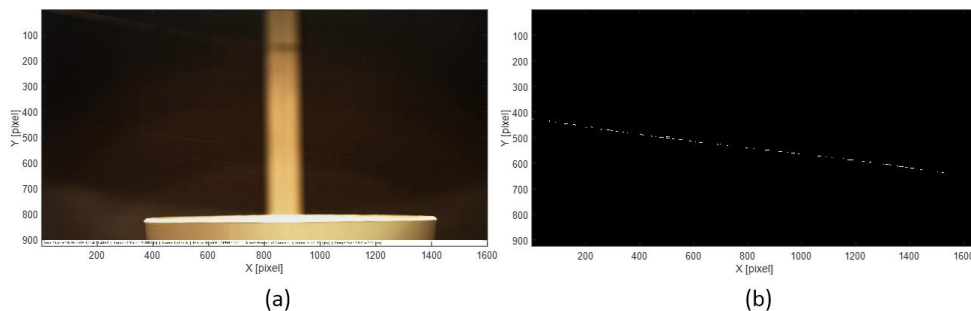


Figure 5.6 Original image, in the vertical plane (X,Y in pixel) along the main flow direction, with the gauge collector rim and the travelling water drop as captured by the high-speed camera at 10 fps (panel a), and post processed image (panel b) after the application of suitable filters, binarization and morphological operations. The final result (panel b) shows the drop trajectory depicted in white against a black background.

5.3.3. Observation of the deflected trajectories

The detected trajectories show a significant deviation when approaching the collector of the gauge following the expected updraft and the recirculation zone above the collector. Wind-induced deviations of the trajectories vary with the shape of the gauge and are consistent with the expected behaviour driven by the different configurations of the recirculation zone in the various cases.

In Figure 5.7 and Figure 5.8 a sample set of the observed drop trajectories shot at 1000 fps and 10 fps, above the collector of the gauges with cylindrical and chimney shape are reported at a wind speed of $U_{ref} = 12.5 \text{ m s}^{-1}$ and $U_{ref} = 11.4 \text{ m s}^{-1}$, respectively. The particle-fluid interaction above the collector of the gauges is responsible for a significant deviation of the trajectories, and this can be observed here for all trajectories when travelling beyond the upwind edge of the collector. Furthermore, in both cases, a few trajectories that seem to aim towards the downwind edge of the collector actually overtake its rim and fall outside of the gauge.

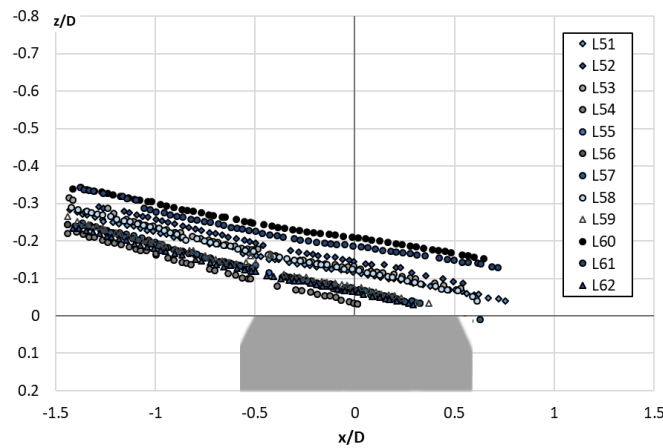


Figure 5.7 Sample set of drop trajectories observed at 1000 fps above the collector of the gauge with cylindrical shape, at a wind speed of $U_{ref} = 12.5 \text{ m s}^{-1}$.

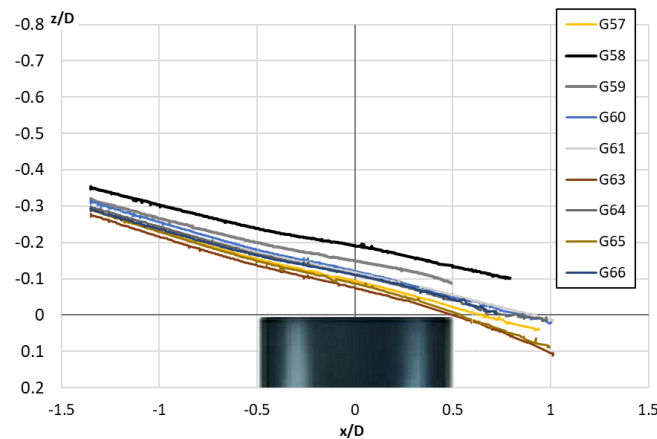


Figure 5.8 Sample set of drop trajectories observed at 10 fps above the collector of the gauge with chimney shape, at a wind speed of $U_{ref} = 11.4 \text{ m s}^{-1}$

In Figure 5.9 the observed trajectories of two drops released at the same initial position for the *Geonor*[®] gauge at a wind speed $U_{ref} = 11.4 \text{ m s}^{-1}$ are reported. This example reveals the very good repeatability of the new bespoke experimental setup since the two trajectories are totally overlapped.

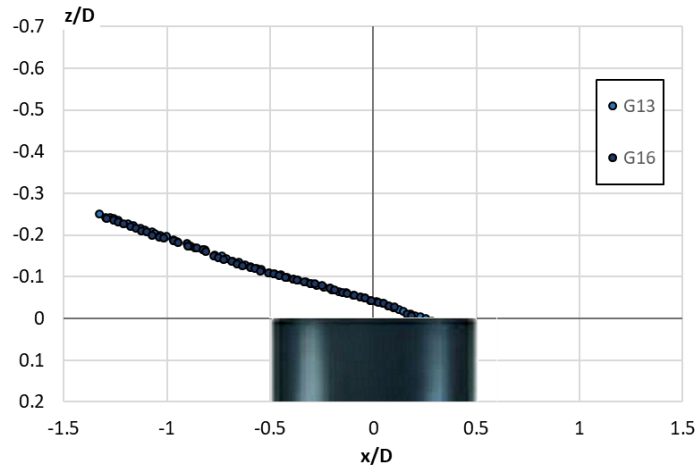


Figure 5.9 Comparison of the observed trajectories of two drops released at the same initial position for the *Geonor*[®] gauge at a wind speed $U_{ref} = 11.4 \text{ m s}^{-1}$.

In Figure 5.10, Figure 5.11 and Figure 5.12, three observed drop trajectories for each gauge geometry, with the associated undisturbed trajectories, are reported at different wind speeds in the dimensionless plane x/D and z/D , where D is the diameter of each gauge collector. In the first figure, a sample drop trajectory is visualised when approaching the chimney shape gauge at a wind speed $U_{ref} = 9.8 \text{ m s}^{-1}$, while in Figure 5.11 the drop trajectory is captured above the collector of a cylindrical gauge at a wind speed $U_{ref} = 12.3 \text{ m s}^{-1}$ and in Figure 5.12 above the collector of the inverted conical shaped gauge at a wind speed $U_{ref} = 11.16 \text{ m s}^{-1}$. In all cases the observed trajectory starts detaching from the undisturbed one when its longitudinal coordinate reaches the upwind edge of the collector (about $x/D = 0.5$), where the airflow updraft is most significant.

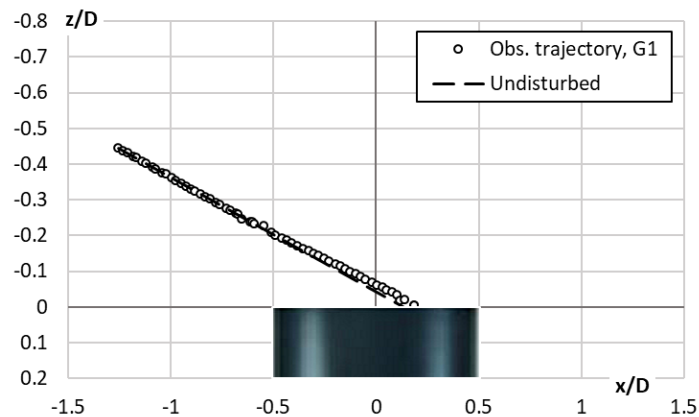


Figure 5.10 Observed drop trajectory (circles) and undisturbed one (dashed line) above the collector of the chimney shaped gauge, at a wind speed $U_{ref} = 9.8 \text{ m s}^{-1}$.

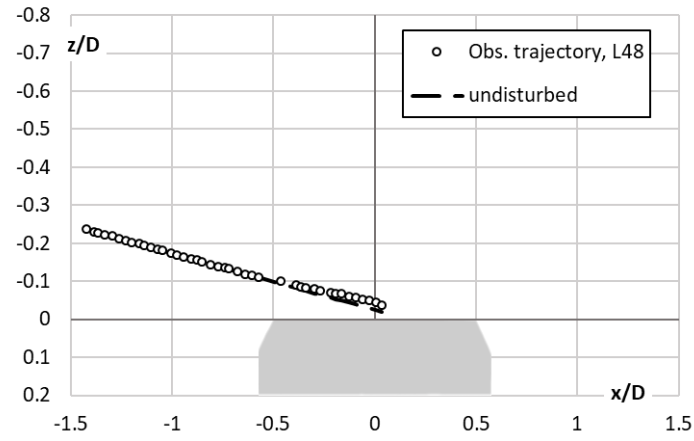


Figure 5.11 Observed drop trajectory (circles) and undisturbed one (dashed line) above the collector of the gauge with cylindrical shape, at a wind speed $U_{ref} = 12.3 \text{ m s}^{-1}$.

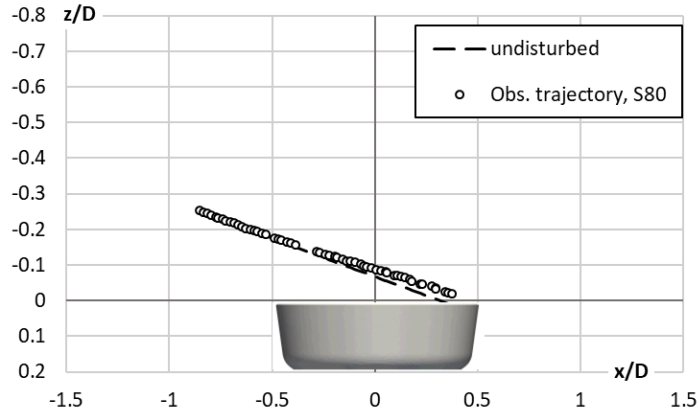


Figure 5.12 Observed drop trajectory (circles) and undisturbed one (dashed line) above the collector of the gauge with inverted conical shape, at a wind speed $U_{ref} = 11.16 \text{ m s}^{-1}$.

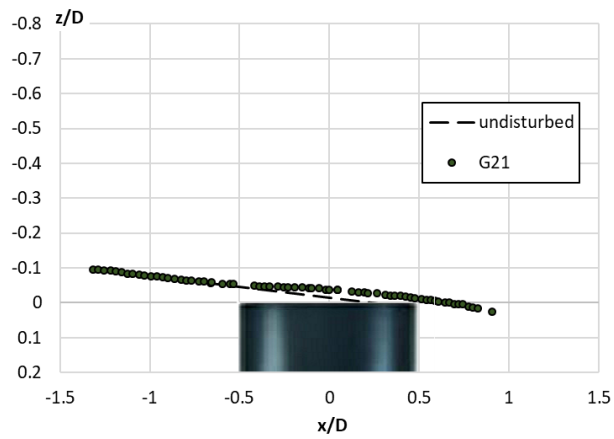


Figure 5.13 Observed drop trajectory (circles) and undisturbed one (dashed line) above the collector of the chimney shaped gauge, at a wind speed $U_{ref} = 12.5 \text{ m s}^{-1}$.

In all graphs the gauge collector is centered in (0,0). The longitudinal coordinate of the drop releasing position is fixed while the elevation (z/D) varies with the wind speed. For example, for the *Geonor*® gauge all trajectories enter the plane shot by the camera at $x/D = -1.31$. By comparing the various figures showed above and Figure 5.13, captured at the higher wind speed of 12.8 m s^{-1} , it is evident that the trajectory falls closer to the gauge collector. Also in this case, however, the undisturbed trajectory would enter the collector while the observed one overtakes the collector and travels beyond the gauge.

Each observed drop trajectory was elaborated by linearly interpolating the positions associated with the undisturbed part of the trajectory, while the disturbed one was fitted with a third order polynomial. An example is shown in Figure 5.14 (top) with a drop which travels above the collector of the cylindrical gauge at a wind speed $U_{ref} = 12.3 \text{ m s}^{-1}$. The undisturbed part of the trajectory is painted with a dark grey while the disturbed part is painted in light grey and the interpolation curves are marked with dots. The threshold between the undisturbed and disturbed part of the trajectory was obtained by adopting a trial and error procedure with the objective to ensure the continuity of the slope curve (z/x) obtained as the first derivative of the fitted trajectory (Figure 5.14 bottom). The parameters of the best-fit curves, for the trajectory L44, with the associated correlation factors are listed in Table 5.5.

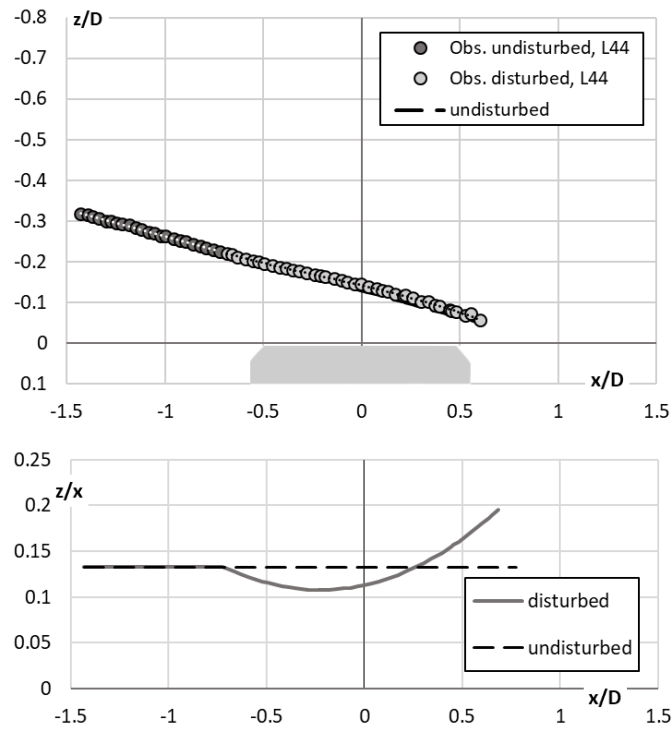


Figure 5.14 Observed drop trajectory (circles) and undisturbed one (dashed line) above the collector of the gauge with cylindrical shape (top) and the associated slope curves (bottom) for wind speed of $U_{ref} = 12.3 \text{ m s}^{-1}$.

Table 5.5 Parameters of the linear regression (m and q) for the undisturbed part of the trajectory L44, and of the third order polynomial for the disturbed part (a , b , c and d), with the associated correlation factors.

ID	m	q	R^2	a	b	c	d	R^2
L44	0.1329	-0.1295	0.9986	0.0352	0.0238	0.1132	-0.1418	0.9984

In Figure 5.15 two drop trajectories travelling above the collector of the *Geonor*[®] gauge at a wind speed $U_{ref} = 10.2 \text{ m s}^{-1}$, are depicted. The two droplets have a similar size because their initial, undisturbed slope is the same. As expected, following the airflow pattern, the drop starting at a higher elevation is deviated a bit later. The difference between the observed and undisturbed trajectories is shown on the right axis. These differences are larger in the second half part of the collector where it can be observed that the two droplets fall outside instead of inside of the collector.

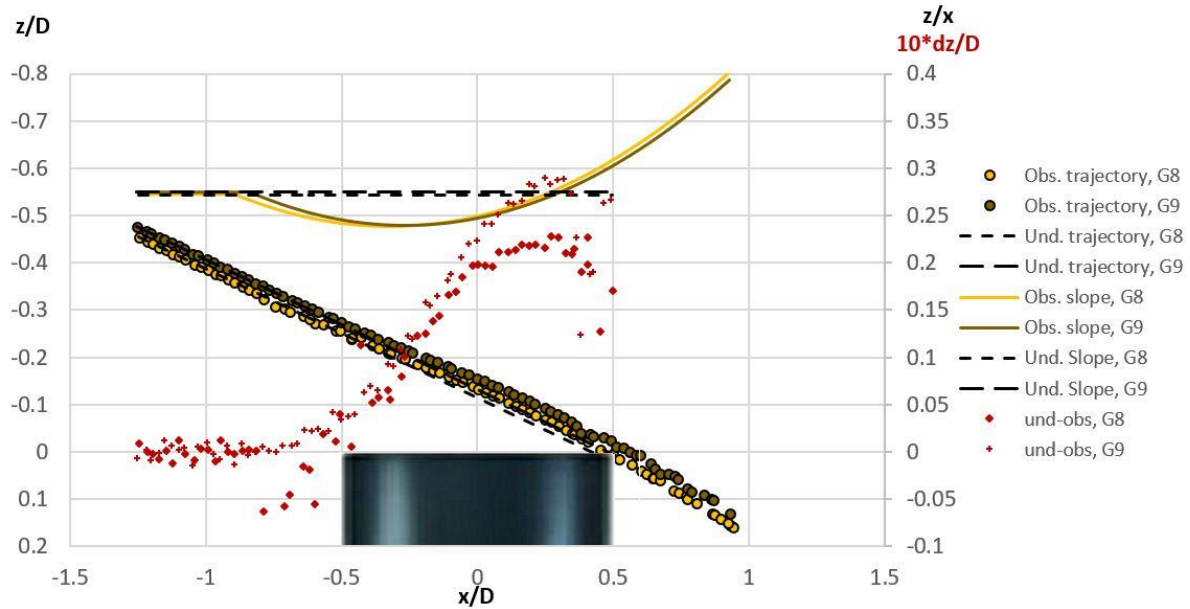


Figure 5.15 Comparison of two drop trajectories (circles) having similar size, travelling above the collector of the chimney shaped *Geonor*[®] gauge at a wind speed $U_{ref} = 10.2 \text{ m s}^{-1}$, together with the associated undisturbed trajectories depicted with dashed lines. The associated slope curves (scale on the right-hand axis) are shown with solid and dashed lines for the disturbed and undisturbed trajectories, respectively. Red markers represent the difference between the observed and undisturbed trajectories in terms of vertical normalized positions (scale on the right-hand axis).

5.3.4. Particle Image Velocimetry velocity fields and observed drop trajectories

In the wind tunnel facility, available at the Politecnico di Milano, Particle Image Velocimetry (PIV) measurements were conducted on three gauges with cylindrical, chimney and inverted conical shape as already shows for the *Hotplate* gauge in the chapter 4.

The upper part of the gauges was painted in black (see Figure 5.16) in order to avoid the reflection of light. Nevertheless, in the airflow velocity maps, shown in Figure 5.17, Figure 5.18 and Figure 5.19, suitable masking of the images was adopted to allow the correct post processing of the PIV acquisitions. For each precipitation gauge, PIV tests were conducted at wind speeds equal to 5 and 10 m s⁻¹.



Figure 5.16 Installation of the cylindrical gauge in the wind tunnel for PIV experiments, the upper part is painted in black in order to avoid the reflection of light.

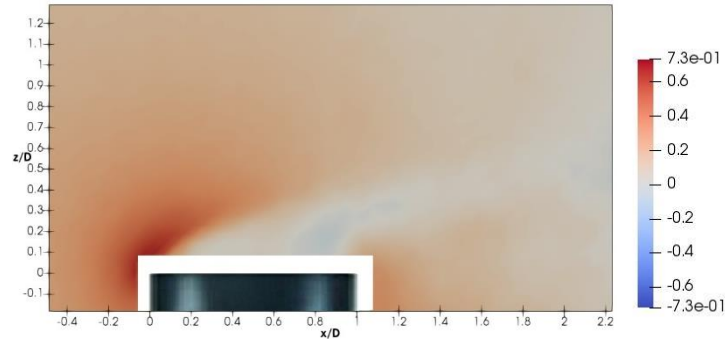


Figure 5.17 PIV field of the normalized vertical velocity component in the central ($y/D = 0$) stream-wise section, for the chimney shaped gauge at a wind speed of 10 m s⁻¹.

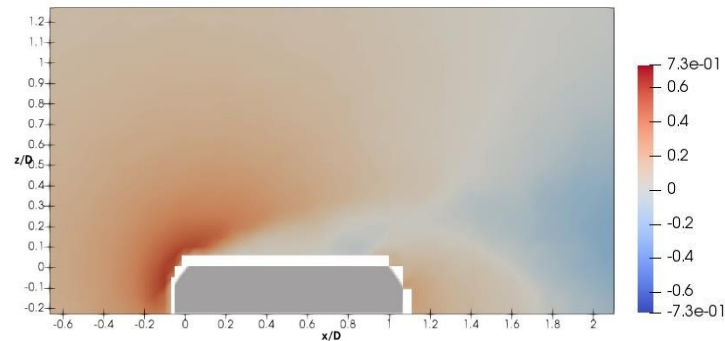


Figure 5.18 PIV field of the normalized vertical velocity component in the central ($y/D = 0$) stream-wise section, for cylindrical gauge at a wind speed of 10 m s⁻¹.

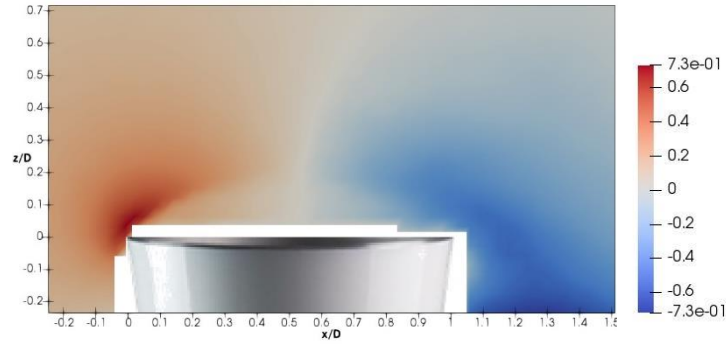


Figure 5.19 PIV field of the normalized vertical velocity component in the central ($y/D = 0$) stream-wise section, for the inverted conical gauge at a wind speed of 10 m s^{-1} .

Consistent with the work of Cauteruccio et al. 2019, for the inverted-conical gauge in uniform free-stream conditions, the updraft in the upwind part of the collector and the downdraft in the downwind part as obtained in the PIV analysis are comparable in magnitude. For the other cylindrical and chimney shaped geometries the region above the collector is almost totally affected by updraft components, although the cylindrical gauge shows lower updraft values than the other two geometries.

Figure 5.20 reports the normalized positions of the maximum velocity values obtained by means of PIV measurements for the three gauge geometries investigated. This result reveals that these positions are higher and more dispersed for the chimney-shaped *Geonor*® gauge, while they are lower and more bounded for the inverted conical shape. The behaviour of the cylindrical gauge is intermediate. In Figure 5.21, Figure 5.22 and Figure 5.23, the normalized positions of the maximum velocity values for each gauge geometry and for the wind speed of 5 and 10 m s^{-1} are compared and colour coded with the magnitude of the airflow velocity. The magnitude of flow velocity is higher for the gauge with inverted conical shape and lower for the other two geometries. Moreover, for the chimney-shaped gauge the maximum velocity patterns are not scalable both in terms of normalized velocity magnitude and positions.

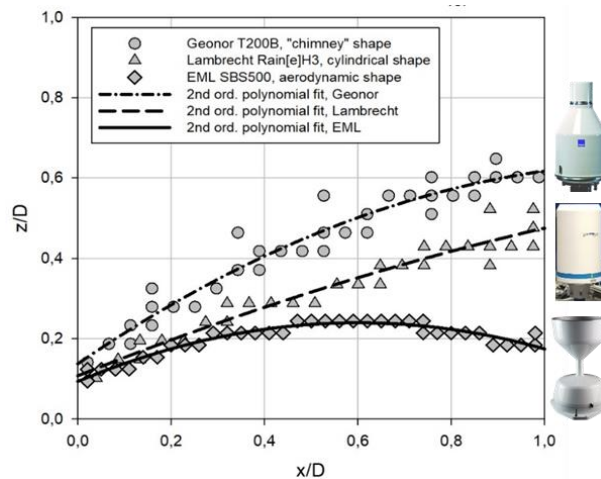


Figure 5.20 Normalized positions of the maximum velocity values obtained by means of PIV measurements for the wind speed of 5 m s^{-1} , for the chimney (circles), cylindrical (triangles) and inverted conical (diamonds) shapes, in the central ($y/D = 0$) stream-wise section. The upwind edge of the collector is in $(0,0)$.

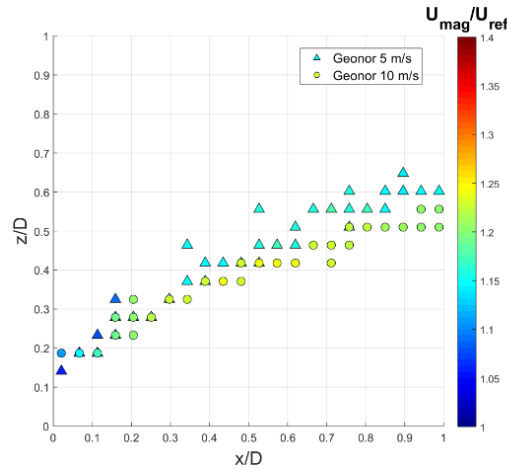


Figure 5.21 PIV measurements of the magnitude of flow velocity at the maximum elevation positions, in the central ($y/D = 0$) stream-wise section, for the chimney shaped gauge at wind speed of 5 and 10 m s^{-1} .

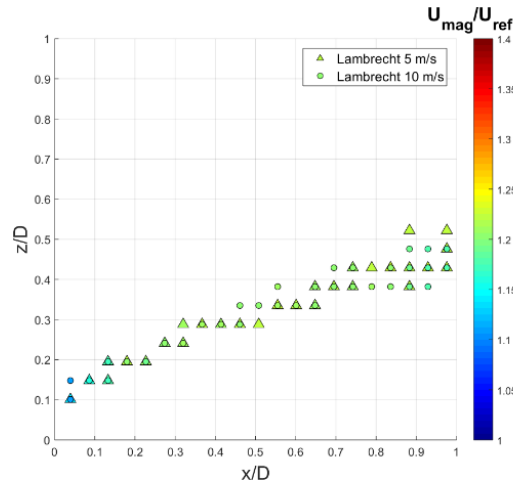


Figure 5.22 PIV measurements of the magnitude of flow velocity at the maximum elevation positions, in the central ($y/D = 0$) stream-wise section, for the cylindrical gauge at wind speed of 5 and 10 m s^{-1} .

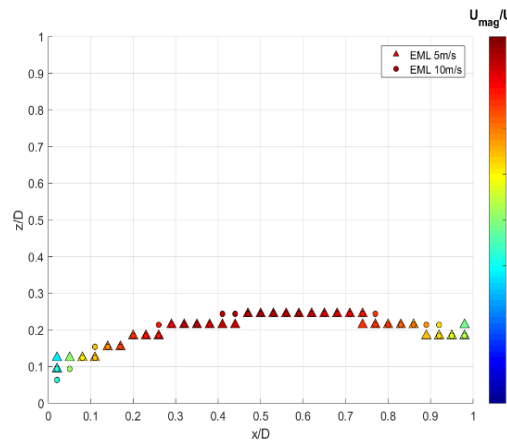


Figure 5.23 PIV measurements of the magnitude of flow velocity at the maximum elevation positions, in the central ($y/D = 0$) stream-wise section, for the inverted conical gauge at wind speed of 5 and 10 m s^{-1} .

In this section three drops, which in undisturbed conditions should hit the downwind part of the gauge collector but are deviated by the aerodynamic response of the gauge, are shown and compared. Furthermore, their disturbed trajectories are commented in relation with the PIV velocity field just described above. The compared drop trajectories were chosen by minimizing the relative differences between the respective starting positions and the free-stream airflow velocity. These information are listed in Table 5.6. The parameters of the best-fit curves, which describe the trajectories of the droplets, and the associated correlation factors (R^2) are listed in Table 5.7.

Table 5.6 Starting position, wind speed and identification codes for the three analyzed drop trajectories and the associated gauge geometry

Gauge shape and diameter D [m]	ID	Wind [m s^{-1}]	x/D	z/D
Cylindrical, D = 0.160	L31	12.10	-1.3806	-0.26418
Chimney, D = 0.160	G11	11.40	-1.31926	-0.29778
Inverted conical, D = 0.252	S83	11.16	-0.79748	-0.27044

Table 5.7 Parameters of the linear regression (m and q) for the undisturbed trajectories and of the third order polynomial for the disturbed ones (a, b, c and d), with the associated correlation factor

ID	m	q	R2	a	b	c	D	R2
L31	0.1411	-0.0711	0.997	0.0293	0.0223	0.1133	-0.0921	0.9981
G11	0.1733	-0.0681	0.9985	0.0263	0.0138	0.1301	-0.0995	0.9998
S83	0.1991	-0.111	0.9965	0.0504	0.0100	0.1495	-0.1329	0.9999

Figure 5.24 and Figure 5.25 reports the observed drop trajectories which travel above the collector of the cylindrical and chimney shaped gauges, respectively. In Figure 5.26 and Figure 5.27 their slopes are compared with the undisturbed ones. When the drops approach the gauge collector they deviate from the undisturbed trajectory and their slope decreases. In both cases, the drops fall outside instead of inside of the collector, therefore highlighting the very nature of the wind-induced undercatch affecting precipitation measurements.

The collectors of the cylindrical and chimney shaped gauges have the same dimensions, while the collector of the inverted conical shape gauge is larger. The injection system was maintained at a fixed distance from the center of the gauge collector, therefore the droplets were released closer to the gauge with inverted conical shape than for the other two gauges. In Figure 5.28 a drop trajectory travelling above the inverted conical gauge is depicted. The effect of the comparability between the airflow updraft and downdraft for the gauge with inverted conical shape, discussed above, can be observed here by noting that the deviation of the drop trajectory is almost totally bounded within the region delimited by the projection of the collector edges ($x/D = \pm 0.5$, Figure 5.29). Consistently with the PIV velocity field, the slope of the trajectory in the downwind part of the collector, for the cylindrical gauge increases faster than for the chimney shaped gauge (see Figure 5.30). Moreover, the wind speed for the trajectory that travels above the

collector of the chimney shaped gauge ($U_{ref} = 11.4 \text{ m s}^{-1}$) is lower than for the trajectory captured above the cylindrical gauge ($U_{ref} = 12.1 \text{ m s}^{-1}$). These results confirm that the aerodynamic response of the chimney shaped gauge is the most negatively impactful on the collection performance of the gauge (yielding a larger undercatch).

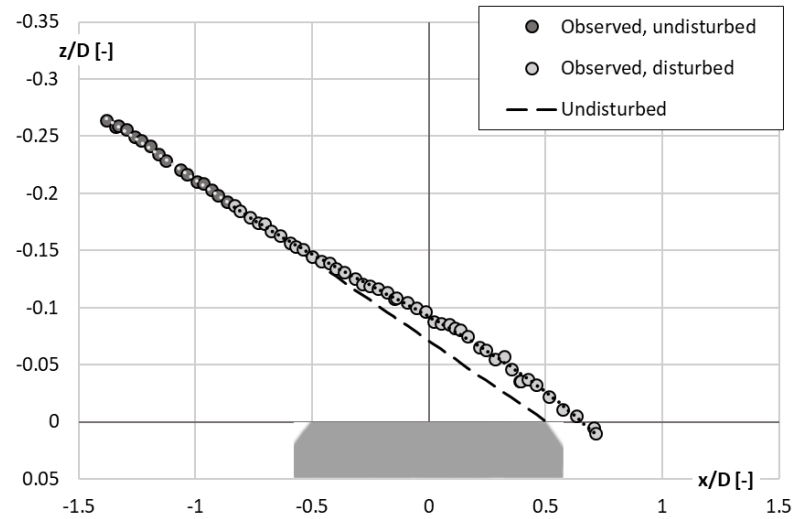


Figure 5.24 Observed drop trajectory (circles), and undisturbed one (dashed line) that travels above the collector of the gauge with cylindrical shape for the wind speed of 12.1 m s^{-1} .

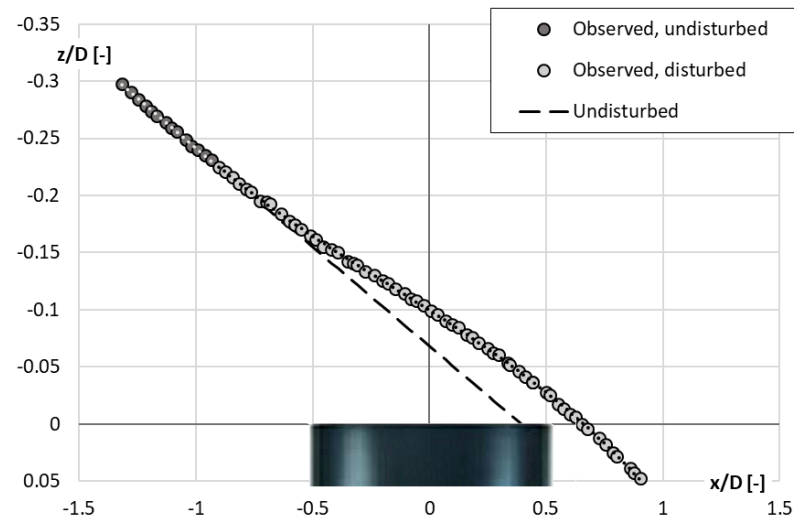


Figure 5.25 Observed drop trajectory (circles) and undisturbed one (dashed line) that travels above the collector of the gauge with chimney shape for the wind speed of 11.4 m s^{-1} .

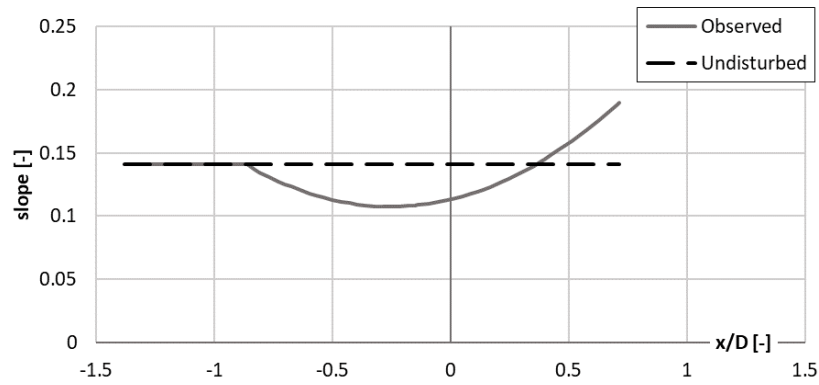


Figure 5.26 Observed (continuous line) and undisturbed (dashed line) slope of the drop trajectory that travels above the collector of the gauge with cylindrical shape for the wind speed of 12.1 m s^{-1} .

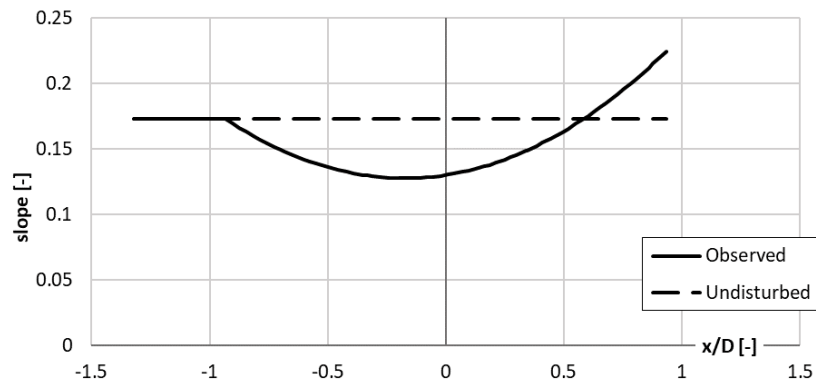


Figure 5.27 Observed (continuous line) and undisturbed (dashed line) slope of the drop trajectory that travels above the collector of the gauge with chimney shape for the wind speed of 11.4 m s^{-1} .

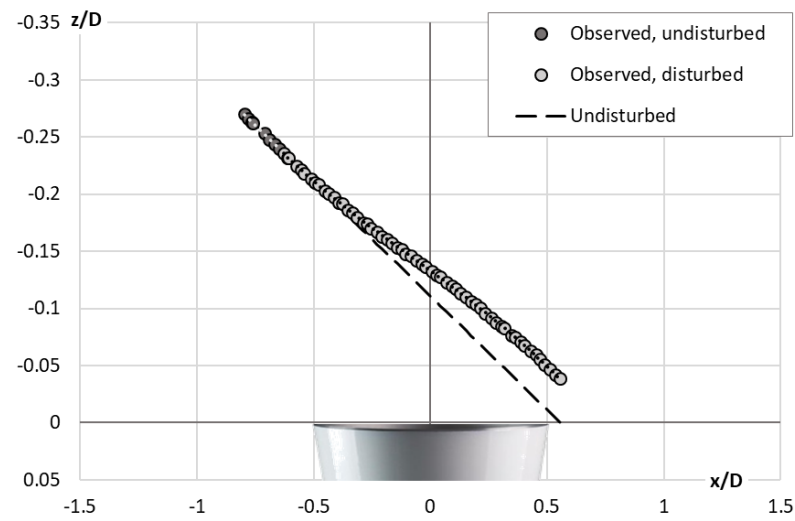


Figure 5.28 Observed drop trajectory (circles) and undisturbed one (dashed line) that travels above the collector of the gauge with inverted conical shape for the wind speed of 11.16 m s^{-1} .

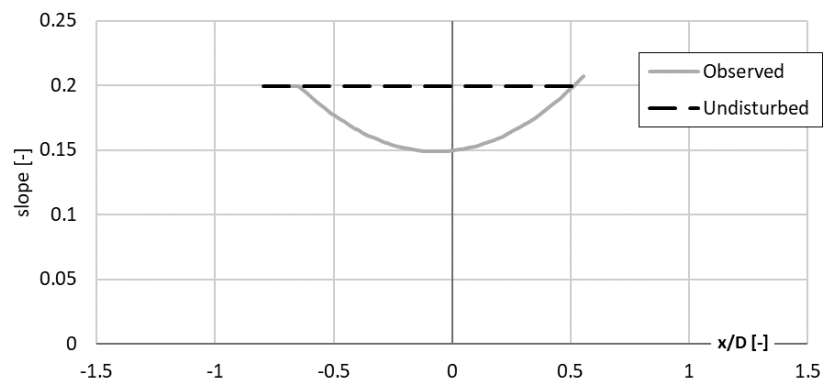


Figure 5.29 Observed (continuous line) and undisturbed (dashed line) slope of the drop trajectory that travels above the collector of the gauge with inverted conical shape for the wind speed of 11.16 m s^{-1} .

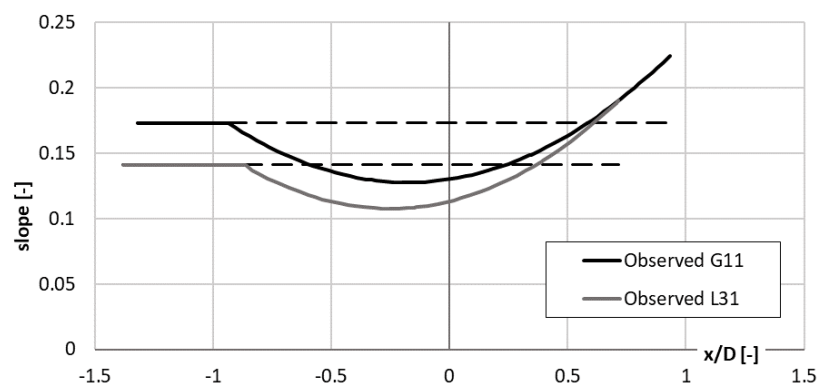


Figure 5.30 Comparison between the slope curves for the two gauges with cylindrical and chimney shape and the same size of the collector.

5.3.5. Comparison of measured and simulated particle trajectories

The validation of the Particles Tracking model was obtained by comparison between observed and simulated trajectories. In the numerical model the initial conditions, position and velocity, of the simulated trajectories are set consistently with the wind tunnel observations. The initial velocity components are set equal to the mean values of the three to five initial positions of each drop as shot by the camera, so as to avoid the noise due to the uncertainty in the initial positions.

The following figures show observed and simulated drop trajectories, together with specific characteristic (e.g. slope and acceleration), captured in the wind tunnel above the collector of a chimney shaped gauge at a wind speed $U_{ref} = 10.2 \text{ m s}^{-1}$ and simulated by means of the Lagrangian Particle Tracking model (described above) after imposing the same initial conditions.

In Figure 5.31 the two observed drop trajectories are identified with the codes G3 and G6. The initial elevation (z/D) of the two droplets is not much different. As expected, the slope curves reveal that the trajectory G6, which travels closer to the gauge body, is deviated earlier from its undisturbed condition. Observing the undisturbed slopes, which are characterized by a constant value and depend on the wind speed and the drops size but are independent from the aerodynamic response of the gauge, it is possible to affirm that the two droplets have the same size. This assumption is confirmed by the obtained numerical trajectories because the optimal agreement between the observed and simulated trajectories is reached by setting the drop diameter equal to one millimeter for both G3 and G6 (see Figure 5.32). The initial conditions of each drop, used to run the numerical model, are listed in Table 5.8. The observed and simulated trajectories are not totally overlapped close to the downwind edge of the collector. This effect is probably ascribable to the installation of the gauge in the wind tunnel, where a slight inclination was observed due to the push load induced by the wind on the gauge body.

In Figure 5.33 the observed drop trajectory (left-hand axis), identified with the code G2, is depicted with the associated slope (right-hand axis). In this case, the drop was released at a higher elevation than the previous drops, therefore, the aerodynamic effect of the gauge is less sensitive to the non-perfect orthogonality of the installation and the observed and simulated trajectories (Figure 5.34) show a good overlap also in the second half part of the trajectory. The maximum difference between the vertical positions (z in mm) of the observed and simulated trajectories, computed at each normalized longitudinal (x/D) coordinate of the observed trajectory, arises at the upwind edge of the collector and is about 1.2 mm. This difference is fully comparable to the drop size, therefore is comparable with the uncertainty in the assessment of the drop position, identified as a bright moving object in each frame. The calculated horizontal acceleration of the drop, normalized with the one experienced in the initial undisturbed part of the trajectory, is also shown in Figure 5.34.

According to the PIV airflow velocity fields the drop significantly accelerates when travelling above the upwind part of the collector, where the airflow is indeed accelerated, until crossing the separation layer between the airflow recirculation and accelerated zones when it starts decelerating abruptly towards the downwind edge of the collector.

The good repeatability of the trajectories of very similar drops in the wind tunnel is shown in Figure 5.35, together with the calculated slope curves. By injecting drops of the same size in the wind tunnel the

observed trajectories are indeed very close to each other, and they experience the same deviation above the collector. The particle tracking model is able to replicate even the small variations due to slight differences in the initial conditions about the drop velocity (see Figure 5.36).

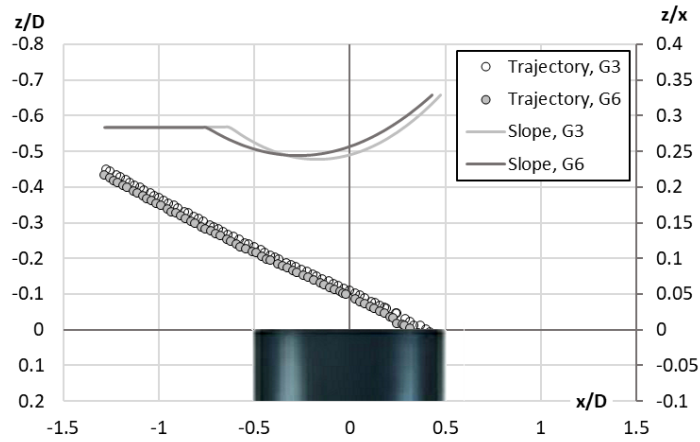


Figure 5.31 Observed drop trajectories (circles) and associated slope curves (continuous lines) above the collector of a chimney shaped gauge at a wind speed $U_{ref} = 10.2 \text{ m s}^{-1}$.

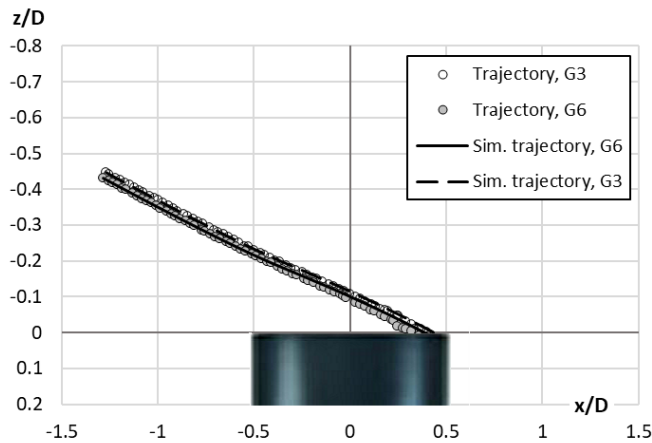


Figure 5.32 Observed (circles) and simulated (lines) drop trajectories above the collector of a chimney shaped gauge at a wind speed $U_{ref} = 10.2 \text{ m s}^{-1}$.

Table 5.8 Wind tunnel flow velocity, initial coordinates and velocity components for the simulated drop trajectories and the resulting drop diameter.

ID	Wind [m s^{-1}]	x/D	z/D	u [m s^{-1}]	w [m s^{-1}]	d [mm]
G3	10.2	-1.272	-0.447	3.968	-1.151	1
G6	10.2	-1.284	-0.433	3.809	-1.095	1

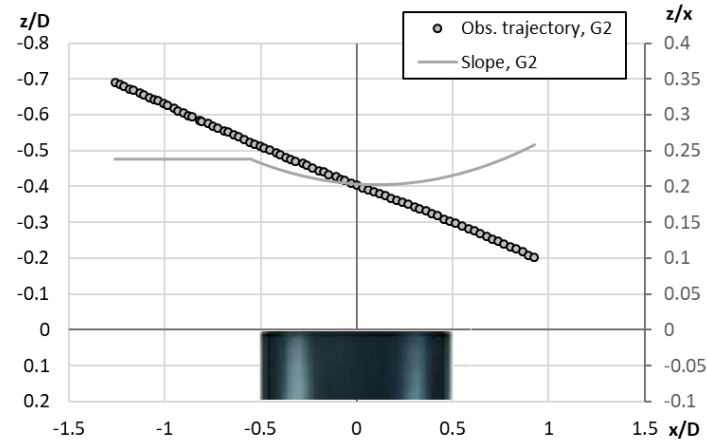


Figure 5.33 Observed drop trajectory (circles) and associated slope curve (continuous line) above the collector of a chimney shaped gauge at a wind speed $U_{ref} = 10.2 \text{ m s}^{-1}$.

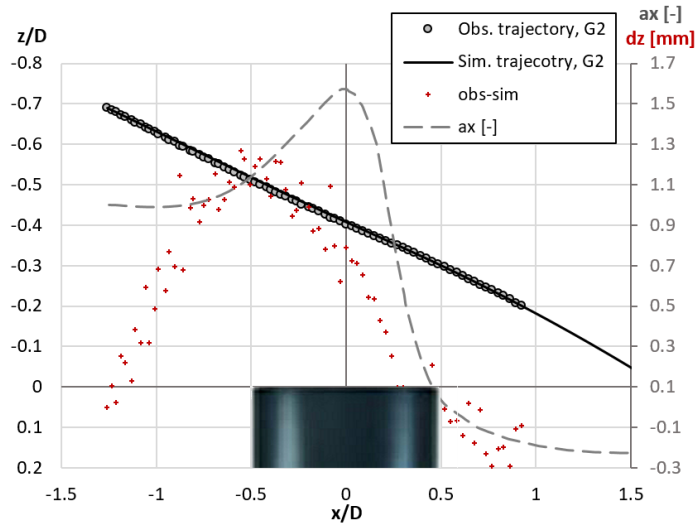


Figure 5.34 Observed (circles) and simulated (continuous line) drop trajectories above the collector of a chimney-shaped gauge at a wind speed $U_{ref} = 10.2 \text{ m s}^{-1}$. The difference dz (mm) between the observed and simulated vertical positions of the drop trajectories (red crosses) at each normalized observed longitudinal coordinate (x/D) is reported (scale on the right-hand axis), together with the numerical longitudinal acceleration (a_x) of the drop (dashed line).

Table 5.9 Wind tunnel flow velocity, initial coordinates and velocity components for the simulated drop trajectory and the resulting drop diameter.

ID	Wind [m s^{-1}]	x/D	z/D	u [m s^{-1}]	w [m s^{-1}]	d [mm]
G2	10.2	-1.259	-0.690	4.286	4.286	1.2

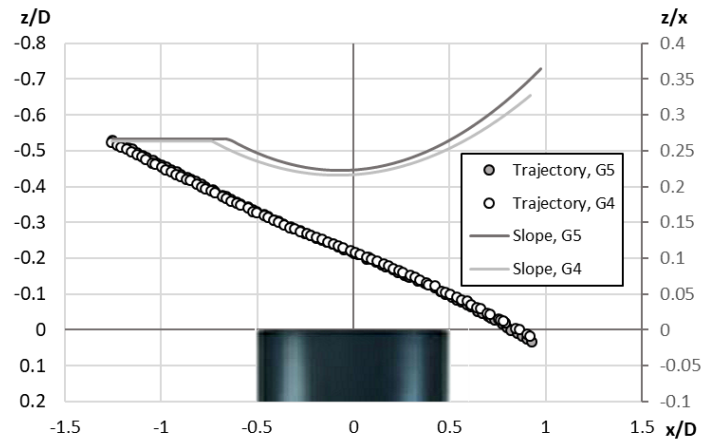


Figure 5.35 Observed drop trajectories (circles) and associated slope curves (continuous lines) for two similar drops travelling above the collector of a chimney shaped gauge at a wind speed $U_{ref} = 10.2 \text{ m s}^{-1}$.

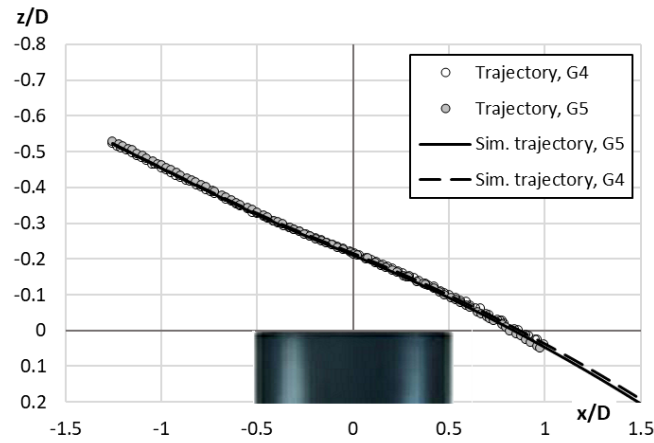


Figure 5.36 Observed (circles) and simulated (lines) trajectories of two similar drops travelling above the collector of a chimney shaped gauge at a wind speed $U_{ref} = 10.2 \text{ m s}^{-1}$.

Table 5.10 Wind tunnel flow velocity, initial coordinates and velocity components for the simulated drop trajectories and the resulting drop diameter.

ID	Wind [m s^{-1}]	x/D	z/D	u [m s^{-1}]	w [m s^{-1}]	d [mm]
G4	10.2	-1.257	-0.523	4.140	1.104	1
G5	10.2	-1.257	-0.523	4.122	1.122	1

A comparison of two simulated trajectories for the *Geonor*[®] gauge is shown in Figure 5.37, together with the observed ones. The difference between observed and simulated trajectories is comparable with the uncertainty in the assessment of the drop position, given the dimension of the drop and the image resolution.

Dashed lines represent the normalized numerical vertical acceleration of the drop along the trajectories calculated by the LPT model. The two drops accelerate when reaching the upwind edge due to the updraft and then decelerate due to the downdraft. This behavior is in line with the measured PIV velocity field, where from $x/D = -0.3$ the accelerated zone is always located above the normalized elevation equal to $z/D = 0.3$ and the two drops are fully immersed in the recirculation zone.

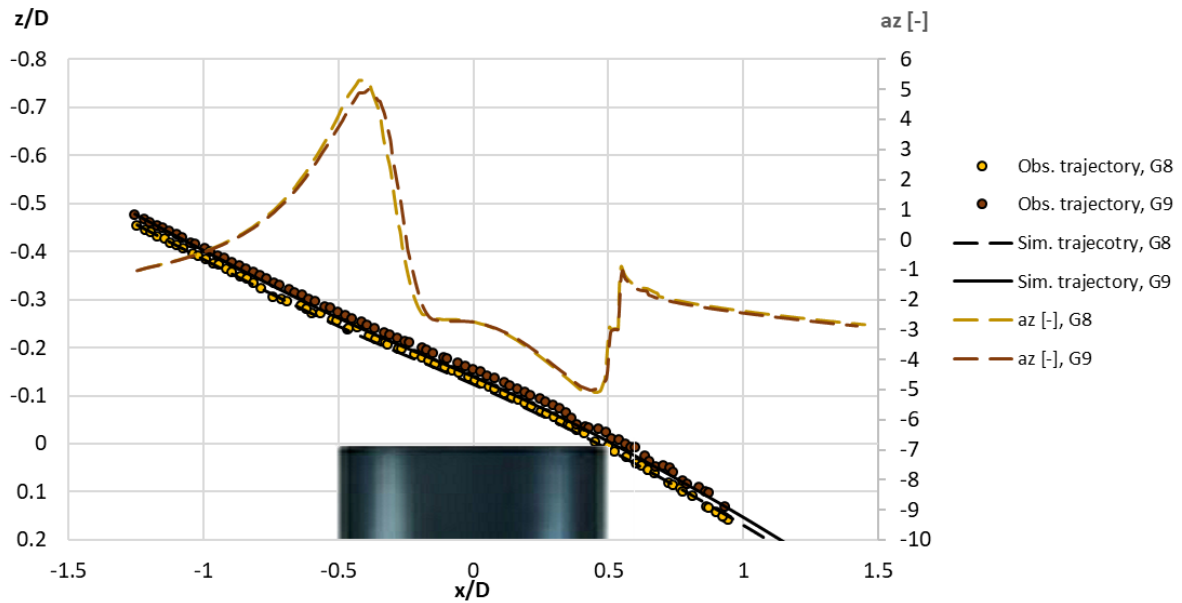


Figure 5.37 Comparison of two simulated trajectories, and the respective observed ones, for two drops travelling above the collector of the chimney shaped *Geonor*® gauge at a wind speed $U_{ref} = 10.2 \text{ m s}^{-1}$, together with the simulated profiles of their vertical acceleration (scale on the right-hand axis).

NUMERICAL COLLECTION EFFICIENCY

The Collection Efficiency is defined as the ratio between the precipitation collected by the gauge when impacted by wind in operational conditions and the ideal precipitation which would be collected in the absence of the aerodynamic response of the gauge.

Based on the airflow field obtained by means of CFD simulations (see Chapter 4) the number of particles for each diameter, $n(d)$, which fall inside the gauge collector in disturbed conditions due to the aerodynamic response of the gauge body could be calculated by means of the Lagrangian Particle Tracking (LPT) model (see chapter 5). After the introduction of the Particle Size Distribution (PSD) the integral on the range of diameters provides the numerical Collection Efficiency CE, expressed as:

$$CE(U_{ref}) = \frac{\int_0^d \rho_p V_p n(d) N(d) dd}{\int_0^d \rho_p V_p n_{max}(d) N(d) dd} \quad (6.1)$$

where ρ_p and V_p are the density and volume of the rain drops modelled with spherical shape, $n_{max}(d)$ is the number of particles which should fall inside the gauge collector if the airflow field was not affected by the aerodynamic response of the gauge body and $N(d)$ is the total number of particles per unit volume of air and per unit size interval having volume equal to the sphere of diameter d (see section 6.1 below).

The catch ratio, r , as a function of the particle size (d) and wind speed (U_{ref}), is defined as the ratio between the number of particles, which are captured by the gauge collector in disturbed airflow conditions, $n(d)$, and the maximum number of particles, $n_{max}(d)$, captured in undisturbed conditions.

In this chapter the collection efficiency curves are derived for two sample measurement instruments. The first one is best suited for rainfall measurements and is characterised by the common cylindrical shape of traditional catching type gauges, therefore a numerical formulation of the CE curves as a function of rainfall intensity is proposed. The second one is best suited for snowfall measurements and is characterised by an innovative measuring principle implying a dedicated geometry of the sensor. In this case, the numerically derived CE curves are expressed as a function of snowfall intensity.

6.1. PARTICLE SIZE DISTRIBUTION

The Particle Size Distribution (PSD), usually indicated with $N(d)$ and expressed in $[L^{-3} L^{-1}]$, indicates the number of particles (liquid or solid) per unit volume of air and unit size interval having a volume equal to the sphere of diameter d [L]. Usually the PSDs are depicted in a $(d, N(d))$ semi-logarithmic plot. A universal formulation for the PSD is not available, since it is influenced by the regional and seasonal climatology governing the formation of hydrometeors in the atmosphere. Moreover, information about the PSD comes from observations, which are affected by the limitation of disdrometers to detect small size particles, especially when $d < 1$ mm (Caracciolo et al. 2008). Physical properties of solid and liquid particles were derived in the past by employing raindrop spectrometers or radar sensors (e.g. Waldvogel, 1974), while disdrometers are currently used to observe the size distribution characteristics of the precipitation process (e.g. Caracciolo et al., 2008).

Two formulations for the PSD are commonly used in the literature: the Exponential (Marshall and Palmer, 1948) – hereinafter MP – and the Gamma (Ulbrich, 1983) distributions. Marshall and Palmer (1948), by fitting experimental observations, provided the exponential form of the PSD as follows:

$$N(d) = N_0 e^{-\Lambda d} [\text{mm}^{-1} \text{m}^{-3}] \quad (6.2)$$

where N_0 and Λ are two suitable parameters, with N_0 $[\text{mm}^{-1} \text{m}^{-3}]$ the intercept and Λ the slope of the linear form of this curve in a semi-log plot.

Marshall and Palmer, for a widespread mid-latitude rain, found a constant value for N_0 (Eq.6.3) and a relationship for Λ as a function of the rainfall intensity (RI $[\text{mm h}^{-1}]$), as reported in Eq.6.4.,

$$N_0 = 8 \cdot 10^3 [\text{mm}^{-1} \text{m}^{-3}] \quad (6.3)$$

$$\Lambda = 41 RI^{-0.21} [\text{cm}^{-1}] \quad (6.4)$$

In the work of Gunn and Marshall (1958), based on field experiments, the two parameters of the MP distribution for solid precipitation are expressed as a function of the snowfall intensity (SI $[\text{mm h}^{-1}]$) as follows:

$$N_0 = 3.8 \cdot 10^3 SI^{-0.87} [\text{mm}^{-1} \text{m}^{-3}] \quad (6.5)$$

$$\Lambda = 25.5 SI^{-0.48} [\text{cm}^{-1}] \quad (6.6)$$

By assuming a constant value for the slope parameter, for example 16.5 cm^{-1} , Eq. 6.4 and Eq. 6.6 provide precipitation intensity values equal to 100 and 2.5 mm h^{-1} for liquid and solid precipitation, respectively. The authors also elaborated a formulation for the mass of snow per unit volume of air (M) as shown in Figure 6.1. where it is compared the Marshall and Palmer (1948) distribution proposed for rain.

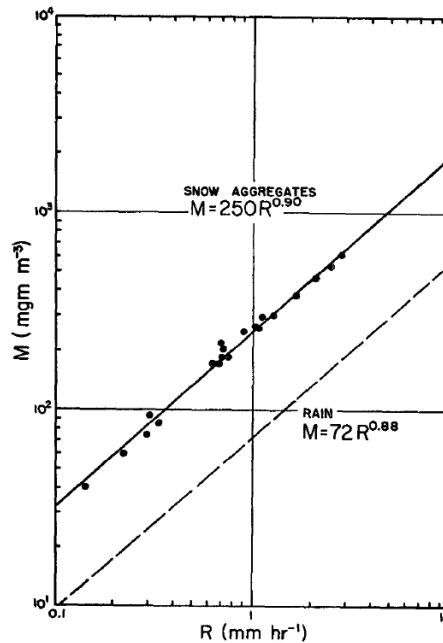


Figure 6.1 Mass of precipitation per unit volume of air (M , [mgm m^{-3}]) as a function of the precipitation intensity (R , [mm h^{-1}]) for snow and rain in a log-log plot (from Gunn and Marshall, 1958). Dots indicate experimental data obtained by Gunn and Marshall (1958) with the associated best fit curve (continuous line), while the dashed line is the formulation proposed by Marshall and Palmer (1948) for rain.

Waldvogel A. (1974), by measuring the distribution of raindrops with an electromechanical spectrometer and by means of a radar reflectivity analysis, for different type of precipitation (showers, thunderstorms and widespread rain), showed that the parameter N_0 is not at all constant and changes abruptly. He called this phenomenon “*The N_0 jump*”. Radar measurements indicated that the N_0 jump occurred when one of the mesoscale convective areas moved in or out the region above the station, which means that the situation changed from uniform (widespread rain) to convective (shower or thunderstorm) or vice versa.

For very small drop diameters (below 1 mm) the $N(d)$ values decrease with decreasing particle diameter, therefore, a downward concavity of the PSD is obtained. Currently, it is not clear whether this characteristic is ascribable to the limitation of the measuring instruments to detect very small particles or it is physically based. Moreover, some disdrometers, especially radars, provide higher $N(d)$ values for small diameters causing an upward concavity in the distribution. Ulbrich (1983) proposed the Gamma distribution in the form:

$$N(D) = N_0 D^\mu e^{-\lambda D} \quad [\text{mm}^{-1} \text{m}^{-3}] \quad (6.7)$$

where the exponent μ is the shape parameter and can have positive or negative values and the intercept N_0 is in $[\text{mm}^{-1-\mu} \text{ m}^{-3}]$.

Ulbrich summarized experimental observations reported by other authors including Mueller (1965), Caton (1966) and Blanchard (1953). In the work of Mueller, a variety of rainfall types including continuous rain, showers and thunderstorms were observed and for all of them the observed PSDs are concave downward. When fitted with the gamma formulation these PSDs would have $\mu > 0$. Almost all Caton's PSDs are similar to those reported by Mueller, and can be described by a Gamma distribution with $\mu > 0$. Differently, orographic precipitation was observed by Blanchard, which is characterized by a large number of small size drops. Such precipitation events can be described by a Gamma distribution with $\mu < 0$. In addition, Ulbrich conducted a theoretical analysis with the aim of describing the modification of the distribution from the exponential form to a concave shape. The author affirmed that the variation in N_0 is independent from the variation of Λ while a direct relationship between N_0 and μ exists in the form:

$$N_0 = 6 * 10^4 e^{3.2\mu} [\text{cm}^{-1-\mu} \text{ m}^{-3}] \quad (6.8)$$

Caracciolo et al. (2006) provided a discrimination algorithm to classify precipitation in convective or stratiform classes based on a large dataset covering about 3 years of observations (2001–2004) for about 1900 minutes of rain, collected in Ferrara (northern Italy) using a Joss-Waldvogel (JW) disdrometer and supported by radar measurements.

First, both precipitation intensity and radar reflectivity were used for the classification into convective and stratiform precipitation as reported below:

$R < 10 \text{ mm h}^{-1}$ and $Z < 38 \text{ dBZ}$	stratiform;
$R < 10 \text{ mm h}^{-1}$ and $Z > 38 \text{ dBZ}$	convective;
$R > 10 \text{ mm h}^{-1}$	convective;

Then, based on the PSD parameters the so-called *peak* (or *modal*) diameter D_p was defined as:

$$D_p = \mu/\Lambda [\text{mm}] \quad (6.9)$$

Using this criterion, the stratiform spectra are characterized by lower D_p values with respect to the convective ones and the threshold between the two precipitation types is defined by:

$$1.635\Lambda - \mu = 1 \quad (6.10)$$

The work of Caracciolo et al. (2008) is based on rain events measured in the Italian territory by employing radar and two different types of disdrometers (JW and Pludix) with a sampling time of one minute. Each 1-minute PSD value was classified into one out of six categories, based on the measured

precipitation intensity (RI). Two examples of the average observed PSD for the Florence database obtained by JW and Pludix disdrometers are reported in Figure 6.2, where the minimum diameter observed by Pludix is 1 mm while the JW also reports data for $d < 1$ mm.

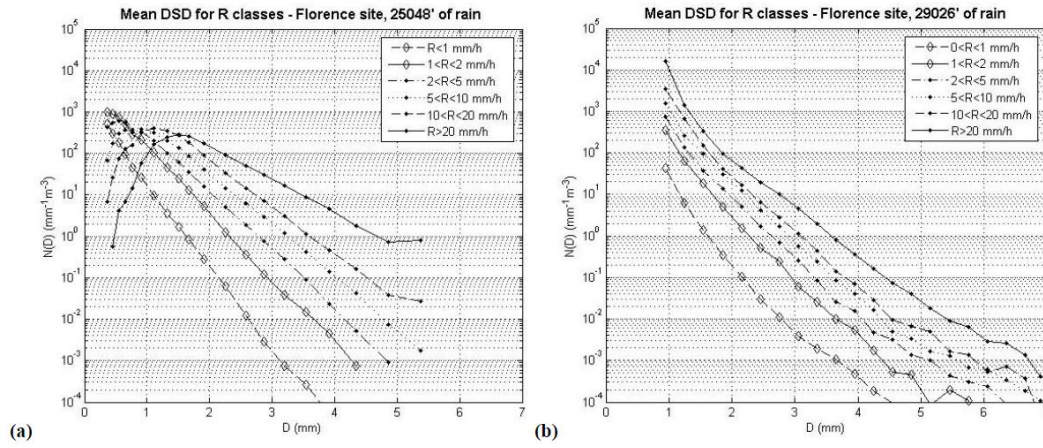


Figure 6.2 Average observed PSDs for the Florence database: JW disdrometer (a) and Pludix disdrometer (b), for six rainfall rate categories as reported by Caracciolo et al. (2008).

Both the exponential and Gamma formulations were used by the authors to provide new discrimination criteria between convective and stratiform precipitation according to radar reflectivity measurements. Using the JW data a convective/stratiform discrimination criterion, which takes into account also shallow convective and heavy stratiform rain was developed:

If	$RI < 10 \text{ mm h}^{-1}$	and	$Z < 38 \text{ dBZ}$	stratiform;
If	$RI > 10 \text{ mm h}^{-1}$	and	$Z < 38 \text{ dBZ}$	heavy stratiform;
If	$RI \geq 10 \text{ mm h}^{-1}$	and	$Z \geq 38 \text{ dBZ}$	convective;
If	$RI < 10 \text{ mm h}^{-1}$	and	$Z > 38 \text{ dBZ}$	shallow convective.

From these classes a new discrimination line in the (Λ, μ) diagram was identified:

$$1.635\Lambda - \mu = 2 \quad (6.11)$$

By analysing the Pludix exponential PSD parameters, the shallow convective and heavy stratiform precipitation, characterized by RI between 2 and 10 mm h^{-1} , fall in the middle between the stratiform ($RI < 2 \text{ mm h}^{-1}$) and convective ($RI > 10 \text{ mm h}^{-1}$) categories and the threshold in the $(\log N_0, \Lambda)$ can be expressed by:

$$\Lambda + 4.17 = 1.92 \log N_0 \quad (6.12)$$

The LPT model, adopted to calculate the CE, is a one-way coupled model. After introducing the particle size distribution, it is possible to justify this simplification by calculating the volume occupied by rainfall in one cubic meter of air, called the *volume concentration*. This quantity is expressed by the following integral:

$$\int_0^d V_p N(d) dd \quad (6.13)$$

where V_p is the particle volume. For instance, the maximum volume concentration occupied by the precipitation observed by Caracciolo et al. (2008) – associated with the maximum RI range ($RI > 20 \text{ mm h}^{-1}$ with $N_0 = 18370 \text{ mm h}^{-1} \text{ m}^{-3}$ and $A = 2.609 \text{ mm}^{-1}$, see below Table 6.2) – is 0.105×10^{-6} .

6.2. PARAMETERIZATION OF THE CE CURVES AS A FUNCTION OF RAINFALL INTENSITY

Currently, in operational practice, e.g. by National Weather Services, adjustment curves to account for wind-induced biases are rarely adopted. In this section a CE formulation as a function of wind speed (U_{ref}) and parameterized with the Rainfall Intensity (RI) is derived for a typical cylindrical gauge. An easy to use adjustment curve, as a function of the rainfall intensity measured by the gauge (RI_{meas}) and wind speed is formulated.

The airflow fields (velocity magnitude and components) around a cylindrical gauge, the *Casella*® tipping-bucket gauge (see Figure 6.3), obtained by means of RANS simulations for various wind speeds ($U_{ref} = 2-5-7-10-18 \text{ m s}^{-1}$) and partially published in the work of Colli et al. (2018), were adopted. Starting from these simulations the Lagrangian Particle Tracking model (see chapter 5) allowed the catch ratios to be obtained for drops with equivalent diameter equal to $d = 0.25 - 0.5 - 0.75 \text{ mm}$ and from 1 to 8 mm, with bin size of 1mm.



Figure 6.3 The *Casella*® tipping-bucket rain gauge with cylindrical shape.

Results are summarized and shown in Table 6.1 and Figure 6.4 where the catch ratios of each drop size and wind speed are compared. For drop size less than 1 mm the catch ratio increases with decreasing the wind speed. For larger drops it is possible to observe that the trend is not always growing but increases and then decreases with increasing wind speed. This behavior is intrinsic in the balance between the drop size and the wind speed.

To explain this concept Figure 6.5 was prepared; in the picture the spatial grid used in the LPT model to release drops in the airflow field is reported. The grid was located upstream of the gauge and at a higher elevation compared with the z-coordinate of the collector, depending on the wind speed and drop diameter. The proper location was preliminarily calculated to ensure that the released drops fall in the region occupied by the gauge. This was obtained by computing backward the trajectory of a single drop which reaches the center of the gauge collector in undisturbed airflow conditions.

The black circles depicted in Figure 6.5 represent the projection of the collector's rim on the drop releasing grid, and contain the starting positions of those particles that in undisturbed conditions would enter the gauge collector. The initial positions of all drops that in real conditions are expected to fall inside the gauge collector and are actually collected are depicted in red, while those falling inside the gauge collector but are expected to fall outside are depicted in green.

In the case illustrated in the left-hand panel of Figure 6.5, corresponding to a low wind and/or heavy particles situation, every drop that is expected to fall inside the collector in undisturbed conditions also reaches the collector in the disturbed ones. A few additional drops, whose releasing positions are depicted

in green, also enter the collector while expected to fall outside. This implies an overestimation of the precipitation collected by the gauge and therefore the resulting catch ratio is larger than one. By increasing the wind speed or reducing the drop size, the wind field deformation reduces the number of particles depicted with red dots, and slightly increases the green ones (right-hand panel of Figure 6.5). In this sample case, the sum of the red and green dots is lower than the number of particles confined inside the black circle, yielding an overall underestimation of the number of particles collected and $r < 1$.

Table 6.1 Catch ratios for each drop size and at different wind speeds, calculated by means of the LPT model and based on the RANS airflow fields for the *Casella*® precipitation gauge.

d [mm] U_{ref} [m s ⁻¹]	0.25	0.5	0.75	1	2	3	4	5	6	7	8
2	0.791	0.983	1.010	1.019	1.017	1.010	1.010	1.010	1.010	1.010	1.010
5	0.356	0.927	0.977	1.006	1.023	1.021	1.017	1.014	1.010	1.010	1.010
7	0.110	0.803	0.938	0.981	1.010	1.021	1.021	1.021	1.017	1.017	1.017
10	0.085	0.752	0.927	0.963	1.006	1.017	1.021	1.021	1.021	1.017	1.013
18	0.015	0.660	0.868	0.938	0.992	1.006	1.014	1.017	1.021	1.021	1.021

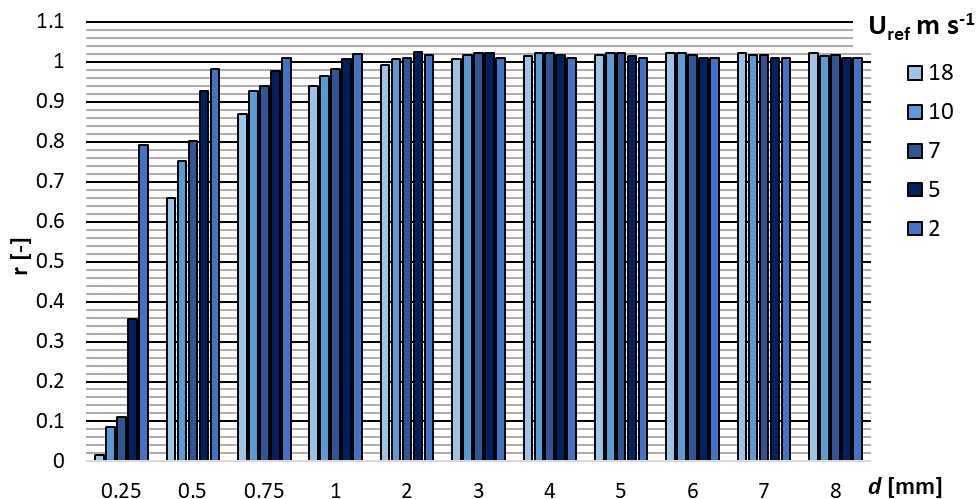


Figure 6.4 Comparison between catch ratios, for each drop size obtained for different wind speeds, calculated by means of the LPT model and based on the RANS airflow fields for the *Casella*® cylindrical gauge.

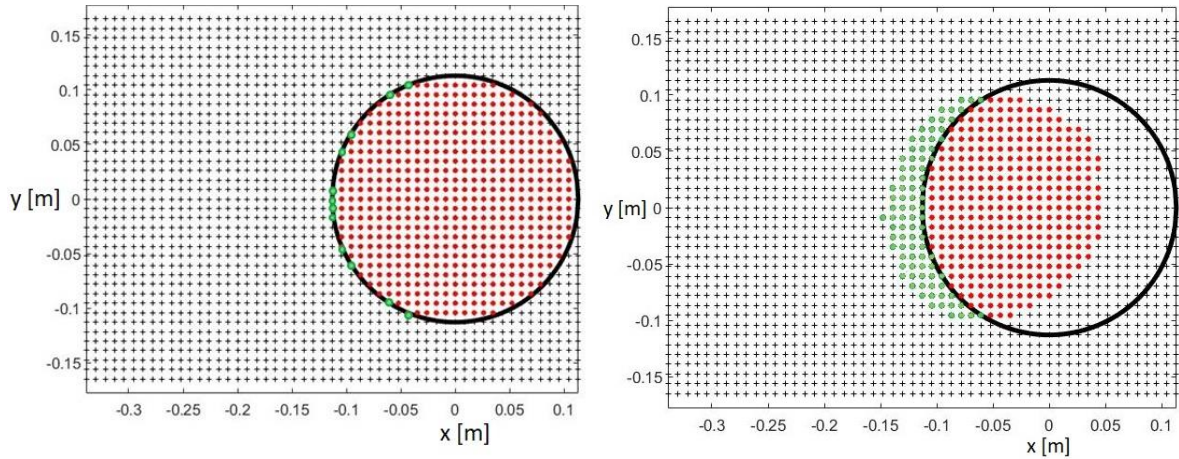


Figure 6.5 Schematics of the initial positions of the modelled trajectories, color coded according to their final destination, and projection of the collector's rim (black circles). Red dots indicate drops that actually fall inside the gauge collector in real conditions and that were expected to do so, while green dots indicate those falling inside the gauge collector instead of outside.

The collection efficiency curve was derived by assuming that the microphysical characteristics of precipitation are those obtained for the Italian territory and fitted by the typical exponential function (MP distribution). To obtain this result three steps were followed, as summarized below:

- the PSD data were fitted with the MP distribution and the associated parameters N_0 and A , per each RI class, were adopted to calculate the CE values, (here called raw CE values). The CE curves as a function of wind speed (U_{ref}), for each RI class, were obtained from the raw values by fitting a four parameter sigmoidal function ($CE = f(U_{ref})$ – see Eq. 6.14).
- The parameters N_0 and A obtained in a), attributed to the mean value of each RI class, were fitted with power law curves as a function of RI , and the new CE sigmoidal curves were obtained from the fitted parameters. The definition of N_0 and A as a function of RI has the advantage of obtaining the MP parameters for each RI value, within the range investigated. After calculating the CE values for the associated RI and wind speed, the CE curves could be obtained again as a sigmoidal best-fit.
- Finally, with the objective of obtaining a simple formulation for the CE as a function of both RI and U_{ref} in the investigated ranges, also the four parameters of the sigmoidal function were calculated as a function of RI .

The above summarized procedure is applied below to real-world observations. The average observed PSD measured by the Pludix disdrometer in the Florence experimental site as provided by Caracciolo et al. (2008) (Figure 6.2 right), classified for six rainfall intensity categories, were adopted here and fitted using the typical MP exponential function, as shown in Figure 6.6. The MP parameters N_0 [$\text{mm}^{-1} \text{m}^{-3}$] and A [mm^{-1}], and the correlation factors (R^2) for each rainfall intensity class are listed in Table 6.2.

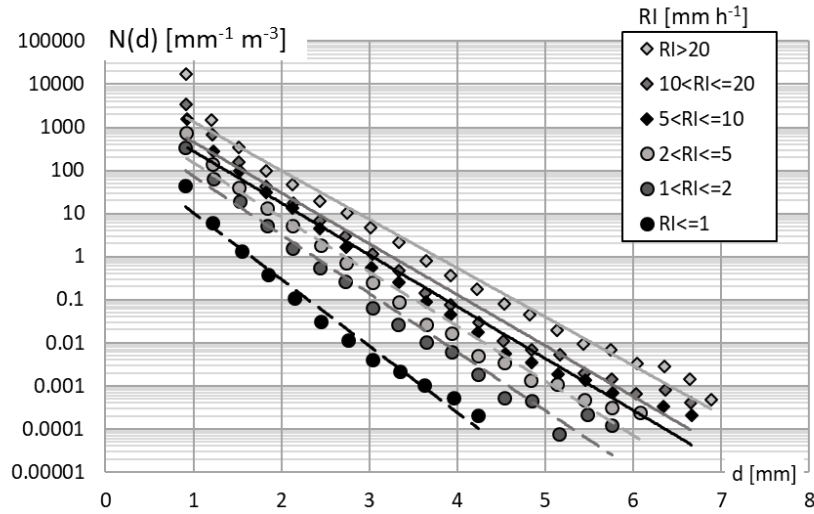


Figure 6.6 PSD data, for each rainfall intensity class, from Caracciolo et al. (2008) and the associated best-fit exponential functions suggested by Marshall and Palmer (1948)

Table 6.2 Parameters N_0 and Λ of the MP distribution and the correlation factors for each rainfall intensity class, obtained by fitting the PSD provided by Caracciolo et al. (2008).

	RI ≤ 1	1 < RI ≤ 2	2 ≤ RI < 5	5 ≤ RI < 10	10 ≤ RI < 20	RI > 20
	[mm h ⁻¹]	[mm h ⁻¹]	[mm h ⁻¹]	[mm h ⁻¹]	[mm h ⁻¹]	[mm h ⁻¹]
N_0 [mm h⁻¹ m⁻³]	365.1	1692.8	2775	4459	6989.4	18370
Λ [mm⁻¹]	3.561	3.134	2.914	2.771	2.723	2.609
R^2	0.979	0.976	0.979	0.975	0.972	0.979

As expected, the parameter Λ decreases, while N_0 increases, with increasing RI . This is due to the fact that heavy rainfall events are characterized by a relatively higher number of drops of large diameter in the distribution and by an overall higher number of particles in one cubic meter of air. Therefore, by increasing RI the slope of the distribution decreases and the curve is displaced upward. For all RI classes, the correlation factor is larger than 0.97, which indicates a very good fit between observations and the MP exponential curves.

Following step a), for each simulated wind speed (U_{ref}), the raw CE values were numerically calculated as reported in Eq. 6.1, by using for the PSD the best-fit MP parameters associated with each RI class (from Table 6.2). Then, the raw CE values were fitted with a four parameters sigmoidal curve (Eq. 6.14) as shown in Figure 6.7, with the obtained parameters' values listed in Table 6.3.

$$CE(U_{ref}) = y_0 + \frac{a}{1 + e^{-\frac{(U_{ref} - x_0)}{b}}} \quad (6.14)$$

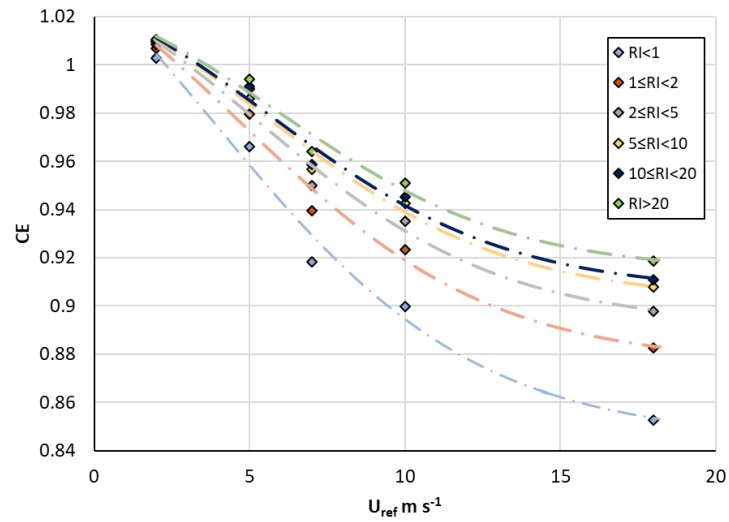


Figure 6.7 Raw CE values (diamonds) obtained by using the MP parameters derived from the MP exponential interpolation function, for each RI class, and the associated sigmoidal functions (lines-points).

Table 6.3 Parameters of the sigmoidal functions obtained by fitting the raw CE values derived by using the MP parameters from the exponential interpolations and correlation factors for each RI class.

	$RI \leq 1$ [mm h ⁻¹]	$1 \leq RI < 2$ [mm h ⁻¹]	$2 \leq RI < 5$ [mm h ⁻¹]	$5 \leq RI < 10$ [mm h ⁻¹]	$10 \leq RI < 20$ [mm h ⁻¹]	$RI > 20$ [mm h ⁻¹]
a	0.2632	-0.1995	0.1696	0.1513	0.1454	0.1317
b	-4.2495	4.067	-3.9526	-3.871	-3.8422	-3.7713
x₀	3.8429	4.7512	5.251	5.5914	5.709	5.996
y₀	0.8445	1.0753	0.892	0.9024	0.9058	0.914
R²	0.984	0.984	0.983	0.982	0.982	0.982

Following step b), with the objective to make explicit the dependence of the collection efficiency on the RI , the parameters N_0 and A were assigned to the mean value of each RI class and fitted with power law interpolation curves (Eq. 6.15).

$$Y(RI) = a_Y RI^{b_Y} \quad (6.15)$$

where Y assumes the nomenclature of the PSD intercept N_0 and slope A , while a_Y and b_Y are the associated parameters of the best-fit power law curves. The values of the power law parameters are listed in Table 6.4, together with the correlation factors for both N_0 and A .

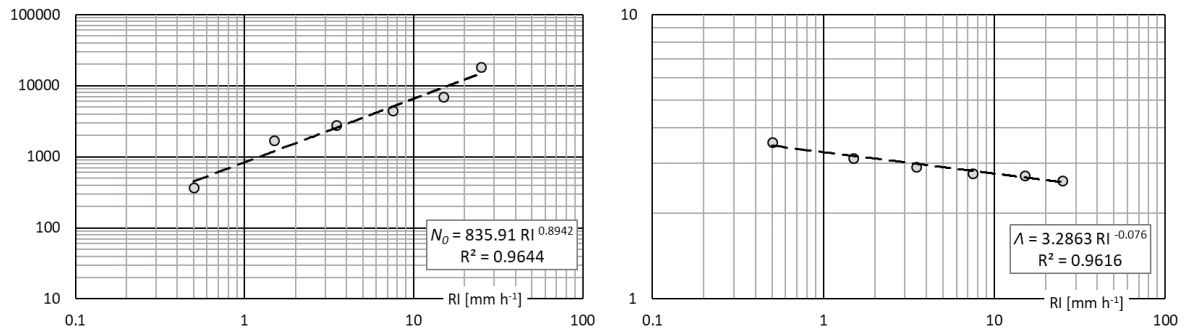


Figure 6.8 MP parameters (N_0 on the left and λ on the right) associated with the mean values of each RI class (circles) and fitted by power law curves (dashed lines).

Table 6.4 Parameters a_Y and b_Y of Eq. 6.15, for both N_0 and λ expressed as a function of RI and the associated correlation factors.

	N_0 [$\text{mm h}^{-1} \text{m}^{-3}$]	λ [mm^{-1}]
a_Y	835.91	3.2863
b_Y	0.8942	-0.076
R^2	0.964	0.962

Now, the CE values were calculated by adopting the N_0 and λ values provided by the power law curves (Figure 6.8 dashed lines). The best-fit sigmoidal functions provide the new parameters for the CE, as listed in Table 6.5. The new CE curves are depicted in Figure 6.10 (dashed lines) and compared with the raw CE values (diamond) calculated under step a). This further step provides an important advantage because it allows the PSD to be derived for any desired rainfall intensity within the measured RI range (0.5-25 mm h^{-1}).

Table 6.5 Parameters of the sigmoidal functions obtained by using $N_0(RI)$ and $\lambda(RI)$ expressed by the power law curves and correlation factors for each RI class.

	$RI \leq 1$ [mm h^{-1}]	$1 \leq RI < 2$ [mm h^{-1}]	$2 \leq RI < 5$ [mm h^{-1}]	$5 \leq RI < 10$ [mm h^{-1}]	$10 \leq RI < 20$ [mm h^{-1}]	$RI > 20$ [mm h^{-1}]
a	0.2481	0.2069	0.1794	0.1574	0.1395	0.1275
b	-.2127	-4.0923	-3.9925	-3.8994	-3.8128	-.7481
x_0	4.043	4.6353	5.0803	5.4739	5.8284	6.0888
y_0	0.8516	0.872	0.8866	0.8988	0.9093	0.9165
R^2	0.984	0.984	0.983	0.983	0.982	0.981

Finally, as summarized in step c), a general formulation for the CE (Eq. 6.16) as a function of both RI and U_{ref} , but independent on the initial RI classes and valid throughout the investigated RI range, was obtained by fitting the sigmoidal parameters associated with the mean value of each RI class with logarithmic (for b , x_0 , y_0) and power law (for the parameter a) curves. The general expression is as follows:

$$CE(U_{ref}) = y_0(RI) + \frac{a(RI)}{1 + e^{-\frac{(U_{ref}-x_0(RI))}{b(RI)}}} \quad (6.16)$$

The best-fit curves for each sigmoidal parameter are listed below and shown in Figure 6.9 with the associated correlation factors.

$$a = 0.2213 RI^{-0.17} \quad (6.17)$$

$$b = 0.1191 \ln(RI) - 4.1365 \quad (6.18)$$

$$x_0 = 0.5222 \ln(RI) + 4.4164 \quad (6.19)$$

$$y_0 = 0.0166 \ln(RI) + 0.8645 \quad (6.20)$$

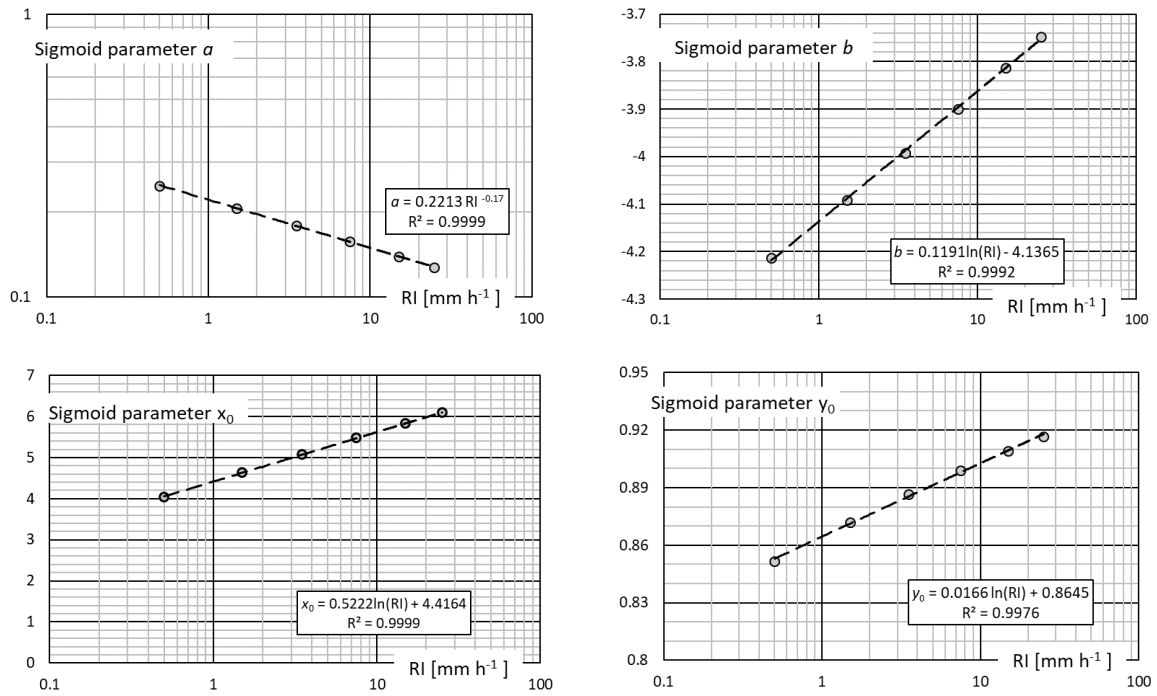


Figure 6.9 Sigmoidal parameters (a and b in the upper panels, x_0 and y_0 in the bottom panels), associated with the mean value of each RI class (circles) and fitted by either power law or logarithmic curves (dashed lines).

With the aim to verify the quality of this result the collection efficiency curves were calculated by using Eq. 6.16 for the mean value of each *RI* class (Figure 6.10 continuous lines) as already done in steps a) and b). Then, the correlation between the raw CE values and the CE curves obtained in the three steps (a), b) and c)) were compared. Figure 6.11 shows the correlation factors for each *RI* class and the partial step adopted (a), b) and c)). This result reveals that in all cases the correlation factors are very high, larger than 0.99, and for step a) is only slightly higher than step c) (about $+10^{-5}$). This very minimal worsening of performance is counterbalanced by the simplification introduced by the final CE curve, which allows a correction factor to be easily applied for the wind induced-error of operational precipitation measurements.

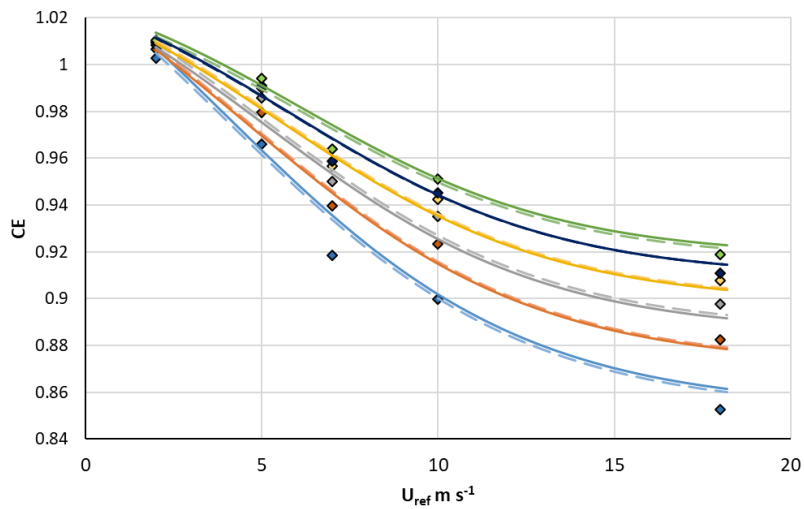


Figure 6.10 Raw CE values (diamonds) obtained by using the MP parameters derived from the exponential interpolation (step a)), for each *RI* class. CE curves obtained by expressing N_0 and Λ as a function of *RI* (dashed lines, step b)) and by expressing the sigmoidal parameters as a function of *RI* (continuous lines, step c)).

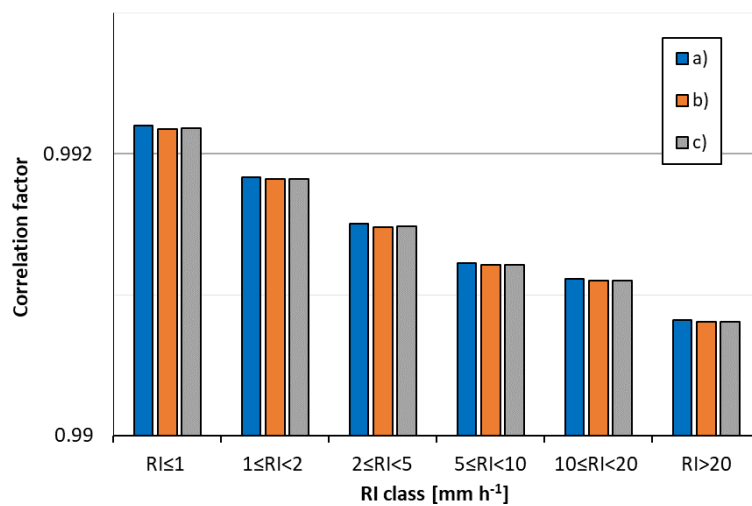


Figure 6.11 Correlation factors between the raw CE values and the CE curves obtained, for each *RI* class, under step a) (blue), b) (orange) and c) (grey).

The derived numerical CE curve is a function of the actual rainfall intensity that, in this case, was obtained from the PSD provided by Caracciolo et al. (2008). However, in operational practice, the only knowledge available for RI is that measured by the gauge and therefore affected by the wind-induced bias. In this work, the adjustment curve was therefore derived, for application purposes, as a direct relation between the reference rainfall intensity (RI) and the measured one (RI_{meas}), so that starting from the measurement provided by the gauge, the actual rainfall intensity (and the wind-induced bias) can be calculated once the wind velocity is known.

Remembering that in the field the CE is the ratio between the precipitation measured by the gauge (RI_{meas}) and the reference one (RI), it is possible to derive from Eq. 6.16 the RI_{meas} associated to each (U_{ref} , RI) couple within the investigated range. Results can be depicted in the (RI , RI_{meas}) plane for each wind speed, as shown in Figure 6.12. The RI_{meas} values calculated from Eq. 6.16 for the mean values of each RI class and the simulated wind speed are depicted with markers, while the associated adjustment curves were obtained as best-fit power law curves. The parameters of the adjustment curves for the simulated wind speed are summarized in Table 6.6, with a correlation factor (R^2) equal to one in all cases.

Table 6.6 Parameters (a and b) of the power law best-fit curves at different wind speeds (U_{ref})

	$U_{ref}=2$ [mm s ⁻¹]	$U_{ref}=5$ [mm s ⁻¹]	$U_{ref}=7$ [mm s ⁻¹]	$U_{ref}=10$ [mm s ⁻¹]	$U_{ref}=18$ [mm s ⁻¹]
a	1.0057	0.9668	0.9413	0.9099	0.8726
b	1.0023	1.0076	1.0106	1.0138	1.0175

In the graph, the diagonal (continuous black line) indicates $CE = 1$, while the grey dashed lines correspond to CE values from 0.95 to 0.99. As expected, the adjustment curve for $U_{ref} = 2 \text{ m s}^{-1}$ is located above the diagonal, due to the overcatch observed at this low wind speed, while the other curves are lower due to the wind-induced undercatch. Moreover, the adjustment curves are described by power law functions, with coefficients (see Table 6.6) that are increasingly different from one (the linear case when CE is constant) as the wind speed increases, reflecting the trend towards higher values of CE while increasing the rainfall intensity.

Although the deviation is small, it is possible to note in the graph that the adjustment curve at e.g. 18 m s^{-1} progressively diverges from the dashed line at $CE = 0.96$ with increasing the rainfall intensity (towards the right-hand side of the graph), while they are practically superimposed to each other at low RI (left-hand side of the graph). This means that, at any given wind speed, the collection efficiency varies with the rainfall intensity, rather than lying on a curve (line) at $CE = \text{constant}$, as expected.

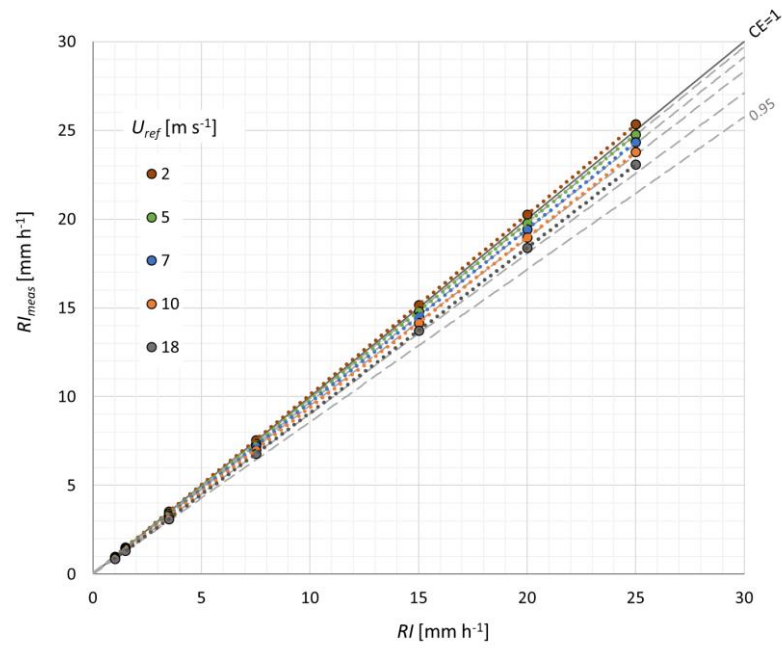


Figure 6.12 Adjustment curves (dotted lines) for the *Casella*® gauge and linear curves at constant CE values (dashed lines). Circles indicate the results of the performed numerical simulations and are colour coded according to the wind speed (U_{ref}).

6.3. COLLECTION EFFICIENCY CURVE FOR THE HOTPLATE® PRECIPITATION GAUGE

This section reports the catch ratios for snowflakes of equivalent diameter $d = 0.25 - 0.5 - 0.75$ mm and from 1 to 8 mm, with bin size of 1mm, computed from the airflow fields obtained by means of CFD simulations (see Chapter 4) for the *Hotplate*® snow gauge. Then the derived numerical collection efficiency curve and the associated adjustment curves are shown. The catch ratio and CE values were calculated, after having defined the parameters of the PSD, for each simulated wind speed (2, 5, 10, 15 and 20 m s⁻¹) and for intermediate wind speeds of 3.5, 7.5, 12.5 and 17.5 m s⁻¹ thanks to the good scalability of the airflow fields as demonstrated in Chapter 4.

Despite different gauge geometries existing, all traditional catching-type precipitation gauges have a funnel and the entire collecting area is located at a fixed elevation. This is not true for the *Hotplate*® precipitation gauge where the presence of the three concentric rings, fixed on the collecting heated plate, is responsible for a significant variation of the collecting area, which is not a simple projection of the plate surface. In the left-hand panel of Figure 6.13 it is possible to observe that a large number of snowflake trajectories, reaching the *Hotplate*® in the central vertical section, and simulated by imposing undisturbed airflow conditions are stopped by the obstruction due to the rings. The same result is shown in the right-hand panel by using the disturbed airflow field in the simulation of the solid particle trajectories. In both cases the wind speed is equal to 10 m s⁻¹. From the comparison, the deformation which affects the snowflake trajectories due to the aerodynamic response of the gauge is evident. Moreover, this result explains the effect of the rings on the collection performance of the gauge: the external ring, located on the edge of the gauge, blocks some trajectories which fall outside instead of inside the plate surface, and therefore are not measured. On the contrary, the internal rings block some trajectories that otherwise would be dragged beyond the gauge. The catch ratios in Figure 6.14 and listed in Table 6.7 were calculated by assuming undisturbed airflow conditions, and therefore by considering only the geometrical effect of the instrument due to presence of the rings, while the catch ratios of Figure 6.15 and listed in Table 6.8 take into account both the geometrical effect and the aerodynamic disturbance induced by the wind-gauge interaction. In the first case, the catch ratios for all particle diameters are equal or larger than one. In disturbed airflow conditions the catch ratios decrease, as is typical of the traditional catching type gauges, for wind speed from 2 to 5 m s⁻¹, then by increasing wind speed the catch ratio starts to increase and reaches the value $r = 1$ at $U_{ref} = 15$ m s⁻¹ for particle sizes larger than 1 mm. At high wind speed, the geometrical effect becomes predominant and is larger than one for all particle sizes.

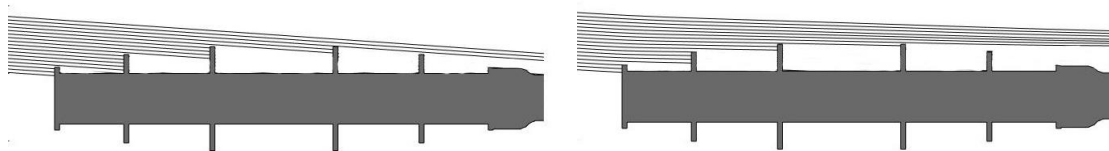


Figure 6.13 Simulated trajectories of solid particles ($d = 0.25$ mm and $U_{ref} = 10$ m s⁻¹) reaching the *Hotplate*® collecting area in undisturbed airflow conditions (left-hand panel) and in the disturbed ones (right-hand panel).

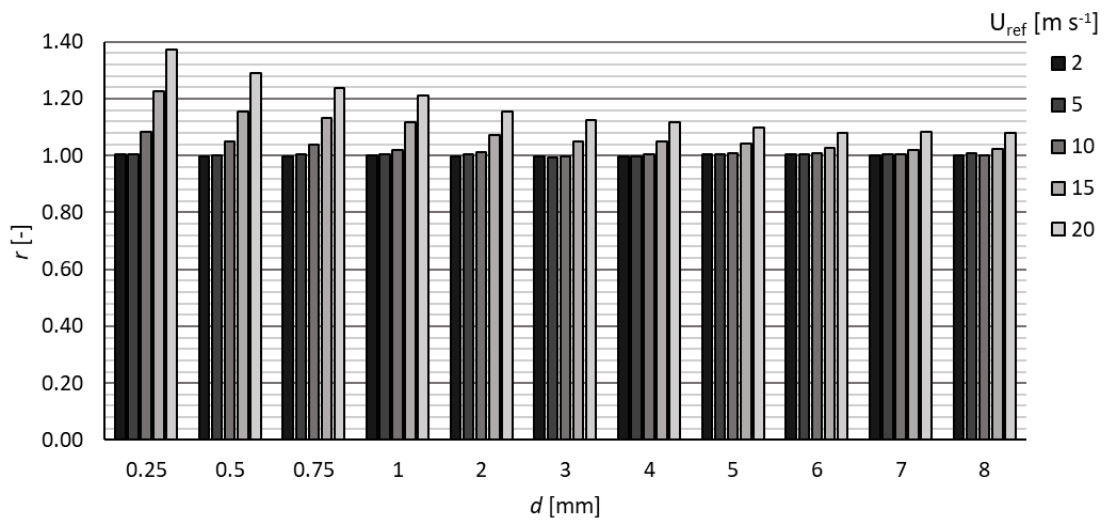


Figure 6.14 Comparison between the catch ratios, for each drop size and at different wind speeds, calculated by means of the LPT model and based on the undisturbed airflow fields for the *Hotplate*® precipitation gauge

Table 6.7 Catch ratios for each drop size bin and at different wind speeds, calculated by means of the LPT model and based on the undisturbed airflow fields for the *Hotplate*® precipitation gauge

d [mm] U_{ref} [m s ⁻¹]	0.25	0.5	0.75	1	2	3	4	5	6	7	8
2	1.01	1.00	1.00	1.00	1.00	1.00	1.00	1.01	1.01	1.00	1.00
3.5	1.01	1.00	1.00	1.01	1.01	1.01	1.00	1.01	1.00	1.00	1.00
5	1.01	1.00	1.01	1.01	1.01	0.99	1.00	1.01	1.01	1.01	1.01
7.5	1.02	1.01	1.00	1.01	1.00	1.00	1.00	1.00	1.00	1.01	1.01
10	1.08	1.05	1.04	1.02	1.01	1.00	1.01	1.01	1.01	1.01	1.00
12.5	1.15	1.11	1.08	1.07	1.05	1.02	1.02	1.02	1.01	1.01	1.01
15	1.23	1.15	1.13	1.12	1.07	1.05	1.05	1.04	1.03	1.02	1.02
17.5	1.29	1.23	1.19	1.15	1.11	1.08	1.08	1.07	1.07	1.05	1.05
20	1.37	1.29	1.24	1.21	1.15	1.12	1.12	1.10	1.08	1.08	1.08

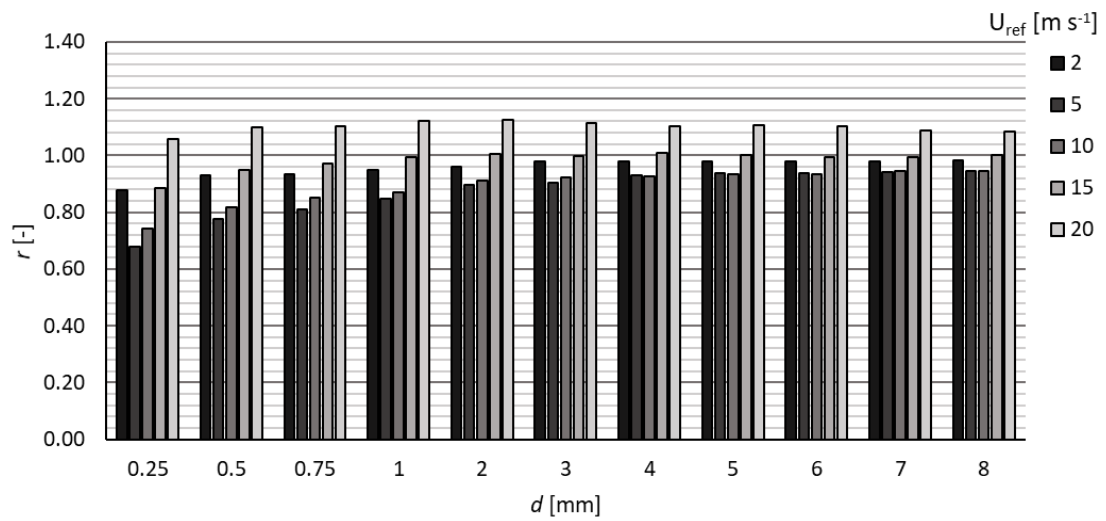


Figure 6.15 Comparison between the catch ratios, for each drop size and at different wind speeds, calculated by means of the LPT model and based on the URANS airflow fields for the *Hotplate*® precipitation gauge.

Table 6.8 Catch ratios for each drop size and at different wind speeds, calculated by means of the LPT model and based on the URANS simulated or rescaled airflow fields for the *Hotplate*® precipitation gauge

d [mm]	0.25	0.5	0.75	1	2	3	4	5	6	7	8
U_{ref} [m s ⁻¹]											
2	0.88	0.93	0.93	0.95	0.96	0.98	0.98	0.98	0.98	0.98	0.98
3.5	0.75	0.84	0.88	0.90	0.93	0.94	0.95	0.96	0.96	0.97	0.97
5	0.68	0.78	0.81	0.85	0.90	0.90	0.93	0.94	0.94	0.94	0.95
7.5	0.72	0.80	0.83	0.86	0.89	0.92	0.92	0.92	0.92	0.93	0.94
10	0.74	0.82	0.85	0.87	0.91	0.92	0.93	0.94	0.94	0.95	0.95
12.5	0.80	0.87	0.91	0.92	0.94	0.96	0.96	0.96	0.97	0.98	0.97
15	0.89	0.95	0.97	0.99	1.00	1.00	1.01	1.00	0.99	0.99	1.00
17.5	0.92	1.00	1.03	1.05	1.06	1.06	1.05	1.05	1.05	1.05	1.04
20	1.06	1.10	1.10	1.12	1.12	1.11	1.10	1.11	1.10	1.09	1.08

The Marshall-Palmer parametrization of the PSD is commonly adopted also for solid precipitation. Its suitability for solid precipitation is confirmed by Yuter et al. (2006) and Brandes et al. (2007). Maintaining a strict analogy with the work of Thériault et al. (2012), where the Collection Efficiency is calculated by assuming the parameters of the PSD proposed by Houze et al. (1979), in this work the parameters of the intercept N_0 and the slope Λ were set equal to $5 \cdot 10^6 \text{ m}^{-4}$ and 0.5 mm^{-1} , respectively. In addition, the dependency on the Snowfall Intensity (SI) was introduced by using the formulations proposed by Gunn and Marshall (1958) for the PSD parameters (Equations 6.5 and 6.6).

In Figure 6.16, the geometrical collection efficiency curves calculated by means of undisturbed airflow fields and $SI = 1, 2.5, 5, 10$ and 50 mm h^{-1} are shown with continuous lines. Whichever the wind speed, an overcatch is observed with increasing values beyond approximately 5 m s^{-1} , while by increasing SI the geometrical overcatch decreases as expected. The CE values calculated for both simulated and rescaled airflow fields are depicted with circles. For each SI value, identified with the color coding, the CE decreases linearly up to $U_{ref} = 5 \text{ m s}^{-1}$, while for wind speed larger than 5 m s^{-1} the CE starts to increase quadratically because of the increasing contribution of the geometrical effect, which implies that the catch ratios are larger than one for each drop size (Table 6.7). For wind speed larger than 15 m s^{-1} the geometrical effect becomes predominant and an overcatch appears for high SI values, and progressively even for low SI the CE becomes larger than one. The CE values calculated with the parameterization proposed by Houze et al. (1979) would closely overlap to those corresponding to $SI = 50 \text{ mm h}^{-1}$. In the same conditions, when the gauge is rotated by 180° and the airflow impacts on the supporting arm and then on the *Hotplate*® body, at wind speed equal to 10 m s^{-1} , the CE value is 0.5% higher.

Table 6.9 Slope and intercept parameters (m , n) of the linear best-fit for $U_{ref} \leq 5 \text{ m s}^{-1}$ at different SI values with the associated correlation factors.

$SI [\text{mm h}^{-1}]$	1	2.5	5	10	50
m	-0.0372	-0.0297	-0.025	-0.0213	-0.0165
n	1.0164	1.0147	1.0138	1.0125	1.0096
R^2	0.9986	0.9998	1	0.9993	0.9952

Table 6.10 Parameters (a , b , c) of the second-order polynomial best-fit for $U_{ref} \geq 5 \text{ m s}^{-1}$ at different SI values with the associated correlation factors

$SI [\text{mm h}^{-1}]$	1	2.5	5	10	50
a	0.0010	0.0010	0.0010	0.0010	0.0010
b	-0.0068	-0.0088	-0.0101	-0.0111	-0.0117
c	0.8329	0.8778	0.9075	0.9303	0.9456
R^2	0.9952	0.9952	0.9955	0.9959	0.9961

The shape of the CE curve differs from the sigmoidal curve, typical of the traditional catching type gauges, due to the complex geometry of the *Hotplate*®. For each *SI* category the CE values were fitted with a linear function for wind speed between 2 and 5 m s⁻¹, while a second order polynomial was adopted for $U_{ref} \geq 5$ m s⁻¹. The parameters of the best fit curves for each *SI* category, with the associated correlation factors, are listed in Table 6.9 and Table 6.10 for the linear and second order functions, respectively.

Note that, contrary to the geometrical CE, the actual CE curves move upward with increasing *SI* (progressively showing a lower undercatch) and they become closer, implying a reduced dependency on the precipitation intensity at high *SI*. Also, the dependency on *SI* reduces with increasing wind speed until, at high wind speed, it vanishes due to the more uniform distribution of the catch ratios through the particle diameters range (see Figure 6.15).

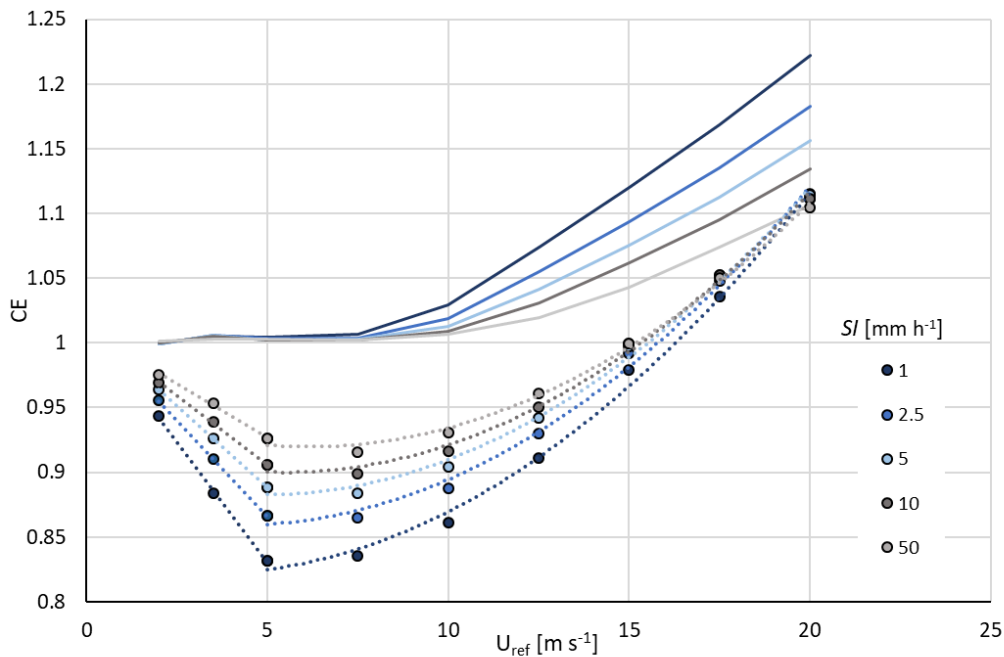


Figure 6.16 Geometrical (undisturbed airflow fields - solid lines) and actual (disturbed airflow fields - dotted lines) CE curves for the *Hotplate*® precipitation gauge. Circles indicate the results of the performed and rescaled numerical simulations and are colour coded according to the snowfall intensity (*SI*).

The dependency of the CE curves on the snowfall intensity *SI* can be made explicit in the coefficients of both the linear and the quadratic portions. In order to better fit the numerical results, the CE values were calculated for further intermediate intensity levels, between those reported in Figure 6.16, specifically at 20, 30 and 40 mm h⁻¹. The dependency of the slope (*m*) and intercept (*n*) parameters of the linear portion of the CE on *SI* is depicted in the left and right panels of Figure 6.17, respectively, together with their inverse second-order polynomial, generically indicated with $f=f(SI)$ as in Eq. 6.21, and power law best-fit curves. These results reveal that the dependency of the CE curve on *SI* tends to reduce with increasing *SI*, confirming the reduced distance between contiguous curves as observed in Figure 6.16 at progressively higher *SI*. Table 6.11 and Table 6.12 report the specific coefficients for the two curves.

$$f = \frac{p}{SI^2} + \frac{q}{SI} + y_0 \quad (6.21)$$

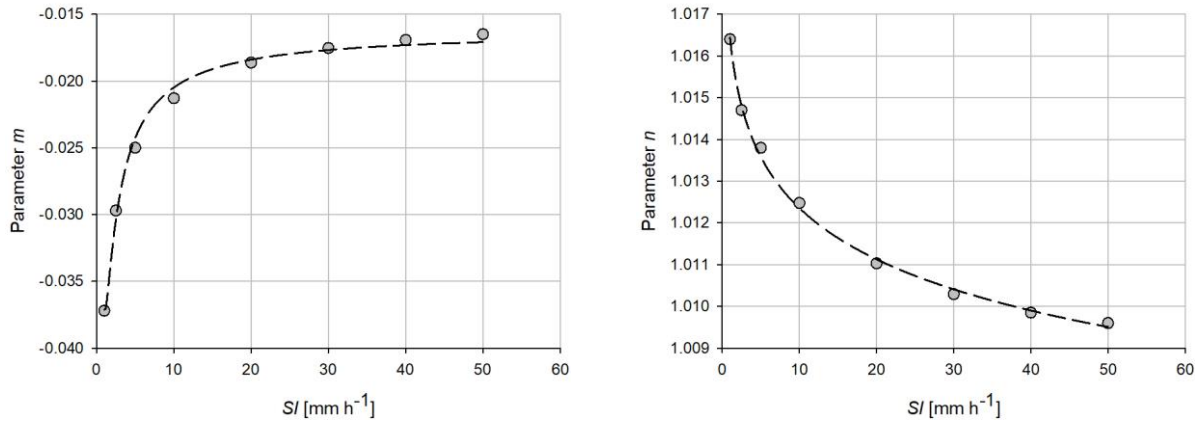


Figure 6.17 Trends of the slope (m – left) and intercept (n – right) parameters with SI for the linear portion of the CE curves. Dashed lines are the inverse second-order polynomial and power law best-fit curves.

Table 6.11 Coefficients of the best-fit inverse second order polynomial for the dependency of m on SI .

p	-0.0453
q	0.0244
y_0	-0.0162
R^2	0.997

Table 6.12 Coefficients of the best-fit power law for the dependency of n on SI .

g	1.0164
h	-0.0018
R^2	0.999

As for the quadratic portion of the CE curves, it can be noted from Table 6.10 that the parameter a is constant for all CE curves at any SI level, indicating that the degree of curvature of the best-fit quadratic function is the same. The parameters b and c are depicted in the left and right panels of Figure 6.18, respectively, together with their inverse second-order polynomial best-fit curves, generically indicated with $f=f(SI)$ as in Eq. 6.21. Similarly to the linear portion of the CE curves, also the parameters of the quadratic portion reveal that the dependency of the CE curve on SI tends to reduce with increasing SI , confirming the

reduced distance between contiguous curves as observed in Figure 6.16 at progressively higher SI . Table 6.13 reports the specific coefficients for the two curves.

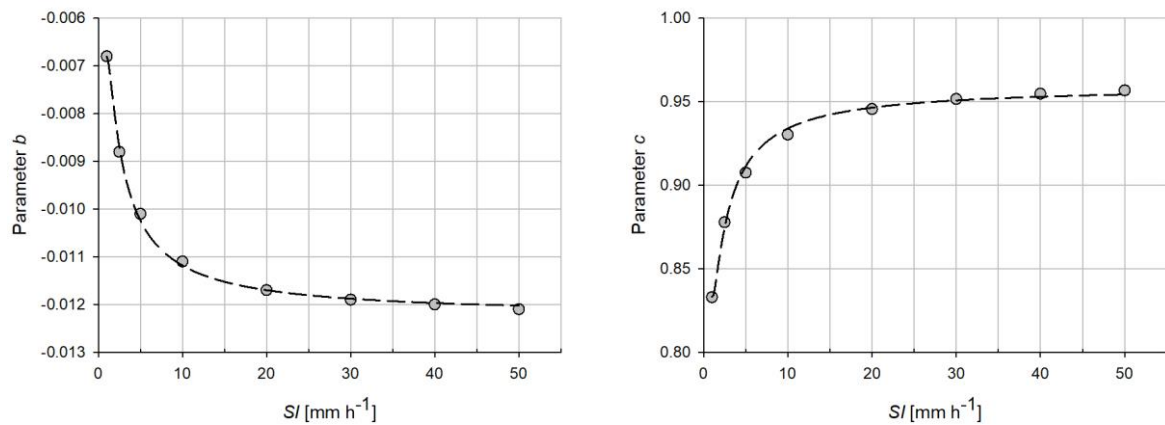


Figure 6.18 Trends of the b (left) and c (right) parameters with SI for the quadratic portion of the CE curves. Dashed lines are the inverse second-order polynomial best-fit curves.

Table 6.13 Coefficients of the best-fit inverse second order polynomial for the dependency of b and c on SI .

	Parameter b	Parameter c
p	0.0112	-0.2716
q	-0.0058	0.1452
y_0	-0.0122	0.9597
R^2	0.999	0.998

While the CE curves illustrated in Figure 6.16 provide a clear picture of the behavior of the instrument under different wind speed and SI conditions, they are hardly applicable in this form for operational use. Indeed, their construction steps from the knowledge of the reference (actual) SI , which is unknown in the real world. Adjustment curves were therefore derived for the *Hotplate*® precipitation gauge, with the aim to provide a useful tool that can be used operationally to apply a correction for the wind-induced bias when measuring solid precipitation. These are reported in Figure 6.19 in a (SI, SI_{meas}) graph, where the user can derive the corrected value of SI , starting from the measured one (SI_{meas}) and the observed wind speed.

At high wind speed some overcatch is obtained, while undercatch starts to be observed when the wind speed is lower than 15 m s^{-1} , as already discussed above. The parameters of the adjustment curves for the simulated and rescaled airflow fields are summarized in Table 6.12, where for all curves the correlation factor (R^2) is equal to one.

Note that the parameters of the power law best-fit curves become closer to one with increasing the wind speed, as it was also clear from Figure 6.16 where the circles indicating the different SI levels collapse onto the same CE value as the wind speed increases, while they are dispersed across a range of CE values at low wind speed.

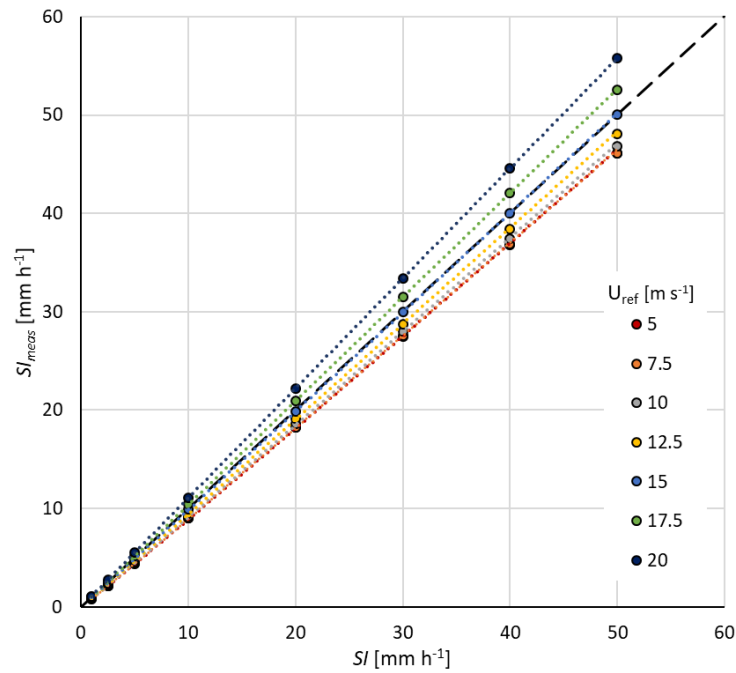


Figure 6.19 Adjustment curves (dotted lines) for the *Hotplate*® gauge at various wind speed larger than 5 m s⁻¹. The diagonal dashed line indicates optimal performance, therefore CE = 1, while circles indicate the numerical results of the performed and rescaled simulations, colour coded according to the wind speed (U_{ref}).

Table 6.14 Coefficients of the best-fit power laws for the adjustment curves at various wind speeds.

U_{ref} [m s ⁻¹]	5	7.5	10	12.5	15	17.5	20
g	0.835	0.848	0.873	0.910	0.960	1.022	1.098
h	1.028	1.024	1.020	1.016	1.011	1.008	1.004

THE ROLE OF FREE-STREAM TURBULENCE

The numerical studies reported in the literature, assume that turbulence is only generated by the interaction of the airflow with the gauge, therefore, CFD simulations generally impose a steady and uniform incoming flow. However, wind is turbulent in nature due to the roughness of the site and the presence of obstacles. Therefore, in operational conditions, precipitation gauges are immersed in a turbulent flow.

In this thesis, further to the role of the local generation of turbulence due to the obstruction to the airflow caused by the bluff body nature of the precipitation gauge (addressed in chapter 4), the natural free-stream turbulence inherent to the wind, and its influence on precipitation measurements, are investigated. Wind speed measurements recorded, at high frequency and at the gauge elevation, in the Nafferton Farm site (UK) were analysed in order to calculate the turbulence intensity as a function of the wind speed. First, the free-stream turbulence effect was investigated, concerning the airflow disturbance around a calyx-shaped precipitation gauge, by means of CFD simulations and WT tests. Then, the free-stream turbulence effect was addressed also in terms of CE by simulating the hydrometeors trajectories for the *Hotplate* snow gauge and for a chimney shaped gauge. In the first case, a literature value of the free-stream turbulence (Øistad, 2015) was set by imposing a constant turbulent kinetic energy value as a boundary condition upstream of the gauge, while for the chimney shaped gauge the desired level of turbulence, as measured in the Nafferton Farm site, was imposed by introducing physical obstacles and performing LES simulations.

7.1. THE FREE-STREAM TURBULENCE IN NATURAL WIND

In the literature, various studies report estimates of the free-stream turbulence intensity, generally at high elevation (e.g. Kumer et al., 2016; Øistad, 2015), mainly focused on the evaluation of the efficiency of wind turbines.

The work of Øistad (2015) reports the analysis of the Turbulence Intensity in onshore and offshore conditions obtained from two years of wind measurements from the west coast of Norway (Skipheia site). Measurements were carried out by employing twelve ultrasonic anemometers positioned in pairs at six different heights from 10 to 100 meters. Measurements were recorded at 1 Hz and averaged over a time period of 1 minute. The experimental site allowed wind originating from both earth and sea to be measured. Water is generally smoother than onshore surfaces, which leads to less turbulence, and the marine atmospheric boundary layer is usually more stable than the atmospheric boundary layer over land. Therefore, offshore turbulence intensity is expected to be weaker. The Skipheia wind observations were divided in wind speed classes with bin width of 1 m s^{-1} . The mean value σ_m , the 90th percentile σ_{90} , and the standard deviation of the horizontal wind speed (σ_i) measurements were calculated for each bin. Then, the turbulence intensity was calculated according to Eq. 7.1 using the standard deviation and the mean wind speed in each available time step as:

$$I_{turb} = \frac{\sigma_i}{U_i} \quad (7.1)$$

where U_i is the mean wind speed over that time step.

The calculated I_{turb} values were associated with the appropriate wind speed bins and the mean value (TI_m) and 90th percentile (TI_{90}) were calculated for each bin. Figure 7.1 shows the calculated turbulence intensity obtained from measurements at an elevation of 70 m as a function of wind speed. For low wind speed, the turbulence intensity decreases faster with increasing wind speed, then it tends to reach an approximatively constant value (about $I_{turb} = 0.1$).

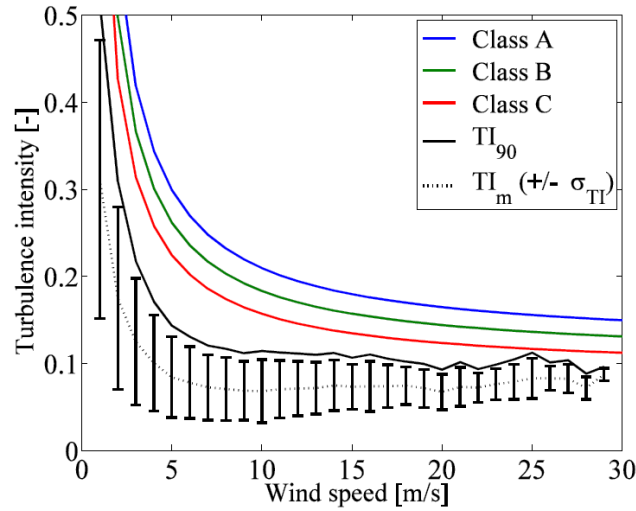


Figure 7.1 Turbulence Intensity as a function of wind speed obtained at an elevation of 70 m. The mean value (thin dotted line) with the associated standard deviation (bars) and the upper 90th percentile (black continuous line) calculated for each bin are reported. The A, B and C curves represent standard curves used for wind turbine design (from the International Electrotechnical Commission IEC), for high, medium and low turbulence intensities, respectively (from Øistad, 2015).

Precipitation gauges are located with the collector at a few meters above the ground surface, usually at about 2 m for gauges supported by poles, and about 0.5 m for gauges directly installed on the ground surface. With the aim of obtaining turbulence intensity values characterising the wind near to the ground surface, in this thesis, 3-D sonic anemometer measurements were analysed. Data were provided by Environmental Measurements Ltd. (EML[®]) from the Nafferton (UK) experimental site (see Figure 7.2) and are composed of 38 minutes of high-frequency (20 Hz) wind measurements (Figure 7.3, black line). The moving average (Figure 7.3, grey line) was calculated by testing different sizes (N) for the moving window. A value of $N = 125$ was chosen because of its consistency with the average approach proposed by Reynolds (see Chapter 4), which requires that the mean values of the turbulent fluctuations in all directions (x, y, z) must be null. For this scope, a trial and error procedure was adopted: after choosing a tentative value for N, the wind measurements were divided in wind classes based on the mean values of their average magnitude (grey line in Figure 7.3), then for each wind class the mean of the turbulent fluctuations ($\overline{u'(t)}, \overline{v'(t)}, \overline{w'(t)}$) was calculated and the N value associated with the minimum of average fluctuations was chosen.



Figure 7.2 3-D sonic anemometer in the Nafferton (UK) experimental site with EML[®] aerodynamic rain gauges located on the ground surface.

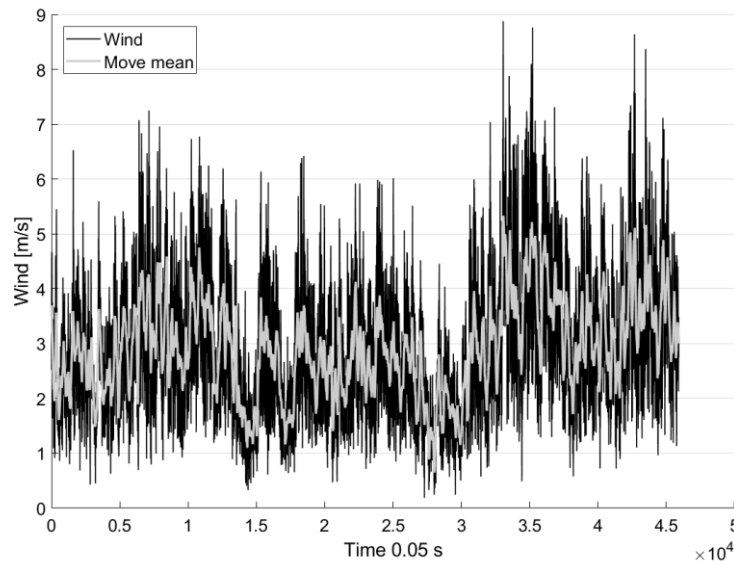


Figure 7.3 High-frequency wind measurements from the Nafferton (UK) experimental site (black line) and moving average with $N = 125$ (grey line).

Figure 7.4 reports the mean value of turbulent fluctuations and the associated standard deviation for each wind class; on the right-hand axis the sample size for each wind class is indicated. This result shows that the condition on the null average of the turbulent fluctuations is mostly fulfilled, except for the wind classes characterized by a low number of data (wind $> 5 \text{ m s}^{-1}$). Finally, the relative turbulence intensity values (defined in chapter 4), were calculated for each wind class. As expected, along the two longitudinal directions (x and y) the behaviour is very similar, while for the vertical direction (z) the turbulent intensity values are lower (Figure 7.5). As shown in the literature for high elevation measurements (e.g., Øistad, 2015) even close to the ground the turbulence intensity decreases with increasing the wind speed and seems to have an asymptotical constant limit, although data for high wind speed classes are few.

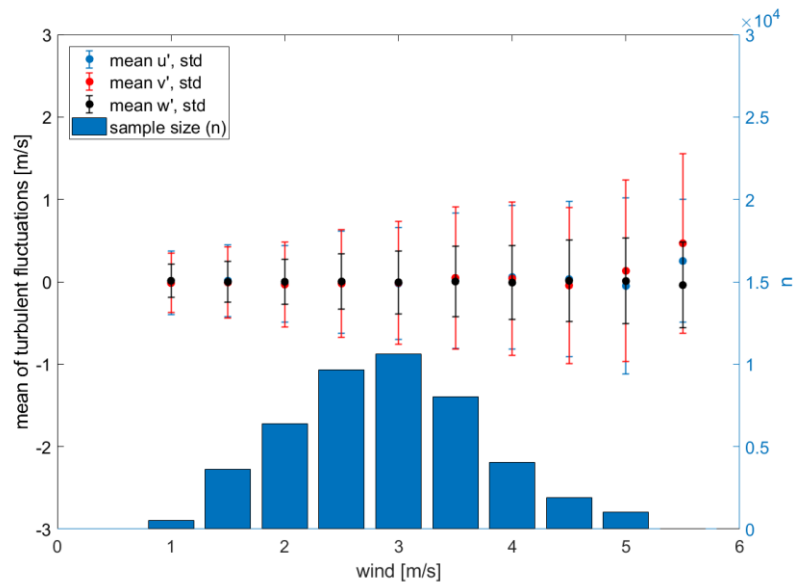


Figure 7.4 Mean values and standard deviations of turbulent fluctuations (left-hand axis) and sample size (right-hand axis) for each wind class.

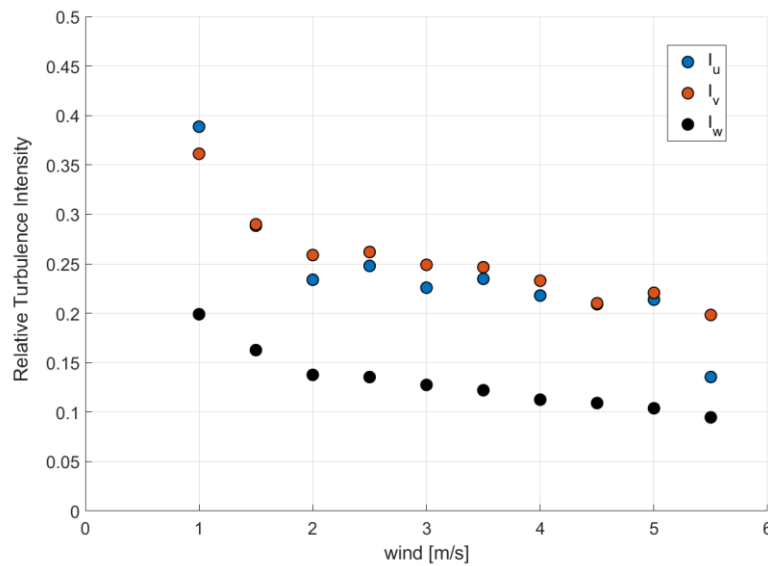


Figure 7.5 Relative turbulence intensity for the three Cartesian directions for each wind class.

Based on the literature and the analysis of experimental measurements, two values of the free-stream turbulence intensity are adopted in this thesis, namely 0.1 from high elevation literature results and 0.25 from the processing of measurements obtained at the Nafferton site at near-ground elevation. The free-stream turbulence effect is evaluated in the following by comparing the simulated flow velocity field and CE for the uniform and turbulent free-stream configurations.

7.2. THE ROLE OF FREE-STREAM TURBULENCE IN ATTENUATING THE WIND UPDRAFT AT THE COLLECTOR OF A CALYX SHAPED GAUGE ¹

The present section aims to investigate the role of free-stream turbulence on the airflow above the collector of a calix-shaped precipitation gauge. This was quantified based on the comparison between the aerodynamic response of the gauge under uniform and turbulent free-stream conditions, assessed by means of both CFD simulations and WT tests.

Although most traditional catching type precipitation gauges usually have cylindrical or “chimney” shapes, with the increasing awareness of the wind effect on collection performance new precipitation gauges characterized by aerodynamic shapes have been recently developed. The airflow patterns above gauges of various geometries and the benefits of the aerodynamic shape, were shown using results of CFD simulations (Colli et al. 2018) and supported by field investigations (Pollock et al. 2018). Specifically, Colli et al. (2018) showed that the turbulent kinetic energy induced by the flow-gauge interaction above the collector for the calyx-shape gauge is about one third of that generated by gauges with cylindrical or “chimney” shape. For this reason, in order to better single out the role of free-stream turbulence on the airflow features above the gauge collector the focus is, in the present section, on the calyx-shape precipitation gauge.

The test gauge is the Kalyx-RG[®] tipping-bucket aerodynamic gauge, manufactured by EML. In a first configuration, the incoming flow is imposed steady and uniform, with no significant turbulence intensity of the incoming airflow upstream of the gauge. In a second configuration, the free-stream turbulence is simulated by using a fixed solid fence with a regular square mesh located upstream of the gauge. In this second configuration the obtained turbulence intensity upstream of the gauge is about 0.10. Two wind regimes are investigated per each configuration, with incoming horizontal mean wind velocity equal to 18 and 10 m s⁻¹, respectively. CFD simulations are performed using the open-source OpenFOAM numerical solver, adopting the Unsteady Reynolds Average Navier-Stokes (URANS) model and the Shear Stress Tensor (SST) $k-\omega$ closure model. Simulation results are processed to compute the velocity profiles (magnitude and components) in representative portions of the domain. Validation is provided by reproducing the two airflow configurations in WT tests and measuring the horizontal and vertical velocity profiles (magnitude and components) at fixed positions using pressure probes.

7.2.1. The numerical model and wind tunnel setup

Compared to the most common tipping-bucket rain gauges (having a cylindrical shape) the Kalyx-RG[®] (Figure 7.6a) is an aerodynamic inverted conical shaped gauge with a smaller size. The instrument has an orifice diameter D equal to 0.13 m and height equal to 0.192 m. The model of the gauge geometry was prepared in the Standard Triangulation Language (STL) format (Figure 7.6b) using a 3D CAD software.

By means of spatial discretization, the computational mesh and domain were defined. The three Cartesian coordinates were set with the x axis orientated along the stream wise direction, the y axis along the crosswise direction and the z axis along the vertical direction. For the uniform airflow configuration, the spatial

¹ This section contains material published as Cauteruccio et al. (2020)

computational domain consists of a $5 \times 2 \times 2 \text{ m}^3$ box, and is decentralized downward to optimize the computational cost and ensure full development of the airflow wake downstream of the gauge. For the turbulent case, the computational domain was stretched upstream by 1 m in order to introduce a turbulence-generating fence composed by a regular square mesh of thickness equal to 0.02 m and spacing equal to 0.15 m.

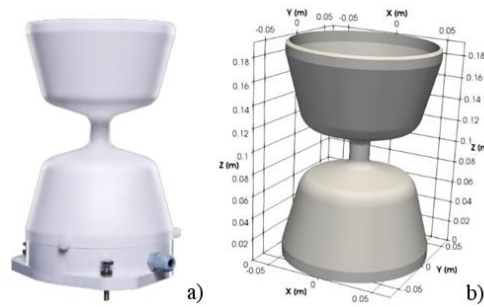


Figure 7.6 The Kalyx© EML aerodynamic rain gauge (a) and the numerical model of the gauge (b).

The three-dimensional spatial domain was discretized using an unstructured hybrid hexahedral/prismatic finite volume mesh. The quality of the mesh was checked by using the geometry parameters of orthogonality, skewness and aspect ratio. The computational domain was subdivided in refinement boxes stretched along the downwind direction, with increasing refinement of the mesh when approaching the gauge body (Figure 7.7 a) and the turbulence-generating fence (Figure 7.7 b).

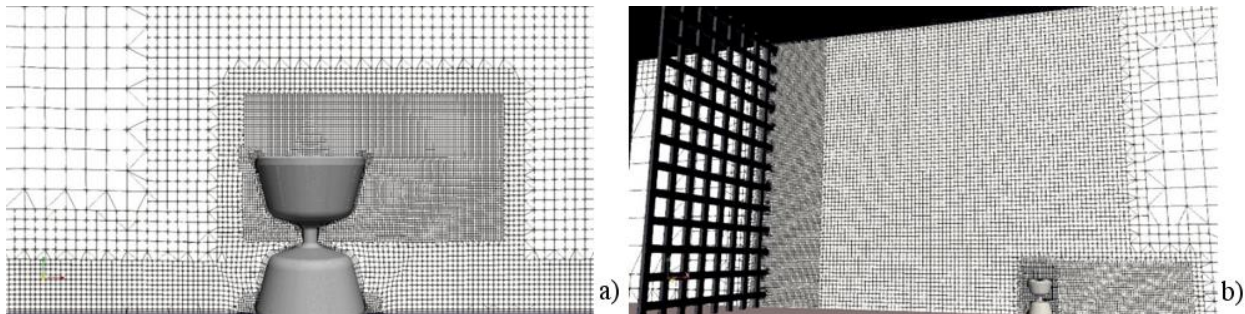


Figure 7.7 Mesh refinements around the precipitation gauge (a) and the CFD mesh and domain for the configuration with a solid turbulence-generating fence positioned upstream of the gauge (b).

The number of cells in the configuration with the turbulence-generating fence was more than twice the steady-uniform case, i.e. 2.7×10^6 and 1.2×10^6 cells, respectively. The refinement boxes allowed the equation of motion to be better solved in the region affected by large gradients of velocity and pressure. For this reason, three refinement layers were introduced close to the gauge surface and the minimum dimension of the nearest cells to the geometry is about $1/3$ of the collector rim thickness. To check that the grid size near the gauge surface was consistent with the use of a wall function (see e.g. Menter and Esch 2001), so that the computational burden is reduced, the wall y^+ was calculated. In the simulations, the average value of y^+ is about 15, the median is 12 and most values (90 %) are below 30, with the larger values occurring in the downwind part of the gauge, therefore a scalable wall function was adopted. This

allowed the flow velocity to be modelled with linear and logarithmic profiles below and above a threshold value defined at $y^+ = 11.067$ by Menter and Esch (2001).

The finite-volume Computational Fluid Dynamic (CFD) simulations were performed based on the solution of the Unsteady Reynolds Average Navier-Stokes (URANS) equations. The SST $k-\omega$ closure model was adopted here, so as to switch to a $k-\epsilon$ behaviour in the free stream far from the object and to the $k-\omega$ model near the walls. Constantinescu et al. (2007), while investigating the shielding problem between two contiguous precipitation gauges, tested different numerical methods and concluded that the SST $k-\omega$ is more consistent with the LES results on the upstream gauge, in conditions that are similar to the present work.

The fluid air was modelled as a Newtonian incompressible fluid with kinematic viscosity $\nu_a = 1.5 \times 10^{-5} \text{ m}^2\text{s}^{-1}$ and density $\rho_a = 1.25 \text{ kg m}^{-3}$ at a reference environmental temperature $T_a = 20^\circ\text{C}$. At the inlet of the computational domain (y - z plane) the undisturbed wind speed, U_{ref} , was imposed parallel to the x axis and is maintained uniform and constant in time, while a null gradient condition was set for pressure. Atmospheric pressure and null gradient conditions for the velocity were imposed at the outlet (y - z plane opposite to the inlet). The lateral surfaces of the domain were set as symmetry planes. The ground and the gauge surface were assumed impermeable with a no-slip condition. In all computational cells of the spatial domain, initial conditions were imposed equal to U_{ref} for the velocity and equal to zero for the relative pressure.

The experimental tests were performed in the wind tunnel (WT) of the Department of Civil, Chemical and Environmental Engineering (DICCA) of the Polytechnic School of the University of Genoa. In order to carry out tests in uniform flow, the rain gauge was placed on an end-plate (Figure 7.8a).



Figure 7.8 The Kalyx© EML rain gauge and the turbulence-generating fence in the DICCA WT, the flow direction being from right to left (a) and detail of the Cobra probe used to measure the local flow velocity near the gauge collector (b).

A static Pitot tube placed at the top of the test section was used to measure the reference wind speed, U_{ref} . Local measurements of the wind speed were acquired using a fast-response multi-hole probe (a 4 holes “Cobra” probe, Figure 7.8b). The Cobra probe was mounted on a 3 degrees of freedom traversing system, which allowed measurements to be taken at any coordinates of interest. Measurements were sampled at 2 kHz.

Two conditions of incoming flow have been considered: (1) smooth flow characterized by a turbulence intensity $I_{turb} \approx 0.5\%$ and (2) turbulent flow, produced through a grid realized by square bars (Figure 7.8a), characterized by $I_{turb} \approx 10\%$.

7.2.2. Results and validation

The main area of interest for this study is just above the gauge collector, where the modified airflow patterns may influence particle trajectories and therefore the precipitation collection. In this region, results are visualized in terms of normalized maps and profiles on the vertical along-wind symmetry plane of the gauge collector ($y = 0$). The magnitude, U_{mag} , and the vertical component, U_z , of the airflow velocity are reported and compared for the two free-stream turbulence configurations. Both are normalized using the undisturbed wind speed, U_{ref} , while the spatial coordinates are normalized with the gauge collector diameter D (the origin of the axes is located at the centre of the collector). The turbulence intensity profile and contour map along the stream wise direction are also reported.

Validation of the numerical setup is provided below by comparing wind tunnel local measurements and numerical results, with the simulated profiles depicted with lines while markers denote wind tunnel measurements.

To ensure the comparability of results for the uniform and turbulent free-stream conditions, that were obtained at different undisturbed wind speed ($U_{ref} = 18 \text{ m s}^{-1}$ and $U_{ref} = 10 \text{ m s}^{-1}$), the scalability of the results was preliminarily checked by performing CFD simulations under uniform free-stream conditions for both velocities. Figure 7.9 shows that the resulting normalized vertical velocity profiles along the stream wise direction are totally overlapped above the gauge collector. The gauge collector is painted in grey and black dashed lines indicate the edge projections.

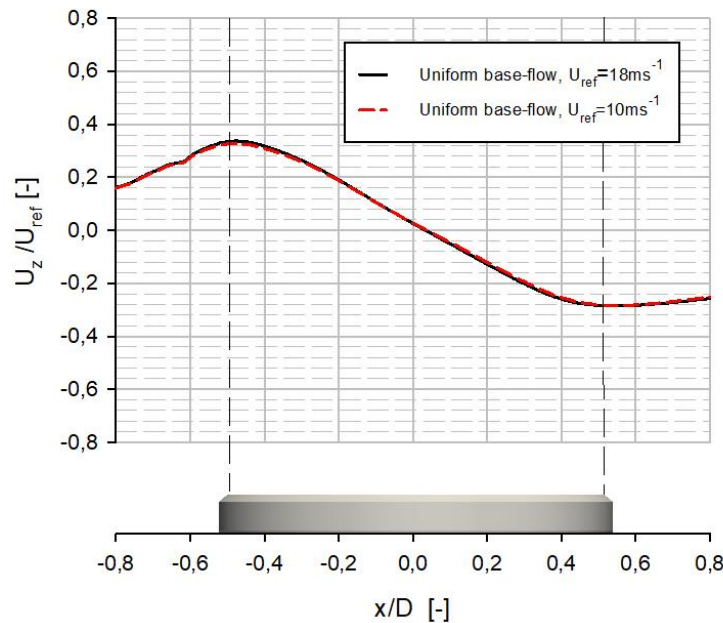


Figure 7.9 Simulated profiles of the normalized vertical velocity U_z/U_{ref} along the non-dimensional stream wise direction x/D , with D the collector's diameter, at $y = 0$ and elevation $z = 0.1515 D$ above the gauge collector (in grey with dashed line projections in black), for uniform free-stream velocity equal to $U_{ref} = 10 \text{ m s}^{-1}$ and $U_{ref} = 18 \text{ m s}^{-1}$.

Wind tunnel measurements of the longitudinal profiles (at $y = 0$ and $z = 0.038 D$) of the normalized vertical component of flow velocity and the turbulence intensity are depicted in Figure 7.10 for the uniform (black points) and turbulent (grey triangles) free-stream conditions. In both cases, the turbulence intensity increases above the collector due to the obstruction caused by the gauge body. As already observed by Warnick (1953), a significant updraft is expected to arise in front and above of the gauge collector, which is evident in Figure 7.10.

Thanks to the aerodynamic shape of the Kalyx[®] gauge, the recirculating zone is confined above the gauge collector and the airflow pattern is characterized by upward components in the upwind part, upstream the centre of the collector, and downward components in the downwind part. This had been shown by Colli et al. (2018) when comparing the numerically simulated aerodynamic response of other inverted conical shapes similar to the Kalyx[®] gauge. Contrary to the turbulence intensity, the normalized vertical velocity components are less accentuated for the turbulent free-stream configuration than in a uniform free-stream, with relative percentage differences of about 18 % and 46 % on the upwind and downwind edges, respectively (see Figure 7.10). This behaviour can also be observed in Figure 7.11, where the normalized vertical component of the flow velocity, along the vertical direction close to the upwind edge of the collector ($x = -0.568 D$), decreases faster in the turbulent free-stream condition, reaching e.g. 0.015 at a normalized elevation of $0.68 z/D$ rather than at $1.18 z/D$ like in the uniform free-stream condition.

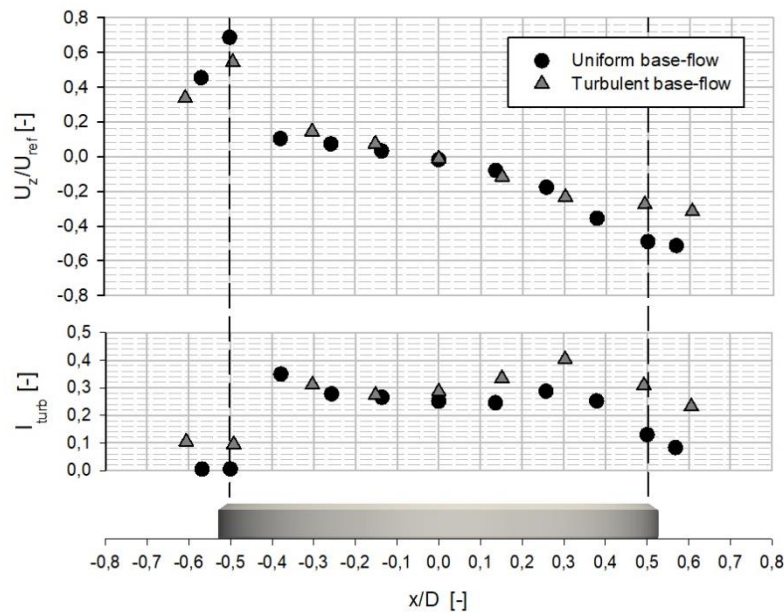


Figure 7.10 Wind-tunnel measurements of the normalized vertical velocity U_z/U_{ref} and turbulence intensity I_{turb} along the non-dimensional stream wise direction x/D , with D the collector's diameter, at $y = 0$ and elevation $z = 0.038 D$ above the gauge collector (in grey with dashed line projections in black), for the uniform ($U_{ref} = 18 \text{ m s}^{-1}$) and turbulent ($U_{ref} = 10 \text{ m s}^{-1}$) free-stream experiments.

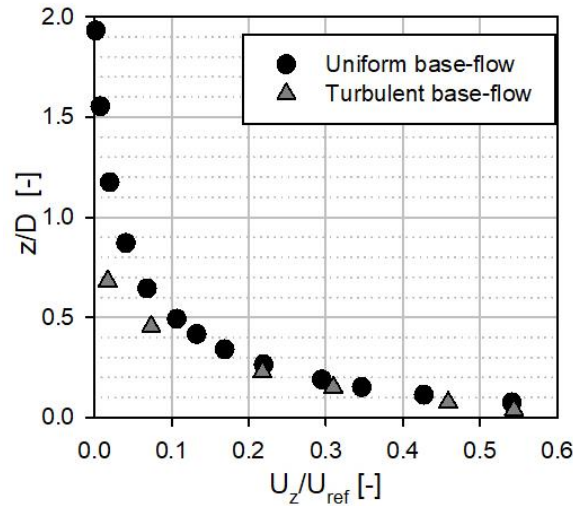


Figure 7.11 Wind-tunnel measurements of the normalized vertical velocity U_z/U_{ref} along the non-dimensional vertical direction z/D , with D the collector's diameter, at $y = 0$, upstream of the gauge collector at $x = -0.568 D$, for the uniform ($U_{ref} = 18 \text{ m s}^{-1}$) and turbulent ($U_{ref} = 10 \text{ m s}^{-1}$) free-stream experiments.

The CFD simulations allowed the airflow variables to be computed in the whole spatial domain surrounding the gauge collector, differently to the wind tunnel measurements that were taken locally in representative positions of the domain. Figure 7.12 shows the simulated airflow fields in terms of normalized magnitude of the flow velocity and normalized vertical velocity component, for the uniform and turbulent free-stream conditions. For the normalized magnitude of flow velocity, the white band indicates the region where the flow velocity is equal to the undisturbed wind speed ($U_{mag} = U_{ref}$); this boundary separates the region characterized by accelerated airflow regime ($U_{mag} > U_{ref}$, red colour) from the recirculating zone ($U_{mag} < U_{ref}$, blue colour). For the normalized vertical component of the flow velocity, the white band indicates the region with a null vertical velocity component, while the red and blue colours characterize the updraft and downdraft regions, respectively. As already observed in the WT measurements, also in the numerical simulation results the normalized magnitude of the flow velocity for the uniform free-stream configuration is about 20 % larger than in turbulent conditions (see Figure 7.12).

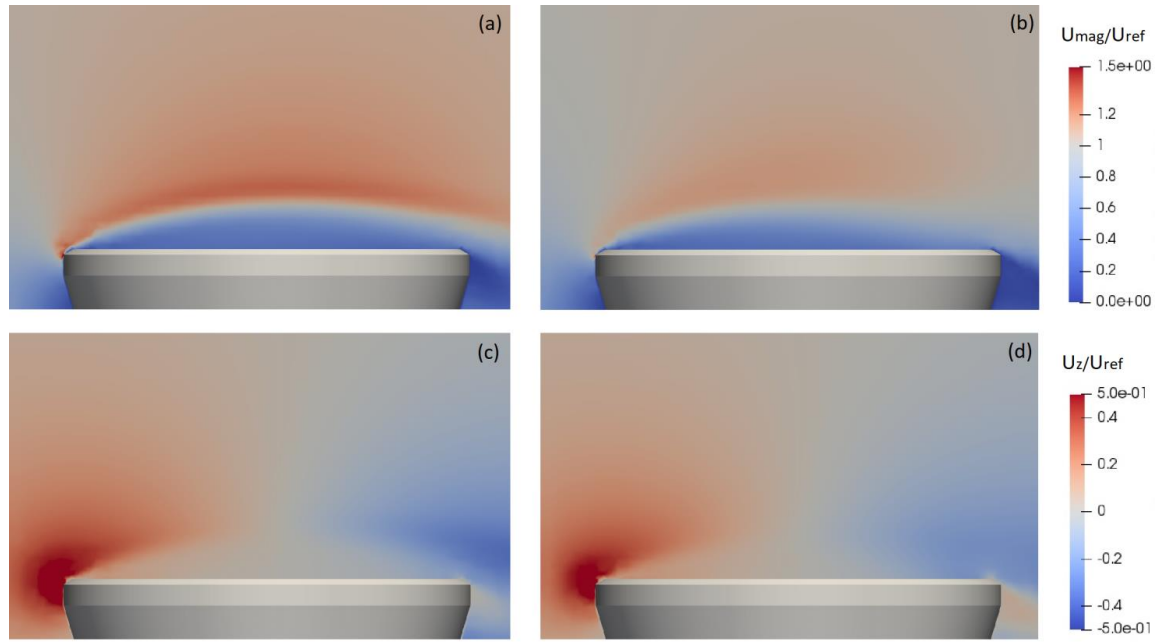


Figure 7.12 Colour maps of the simulated normalized magnitude of flow velocity U_{mag}/U_{ref} (a,b) and normalized vertical velocity U_z/U_{ref} (c, d) in the vertical section along the stream wise direction at $y = 0$, for the uniform (a, c) and turbulent (b, d) free-stream conditions.

With the aim of validating numerical simulations, CFD results were compared with wind tunnel measurements. In Figure 7.13, the normalized vertical velocity component at the upwind edge of the collector along the vertical direction at $y = 0$ (left) and the normalized magnitude of flow velocity along the stream wise direction at $y = 0$ and elevation $z = 0.075 D$ (right) are represented for the uniform flow. Figure 7.14 depicts the same situations in turbulent free-stream conditions. A good agreement between wind tunnel measurements and numerical results was observed for the uniform free-stream condition along the vertical profile with differences in the order of $0.010 U_z/U_{ref}$ at a few measurement elevations (see Figure 7.13). Along the longitudinal profiles the quantitative velocity values differ in some positions but the airflow behaviour is mostly kept. Similarly, for the velocity profiles illustrated in Figure 7.14 under turbulent free-stream conditions, a good match between numerical simulation and experiments was observed along the vertical profile, with differences in the order of $0.030 U_z/U_{ref}$ at a few measurement elevations.

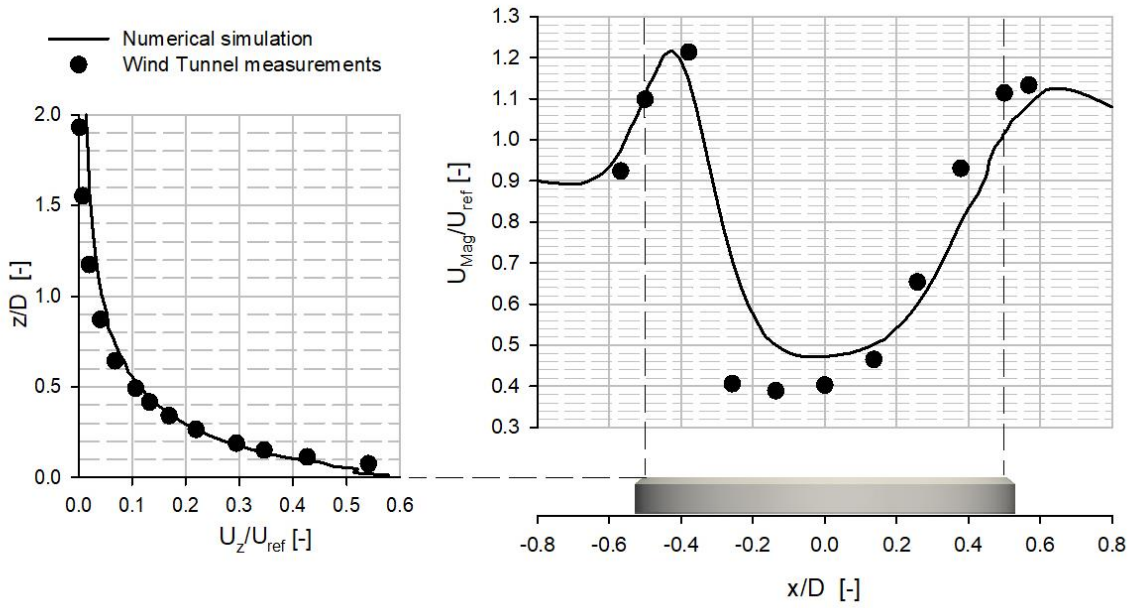


Figure 7.13 Wind-tunnel measurements and simulated profile of the normalized vertical velocity U_z/U_{ref} at the upwind edge of the collector along the non-dimensional vertical direction z/D , with D the collector's diameter, at $y = 0$ (left) and normalized velocity magnitude U_{mag}/U_{ref} along the non-dimensional stream wise direction x/D at $y = 0$ and elevation $z = 0.075 D$ (right) above the gauge collector (in grey with dashed line projections in black), for the uniform free-stream experiment ($U_{ref} = 18 \text{ m s}^{-1}$).

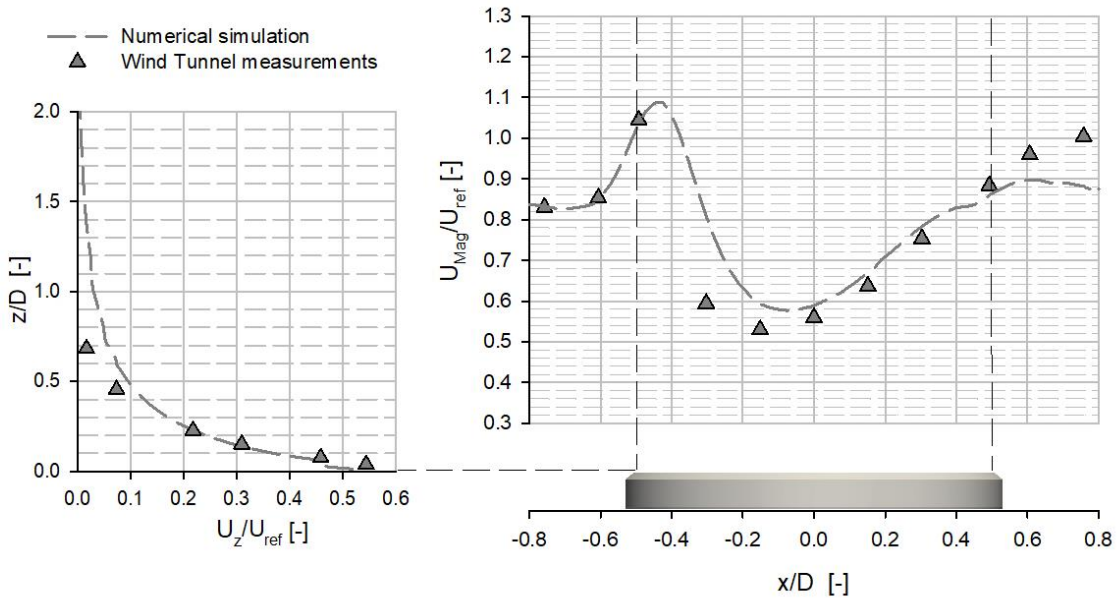


Figure 7.14 Wind-tunnel measurements and simulated profile of the normalized vertical velocity U_z/U_{ref} at the upwind edge of the collector along the non-dimensional vertical direction z/D , with D the collector's diameter, at $y = 0$ (left) and normalized velocity magnitude U_{mag}/U_{ref} along the non-dimensional stream wise direction x/D at $y = 0$ and elevation $z = 0.075 D$ (right) above the gauge collector (in grey with dashed line projections in black), for the turbulent free-stream experiment ($U_{ref} = 10 \text{ m s}^{-1}$).

In Figure 7.15, a comparison between the measured and simulated turbulence intensity is reported. The values of the turbulence intensity measured in the WT (white circles) are in consistent agreement with the contour line levels of the simulated numerical field. Few measurements, in the downwind part of the collector, differ from the numerical field up to a maximum of 0.1; these differences can be justified because the *Cobra* probe is unsuited to measuring reverse flow components and because in this region elevated gradient of turbulence intensity occurred as can be observed close to the edge of the gauge.

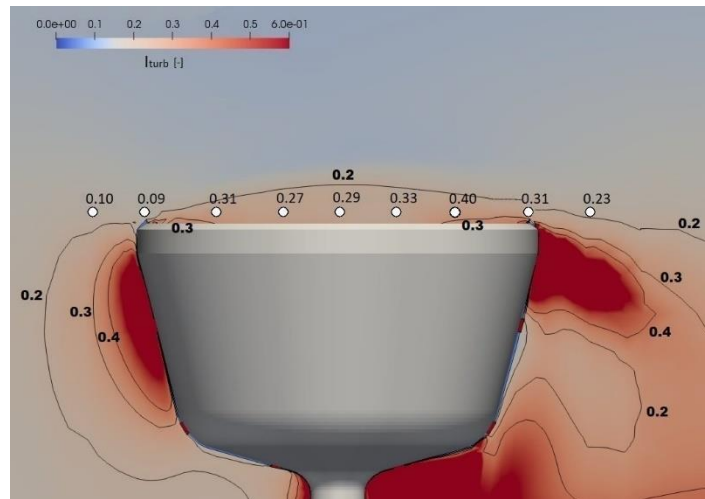


Figure 7.15 Vertical section of the simulated turbulence intensity, I_{turb} (colour coded with contour line levels in bold) along the stream wise direction at $y = 0$ and wind tunnel local measurements (white circles with light numbers) for the turbulent free-stream conditions ($U_{ref} = 10 \text{ m s}^{-1}$).

The comparison of simulated and measured airflow fields, in the uniform and turbulent free-stream configurations as proposed in this work, provided insights about the role of turbulence in attenuating the aerodynamic response of precipitation gauges. Wind tunnel measurements (Figure 7.10) showed that the normalized updraft in the upwind part, upstream the centre of the collector, and the downdraft in the downwind part are less accentuated in the turbulent free-stream configuration than in uniform free-stream conditions. This is ascribable to the energy dissipation induced by turbulent fluctuations. The dissipative effect of the free-stream turbulence also has a damping role on the acceleration of the flow above the collector as demonstrated by CFD results (Figure 7.12 a, b).

This conclusion is consistent with the literature about the free-stream turbulence effect on the interaction of a “bluff body” with the incoming airflow, as reported by various authors including e.g. Kiya and Sasaki (1983). While studying experimentally the free-stream turbulence effect on a separation bubble formed along a side of a blunt plate with right-angled corners, they concluded that the length of the separation bubble reduces significantly with increasing turbulence intensity. Also, Counihan et al. (1974) proposed an analytical theory for the mean velocity behind a two-dimensional obstacle and derived that the wake strength decreases as the surface roughness in front of the obstacle (therefore the free-stream turbulence) increases.

Finally, these conclusions are consistent with the work of Colli et al. (2015) about the collection efficiency of precipitation gauges, where a general overestimation of the wind-induced error when performing simulations under steady-uniform free-stream conditions was evident from the comparison with field observations.

This work is further substantiated by the performed wind tunnel validation of the gauge exposure problem for both turbulent and uniform free-stream configurations, that was yet lacking in the literature. In Figure 7.13 and Figure 7.14 the simulated velocity profiles closely follow the experimental measurements; some differences arise along the stream-wise direction in the region where the magnitude of flow velocity is low and beyond the gauge collector, in the turbulent wake. These differences are justified since the velocity values in such cases approach the minimum threshold velocity that the Cobra probe is able to measure (about 2 m s^{-1} to get reliable values). Also, the Cobra probe is unsuited to measure reverse flow components. However, these inconsistencies occur in a region located beyond the key area of interest to assess the collection performance of the gauge, therefore with a minor impact on the conclusions of this section.

Based on the CFD results and on the validation provided by wind tunnel observations it is possible to conclude that accounting for the free-stream airflow turbulence in the simulation is required to avoid underestimation of the collection efficiency of precipitation gauges. A turbulent free-stream is indeed the natural atmospheric condition of the wind impacting on operational precipitation gauges in the field. This work demonstrates that numerical derivation of correction curves for use in precipitation measurements as proposed hitherto in the literature is affected by a systematic overestimation of the wind-induced error due to the simplifying assumption of uniform free-stream conditions.

7.3. THE EFFECT OF FREE-STREAM TURBULENCE ON SOLID PARTICLES DYNAMICS

7.3.1. Free-stream turbulence as a boundary condition for the *Hotplate*® gauge

Following the results obtained in the previous section and published in the work of Cauteruccio et al. (2020), the role of the free-stream turbulence is here investigated both in terms of airflow field and collection efficiency for the *Hotplate* snow gauge. The turbulence intensity (I_{turb}) value was set equal to 0.1 consistent with the literature measurements describe above (Øistad, 2015).

An URANS numerical simulation at wind speed of 10 m s^{-1} in turbulent free-stream conditions was performed by using the numerical domain, mesh and setup (boundary and initial conditions, numerical schemes, etc.) already adopted for the simulation performed in uniform free-stream conditions (chapter 4). The only difference was imposed on the turbulent kinetic energy value. The free-stream turbulence in the incoming airflow, which impacts on the *Hotplate* body, was obtained by using no physical obstacles because no comparison with wind tunnel experiments was conducted. The desired turbulence intensity was instead obtained by calibrating the value of the turbulent kinetic energy, k , set as a uniform and constant boundary condition in the inlet surface of the computational domain (y, z plane of the simulated domain upstream of the gauge).

The free-stream turbulence effect on the airflow field is shown by comparing the numerical velocity profiles calculated for $I_{turb} = 0.1$ with the one calculated in uniform free-stream conditions ($I_{turb} = 0.01$) and already discussed in Chapter 4. The smoothed effect due to the free-stream turbulence is evident along the longitudinal profile in terms of both the normalized horizontal and vertical components of the flow velocity, as shown in Figure 7.16 and Figure 7.17, respectively.

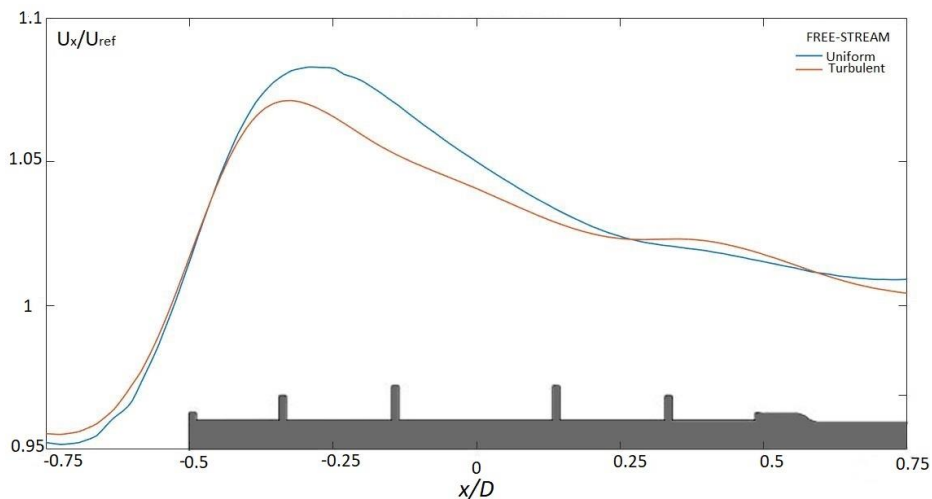


Figure 7.16 Comparison between the longitudinal numerical profiles of the normalized horizontal component of the flow velocity for a wind speed of 10 m s^{-1} , along the stream wise direction at $z/D = 0.23$ above the top plate for the uniform (blue line) and turbulent (orange line) free-stream conditions.

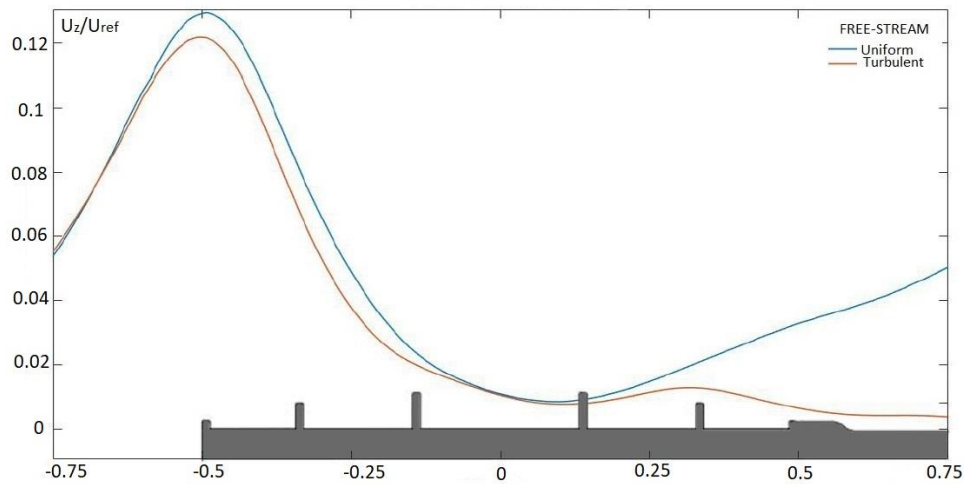


Figure 7.17 Comparison between the longitudinal numerical profiles of the normalized vertical component of the flow velocity for a wind speed of 10 m s^{-1} , along the stream wise direction at $z/D = 0.23$ above the top plate for the uniform (blue line) and turbulent (orange line) free-stream conditions.

The role of the free-stream turbulence on the particle-fluid interaction was investigated by computing the catch ratio for dry snow (Rasmussen et al. 1999, see chapter 5) with equivalent diameters of $d = 0.25 - 0.5 - 0.75 \text{ mm}$ and from 1 to 8 mm as already done for the uniform free-stream configuration (chapter 6). The comparison between the calculated catch ratios for the two free-stream conditions, summarized in Table 7.1 and depicted in Figure 7.18, shows higher values for all particle sizes under turbulent free-stream conditions. The same effect can be observed in the calculated CE values (Table 7.2) and confirms the conclusions of section 7.2, where a potential overestimation of the undercatch obtained in uniform free-stream conditions was hypothesized based on the lower acceleration and updraft observed in turbulent free-stream conditions.

Table 7.1 Catch ratios calculated for each solid particle size and $U_{ref} = 10 \text{ m s}^{-1}$ by means of the LPT model and based on the URANS airflow fields for the *Hotplate* precipitation gauge in uniform and turbulent free-stream conditions.

$d \text{ [mm]}$	0.25	0.5	0.75	1	2	3	4	5	6	7	8
Uniform	0.756	0.827	0.861	0.872	0.916	0.924	0.928	0.935	0.939	0.949	0.947
Turbulent	0.773	0.855	0.884	0.903	0.943	0.943	0.949	0.941	0.943	0.949	0.952

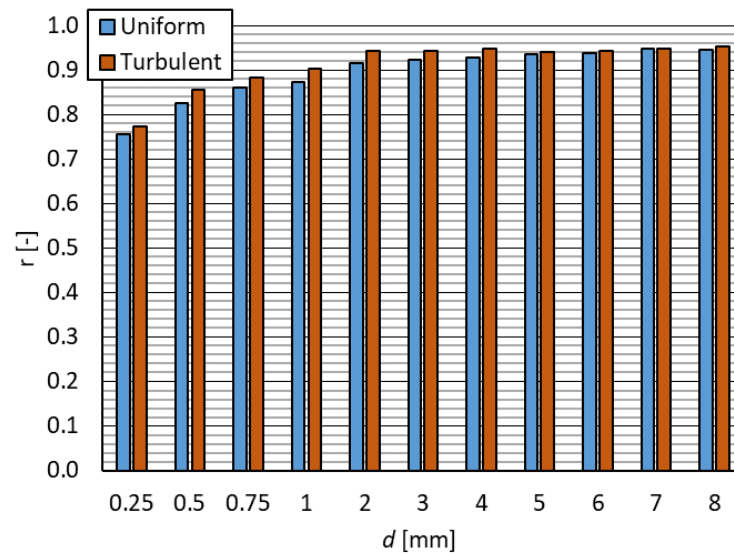


Figure 7.18 Comparison between catch ratios calculated for each solid particle size and $U_{ref} = 10 \text{ m s}^{-1}$ by means of the LPT model and based on the URANS airflow fields for the *Hotplate* precipitation gauge in uniform (blue) and turbulent (orange) free-stream conditions.

Table 7.2 Collection efficiency calculated for the *Hotplate* gauge and for dry snow in uniform and turbulent free-stream condition at $U_{ref} = 10 \text{ m s}^{-1}$.

Free-stream condition	Collection Efficiency
Uniform	0.935
Turbulent	0.945

7.3.2. Numerical generation of free-stream turbulence for the chimney shaped gauge

In this section the role of the free-stream turbulence on the collection performance of a *GeonorT200B*[®] gauge was investigated. Large Eddy Simulations (LES) were performed both in uniform and turbulent free-stream conditions.

The free-stream turbulence was generated by introducing physical obstacles upstream of the gauge in order to reproduce a typical real-world condition where a precipitation gauge operationally works. Three columnar obstacles were located upstream of the gauge. Their distance, along the longitudinal (x) direction, from the gauge was calibrated to obtain the desired level of turbulence intensity, as measured in the *Nafferton (UK)* experimental site (section 7.1). LES were chosen in order to ensure a good development of the turbulence wake downwind to the obstacles before impacting on the gauge surface.

Large Eddy simulations are able to ensure a very high quality of the results by solving the turbulent scales of motion down to the smaller size of the computational mesh. A very fine computational mesh was realized, for instance the depth of the collector rim was discretized with 10 cells. Refinement boxes were realized around the gauge, and the surface of the gauge body was discretized with a gradually increasing mesh while approaching the gauge surface. Details of the computational mesh around the gauge are shown in Figure 7.19 and Figure 7.20.

In turbulent free-stream conditions the computational mesh around the three columnar obstacles with size 0.3 x 0.3 x 7 m was refined, and this produced an increase of the computational burden. The three columnar obstacles are spaced by 0.3 m and extend four meters above and three meters below the elevation of the gauge collector. As an example, details of the computational mesh around one of the columnar obstacle generating turbulence is reported in Figure 7.21. The computational mesh for the simulation under uniform free-stream conditions is composed of twelve million cells, while by introducing the three columnar obstacles the number of cells reached fourteen millions. In both cases the max skewness is lower than 3, the max non-orthogonality is lower than 55 and the maximum aspect ratio is lower than 4.1.

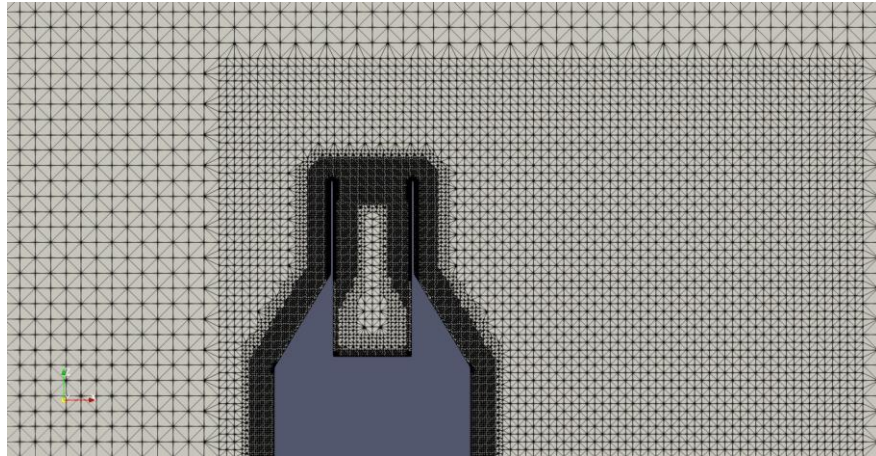


Figure 7.19 Refinement box around the Geonor gauge body and gradual refinement close to its surface in the central vertical section (x,z plane at $y = 0$) for simulations in both the uniform and turbulent free-stream conditions.

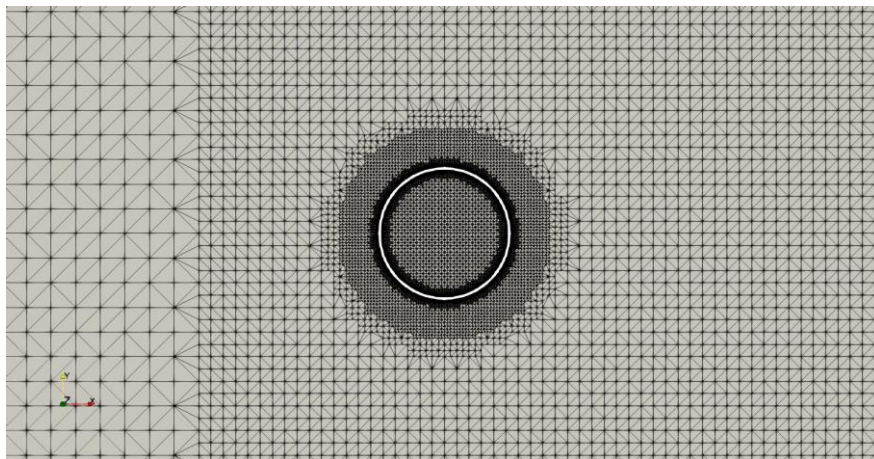


Figure 7.20 Refinement box around the *Geonor* gauge body and gradual refinement close to the its surface in the horizontal section at the gauge collector elevation (x,y plane at $z = 0$) for simulation in both the uniform and turbulent free-stream conditions.

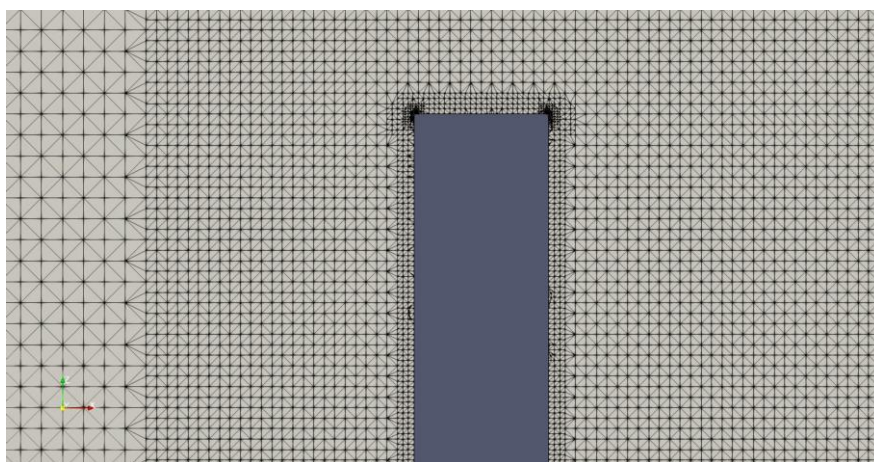


Figure 7.21 Detail of the computational mesh around the column generating turbulence.

For the two free-stream conditions, simulations were performed by imposing a wind speed equal to $U_{ref} = 6 \text{ m s}^{-1}$ in the inlet surface (upwind y, z plane of the computational domain) as a boundary condition. When the airflow overtakes the three obstacles its mean velocity magnitude is decelerated and assumes the value of 2.5 m s^{-1} , which becomes the new reference wind speed (U_{ref}) for the turbulent free-stream configuration. The decay along the longitudinal direction (x/D) of the three relative turbulence intensity profiles at the gauge collector elevation ($z/D = 0$) is shown in Figure 7.22. This distance was calibrated in order to obtain, for the reference wind speed, the level of turbulence measured at the *Nafferton (UK)* experimental site by employing a 3-D sonic anemometer as elaborated in section one of this chapter.

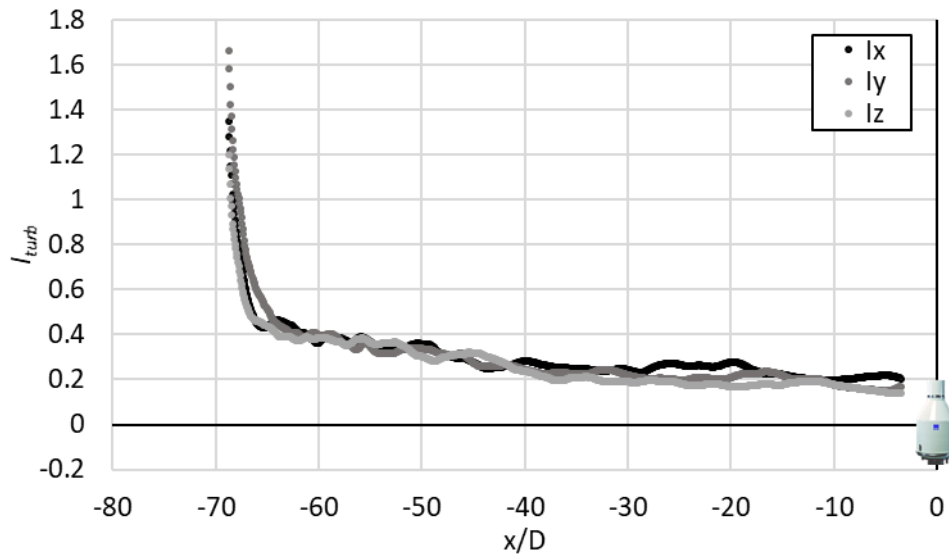


Figure 7.22 Decrease of the three numerical relative turbulence intensity profiles at the gauge collector elevation ($z/D = 0$) along the spatial domain between the position of the columnar obstacles ($x/D = -70$) and the gauge position ($x/D = 0$).

In Figure 7.23 the normalized magnitude of instantaneous ($t = 22.5 \text{ s}$) flow velocity in the horizontal plane (x, y) at the gauge collector elevation ($z/D = 0$) is reported for the turbulent free-stream conditions. This picture shows that the gauge collector is totally immersed in the turbulent flow generated by the three obstacles while in the transversal direction the flow field starts to become uniform many diameters away from the collector. In Figure 7.24 the transversal component of the flow velocity (U_y/U_{ref}) reveals the typical characteristics of vortex shedding which occurs with a regular frequency and with alternate opposite velocity directions. When the turbulent free-stream impacts on the gauge body (see Figure 7.25) the accelerated zone and the updraft and downdraft regions arise above the collector of the gauge.

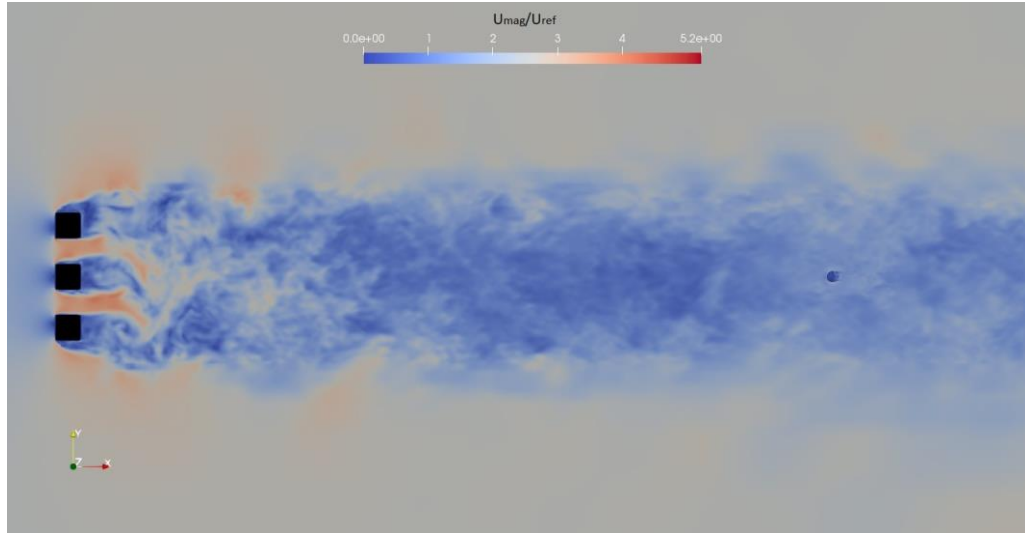


Figure 7.23 Normalized magnitude of the instantaneous flow velocity (U_{mag}/U_{ref}) in the horizontal plane (x,y) at the gauge collector elevation ($z/D = 0$) for the turbulent free-stream conditions.

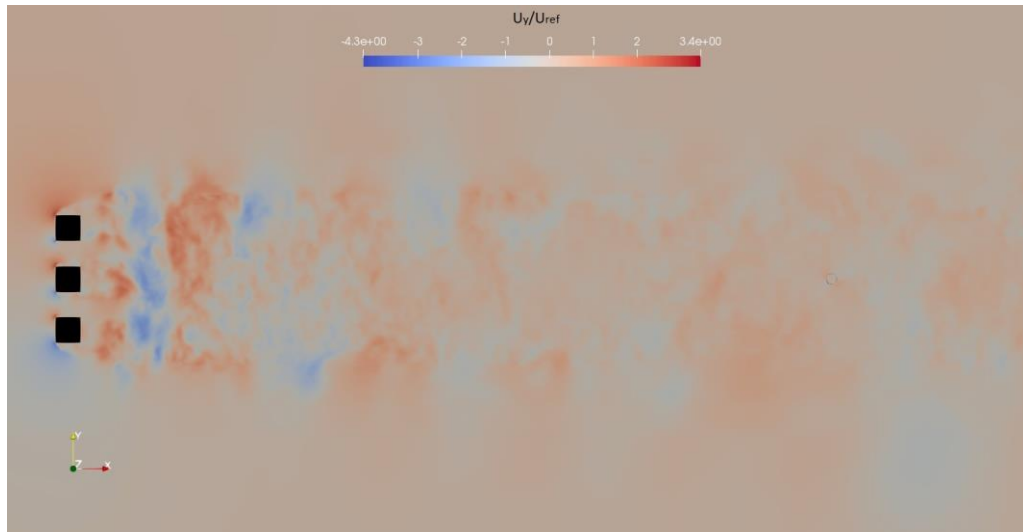


Figure 7.24 Normalized transversal component (U_y/U_{ref}) of the instantaneous flow velocity in the horizontal plane (x,y) at the gauge collector elevation ($z/D = 0$) for the turbulent free-stream conditions.

The two free-stream turbulence conditions are compared below in terms of catch ratios and collection efficiency. The Lagrangian Particle Tracking model (chapter 5) was run upon the LES airflow fields obtained for each free-stream turbulence condition. Dry snow particles were simulated with equivalent diameters $d = 0.25 - 0.5 - 0.75$ mm and from 1 to 8 mm. In order to ensure the comparability between the two cases the airflow field in uniform free-stream conditions was scaled by assuming a reference wind speed equal to 2.5 m s^{-1} instead of 6 m s^{-1} as obtained for the turbulent free-stream condition downstream of the three columnar obstacles.

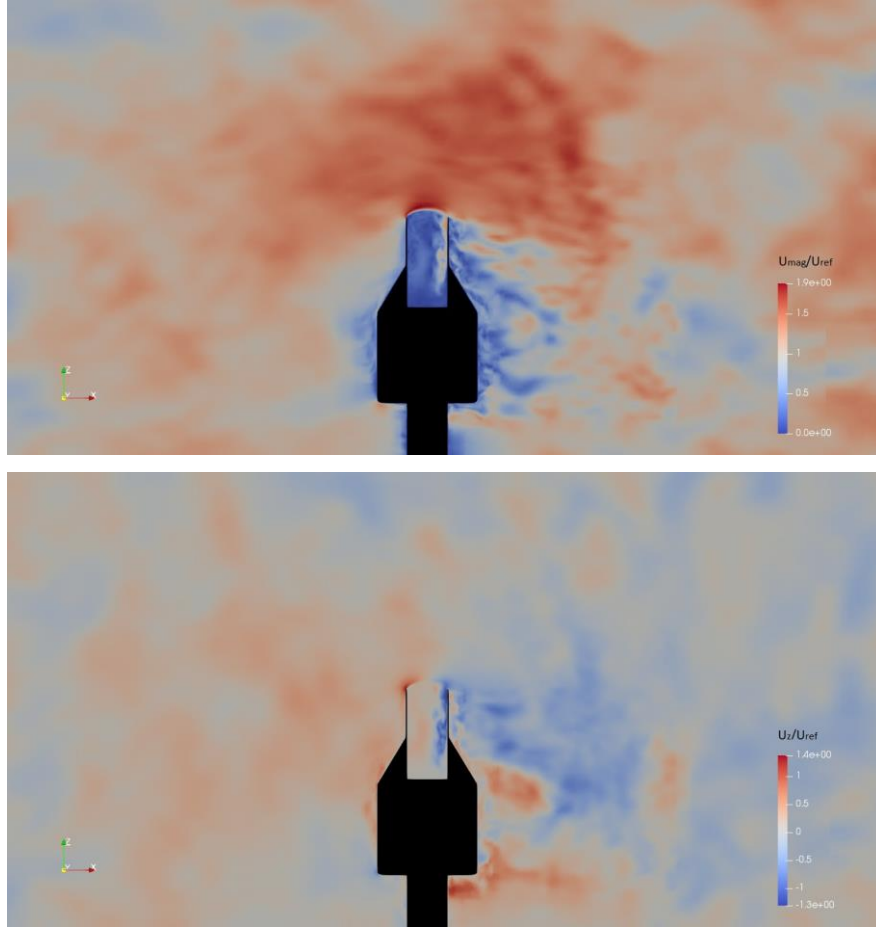


Figure 7.25 Normalized magnitude (U_{mag}/U_{ref} , top panel) and vertical component (U_z/U_{ref} , bottom panel) of the instantaneous flow velocity in the vertical plane (x,z) at $y/D = 0$ for the turbulent free-stream conditions.

The calculated catch ratios for each particle diameter are listed in Table 7.3 and depicted in Figure 7.26. From the comparison, a more pronounced undercatch emerges for small size particles (less than 2 mm) under turbulent free-stream conditions with respect to the uniform case, while the opposite occurs for larger particles ($d > 2$ mm). This is due to the greater aptitude of the small size particles to follow the turbulent velocity fluctuations, while larger particles are more inertial. The free-stream turbulence has two main effects: it reduces the aerodynamic effect of the wind-gauge interaction, with lower velocity components near the gauge body (as demonstrated in section 7.2), and introduces velocity fluctuations in all directions. When the particle size is small, particles are more sensitive to the turbulent fluctuations and therefore catch ratios in uniform free-stream conditions are larger than in turbulent conditions. With increasing the particle size, and therefore its terminal velocity, particle trajectories are less sensitive to the turbulent fluctuations. Moreover, in turbulent free-stream conditions, they cross a less disturbed airflow field so that catch ratios become larger than in uniform free-stream conditions.

The overall effect of the free stream turbulence on the collection performance of the gauge is quantified by computing the Collection Efficiency (CE) as the integral on the range of diameters after the introduction of the Particle Size Distribution (PSD) proposed by Houze et al. (1979) with $N_0 = 5 \times 10^6 \text{ m}^{-4}$ and $\Lambda = 0.5 \text{ mm}^{-1}$. The result, summarized in

Table 7.4 where an higher CE in turbulent free-stream conditions is observed, is in consistent agreement with the work of Cauteruccio et al. (2020), (section 7.2), where the free-stream turbulence effect was only investigated in terms of velocity and turbulence features of the airflow field.

Table 7.3 Catch ratios obtained for each solid particle size and $U_{ref} = 2.5 \text{ m s}^{-1}$ using the LPT model and based on the LES airflow fields for the *GeonorT200B*[®] precipitation gauge in uniform and turbulent free-stream conditions.

d [mm]	0.25	0.5	0.75	1	2	3	4	5	6	7	8
Uniform	0.190	0.393	0.449	0.492	0.590	0.659	0.708	0.734	0.757	0.787	0.787
Turbulent	0.164	0.164	0.216	0.289	0.590	0.718	0.777	0.820	0.849	0.869	0.892

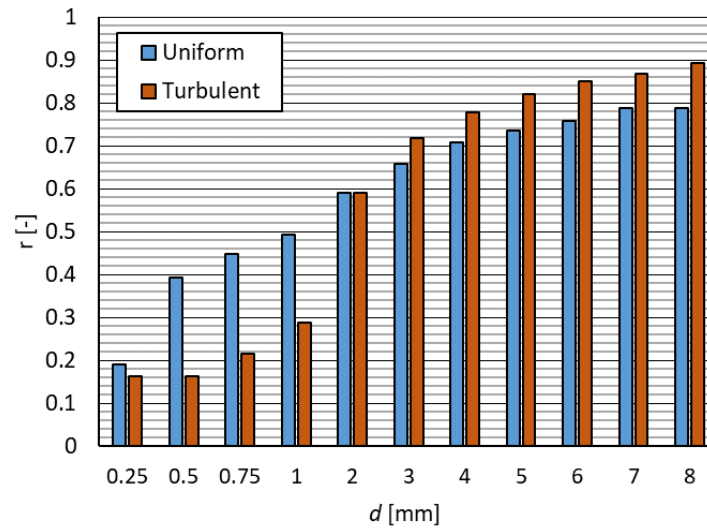


Figure 7.26 Comparison between catch ratios calculated for each solid particle size and $U_{ref} = 2.5 \text{ m s}^{-1}$ by means of the LPT model and based on the LES airflow fields for the *GeonorT200B*[®] gauge in uniform (blue) and turbulent (orange) free-stream conditions.

Table 7.4 CE for the *GeonorT200B*[®] gauge and for dry snow in uniform and turbulent free-stream conditions at $U_{ref} = 2.5 \text{ m s}^{-1}$.

Free-stream condition	Collection Efficiency
Uniform	0.70
Turbulent	0.76

CONCLUSIONS

The external design of catching type gauges has a major impact on the catch efficiency in windy conditions due to the bluff-body aerodynamics of their outer geometry, which can be initially investigated by using CFD simulations of the airflow field surrounding the gauge body. This thesis work first of all confirmed previous literature results and extended the numerical simulation exercise to cover further geometrical and wind shield configurations, and provided an extensive and satisfactory validation of the simulation results based on local measurements of the airflow velocity near the gauge collector. This was obtained in controlled, dedicated wind tunnel tests as described in Chapter 4 “*Computational fluid dynamic simulations*”. In order to address the most popular shapes of catching type gauges the investigated sample was composed of cylindrical, chimney-shaped and inverted-conical gauges, while also the aerodynamic response of a thermodynamic snow gauge and a *Nipher* shield were simulated. Numerical results revealed predominant upward velocity component and airflow acceleration in all cases suggesting that some deflection of the hydrometeor trajectories, which travel above the collecting area, is to be expected. Moreover, the wind shield confirmed its efficiency in reducing updraft and acceleration of the flow above the inside collector, while the chimney shaped gauge appeared the worst performing one. The comparison between flow velocity measurements conducted in the Wind Tunnel (WT) and CFD simulation results showed a very good agreement when the limitations of the *Cobra* probe measurements and the simplification of the numerical model adopted to solve the airflow field around the investigated gauge geometry are taken into account. WT measurements are characterized by an uncertainty of $\pm 0.3 \text{ m s}^{-1}$ and the minimum detectable velocity is 2 m s^{-1} , while the solution of CFD simulations depends on the discretization of the computational domain and the adopted turbulence model and solution scheme.

The influence of the airflow deformation on the trajectory of the approaching hydrometeors is evaluated by means of a Lagrangian Particle Tracking model, available from the literature, and here applied to a thermodynamic snow gauge geometry as described in Chapter 6 “*Numerical collection efficiency*”. It was shown that the resulting collection efficiency curve is peculiar with respect to the typical curves obtained for catching type gauges and that wind-induced errors are limited for this precipitation gauge. Then the literature Lagrangian Particle Tracking model was adapted to simulate the trajectories of water droplets when falling through the atmosphere and approaching the gauge collector using suitable drag coefficient equations as described in Chapter 5 “*Particle tracking model and wind tunnel validation*”. This allowed an easy to use and original collection efficiency formulation to be derived, as a function of wind speed and parameterized with the rainfall intensity, for a typical cylindrical gauge.

An innovative contribution of this thesis work is the design and implementation of a suitable validation setup for the numerical modelling of hydrometeors trajectories and their wind-induced deviation. For the first time water droplets were generated and tracked at high resolution in the wind tunnel, using a high speed camera, and their trajectories closely reproduced by means of the adopted numerical model, although falling at a reduced vertical velocity than the one expected in a natural environment (the terminal velocity). As described in Chapter 5, results showed that the adopted model and the formulation used for the drag coefficient are suitable for reproducing the observed behaviour of the hydrometeors when affected by the

airflow deformation due to the bluff-body aerodynamics of precipitation gauges, and can therefore be applied to derive their collection efficiency curves. Furthermore, the deviated trajectories of the drops detected in the wind tunnel allowed clear visualisation of the problem of the wind-induced undercatch by falling outside instead of inside of the collector, contrary to what would be expected by following their undisturbed trajectory.

Also innovative is the investigation of the effect of free-stream turbulence on the collection efficiency of precipitation gauges, which was systematically neglected hitherto in the literature. It was found that accounting for the turbulence intensity that is inherent to any natural wind field would have a smoothing effect on the deformation of the airflow by reducing the acceleration and upward velocity component and therefore limit the wind-induced undercatch to lower values than those obtained in uniform free-stream conditions. This was proved by means of numerical simulations using three different methods to introduce the desired level of turbulence intensity into the incoming airflow as described in Chapter 7 “*The role of free-stream turbulence*” for three different gauge geometries. In order to introduce a realistic level of free-stream turbulence in the simulations wind speed measurements, recorded in the field at high frequency (20Hz) and at the precipitation gauge elevation, were analysed and turbulence intensity levels for various wind speeds were derived. The overall free-stream turbulence effect on the collection performance of the gauges was quantified by computing and comparing the Collection Efficiency (CE) values in uniform and turbulent free-stream conditions. Results demonstrated that the CE values are higher in turbulent free-stream conditions. Therefore, it is possible to conclude that accounting for the free-stream turbulence in the simulation is needed to avoid overestimation of the wind-induced undercatch. This conclusion was supported in this thesis work by a robust validation obtained in the wind tunnel under turbulent free-stream conditions.

Finally, this thesis work allowed to derive adjustment curves for a typical cylindrical and the innovative thermodynamic gauges. These can be used for operational purposes in order to correct real-world measurements of both liquid and solid precipitation, by using wind velocity observations alone as the ancillary variable required to perform the adjustment. Wind velocity is indeed commonly measured by operational weather stations together with the precipitation intensity, and its use adds no relevant burden to the cost of meteo-hydrological networks.

Application of the results presented in this work spans over many fields of hydrology, meteorology, and climatology, including water resources and flood risk management and agriculture. Rainfall is indeed the forcing input of the land phase of the hydrological cycle. The knowledge of rainfall, its variability and the observed/expected patterns of rain events in space and time, are of paramount importance for most hydrological studies, and a large number of consequences of such studies on the engineering practice are exploited in the everyday technical operation. Results, especially the proposed adjustment curves, have the potential to improve liquid and solid precipitation measurements in order to support enhanced accuracy and reliability of the basic information used in many engineering applications such as the design of hydraulic works, the protection from flood related hazards, the management of potable water supply and its conservation, hydropower production, the enhancement of sustainability and resilience of human settlements and the conservation and protection of the natural and cultural heritage.

REFERENCES

- Alter, J.C., 1937: Shielded precipitation gages. *Mon. Wea. Rev.*, **65**.
- Bastamoff, S.L., and W.J., Witkiewitch, 1926: Les spectres aerodynamiques des pluviometres. *Bull. Geophysique de L'Institut des Recherches Geophyssiqls*, n.**10**, Moscow.
- Beard, K.V., 1976: Terminal velocity and shape of cloud and precipitation drops aloft. *J. Atmos. Sci.*, **33**, 851–864.
- Beard, K.V., and C. Chuang, 1987: A new model for the equilibrium shape of raindrops. *J. Atmos. Sci.*, **44**, 1509–1524.
- Belvins, R., 1990: Flow-induced vibration. *Independent Learning Module Ser.* Van Nostrand Reinhold Company.
- Blanchard, D.C., 1953: Raindrop size distribution in Hawaiian rains. *J. Meteor.*, **10**, 457–473.
- Brandes, E. A., K. Ikeda, G. Zhang, M. Schönhuber, and R. M. Rasmussen, 2007: A statistical and physical description of hydrometeor distributions in colorado snowstorms using a video disdrometer. *J. Appl. Meteor. Climatol.*, **46**(5), 634–650.
- Brooks, C.R., 1938: Need for universal standards for measuring precipitation, snowfall, and snow cover, *Bull. 23, Intern. Assn. of Hydrology, IUGG, Riga*.
- Buisán, S.T., M.E. Earle, J.L. Collado, J. Kochendorfer, J. Alastrué, M. Wolff, C.D. Smith, and J.I. López-Moreno, 2017: Assessment of snowfall accumulation underestimation by tipping bucket gauges in the Spanish operational network. *Atmos. Meas. Tech.*, **10**, 1079–1091.
- Calder, I.R., and C.H.R. Kidd, 1978: A note on the dynamic calibration of tipping-bucket gauges, *J. of Hydrol.* **39**, 383–386.
- Caracciolo, C., F. Prodi, A. Battaglia, and F. Porcù, 2006: Analysis of the moments and parameters of a gamma DSD to infer precipitation properties: A convective stratiform discrimination algorithm. *Atmos. Res.*, **80**, 165–186.
- Caracciolo, C., F. Porcù, and F. Prodi, 2008: Precipitation classification at mid-latitudes in terms of drop size distribution parameter. *Adv. Geosci.*, **16**, 11–17.
- Caton, P.G.F., 1966: A study of raindrop size distribution in the free atmosphere. *Quart. J. Roy. Meteor. Soc.*, **92**, 15–30.
- Cauteruccio A., M. Colli, M. Stagnaro, L.G. Lanza, and E. Vuerich 2019: In situ precipitation measurements in T. Foken (editor) *Springer Handbook of Atmospheric Measurements*, Part B: In-situ Measurement Techniques (in press), Springer Nature, pp. 35.

- Cauteruccio A., M. Colli, A. Freda, M. Stagnaro, and L.G. Lanza, 2020: The role of the free-stream turbulence in attenuating the wind updraft above the collector of precipitation gauges. *J. Atmos. Oceanic Technol.*, **37**, 103–113. DOI:10.1175/JTECH-D-19-0089.1.
- Chandrasekar, V., W.A. Cooper, and V.N. Bringi, 1988: Axis ratios and oscillation of raindrops. *J. Atmos. Sci.*, **45**, 1323–1333.
- Constantinescu, G.S., W.F. Krajewski, C. Ozdemir, and T. Tokyay, 2007: Simulation of airflow around rain gauges: comparison of LES with RANS models. *Adv. Water Resour.*, **30**, 43–58.
- Costello, T.A. and H. J. Williams, 1991: Short duration rainfall intensity measured using calibrated time-of-tip data from a tipping bucket raingage, *Agr. Forest Meteorol.*, **57**(1), 147–155.
- Colli, M., L.G. Lanza, and P.W. Chan, 2013: Co-located tipping-bucket and optical drop counter RI measurements and a simulated correction algorithm. *Atmos. Res.*, **119**, 3–12.
- Colli, M., L.G. Lanza, R. Rasmussen, J.M. Thériault, B.C. Baker, and J. Kochendorfer, 2015: An improved trajectory model to evaluate the collection performance of snow gauges. *J. Appl. Meteor. Climatol.*, **54**, 1826–1836.
- Colli, M., L.G. Lanza, R. Rasmussen, and J.M. Thériault, 2016a: The collection efficiency of shielded and unshielded precipitation gauges. Part I: CFD airflow modelling. *J. Hydrometeorol.*, **17**, 231–243.
- Colli, M., L.G. Lanza, R. Rasmussen and J.M. Thériault, 2016b: The collection efficiency of unshielded precipitation gauges. Part II: modeling particle trajectories. *J. Hydrometeorol.*, **17**, 245–255.
- Colli, M., M. Pollock, M. Stagnaro, L.G. Lanza, M. Dutton, and P.E. O’Connell, 2018: A Computational Fluid-Dynamics assessment of the improved performance of aerodynamic raingauges. *Water Resour. Res.*, **54**, 779–796.
- Colli, M., M. Stagnaro, J.M. Theriault, L.G. Lanza, and R. Rasmussen, 2020: Adjustments for Wind-Induced Undercatch in Snowfall Measurements based on Precipitation Intensity. *J. Hydrometeorol.*, (accepted).
- Constantinescu, G.S., W.F. Krajewski, C. Ozdemir, and T. Tokyay, 2007: Simulation of airflow around rain gauges: comparison of LES with RANS models. *Adv. Water Resour.*, **30**, 43–58.
- Counihan, J., J.C.R. Hunt, and P.S. Jackson, 1974: Wakes behind two-dimensional surface obstacles in turbulent boundary layers. *J. Fluid Mech.*, **64**(3), 529–563.
- EN, 2019: Hydrometry. Measurement requirements and classification of rainfall intensity measuring instruments, EN 17277:2019.
- Folland, C.K., 1988: Numerical models of the raingauge exposure problem, field experiments and an improved collector design. *Q.J.R. Meteorol. Soc.*, **114**, 1485–1516.

- Green, M.J. and P. R. Helliwell, 1972: The effect of wind on the rainfall catch. Distribution of precipitation in mountainous areas. *World Meteorological Organization*, Rep. **326**, Vol. 2, 27–46.
- Green, A.W., 1975: An approximation for the shape of large raindrops. *J. Appl. Meteor.*, **14**, 1578–1583.
- Habib, E., W.F. Krajewski, and A. Kruger, 2001: Sampling Errors of Tipping-Bucket Rain Gauge Measurements, *J. Hydrol. Eng.*, **6**(2), 159–166.
- Houze, R.A., P.V. Hobbs, P.H. Herzegh, and D.B. Parsons, 1979: Size distributions of precipitation particles in frontal clouds. *J. Atmos. Sci.*, **36**, 156–162.
- Jevons, W.S., 1861: On the deficiency of rain in an elevated rain-gauge, as caused by wind. *The London, Edinburgh, and Dublin Philosophical Magazine and Journal of Science*, **21**(4), 421–433.
- Jones, W.P., and B.E., Launder, 1972: The prediction of laminarization with a two-equation model of turbulence. *Int. J. Heat Mass. Tran.*, **15**, 301–314.
- Khvorostyanov, V.I., and J.A. Curry, 2005: Fall Velocities of Hydrometeors in the Atmosphere: Refinements to a Continuous Analytical Power Law. *J. Atmos. Sci.*, **62**, 4343–4357.
- Kiya, M., and K. Sasaki, 1983: Free-stream turbulence effects on a separation bubble. *J. Wind Eng. Ind. Aerodyn.*, **14**, 375–386.
- Kochendorfer, J., R. Rasmussen, M. Wolff, B. Baker, M. E. Hall, T. Meyers, S. Landolt, A. Jachcik, K. Isaksen, R. Brækkan, and R. Leeper, 2017a: The quantification and correction of wind-induced precipitation measurement errors. *Hydrol. Earth Syst. Sci.*, **21**(4), 1973–1989.
- Kochendorfer, J., R. Nitu, M. Wolff, E. Mekis, R. Rasmussen, B. Baker, M. E. Earle, A. Reverdin, K. Wong, C. D. Smith, D. Yang, Y.-A. Roulet, S. Buisan, T. Laine, G. Lee, J. L. C. Aceituno, J. Alastrué, K. Isaksen, T. Meyers, R. Brækkan, S. Landolt, A. Jachcik, and A. Poikonen, 2017b: Analysis of single-Alter-shielded and unshielded measurements of mixed and solid precipitation from WMOSPICE. *Hydrol. Earth Syst. Sci.*, **21**(7), 3525–3542.
- Koshmieder, H., 1934. Methods and results of definite rain measurements. *Mon. Weath. Rev.*, **62**(1), 5–7.
- Kumer, M.V., J. Reuder, M. Dörninger, R. Zauner, and V. Grubišić, 2016: Turbulent kinetic energy estimates from profiling wind LiDAR measurements and their potential for wind energy applications. *Renew. Energy*, **99**, 898–910.
- Lanza, L.G., and L. Stagi, 2008: Certified accuracy of rainfall data as a standard requirement in scientific investigations. *Adv. Geosci.*, **16**, 43–48.
- Lanza, L.G., and L. Stagi, 2009: High resolution performance of catching type rain gauges from the laboratory phase of the WMO Field Intercomparison of Rain Intensity Gauges. *Atmos. Res.*, **94**(4), 555–563.

- Vuerich, E., C., Monesi, L.G. Lanza, L. Stagi, and E. Lanzinger, 2009: WMO Field Intercomparison of Rainfall Intensity Gauges. *World Meteorological Organisation – Instruments and Observing Methods Rep. No. 99*, WMO/TD No. 1504, pp. 286.
- Löffler-Mang, M., D. Schön, and M. Landry, 2011: Characteristics of a new automatic hail recorder, *Atmos. Res.*, **100**(4), 439–446.
- Meikle, H., 1819: *Annals of Philosophy*, **14**, p. 312.
- Menter, F., 1993: Zonal two equation $k-\omega$ turbulence models for aerodynamic flows. *AIAA 24th Fluid Dynamics Conference*, **93**, p.2906.
- Mason, B.J., 1971: *The Physics of Clouds. 2nd edition*, Clarendon Press.
- Menter, F. and T. Esch, 2001: Elements of industrial heat transfer predictions. *COBEM 2001, 16th Brazilian Congress of Mechanical Engineering*.
- Marshall, J.S. and W.M.K. Palmer, 1948: The distribution of raindrops with size. *J. Meteorol.*, **5**, 165–166.
- Michaelides, S., V. Levizzani, E. Anagnostou, P. Bauer, T. Kasparis, and J.E. Lane, 2009: Precipitation: Measurement, remote sensing, climatology and modeling, *Atmos. Res.*, **94**(4), 512-533.
- Mueller, E., 1965: Radar rainfall studies. *Ph.D. dissertation*, University of Illinois.
- Mueller C.C. and E.H. Kidder, 1972: Rain gage catch variation due to airflow disturbances around a standard rain gage. *Water Resour. Res.*, **8**(4), 1077-1082.
- Nešpor, V. and B. Sevruk, 1999: Estimation of wind-induced error of rainfall gauge measurements using a numerical simulation. *J. Atmos. Ocean. Technol.*, **16**, 450 - 464.
- Øistad, I.S., 2015: Analysis of the Turbulence Intensity at Skipheia Measurement Station, *Master thesis*, Norwegian University of Science and Technology.
- Pollock, M.D., G. O'Donnell, P. Quinn, M. Dutton, A. Black, M.E. Wilkinson, M. Colli, M. Stagnaro, L.G. Lanza, E. Lewis, C.G. Kilsby, and P. E. O'Connell, 2018: Quantifying and mitigating wind-induced undercatch in rainfall measurements. *Water Resour. Res.*, **54**, 3863 - 3875.
- Pruppacher, H.R., and K.V. Beard, 1970: A wind tunnel investigation of the internal circulation and shape of water drops falling at terminal velocity in air. *Quart. J. Roy. Meteor. Soc.*, **96**, 247–256.
- Pruppacher, H.R., and D.K. James, 1997: Microphysics of clouds and precipitation, *Atmospheric and Oceanographic Sciences Library*, **18**, 955 pp.
- Rasmussen, R., J. Vivekanandan, J. Cole, and B.M.C. Masters, 1999: The estimation of snowfall rate using visibility. *J. Appl. Meteor.*, **38**, 1542–1563.
- Rasmussen, R.M., J. Hallett, R. Purcell, S. Landolt, and J. Cole, 2011: The hotplate precipitation gauge. *J. Atmos. Oceanic Technol.*, **28**, 148 - 164.

- Rasmussen, R., B. Baker, J. Kochendorfer, T. Meyers, S. Landolt, A. P. Fischer, J. Black, J. M. Theriault, P. Kucera, D. Gochis, C. Smith, R. Nitu, M. Hall, K. Ikeda, and E. Gutmann, 2012: How well are we measuring snow: The NOAA/FAA/NCAR winter precipitation test bed, *Bulletin of the American Meteorological Society*, **93**(6), 811-829.
- Robinson, A.C., and J.C., Rodda, 1969: Rain wind and aerodynamic characteristics of rain-gauges. *Meteorol. Mag.*, **98**, 113-120.
- Sanuki, M., N. Tsuda, and S. Kimura, 1952: Water tank and wind tunnel tests on rain gauge wind shield. *Pap. Met. Geophys.*, Tokyo, **3**, p.54.
- Sevruk, B., 1982: Methods of correction for systematic error in point precipitation measurement for operational use. *World Meteorological Organization*, Rep. **21**, 106 pp.
- Sims, E. M., and G., Liu 2015: A parameterization of the probability of snow–rain transition. *J. Hydrometeor.*, **16**(4), 1466-1477.
- Stagnaro, M., M. Colli, L. G. Lanza, P. W. Chan, 2016: Performance of post-processing algorithms for rainfall intensity using measurements from tipping-bucket rain gauges, *Atmos. Meas. Tech.*, **9**(12), 5699-5706.
- Stagnaro, M., Cauteruccio, A., Colli, M., Lanza, L. G. and P.W. Chan, 2018: Laboratory assessment of two catching type drop-counting rain gauges., *Geophysical Research Abstracts*, EGU General Assembly 20, EGU2018-12407.
- Strangeways, I., 2004: Improving precipitation measurement. *Int. J. Climatol.*, **24**, 1443–1460.
- Strangeways, I., 2006: Precipitation: theory, measurement and distribution (Cambridge University).
- Thériault, J.M., R. Rasmussen, K. Ikeda, and S. Landolt, 2012: Dependence of snow gauge collection efficiency on snowflake characteristics. *J. Appl. Meteor. Climatol.*, **51**, 745–762.
- Thériault, J.M., R. Rasmussen, E. Petro, J.Y. Trépanier, M. Colli, and L.G. Lanza, 2015: Impact of wind direction, wind speed, and particle characteristics on the collection efficiency of the double fence intercomparison reference, *J. Appl. Meteor. Climatol.*, **54**(9), 1918–1930.
- Ulbrich, C. W. 1983: Natural variations in the analytical form of the raindrop size distribution. *J. Appl. Meteor. Climatol.*, **22**, 1764–1772.
- UNI, 2012: Hydrometry - Measurement of rainfall intensity (liquid precipitation) - Metrological requirements and test methods for catching type gauges, UNI 11452:2012.
- Waldvogel, A., 1974: The N0 jump of raindrop spectra. *J. Atmos. Sci.*, **31**, 1067–1078.
- Warnik, C.C., 1953: Experiments with windshields for precipitation gages. *Transactions of the American Geophysical Union*, **34**(3), 379 - 388.

- Wilcox, D. C., 1988: Reassessment of the scale-determining equation for advanced turbulence models. *AIAA journal*, **26**(11), 1299–1310.
- Wilcox, D.C., 2006: Turbulence Modeling for CFD. *D C W Industries*, 3rd edition.
- WMO – World Meteorological Organization, 2014 (updated 2017): Guide to Meteorological Instruments and Methods of Observation. WMO-N. 8, ISBN 978-92-63-10008-5.
- WMO – World Meteorological Organization, 2018: Solid Precipitation Intercomparison Experiment. IOM Report – N. 131.
- Wolff, M.A., K. Isaksen, A. Petersen-Øverleir, K. Ødemark, T. Reitan and R. Brækkan, 2015: Derivation of a new continuous adjustment function for correcting wind-induced loss of solid precipitation: results of a Norwegian field study. *Hydrol. Earth Syst. Sci.*, **19**, 951–967.
- Yuter, S.E., D.E. Kingsmill, L.B. Nance, and M. Löffler-Mang, 2006: Observations of precipitation size and fall speed characteristics within coexisting rain and wet snow. *J. Appl. Meteor. Climatol*, **45**(10), 1450–1464.